

Spring 2021

Degradative Processes of Commercial and Next-Generation Lithium-Ion Battery Materials

Benjamin Ng

Follow this and additional works at: <https://scholarcommons.sc.edu/etd>



Part of the [Chemical Engineering Commons](#)

Recommended Citation

Ng, B.(2021). *Degradative Processes of Commercial and Next-Generation Lithium-Ion Battery Materials*. (Doctoral dissertation). Retrieved from <https://scholarcommons.sc.edu/etd/6372>

This Open Access Dissertation is brought to you by Scholar Commons. It has been accepted for inclusion in Theses and Dissertations by an authorized administrator of Scholar Commons. For more information, please contact dillarda@mailbox.sc.edu.

DEGRADATIVE PROCESSES OF COMMERCIAL AND NEXT-GENERATION
LITHIUM-ION BATTERY MATERIALS

by

Benjamin Ng

Bachelor of Science
University of Connecticut, 2017

Submitted in Partial Fulfillment of the Requirements

For the Degree of Doctor of Philosophy in

Chemical Engineering

College of Engineering and Computing

University of South Carolina

2021

Accepted by:

William E. Mustain, Major Professor

Ralph E. White, Committee Member

Kevin Huang, Committee Member

John Regalbuto, Committee Member

Melissa Moss, Committee Member

Tracey L. Weldon, Interim Vice Provost and Dean of the Graduate School

© Copyright by Benjamin Ng, 2021
All Rights Reserved.

ACKNOWLEDGEMENTS

Over the course of many years, and through all the excitement, laughter, hopes and dreams, disappointment, fear, battle, and perseverance, I take another look at this torch that is in my hand, and to see now, I am ready to pass it on to the next person. The flashbacks come rushing back, like running your thumb through the pages of a book and un-encapsulating those small time capsules that are sealed in the form of memories. I had very few people throughout my life that were willing to go that extra mile to mentor, to mold, to push me like I never pushed before, and to assure than my mentor William Mustain. Bill, I want to pause, and take a moment to thank you for being that pivotal person, that critical eye, and that simultaneously big pictured, deep brained, and curious person that you are for all these years. I am deeply grateful.

Next, I want to thank Paul Coman and Ralph White, whose collaboration with Bill taught me to juggle many new ideas and taught me how to execute each idea to the best of my capability. Paul and Ralph, I want to thank you for the exciting projects, guidance, and all the fun times we had, and may we continue that into the future. I also want to thank Scott Roberts for the opportunity and mentorship during my time at Sandia National Labs - especially all the trials and difficulties during the COVID-19 pandemic. Next, I want to thank my Committee members Kevin Huang and John Regalbuto for their continuous support, critical thinking, and guidance along this journey. And finally, I have to give a special thanks to all my friends and colleagues that were monumental in my success

(Alessandro Palmieri, Xiong Peng, Ehsan Faegh, Sujan Shrestha, Xinfang Jin, Travis Omasta, Yiwei Zheng, Niloofar Kamyab, Hori Adabi Firouzjaie, Noor Ul Hassan, Hanna Soucie, Saheed Lateef, Golareh Jalilvand, Emanuele Magliocca, Lyzmarie Colon, Xinyi Zhao).

For prospective people, the journey is much like a marathon, and that there is wisdom in everything. “Even when the man with the hammer comes swinging, we endure, and through that endurance, we find out who we truly are, and that those boundaries are just defined by us.” – Analogous to “*der Mann mit dem Hammer*” and referring to when your glycogen-levels severely deplete in your liver and muscles during a marathon and you hit a wall - but you keep pushing forward.

ABSTRACT

The work embodied in this thesis bridges the gap between modern and next-generation Li-ion batteries (LIBs). First, a detailed study of the complex interfacial interactions (e.g. electrode/electrolyte, particle/particle, particle/solid-electrolyte interphase) in existing LIBs (graphite anode, $\text{Li}(\text{Ni}_{0.5}\text{Mn}_{0.3}\text{Co}_{0.2})\text{O}_2$ cathode) are investigated and then used to develop strategies for safer, more energy-dense, and more durable electrode materials (i.e. tailored hybrid materials). The first portion of this thesis focuses heavily on decoupling the complex thermodynamics, reaction kinetics, and mass transport properties in commercially available LIBs. This thesis includes a detailed investigation into the operating parameter space for LIBs, including temperature (-30°C to $+52^\circ\text{C}$), state-of-charge (SOC, 0% to 100%), applied currents, and lifetime (>1000 cycles). Fundamental parameters are extracted from experimental data and implemented into two different computational models (tau lumped model and pseudo-2D model) to provide system-level predictions and isolate the inherent loss mechanisms that hinder performance, such as electrical conduction, lithium diffusion, electrolyte diffusion, and charge transfer resistance.

The next section of this thesis applies a large suite of characterization tools – including microscopy, multiple-location liquid N_2 Raman spectroscopy, gas chromatography/mass spectroscopy, and X-ray photoelectron spectroscopy – to probe complex reactions that lead to cell failure. Modern LIBs, particularly commercial cells

with large electrodes, can experience severe gassing, Li-plating, and anisotropic lithiation/delithiation. These negative behaviors can trigger a cascade of complex reactions that lead to thermal runaway. Such reactions include high surface area plated Li with the organic electrolyte (ethylene carbonate, dimethyl carbonate, diethyl carbonate, lithium hexafluorophosphate) under charge/discharge vs. open circuit storage. Electrolyte decomposition reactions can also occur that result in the release of large volumes of CO₂, H₂, O₂, CO, CH₄, C₂H₄, and C₂H₆ gases, which causes drastic morphological and microstructural changes to the electrode. Also, the severe polarization of the electrode at low temperatures can cause significant Li⁰ residence at high-stress regions (i.e. high curvature, edges, electrode ripples).

A paradigm shift is needed to move past the limiting factors that plague current LIB systems (e.g. low-moderate energy densities and inherent safety risks realized in Chapter 2 - Chapter 4). A search for new materials is required to meet the demands of the future. Conversion-based materials – such as transition metal sulfides, fluorides, and oxides – that leverage bond-breaking reactions are promising candidates to provide higher gravimetric and volumetric energy densities in comparison to the incumbent intercalation-based materials. Conversion materials also have a higher redox potential (~1V vs Li/Li⁺), which additionally provides protection from Li-plating, resulting in safer batteries. However, in the literature, conversion-based materials have suffered from poor reaction reversibility that can lead to short battery life. Chapter 5 applies electroanalytical techniques and electron transfer theory to probe the reaction mechanisms that form the solid electrolyte interphase (SEI) and the conversion reaction for one conversion-based anode material, NiO. First, a combination of physical and electro-analytical techniques were used to

investigate the SEI formation, which is the predominant capacity-degrading process in LIBs. One of the most important methods was the current-pulse relaxation method via galvanostatic intermittent titration technique (GITT), which allows for both diffusion and kinetics to be quantified along the reaction pathway (0%-100% SOC). Also, the Butler-Volmer (BV) and Marcus-Hush-Chidsey (MHC) models are used to investigate the effective transfer coefficients and reaction reorganizational energies. This information is used to provide new mechanistic insight into the rate-determining step and the SEI formation reaction pathway at different SOC and to compare the SEI formation chemistry with modern materials.

In addition to SEI formation, conversion materials undergo other degradative processes as well, including metal (charge) trapping, transformation of the transition metal in the oxide (NiO) to higher oxidation states, and agglomeration-induced loss of electrochemically active sites. Taking that into consideration, Chapter 5 introduces a new concept that isolates the NiO from the electrolyte, effectively eliminating all of the above-mentioned degradation mechanisms. This concept uses nanoconfinement of the conversion-based anode inside of small diameter carbon nanotubes. The CNT host was found to provide a termination-length for the SEI by specifically isolating the active material from the bulk electrolyte. In addition, the CNT host provides long-range interparticle electronic conductivity and immobilizes the reactants/products to one semi-closed packet. The result is a very high-capacity material (ca. 700 mAh g⁻¹) with very high coulombic efficiency (> 99.9%) that also has the ability for long-term operation (> 2000 deep charge/discharge cycles between 0-100% SOC at 1C).

Chapters 7 and 8 of this thesis are meant to provide some perspective on the state of the technology and where it is going. More specifically, Chapter 7 is a summary of all the fundamental findings in this work. Chapter 8 proposes future work that can be done to achieve long-life, high energy density lithium-ion batteries in the near future.

TABLE OF CONTENTS

ACKNOWLEDGEMENTS	iii
ABSTRACT.....	v
LIST OF TABLES.....	xii
LIST OF FIGURES	xv
LIST OF SYMBOLS.....	xxv
CHAPTER 1: INTRODUCTION TO LI-ION BATTERIES.....	1
1.1 ELECTROCHEMISTRY OF COMMERCIAL LI-ION BATTERIES	3
1.2 INTERCALATION REACTION MECHANISMS	7
1.3 AGING MECHANISMS AND TEMPERATURE EFFECTS IN LIBs.....	10
1.4 CAPACITY LIMITATIONS WITH INTERCALATING MATERIALS IN LIBS	13
1.5 SELECTION OF NEXT-GENERATION BATTERY MATERIALS	13
1.6 THEORETICAL FRAMEWORK FOR UNDERSTANDING THE PERFORMANCE AND LOSS MECHANISMS OF LI-ION BATTERIES.....	22
CHAPTER 2: DECONVOLUTION OF THE THERMODYNAMIC, KINETIC, AND TRANSPORT PROPERTIES FROM COMMERCIAL LARGE FORMAT LI-ION BATTERIES	28
2.1 EXPERIMENTAL	31
2.2 EXTRACTED COMMERCIAL BATTERY PARAMETERS	35

2.3 ELECTROCHEMICAL-THERMAL MODEL: PERFORMANCE PREDICTIONS OF COMMERCIAL LI-ION BATTERIES	44
2.4 SUMMARY	52
CHAPTER 3: INVESTIGATION OF THE KINETIC AND TRANSPORT NON-IDEALITIES IN COMMERCIAL LI-ION ELECTRODES - DECONVOLUTING COMPLEX ELECTROCHEMICAL IMPEDANCE SPECTROSCOPY DATA.....	
3.1 EXPERIMENTAL EXTRACTION OF ELECTRODE-LEVEL PARAMETERS.....	56
3.2 PERTURBATION FORM OF PSEUDO-2-DIMENSIONAL MODEL	62
3.3 PARAMETER ESTIMATION	62
3.4 EIS MODEL PARAMETERS.....	63
3.5 THERMODYNAMIC NONIDEALITY.....	69
3.6 IMPORTANCE OF INTEGRATING NONIDEALITY INTO PHYSICS- BASED MODELS.....	71
3.7 SUMMARY	73
CHAPTER 4: EXTREME OPERATION OF LI-ION BATTERIES	
4.1 FAILURE MODES	77
4.2 LITHIUM PLATING MECHANISM AND RAPID BATTERY DEGRADATION OF COMMERCIAL LI-ION BATTERIES UNDER LOW TEMPERATURE	78
4.3 EXPERIMENTAL	79
4.4 RESULTS AND DISCUSSION.....	82
4.5 SUMMARY	100
CHAPTER 5: STRATEGIC DESIGN OF DURABLE, SAFE, ENERGY DENSE LIB ANODES	
	101

5.1 MATERIAL SELECTION AND DESIGN STRATEGIES	102
5.2 THE STRUCTURE AND CHEMISTRY OF THE SOLID ELECTROLYTE INTERPHASE	103
5.3 EXPERIMENTAL AND THEORETICAL FRAMEWORK	108
5.4 RESULTS AND DISCUSSION.....	114
5.5 SUMMARY	135
CHAPTER 6: AVOIDING THE SOLID ELECTROLYTE INTERPHASE DEGRADATION MECHANISM IN NEXT GENERATION CONVERSION ANODES	136
6.1 EXPERIMENTAL	138
6.2 RESULTS AND DISCUSSION.....	145
6.3 SUMMARY	160
CHAPTER 7: CONCLUSIONS.....	163
CHAPTER 8: RECOMMENDATION FOR FUTURE WORK.....	168
8.1 PARAMETERIZATION OF NEXT-GENERATION LI-ION BATTERIES.....	169
8.2 LI-SULFUR BATTERIES	175
8.3 IMPLEMENTING AN ION-EXCHANGE TRAPPING AGENT TO STOP THE POLYSULFIDE DEGRADATION PROCESS	181
8.4 <i>OPERANDO</i> TECHNIQUES FOR STUDYING THE CORROSION OF Li^0 ELECTRODEPOSITS IN LI/S BATTERIES	185
REFERENCES.....	190
APPENDIX A: COPYRIGHT & PERMISSIONS	208

LIST OF TABLES

Table 1.1. United States Advanced Battery Consortium (USAB) goals for advanced high-performance batteries for electric vehicle (EV) applications in 2023 ¹⁰	2
Table 1.2. Summary of the energy density of commercial and commonly proposed next-generation Li-based batteries.	6
Table 1.3. Reaction description and mechanism for the transport of Li ⁺ from the bulk electrolyte to the conversion of NiO to Ni.....	18
Table 2.1. Table showing the atomic ratio of Li, Co, Ni, Mn in the cathode and anode obtained by ICP-OES.	33
Table 2.2. List of parameters measured experimentally.	36
Table 2.3 Table showing the dimensions of the 50Ah cell and the 1000Hz AC ohmic resistance measurement.	41
Table 2.4 Table showing the method used to measure the average active material loading of the anode and the cathode.....	43
Table 2.5 Table showing the equations in the lumped model from Ekström et al. ⁷⁴	45
Table 2.6 Model parameters calculated using the Levenberg-Marquardt optimization method.	49
Table 2.7 Parameters used for model.	51

Table 3.1 Perturbation form of the Lithium-Ion battery P2D model	61
Table 3.2 Parameters used in the EIS Model.	63
Table 3.3 Optimized parameters.....	65
Table 3.4 Parameters used in Fitting of A in Figure 3.9	68
Table 3.5 Advantages and Disadvantages of different model techniques.....	74
Table 4.1. Presents the spatial heterogeneity of both the $\text{Li}(\text{Ni}_{0.5}\text{Mn}_{0.3}\text{Co}_{0.2})\text{O}_2$ cathode and graphite anode for the full jellyroll analysis.	88
Table 4.2 Transition metal speciation for various regions (e.g. edge, center, curvature) of surface $\text{Li}(\text{Ni}_{0.5}\text{Mn}_{0.3}\text{Co}_{0.2})\text{O}_2$ and Li_xC_6	99
Table 4.3 Mass and atomic percentages (%) of the elements Li, P, C, O, F, Mn, Co, and Ni at different regions for $\text{Li}(\text{Ni}_{0.5}\text{Mn}_{0.3}\text{Co}_{0.2})\text{O}_2$ and Li_xC_6 from XPS spectra analysis after non-thermal runaway venting.....	99
Table 5.1. Hypothetical generalized mechanism where n is the total number of e^- , γ is the number of e^- before RDS, γ' is the number of e^- after RDS, and ρ is either 0 (chemical) or 1 (electrochemical) ^{180,183}	115
Table 5.2. Tafel calculations of α_{eff} for Vulcan XC-72R carbon black.	120
Table 5.3. Effective transfer coefficient calculated by Tafel slope and reorganizational energy calculated by the low overpotential approximation for the Marcus-Hush-Chidsey theory	128
Table 5.4. Mechanistic insight in the reaction pathway for Region IV ($2.2 < x < 2.8$), showing chemical (C) and electrochemical (E) steps.	133
Table 6.1. Evaluation of Oxidation States. The overall reaction pathways associated with various degrees of constraints of confinement of metal oxides.	162

Table 8.1 | Reactions in Li/S batteries..... 176

LIST OF FIGURES

- Figure 1.1.** | Diagram elucidating the operating principles of a Li-ion battery with the conventional anode (e.g. graphite, $\text{Li}_4\text{Ti}_5\text{O}_{12}$), cathode materials (e.g. LiCoO_2 , Li_2MnO_3), and electrolyte (e.g. LiPF_6 in organic carbonates). Reproduced with permission from IOP Publishing¹¹ 4
- Figure 1.2.** | Atomic structure of Lithium intercalation in graphitic carbon (LiC_x) and showing, (a) the top view, (b) side view of stage-2 LiC_{18} , (c) top view, (d) side view of stage-3 LiC_{18} , (e) LiC_{12} , and (f) LiC_6 . Reproduced with permission from IOP Publishing.¹⁷ 8
- Figure 1.3.** | Comparison of layered, disordered rocksalt, and spinel cation ordering. Reproduced with permission from John Wiley and Sons¹⁸ 9
- Figure 1.4.** | Depicts the instability of the anode interface under high and low temperatures. High temperatures can result in (a) deterioration of the SEI, (b) decomposition of the electrolyte and release of gas, (c) transition metal dissolution from cathode and reaction at anode, (d) severe chemical changes to the SEI. Low temperatures can cause (e) severe anode polarization to drive Li-plating, and (f) reduced reaction kinetics and increase in SEI resistances. Reproduced with permission from Macmillan Publishers Ltd²³ 11
- Figure 1.5.** | Depicts the instability in the structure of cathode materials at different temperatures (red = high T and blue = low T). The cathodes include (a) LiCoO_2 , (b) $\text{LiNi}_{1/3}\text{Mn}_{1/3}\text{Co}_{1/3}\text{O}_2$, (c) spinel LiMn_2O_4 , and olivine LiFePO_4 . Reproduced with permission from Macmillan Publishers Ltd²³ 12
- Figure 1.6.** | Anode selection list and their theoretical capacities. Reproduced with permission from Royal Society of Chemistry.³⁰ 16

Figure 1.7. Depicts the conversion reaction mechanism with MF_3 as a representative material. The conversion process involves limited diffusion of the anion (e.g. F, O, N, P, etc.) to react with the Li^+ during charge which generates metal (M) crystals and $Li_{\pi}X$. Reproduced with permission from Macmillan Publishers Ltd ³¹	16
Figure 1.8. Typical energy landscape (a) diffusion; (b) reaction. ⁴⁹	25
Figure 2.1. Photograph of (a) the large format 50 Ah prismatic cell and (b) one of two jelly rolls	32
Figure 2.2. Physical and Electrochemical Characterization. Field-emission scanning electron microscope (FE-SEM) of (a,b) NMC532 cathode, and (c) galvanostatic intermittent titration technique (GITT) for the open circuit potential (OCP) of the cathode. (d,e) FE-SEM images of graphite anode and (f) GITT for the OCP of the anode. Reproduced with permission from Elsevier. ⁷⁸	37
Figure 2.3. Entropic Heat Coefficient Calculations. Open circuit potential (OCP) changes due to temperature (T) for the calculation of $dUdT^{-1}$ at various state of charge (SOC). Reproduced with permission from Elsevier. ⁷⁸	38
Figure 2.4 Extracting Modeling Parameters at Different SOC and Temperatures. (a) Open circuit potential, (b) Area independent diffusivity (S^2D), (c) exchange current (i_0S), and (d) internal resistance (R_{IR}) for 50Ah cells at different SOC (100% to 0%) and at varying temperatures (-15°C to 45°C). Reproduced with permission from Elsevier. ⁷⁸	39
Figure 2.5. Modeling Parameters and Cycling Profile. (a) Represents the average exchange current (red line), area independent diffusivity (black line), and ohmic resistance (blue line), (b) entropic heat coefficient at different state of charge, and (c) CC-CP charge-discharge profile with temperature measurements on the 50Ah cell terminal and casing body. Reproduced with permission from Elsevier. ⁷⁸	44
Figure 2.6. Plot showing the cell potential calculated using the TLM and the potential measured experimentally for a discharge process of 0.3C. Reproduced with permission from Elsevier. ⁷⁸	48

Figure 2.7. Plots showing the cell temperature calculated using the TLM and the potential measured experimentally for a CC discharge process of 0.3C when a) the reversible term is included and b) when the reversible term is neglected. Reproduced with permission from Elsevier. ⁷⁸	48
Figure 2.8. Plot showing the cell potential calculated using the TLM and the potential measured experimentally for a discharge process of 0.3C using the measured internal resistance and the exchange current at 25°C. Reproduced with permission from Elsevier. ⁷⁸	50
Figure 2.9. Plots showing the cell potentials calculated using the TLM and the potential measured experimentally for a) a discharge process of 0.5C and for b) a discharge process of 1C, using the measured internal resistance and the exchange current at 25°C. Reproduced with permission from Elsevier. ⁷⁸	51
Figure 3.1. Schematic of a Li-ion half-cell PBM. The porous electrodes are formed by spherical insertion particles. Reproduced with permission from IOP Publishing. ⁹⁸	55
Figure 3.2. Images depicting the teardown process with (a) Ar-filled MBraun glovebox <0.1 ppm H ₂ O and O ₂ , (b) side view of the 2 jelly rolls, (c) tab orientation, and (d) a face view of a jellyroll.	57
Figure 3.3. a) SEM images of electrode cross-sections; b) the box and whisker graph of particle size and one side electrode thickness; (c) the cumulative pore area and porosity distribution of cathode, anode, and separator calculated from mercury intrusion porosimetry.	58
Figure 3.4. Potential vs current experimental data and fitting of the electronic conductivity of NMC532.	60
Figure 3.5. Model and Experimental data comparison in (a) complex plan (Nyquist) plot, (b) magnitude of impedance (Z), and (c) phase angle (θ). Reproduced with permission from IOP Publishing. ⁹⁸	64

Figure 3.6. Comparing the Nyquist plots from model and experimental data with 95% Confidence Intervals under different x_{Li} of the cathode: a) $x_{Li} = 0.96$, b) $x_{Li} = 0.89$, c) $x_{Li} = 0.81$, d) $x_{Li} = 0.74$, e) $x_{Li} = 0.66$, f) $x_{Li} = 0.59$, g) $x_{Li} = 0.52$, h) $x_{Li} = 0.47$, and i) $x_{Li} = 0.40$. Reproduced with permission from IOP Publishing. ⁹⁸	66
Figure 3.7. Optimized Parameters as a function of OCV for (a-f) $A_{k,cathode}$, $A_{k,anode}$, $A_{c,cathode}$, $A_{c,anode}$, $A_{D,cathode}$, and A_R . Reproduced with permission from IOP Publishing. ⁹⁸	66
Figure 3.8. Sensitivity of each parameter. Reproduced with permission from IOP Publishing. ⁹⁸	67
Figure 3.9. Relative pre-factors for k and D for the cathode. Reproduced with permission from IOP Publishing. ⁹⁸	68
Figure 3.10. $d \ln y dx_{Li}$ as a function of x_{Li} obtained from Equation 2.30. Reproduced with permission from IOP Publishing. ⁹⁸	70
Figure 3.11. GITT measurement of NMC532 half-cell during the charging/discharging cycles Reproduced with permission from IOP Publishing. ⁹⁸	71
Figure 3.12. Comparison between different pre-factors: (a) discharge profiles (Current=1C); (b) overpotentials; (c) x_{Li} concentration profiles in active particles at the end of discharge. Reproduced with permission from IOP Publishing. ⁹⁸	72
Figure 4.1. New European Driving Cycle (NEDC) speed correlations to current for a given 1200s experiment.	76
Figure 4.2 Schematic of low-temperature Li^0 plating and gas generation over repetitive cycling and subsequent over-pressurized venting after room-temperature recovery. Reproduced with permission from American Chemical Society. ¹³⁰	78

Figure 4.3. | Low temperature electrochemical and thermal analysis on the effects of Li^0 plating and gas generation. (a) Cycle performance and coulombic efficiency during temperature transitions ($\text{RT} \rightarrow -29^\circ\text{C} \rightarrow \text{RT}$), (b) charge-discharge profile highlighting the temperature transitions and charge/discharge currents (i.e. characteristic no plating curve at 2.5 A and other plating curves at 15A), (c) internal resistance measured by AC-1000Hz method and relaxation voltage before discharge, (d) Q_{max} normalized differential capacity analysis to decouple the no Li^+ stripping characteristic curve and identify Li^+ stripping peaks⁷⁹ under the more extreme charge/discharge current (15A), and (e) temperature recovery back to RT and cycling results catastrophic venting that causes the cell to internally shutdown. Reproduced with permission from American Chemical Society.¹³⁰ 83

Figure 4.4. | Plot showing (a) the gases accumulated during cycling, as detected by the Gas chromatography-Mass spectrometry (GC-MS) analysis of post-mortem electrodes and (b) proposed Li^0 corrosion reaction mechanism for gas generation. Reproduced with permission from American Chemical Society.¹³⁰ 87

Figure 4.5. | SEM images of different areas on the surface of the anode reveal high spatial anisotropy of low-temperature Li^0 plating/gas generation and the sample collection regions on the Li_xC_6 negative electrode at the center with near-tab, center, far-edge, and curvature designations. Reproduced with permission from American Chemical Society.¹³⁰ 89

Figure 4.6. | Enhanced optically filtered images of (a) $\text{Li}(\text{Ni}_{0.5}\text{Mn}_{0.3}\text{Co}_{0.2})\text{O}_2$ and (b) Li_xC_6 , and multi-location liquid nitrogen Raman spectroscopy of the respective electrodes after non-abuse conditions (room temperature) and post-mortem (low temperature) to analyze spatial distribution of chemical species, state of charge, and electrolyte degradation products. Reproduced with permission from American Chemical Society.¹³⁰ 93

Figure 4.7. | X-ray photoelectron spectroscopy analysis of (a) Ni 2p, Mn 2p, O 1s, C 1s for $\text{Li}(\text{Ni}_{0.5}\text{Mn}_{0.3}\text{Co}_{0.2})\text{O}_2$, and (b) Ni 2p, Li 1s, O 1s, C 1s for graphite electrodes after -29°C cycling and non-thermal runaway over-pressurization and venting. Reproduced with permission from American Chemical Society.¹³⁰ 96

Figure 5.1 | Energy diagram of a Li-ion battery and reaction mode inside the electric double layer (pre-cycled) and the solid electrolyte interphase (post-cycled). The schematic captures the interfacial dynamics in the inner/outer Helmholtz plane (I/O-HP) and shows desolvated Li^+ transport through the SEI. Adapted from ^{165,166} Reproduced with permission from The Royal Society of Chemistry.¹⁶⁷ 105

Figure 5.2. | Represents (a) charge/discharge curves for Vulcan XC-72R carbon black, (b) Tafel-like plots with Butler-Volmer (solid line) and Marcus-Hush-Chidsey (dashed lines) models on-top of experimental data (dots), and (c) illustration of the interfacial structure of carbon during initial charge stages and reaction mechanism as proposed by (Wang et al.¹⁸⁶). The reaction mechanism designations are C = chemical step, E = electrochemical step, D = dimerization reaction, and a double line highlight the rate-determining step. Reproduced with permission from The Royal Society of Chemistry.¹⁶⁷ 119

Figure 5.3. | Depicts galvanostatic intermittent titration technique for the parameter extraction of (a) apparent diffusion coefficient and (b) the apparent exchange current. Both plots contain the open circuit potential of NiO marked in (blue). Each section contains a dot that indicates locations where linear sweep voltammetry is done. Four sections are broken down (I, II, III, IV) to delineate dominant mechanisms. Also, high-resolution transmission electron microscopy is depicted as (c) TEM of post-cycled NiO. The atomic resolution HRTEM is depicted in (d) for the Ni domain ($\sim 2.1\text{\AA}[111]$, $\sim 1.8\text{\AA}[200]$) and (e) for the NiO domain ($2.4\text{\AA}[111]$, $2.0\text{\AA}[200]$). The Fast Fourier Transform (FFT) analysis of the HRTEM (f) for Ni and (g) for NiO. (h) Depicts the schematic for NiO particle transformation and showing the conversion reaction front propagation for the particle-level HRTEM image in **Figure 5-3c** (i.e. lithiation propagates from the bulk electrode until the reaction front stops due to high local polarization (i.e. the electrical losses generate a termination distance) and resulting in trapped charge). Reproduced with permission from The Royal Society of Chemistry.¹⁶⁷ 125

Figure 5.4. | Represents Tafel-like plots for Butler-Volmer (solid line) and Marcus-Hush-Chidsey (dashed lines) models on-top of experimental data (dots). Reproduced with permission from The Royal Society of Chemistry.¹⁶⁷ 127

Figure 5.5. | High-resolution XPS spectra of (a) pre-cycled and (b) post-cycled NiO electrodes in the Ni 2p, C 1s, and O 1s spectra. Reproduced with permission from The Royal Society of Chemistry.¹⁶⁷ 130

Figure 5.6. | Transmission electron microscopy was used in (c) which represents the post-cycle surface mesostructure and highlights high anisotropy in SEI formation, (d) high resolution of the SEI, (e) energy-dispersive X-ray spectroscopy, and elemental mapping of the SEI. Reproduced with permission from The Royal Society of Chemistry.¹⁶⁷ 134

Figure 6.1. | Physical and Electrochemical Characterization. (a) SEM, (b) TEM/EDS of NiO/C. (c) X-Ray Diffraction (XRD) patterns comparing the crystallography (e.g. crystallite domain size, structure) of NiO/C (blue line), ID-NiO/CNT (green line), and NC-NiO@CNT₅₀ (purple line). (d) SEM and (e) TEM/ESC of ID-NiO/CNT. (f) Comparing the capacity retention of NiO/C (blue line), ID-NiO/CNT (green line), and NC-NiO@CNT₅₀ (purple line) at 1C charge/discharge rate to observe the reaction and cell-level reversibility. Reproduced with permission from The Royal Society of Chemistry.³⁷ 146

Figure 6.2. | Evaluation of Physical and Chemical Transformations. (a) TEM image of NiO/C after 10 electrochemical cycles. XPS spectra of NiO/C including (b) Ni2p, (c), O1s, and (d) oxidation state percentages for NiO/C. (e) TEM images of ID-NiO/CNT after 10 electrochemical cycles. XPS spectra of ID-NiO/CNT including (f) Ni2p, (g) O1s, and (h) oxidation state percentages for ID-NiO/CNT. Reproduced with permission from The Royal Society of Chemistry.³⁷ 152

Figure 6.3. | Material Nanoconfinement. (a) Illustration of metal oxides spatial rearrangement during charge/discharge in the case of nanoconfinement, (b) SEM images of nano-confined NiO in NC-NiO@CNT₅₀, (c) TEM images and EDS mapping of NC-NiO@CNT₅₀, (c-1) interlayer spacing of CNT, (c-2) interface between MO-CNT, (c-3) lattice fringes of NiO, (d) TEM image of NiO@CNT₅₀ after 10 electrochemical cycles. XPS spectra of NC-NiO@CNT₅₀ including (e) Ni2P, (f) O1s, as well as (g) the percentage of active materials remaining in the 2+ oxidation state after cycling. Reproduced with permission from The Royal Society of Chemistry.³⁷ 156

Figure 6.4. | Electrochemical performance. (a) The charge-discharge curves and (b) differential capacity analysis ($dQdV^{-1}$) of NC-NiO@CNT₅₀. (c) Rate capability evaluation for charge reversibility and rate-specific side reactions at different current densities for NC-NiO@CNT₅₀. (d) EIS spectra after 10, 50, and 100 charge/discharge cycles for ID-NiO/CNT and NC-NiO@CNT₅₀, showing the evolution of chemical and physical processes (e.g. diffusion, charge transfer, electrolyte conductivity, SEI resistance) during cycling. (e) Capacity retention over 2000 cycles for NC-NiO@CNT₁₀ at 1C (718 mAh g⁻¹). (f) Capacity retention, charge-discharge curves, and differential capacity analysis for high loading full cells made from NC-NiO@CNT₁₀ anodes and Li(Ni_{0.5}Mn_{0.3}Co_{0.2})O₂ cathodes (anode loading: 5.16 mg cm⁻²; cathode loading: 18.23 mg cm⁻²) full cell. XPS spectra for NC-NiO@CNT₁₀ before and after cycling including (g) Ni2P, (h) O1s, and (i) the percentage of NiO remaining in the 2+ oxidation post-cycling. Reproduced with permission from The Royal Society of Chemistry.³⁷ 157

Figure 6.5. | Phase Separation and Degradation Pathway. Identifying the degradation pathways in conversion MOs (e.g. M/MO agglomeration, metal trapping, electrical detachment, SEI engulfment of MO, particle delamination) caused by fluctuations in the local e⁻, Li⁺, oxygen, and metal balance during phase separation for (a) physically mixed NiO/C, (b) anchored ID-NiO/CNT, and (c) nano-confined NC-NiO@CNT. Reproduced with permission from The Royal Society of Chemistry.³⁷ 161

Figure 8.1. | Illustration of the simulation domain and geometry 170

Figure 8.2. | Prototype model of a two-particle Intercalation/Conversion (2P-I/C) hybrid FeS₂ chemistry for secondary battery purposes, where (a) represents the model simulation for the discharge/charge reaction with multiple reaction plateaus, and (b) contains the particle-level reaction modes and electrolyte loss. 174

Figure 8.3. | Reconstruction of X-ray computed tomography (XCT) of NMC from Ebner et al.²¹⁷ 175

Figure 8.4. | Next-generation conversion electrodes based on energy-dense Li-Sulfur technologies where (a) is the cycle performance plot, and (b) shows the charge-discharge profile..... 181

Figure 8.5. Homopolymer based on (a) block, (b) random, (c) casting membranes. Reproduced with permission from The Royal Society of Chemistry. ²²⁰	184
Figure 8.6. Charge-discharge curves for (a) GT32 and (b) GT72	185
Figure A.1 Copyright permission for Figure 1.2 . Qi, Y., Guo, H., Hector, L. G. & Timmons, A. Threefold Increase in the Young ' s Modulus of Graphite Negative Electrode during Lithium Intercalation Threefold Increase in the Young ' s Modulus of Graphite Negative Electrode during Lithium Intercalation. <i>J. Electrochem. Soc.</i> 157 , A558–A566 (2010).	208
Figure A.2 Copyright permission for Figure 1.3 . Radin, M. D., Hy, S., Sina, M., Fang, C., Liu, H., Vinckeviciute, J., Zhang, M., Whittingham, M. S., Meng, Y. S. & Van der Ven, A. Narrowing the Gap between Theoretical and Practical Capacities in Li-Ion Layered Oxide Cathode Materials. <i>Adv. Energy Mater.</i> 7 , 1–33 (2017).	209
Figure A.3 Copyright permission for Figure 1.4 and Figure 1.5 Rodrigues, M.-T. F., Babu, G., Gullapalli, H., Kalaga, K., Sayed, F. N., Kato, K., Joyner, J. & Ajayan, P. M. A materials perspective on Li-ion batteries at extreme temperatures. <i>Nat. Energy</i> 2 , 17108 (2017).	209
Figure A.4 Copyright permission for Figure 1.7 . Amatucci, G. G. Stabilized iron fluoride cathodes. <i>Nat. Mater.</i> 18 , 1275–1276 (2019).	210
Figure A.5 Copyright permission for Figure 1.8 and Figure 3.1-Figure 3.12 Spinner, N., Zhang, L. & Mustain, W. E. Investigation of metal oxide anode degradation in lithium-ion batteries via identical-location TEM. <i>J. Mater. Chem. A</i> 2 , 1627–1630 (2014).	211
Figure A.6 Copyright permission for Figure 1.8 and Figure 3.1-Figure 3.12 . Ng, B., Duan, X., Liu, F., Agar, E., White, R. E., Mustain, W. E. & Jin, X. Investigation of Transport and Kinetic Nonideality in Solid Li-Ion Electrodes through Deconvolution of Electrochemical Impedance Spectra. <i>J. Electrochem. Soc.</i> 167 , 020523 (2020).	212

- Figure A.7** | Copyright permission for **Figure 2.2** to **Figure 2.5** and . Ng, B., Duan, X., Liu, F., Agar, E., White, R. E., Mustain, W. E. & Jin, X. Investigation of Transport and Kinetic Nonideality in Solid Li-Ion Electrodes through Deconvolution of Electrochemical Impedance Spectra. *J. Electrochem. Soc.* **167**, 020523 (2020). 213
- Figure A.8** | Copyright permission for **Figure 1.8** and **Figure 3.1-Figure 3.12**. Ng, B., Duan, X., Liu, F., Agar, E., White, R. E., Mustain, W. E. & Jin, X. Investigation of Transport and Kinetic Nonideality in Solid Li-Ion Electrodes through Deconvolution of Electrochemical Impedance Spectra. *J. Electrochem. Soc.* **167**, 020523 (2020)..... 213
- Figure A.9** | Copyright permission for **Figure 5.1** to **Figure 5.6**. Ng, B., Faegh, E., Lateef, S., Karakalos, S. G., Mustain, W. E. Structure and Chemistry of the Solid Electrolyte Interphase on High Capacity Conversion-based Anodes: NiO. *J. Mater. Chem. A*, 2021, 9, 523 214
- Figure A.10** | Copyright permission for **Figure 6.1** to **Figure 6.4**. Ng, B., Faegh, E., Peng, X., Mustain, W. E. Using nanoconfinement to inhibit the degradation pathways of conversion-metal oxide anodes for highly stable fast-charging Li-ion batteries. *Journal of Materials Chemistry A*. (2020) **8**, 2712-2727 215
- Figure A.11** | Copyright permission for **Figure 8.5**. Mandal, M., Huang, G., Hassan, N. U., Mustain, W. E. & Kohl, P. A. Poly(norbornene) anion conductive membranes: homopolymer, block copolymer and random copolymer properties and performance. *J. Mater. Chem. A* **8**, 17568–17578 (2020). 216

LIST OF SYMBOLS

α_a	anode transfer coefficient
α_c	cathode transfer coefficient
A	the surface of the cell exposed to convection
Bi	Biot number
C_p	specific heat capacity
D	chemical diffusion coefficient
$dUdT^{-1}$	entropic heat coefficient
e	electric charge constant
F	Faraday's constant, C/mol
h	heat transfer coefficient
I_{cell}	applied current, A
I_{1C}	the current corresponding to 1C, A
i	current density
i_0	charge exchange current density
i_0S	charge exchange current
k	effective thermal conductivity
k_B	Boltzmann constant
l_p	cathode thickness
l_n	anode thickness
\mathcal{L}	Laplace transform
L	characteristic length
m_{cell}	mass of cell
η_{IR}	ohmic losses in electrode and electrolyte, V
η_{IR1C}	ohmic overpotential at 1C, V

η_{conc}	concentration overpotential, V
η_{CT}	charge transfer overpotential, V
$Q_{\text{cell},0}$	initial state of charge, -
r_p	NMC532 particle radius
r_n	Graphite particle radius
R	gas constant, J mol ⁻¹ K ⁻¹
R_{cell}	internal resistance of the cell
S	electrochemical active surface area
SOC	state of charge
SOC_0	initial state of charge
τ	diffusion time constant, s
t	pulse time
T	cell temperature
T_{amb}	ambient temperature, K
T_{ref}	reference temperature, K
U^o	cell open circuit potential, V
V	cell potential, V
V_m	molar volume
x	dimensionless position inside the particle (x=0@center, x=1@surface)
z	number of electrons

CHAPTER 1: INTRODUCTION TO LI-ION BATTERIES

The global energy consumption and the production of climate changing agents (e.g. waste heat, H₂O vapor, CO₂) have skyrocketed in the 21st century.^{1,2} Of the various forms of energy conversion, alternative energy (e.g. solar, wind, hydro) is projected to help solve the energy demands of the future and control emissions from fossil fuels. However, the intermittent nature of most alternative energy makes their widespread deployment beholden to energy storage technologies. Among all options, electrochemical energy storage (EES) devices are widely recognized as being integral to meeting these energy storage and distribution needs at many scales. This has led to a surge in interest for the development and optimization of batteries and supercapacitors. Li-ion batteries (LIBs) have been widely touted as the most promising EES devices because of their high energy (~250 Wh kg⁻¹), power densities (~500 W L⁻¹), efficiency (~90%), fast charge capability, and remarkable durability,³⁻⁵ which is the reason why LIBs are now implemented in electrified transportation (e.g. electric cars, electric trucks), portable electronics (e.g. computer, cellphones, accessories), medical devices (e.g. cardiac pacemaker, artificial hearts, prostheses), and grid storage.⁶⁻⁹

Of these technologies, electric vehicles (EVs) are pivotal in fostering a cleaner and sustainable future. In comparison to the standard gasoline-powered internal combustion engine (ICE) whose energy efficiency is around 20%-35%, EVs can reach efficiencies greater than 90%. As a bonus, EVs require 50% fewer moving parts which translates to

easier maintenance and less costly repairs. The main drawback, however, is the relatively low energy density of LIBs in comparison to gasoline (12 kWh kg⁻¹), which either increases the weight and volume of the battery pack (10x heavier and 6-7x greater in volume) or limits the driving range (<600km). For EVs to push past commercial ICE vehicles, the energy density must be significantly improved, the pack must have a comparable lifetime, and the cost (\$ kWh⁻¹) must be competitive. The United States Advanced Battery Consortium has established goals for advanced EV batteries for the year 2023 (**Table 1.1**). The USABC develops benchmarking strategies so automobile/battery manufacturers, government agencies (e.g. U.S. Department of Energy and its National Laboratories), universities, and other affiliated institutions can have comparable data and a unified direction for the future of EES devices. To meet these goals, advances are needed at both the material and system levels (including the battery management system, BMS). To make such advances, additional fundamental understanding of the limiting factors of component-level behavior and design is essential.

Table 1.1. | United States Advanced Battery Consortium (USAB) goals for advanced high-performance batteries for electric vehicle (EV) applications in 2023¹⁰

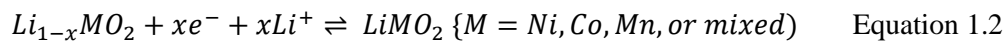
End-of-Life (EOF) Characteristics	System-Level	Cell-Level
Specific Energy at C/3	235 Wh kg ⁻¹	350 Wh kg ⁻¹
Energy Density at C/3	500 Wh L ⁻¹	750 Wh L ⁻¹
Calendar Life	15 Years	15 Years
Life Cycles	1000	1000
Operating Temperature	-40 to +66°C	-40 to +66°C
Cost at 100,000 Units	\$125 kWh ⁻¹	\$100 kWh ⁻¹
Maximum Self-Discharge	<1% month ⁻¹	<1% month ⁻¹
Normal Recharge Time	<7 Hours, SAE J1772	<7 Hours SAE J1772
Fast Charge	80% ΔSOC in 15 mins	80% ΔSOC in 15 mins

1.1 ELECTROCHEMISTRY OF COMMERCIAL LI-ION BATTERIES

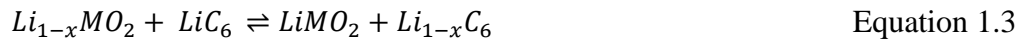
Li-ion batteries are secondary batteries (rechargeable) that traditionally operate based on intercalation-based materials (i.e. reversible insertion or extraction of Li^+ charge carriers). **Figure 1.1** illustrates the electrochemical operating principles of conventional Li-ion batteries. During the discharge, the oxidation of the negative electrode (e.g. graphite, $\text{Li}_4\text{Ti}_5\text{O}_{12}$) releases electrons (e^-), **Equation 1.1**, which travel through the external circuit to reduce the positive electrode (e.g. LiCoO_2 , Li_2MnO_2). Simultaneously, the migration of Li^+ from the anode to the cathode maintains the charge electroneutrality of the system. A generic form for the anode reaction is presented in **Equation 1.1**.



The Li^+ migration is facilitated by dissolved charge carriers in the electrolyte. Here, Li salts, such as LiPF_6 , LiClO_4 , or LiBF_4 , are dissolved in a mixture of ethylene carbonate (EC), diethyl carbonate (DEC), dimethyl carbonate (DMC), or ethyl methyl carbonate (EMC). Many cells also introduce small quantities of additives such as vinylene carbonate (VC) or fluoroethylene carbonate (FEC). When the Li^+ ions reach the positive electrode, standard LiMO_2 (where M can be Ni, Co, Mn, or mixed) materials undergo a reduction, **Equation 1.2**.



The overall electrochemical reaction for a modern Li-ion battery is:



Also, the reaction processes are highly reversible, which makes the charge reaction just the opposite direction of **Equation 1.1** to **Equation 1.3**.

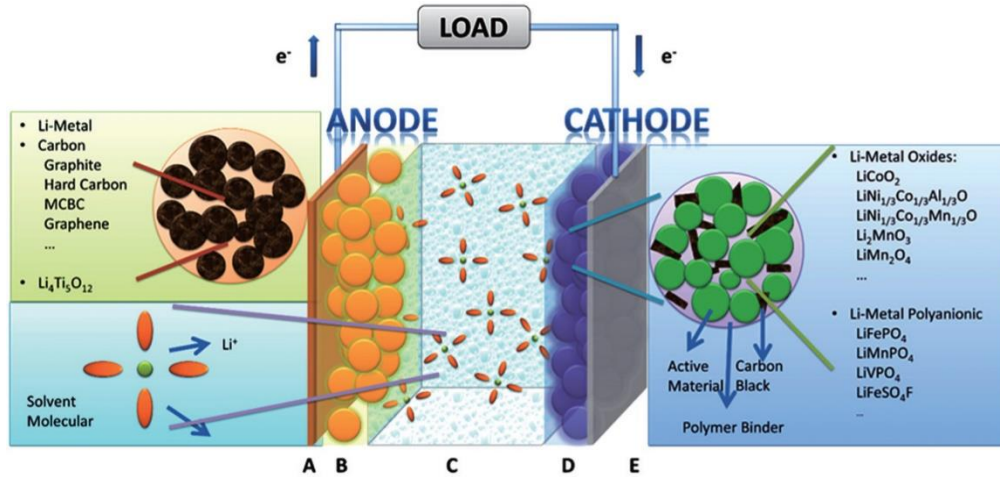


Figure 1.1. | Diagram elucidating the operating principles of a Li-ion battery with the conventional anode (e.g. graphite, $\text{Li}_4\text{Ti}_5\text{O}_{12}$), cathode materials (e.g. LiCoO_2 , Li_2MnO_3), and electrolyte (e.g. LiPF_6 in organic carbonates). Reproduced with permission from IOP Publishing ¹¹

The operating voltage for the overall cell reaction in an operating battery can be determined by both the thermodynamic limit (Nernstian potential) for the electrochemical reactions and the net resistive losses (e.g. ohmic, kinetic, mass transfer). Therefore, the cell operating voltage can be represented as:

$$E_{cell} = E^o - [(\eta_{CT})_a + (\eta_{CT})_c] - [(\eta_{MT})_a + (\eta_{MT})_c] - iR_i = iR \quad \text{Equation 1.4}$$

where E_{cell} is the cell-level voltage, E_{eq} is the cell thermodynamic voltage ($E_{eq} = E_c - E_a = \frac{-\Delta G}{nF}$), ΔG is the Gibbs free energy of the overall cell reaction, F is Faraday's constant ($96485.33 \text{ C mol}^{-1}$), η_{CTa} is the kinetic overpotential for the anode, η_{CTc} is the kinetic overpotential for the cathode, η_{MTa} is the mass transfer overpotential for the anode, η_{MTc} is the mass transfer overpotential for the cathode, and iR_i is the net ohmic loss due to particle-particle contact, ionic conductivity (typically dominant) and electronic conductivity. Higher operating voltages are desired for the discharge process (i.e. higher Gibbs free energy in the spontaneous direction), whereas lower voltages are desired for the charging

(i.e. less energy is required to put energy into the system). One method to increase the energy is by achieving higher operating voltages for the discharge process (**Equation 1.4**), which can be done by increasing the cathode potential and/or decreasing the anode potential. The other method is to minimize the resistive losses (i.e. ohmic, kinetic, and/or mass transport), such that the operating voltage approaches the thermodynamic value.

In addition to the cell operating voltages, the overall energy density of the cell is dictated by the amount of charge that can be stored per unit mass of active material, which is called the capacity. The capacity for any material – either the anode or the cathode – can be calculated from **Equation 1.5**.

$$Q_x = \frac{n F}{3.6 MW} ; Q_{C_6} = \frac{1 (96485.33 \text{ C mol}^{-1})}{3.6 (72.0 \text{ g mol}^{-1})} = 372.2 \text{ mAh g}^{-1} \quad \text{Equation 1.5}$$

where F is Faraday's constant (96485.33 C mol⁻¹), n is the number of electrons transferred per mol of reactant, and MW is the molar mass of the active material. **Equation 1.5** gives a representative theoretical calculation for graphite, which can hold one lithium atom per every six carbon atoms (LiC₆), though the practically achievable capacity (because of resistive losses) is ~330 mAh g⁻¹. Doing the same calculation for a typical cathode material, Li_xCoO₂ (LCO), yields a value of 273.8 mAh g⁻¹, but LCO is unstable when x < 0.5, resulting in practical capacities of ~140 mAh g⁻¹. The theoretical gravimetric energy density is defined by the electrochemical voltage of the cell and the specific capacities of the anode (Q_a) and cathode (Q_c) and can be determined by the following equation,

$$\text{Theor. Energy Density} = \frac{Q_c \times Q_a}{Q_c + Q_a} \times E_{avg} ; \text{LiC}_6/\text{LiCoO}_2 = 354 \text{ Wh kg}^{-1} \quad \text{Equation 1.6}$$

where Q_c = 140 mAh g⁻¹, Q_a = 330 mAh g⁻¹, and the average operating voltage is 3.6V for a theoretical LiC₆/LiCoO₂ system. However, this calculation does not provide the true cell-level energy density, because it does not take the mass of the anode (m_a), cathode (m_c),

electrolyte (m_e), separator (m_s), and packaging material (m_p) into consideration. Also, the negative-to-positive capacity ratio (N/P) is hardly ever unity and typically between 1.03 to 1.2, which increases the amount of inactive mass in the system.¹² Thus, the practical cell-level gravimetric energy density is typically much less than the theoretical value and can be calculated by the following equation,¹³

$$\text{Cell - Level Energy Density} = \frac{Q \times E_{avg}}{m_a + m_c + m_e + m_s + m_p} \quad \text{Equation 1.7}$$

where the anode and cathode mass quantities include active material, inactive components, and current collector. In **Table 1.2** is a summary of the achieved energy density for commercial and proposed next-generation Li-based batteries. The gravimetric energy density of the electrochemical system is one of the most important features because low battery weight is essential in aerospace, space, wearables, and military applications,¹⁴ whereas the volumetric energy density is critical for grid storage and EV applications.

Table 1.2. | Summary of the energy density of commercial and commonly proposed next-generation Li-based batteries. The calculations are based on an average discharge voltage reported in Wu et al,¹⁵ but in short, the calculation considers 4.5 μm thick Al and Cu current collectors, 9 μm separator, and single-sided electrodes with desired volume percentages based on chemistry (70 vol% for intercalation-materials, 60 vol% for next-generation electrodes like Si, Li, sulfur – remaining volume contains inactive components like binder, conductive agents, voids). Note, the calculation also assumes a packaging of 10 wt%.¹⁶

System	Anode	Cathode	Avg. Discharge Voltage (V)	Volumetric Energy (Wh/L)	Gravimetric Energy (Wh/kg)
Commercial	Li_xC_6^a	LiCoO_2 (layered) ^a	3.6	737	245
Commercial	Li_xC_6^a	LiMn_2O_4 (spinel) ^a	3.8	724	264
Commercial	Li_xC_6^a	LiFePO_4 (olivine) ^a	3.2	606	241
Next-Gen	Si^b	$\text{LiNi}_{0.84}\text{Co}_{0.12}\text{Al}_{0.04}\text{O}_4^a$	3.4	1277	459
Next-Gen	Li^d	$\text{LiNi}_{0.84}\text{Co}_{0.12}\text{Al}_{0.04}\text{O}_4^a$	3.7	1363	541
Next-Gen	Li^d	$\text{Li}_2\text{S/Sulfur}^c$	2.15	1066	904

^a intercalation mechanism

^b alloying mechanism

^c conversion mechanism

^d plating/stripping mechanism

1.2 INTERCALATION REACTION MECHANISMS

Intercalation reactions are by far the dominant reaction mechanism in both the anode and cathode of commercial LIBs. In the case of graphitic anodes (theoretical capacity = 372 mAh g⁻¹), the electrochemical insertion of Li into the inner structure of graphite occurs through multiple stages (LiC_x) based on thermodynamic stability. **Figure 1.2** illustrates the atomic structures of various stages (designated stage-*n* or # of layers) in Li-intercalated graphite. In general, Li intercalates into the interstitial sites between graphite layers in a dilute formation and stabilized by the introduction of an electron to the sp² ring of graphite – resulting in a highly reversible reaction.¹⁷ Driving up the Li-concentration in the electrolyte results in the formation of the stage-4 structure for the intercalated compound, and further increasing the Li-concentration leads to the transition towards the dilute stage-3 structure. Electrochemical intercalation can force the dilute stage-3 structure to stage-2 (LiC₁₈) and further reduction can result in a two-phase transition (filled stage-2 LiC₁₂ and saturated concentration stage-1 LiC₆ structure). Therefore, based on the fundamental reaction, only one Li atom can be stored for every six-carbon repeat unit, which gives rise to the a relatively theoretical limit of 372 mAh g⁻¹. Other commercialized anode materials, such as lithium titanate (LTO, Li₄Ti₅O₁₂), also follow intercalation mechanisms, but their higher density and larger unit size than graphite drive their capacity down even further. For example, the theoretical capacity of LTO is only 175 mAh g⁻¹. This means that despite LTO being a very stable anode, it cannot be used in applications where high energy density is required.

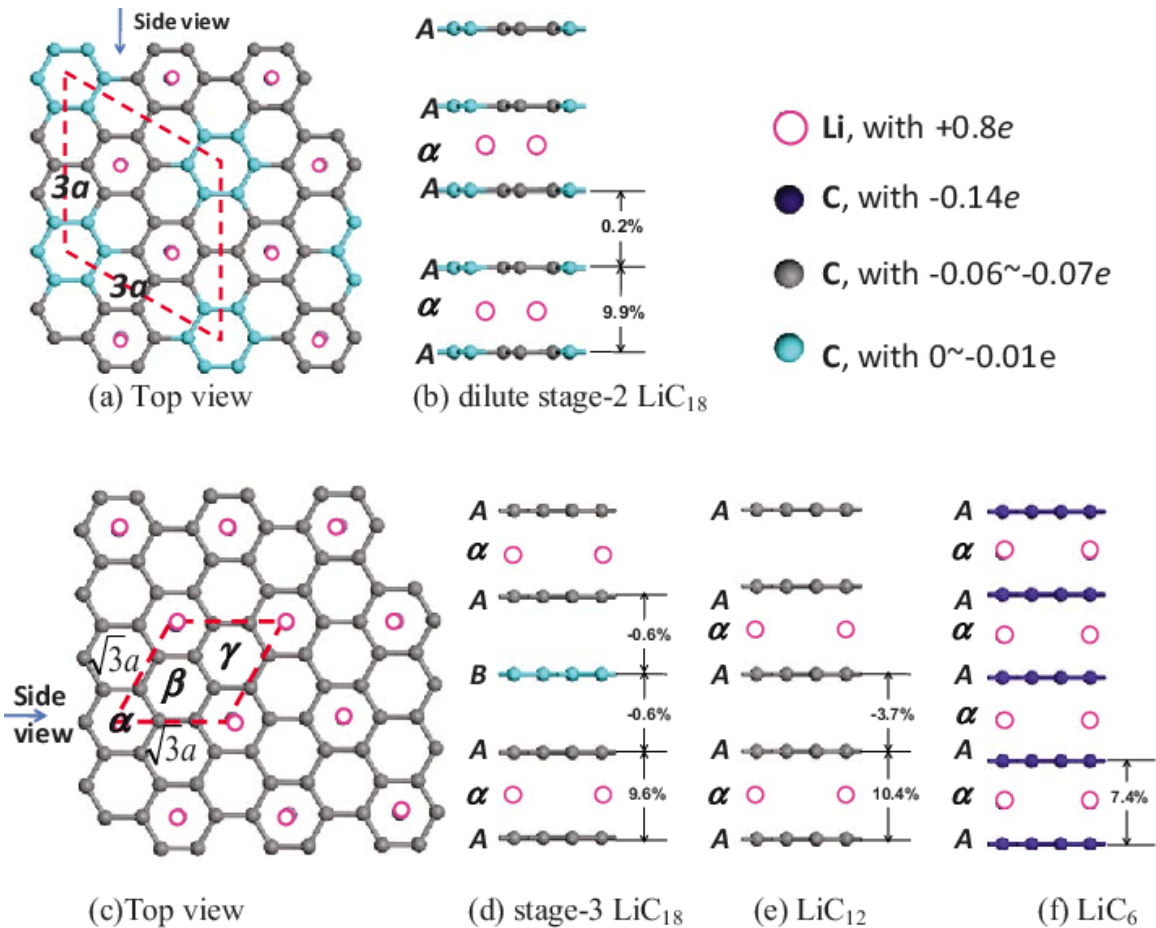


Figure 1.2. | Atomic structure of Lithium intercalation in graphitic carbon (LiC_x) and showing, (a) the top view, (b) side view of stage-2 LiC_{18} , (c) top view, (d) side view of stage-3 LiC_{18} , (e) LiC_{12} , and (f) LiC_6 . Reproduced with permission from IOP Publishing.¹⁷

At the cathode, intercalation compounds are also used. The most common materials are metal oxides with the general formula Li_xMO_2 where $M = \text{Mn, Ni, Co, Al}$. Typically, M is a mixture of most or all of these elements. For example, a very common material is $\text{Li}_x\text{Ni}_{0.5}\text{Mn}_{0.3}\text{Co}_{0.2}\text{O}_2$ (also called NMC532). These Li_xMO_2 typically have a layered crystal structure. The close-packed O-framework shared with metal forms MO_2 -sheets that enables the transfer of Li into and out of the crystal structure. Variations in the interstitial sites are typically designated with a letter that indicates the coordination (O, P, or T) and a number that reveals the number of layers. The majority of Li-intercalation

cathodes are O1 and O3, which means Li is octahedrally coordinated to an anion every layered repeat unit or structured with an *AB CA BC* framework.¹⁸ Also, disordered rocksalt and spinel crystallographic structures are related to the O3 structure (LiMnO_2 and $\text{Li}_{0.5}\text{CoO}_2$) but differ in the Li and M cation arrangement and can be seen in **Figure 1.3**. However, in these materials, the large repeat groups and the fact that these materials collapse when too much Li is removed, severely limits the achievable capacity to only 140-220 mAh g⁻¹.

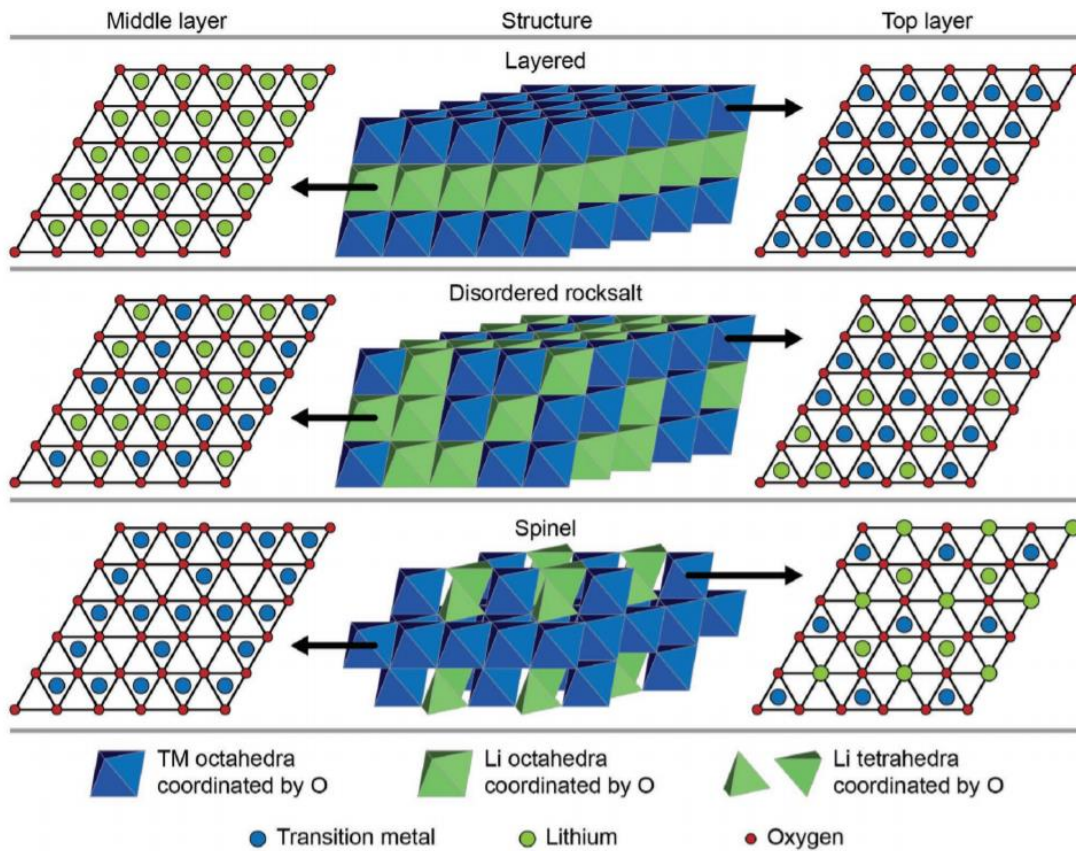


Figure 1.3. | Comparison of layered, disordered rocksalt, and spinel cation ordering. Reproduced with permission from John Wiley and Sons¹⁸

1.3 AGING MECHANISMS AND TEMPERATURE EFFECTS IN LIBS

One of the most important concepts in LIBs is the formation of the solid electrolyte interphase (SEI) and its role in battery performance. Electrodes with redox potentials (graphite, Si, Li-metal) within the reactive region of the electrolyte (i.e. lowest unoccupied molecular orbital or LUMO of the electrolyte is at a higher energy state than the Fermi energy of the anode) like Li/Li^+ will reduce the electrolyte to semi-stable compounds to form the SEI. Likewise, electrolyte oxidation can occur on the cathode-side, if the HOMO of the electrolyte is lower in free energy than the electrode Fermi level, leading to electron transfer. The common consensus¹⁹⁻²² is a stratified film for the SEI, which is composed of a densely-packed inorganic inner layer (i.e. directly at the electrode interface and consists of Li_2CO_3 , LiF , Li_2O) and a porous organic layer consisting of semi-carbonates and polyolefins. The SEI formation process is detrimental to cell performance since it consumes active Li and electrolyte-components (i.e. ethylene carbonate), which leads to capacity loss, resistance build-up, and poor power density.

The temperature plays a significant role in the performance of the cell. Elevated temperatures can temporarily result in a higher achievable capacity due to the improved kinetics and mass transport but can also trigger degradation reactions (represented in **Figure 1.4**). Long term operation at high temperatures causes thickening of the SEI (increased interfacial impedance), electrolyte decomposition (reduction in ionic conductivity), and undesirable SEI compositional change (loss of elastic organic components and generation of brittle inorganics). Electrolyte decomposition reactions can also release gasses that alter the electrode morphology and decrease the safety of the cell. At the cathode side, metal dissolution can occur at elevated temperatures causing

irreversible cathode damage. Subsequently, the metal ions migrate to the anode and can integrate itself into the SEI, generating a conductive pathway, or even catalyze the destruction of the SEI. At low temperatures, the impedance drastically increases due to hindrance in charge transfer and contributions from both the SEI and electrolyte. Also, the solid-state diffusivity of Li^+ into graphite plummets severely at 0°C .²³ As a result, severe polarization of the electrode occurs and enables the deposition of high surface area Li-metal, which is then prone to severe corrosion (i.e. severe safety risk), as well as dendrites.

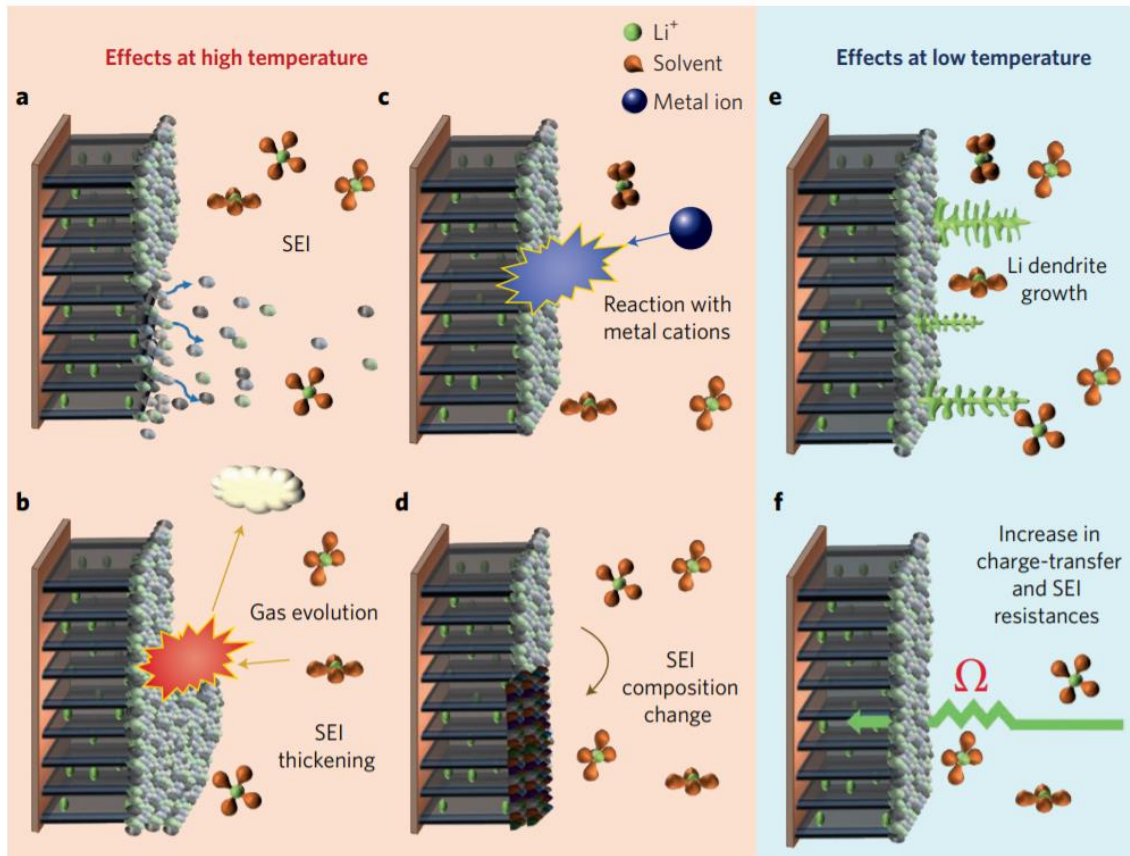


Figure 1.4. | Depicts the instability of the anode interface under high and low temperatures. High temperatures can result in (a) deterioration of the SEI, (b) decomposition of the electrolyte and release of gas, (c) transition metal dissolution from cathode and reaction at anode, (d) severe chemical changes to the SEI. Low temperatures can cause (e) severe anode polarization to drive Li-plating, and (f) reduced reaction kinetics and increase in SEI resistances. Reproduced with permission from Macmillan Publishers Ltd²³

The standard cathodes (layered, spinel, and olivine) used in commercial LIBs are phase-dependent and operate based on a highly ordered insertion and extraction of Li^+ ions. High-temperature operation with these cathodes can lead to accelerated metal dissolution, crystallographic disorder, and oxygen evolution – resulting in severe performance degradation due to loss of active material and destabilization of the structural composition (represented in **Figure 1.5**). The release of oxygen can also lead to electrolyte combustion and thermal runaway, which causes catastrophic cell failure. At low temperatures ($<0^\circ\text{C}$), the cathode performance is hindered by slow charge transfer and poor solid-state diffusion of Li^+ in the cathode - which leads to severe polarization of the electrode and anisotropic lithiation processes at low temperature both on a particle-level and on an electrode-level (later discussed in Chapter 4).

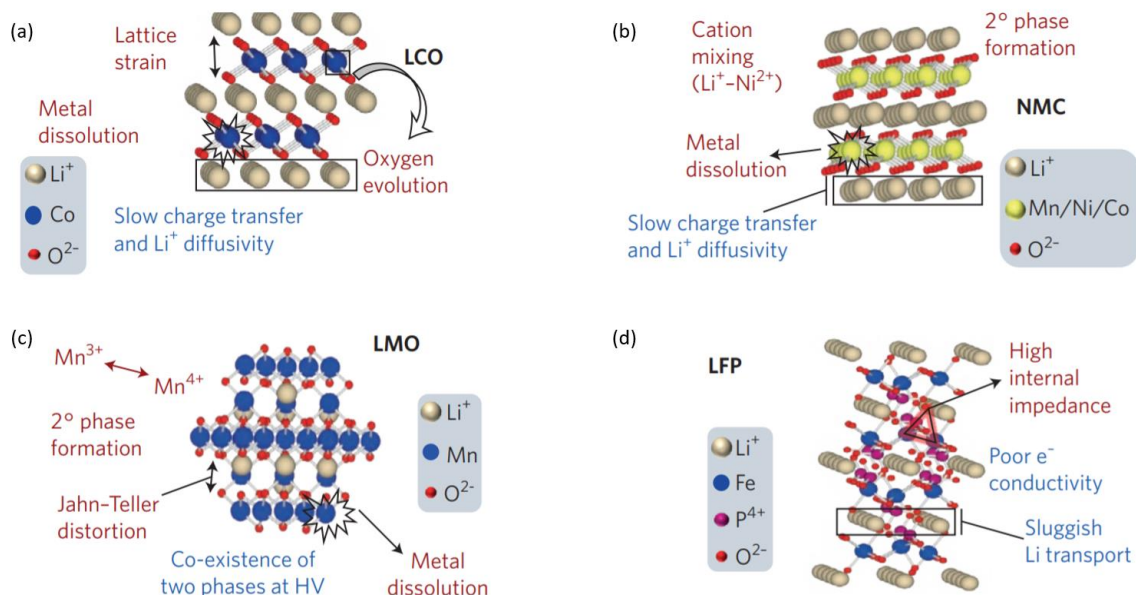


Figure 1.5. | Depicts the instability in the structure of cathode materials at different temperatures (red = high T and blue = low T). The cathodes include (a) LiCoO_2 , (b) $\text{LiNi}_{1/3}\text{Mn}_{1/3}\text{Co}_{1/3}\text{O}_2$, (c) spinel LiMn_2O_4 , and olivine LiFePO_4 . Reproduced with permission from Macmillan Publishers Ltd²³

1.4 CAPACITY LIMITATIONS WITH INTERCALATING MATERIALS IN LIBS

The selection of anodes and cathodes has not changed significantly over the years (e.g. anode = graphite, $\text{Li}_4\text{Ti}_5\text{O}_{12}$ or LTO, cathode = Li_xMO_2). This has some negative consequences. Consider the anode. Yes, the most common anode, graphite, has high natural abundance, is easy to process and manufacture, and has a high cycle life. As mentioned earlier, LTO has ultra-high stability and cycle life. However, both anodes use intercalation reactions to store charge, severely limiting their theoretical capacities (graphite = 372 mAh g^{-1} , LTO = 175 mAh g^{-1}). Existing cathodes are even worse. Though commercial cathodes are reversible over a large number of cycles and have low self-discharge properties, their achievable capacities are only 140 mAh g^{-1} (LiCoO_2) to 220 mAh g^{-1} ($\text{LiNi}_{0.8}\text{Co}_{0.15}\text{Al}_{0.05}\text{O}_2$). Also, Co-based cathodes are expensive.⁶ The low capacities of these materials and high cost translate to a material that cannot meet the demands of the future. To enable the widespread adoption of battery EVs, the driving range must exceed 500 km (300 miles) with affordable prices that are $< \$40,000$ (battery energy density $350 \text{ Wh kg}^{-1}/750 \text{ Wh L}^{-1}$ with a battery pack cost of $\$125 \text{ kWh}^{-1}$).²⁴ This means that new materials must be developed at the anode and cathode side to enable emerging applications that seek to use LIBs.

1.5 SELECTION OF NEXT-GENERATION BATTERY MATERIALS

There is a need to develop reliable and energy-dense materials for LIBs that can operate under extreme conditions (i.e. low T, high T, fast charge) and over long operational life. Regarding materials, a portion of this thesis will focus (in Chapters 5-6) on the development of new high energy density anode materials. Though graphite has been the

standard Li-ion battery anode for decades, it has three undesirable properties. First, as discussed above is the intercalation storage reaction, leading to low capacity (372 mAh/g). Second, graphite intrinsically has a low thermodynamic redox potential, which can lead to Li-plating, dendrite formation, thermal runaway, and thermal propagation over repetitive fast charging cycles (5-10C). Third, is attributed to graphite's fundamental inability to perform well at low temperatures (i.e. stage transformation is hindered by poor-diffusion of Li into the bulk and sluggish transfer through the SEI layer) and at high temperatures (i.e. anode potential is deep in the instability range of the electrolyte, leading to overgrowth of the SEI). Therefore, the development of any advanced material for the LIB anode must address all of these issues.

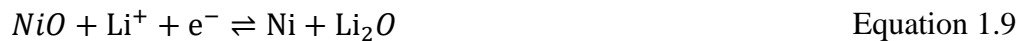
Li-metal has been proposed as the “holy grail” of anode materials due to its extremely high theoretical capacity (3860 mAh g⁻¹) and low electrochemical potential (-3.04V vs SHE). Despite these seductive properties, Li-metal is known to have poor coulombic efficiencies ($\frac{Q_{discharge}}{Q_{charge}}$) due to severe corrosion of high surface area Li electrodeposits – leading to continuous electrolyte decomposition (SEI formation) and consumption of the finite reserve of active material and electrolyte. Also, Li-metal is known to cause severe gassing, which can drastically increase the internal pressure of the cell (i.e. overpressurization). Constant Li redeposition also causes dendrites that can lead to internal short circuits and possibly thermal runaway.²⁵⁻²⁹

High-capacity alternatives to metallic Li include alloying materials (Si, Ge, Sn, Sb). Their capacities typically range from 1600-3800 mAh g⁻¹, which is very good. However, for the host to store that much charge, the material must expand, with typical values being more than 250% from its original volume. As a result, anode electrodes deploying these

materials tend to undergo severe structural change that leads to electrode pulverization (i.e. cracking) and delamination (i.e. electronically detached from the current collector). This is not good for LIB operation. Fortunately, other alternatives exist, such as metal fluorides, nitrides, phosphides, hydrides, and oxides. As shown in **Figure 1.6**, these materials tend to have a capacity between 600– 1000 mAh/g. These alternatives all tend to store charge through conversion-based mechanisms such as the one depicted in **Figure 1.7**. These conversion-based materials leverage the breakage of bonds to store significantly more electrons per unit mass. The general reaction for a conversion-based electrode is shown in **Equation 1.8**,



Of the conversion anodes, metal oxides (MOs) offer distinct advantages over alloying materials such as: i) a redox potential around 1V vs Li/Li+, which means it is thermodynamically less favorable for Li deposition to occur during rapid recharge or low temperature than it is with a graphite anode; ii) a volumetric expansion that is considerably less than other high-capacity materials like Si (60% vs 400%); iii) and their capacities are several times greater than graphite. NiO has been a widely used conversion MO in LIBs. Its overall reaction is given by **Equation 1.9**:



NiO has a theoretical gravimetric capacity of 718 mAh g⁻¹ and a very high density (6.67 g cm⁻³), which makes it an attractive material for both gravimetrically and/or volumetrically-constrained applications (e.g. space applications, electrified transportation, wearable electronics).³²

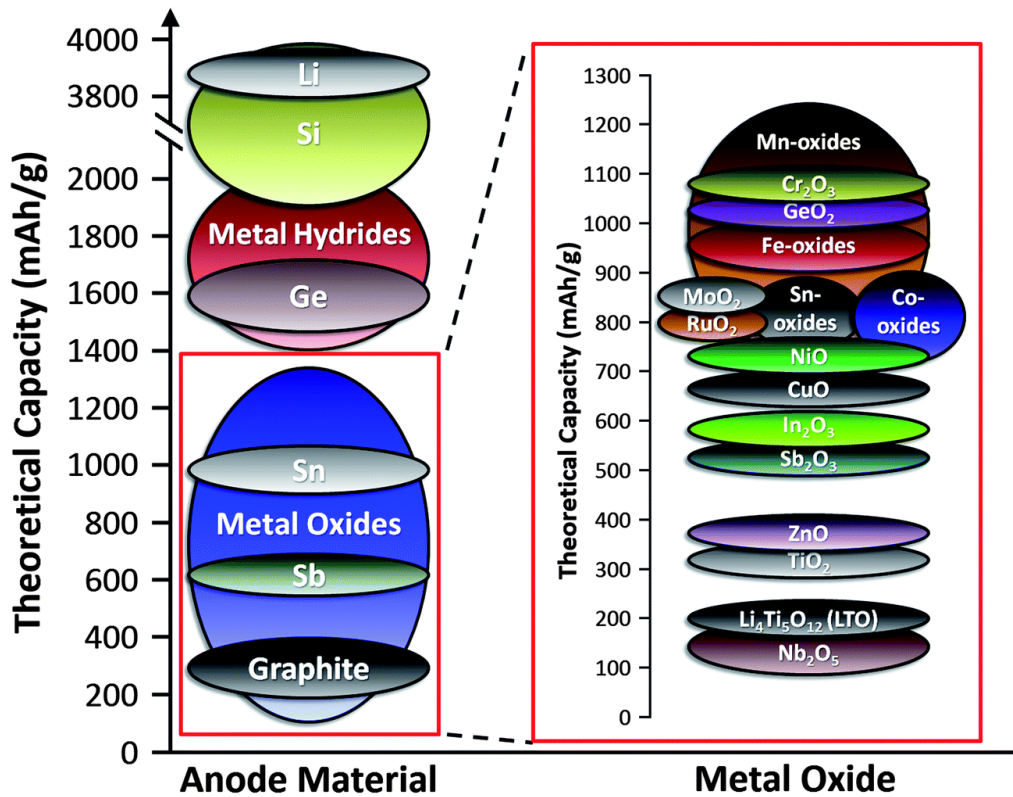


Figure 1.6. | Anode selection list and their theoretical capacities. Reproduced with permission from Royal Society of Chemistry.³⁰

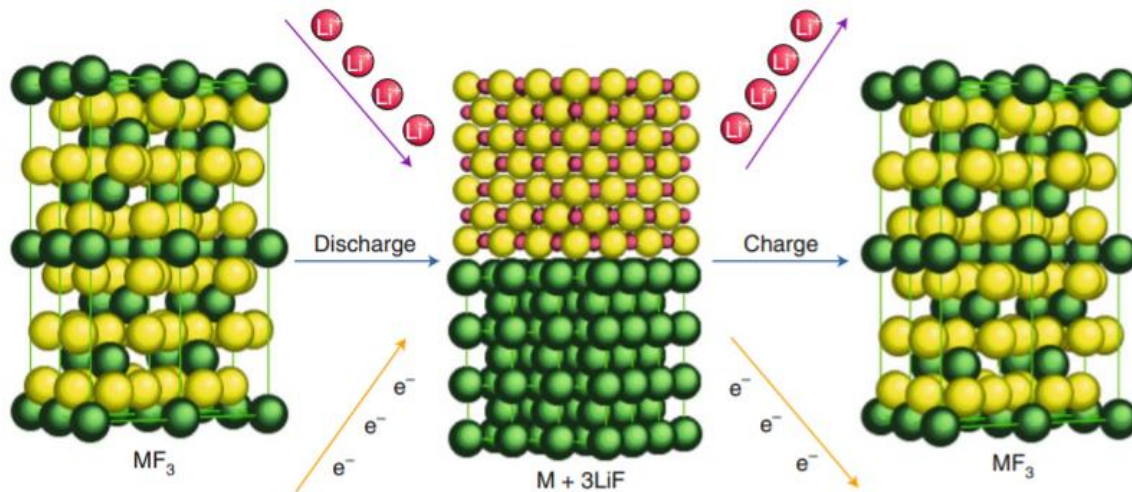


Figure 1.7. | Depicts the conversion reaction mechanism with MF_3 as a representative material. The conversion process involves limited diffusion of the anion (e.g. F, O, N, P, etc.) to react with the Li^+ during charge which generates metal (M) crystals and Li_πX . Reproduced with permission from Macmillan Publishers Ltd³¹

Despite these positive attributes, untailed NiO (raw or simple formulations with conductive carbon) is severely hindered by very poor cycle performance (~20 cycles results in 40-80% capacity loss)^{33,34} and poor rate capability, which is typically attributed to the intrinsically low conductivity ($\sim 10^{-4}$ to $10^{-5} \Omega^{-1} \text{ cm}^{-1}$)³⁴ and the repetitive volumetric expansion/contraction during charge/discharge.³² However, this explanation only scratches the surface of what causes poor cycle performance and rate capability in NiO. Thus, near-elementary steps that occur during the NiO conversion reaction are provided in **Equation 1.10** through **Equation 1.15** in **Table 1.3**, which is a combination of the work by Palmieri et al.³⁴, Jow et al.³⁵, and Soto et al.³⁶ and applied in Ng et al.³⁷ During the charge (reduction), Li desolvation occurs at the SEI/bulk electrolyte interface and then undergoes inclusion into the SEI.³⁸ The propagation of Li_{SEI}^+ through the SEI migrates to the bulk NiO ($\equiv\text{NiO-NiO}$) interface to form a $\equiv\text{NiO-NiO-Li}$ junction.^{35,37} Next, oxygen displacement occurs to form an $\equiv\text{NiO-Ni}_{\text{ads}}^+\text{LiO}_{\text{ads}}^-$. Thermodynamically, Li_2O exists at a lower energy state which makes the chemical reaction of Li_{SEI}^+ and $\equiv\text{NiO-Ni}_{\text{ads}}^+\text{LiO}_{\text{ads}}^-$ highly favorable and represented in **Equation 1.14**.³⁴ During the nucleation event, the oxygen vacant $\equiv\text{NiO-Ni}_{\text{ads}}^+$ reduces to $\equiv\text{NiO-Ni}$. Based on the minimization of surface free energy ($\sigma_{\text{Ni}} > \sigma_{\text{Li}_2\text{O}}$), any Ni that exists on the surface of the nucleation platform will exhibit a driving force for spontaneous rearrangement, and Li_2O or other low surface free energy materials will phase segregate to the surface.³⁹ Li_2O has extremely low electronic conductivity, which can lead to increased kinetic and Ohmic resistances in the cells.

Table 1.3. | Reaction description and mechanism for the transport of Li⁺ from the bulk electrolyte to the conversion of NiO to Ni

Description	Reaction Mechanism	Equation
Li desolvation at the SEI/bulk electrolyte interface	$\text{Li}_{\text{solvated}}^+ \rightleftharpoons \text{Li}^+$	Equation 1.10
Li transport through the SEI	$\text{Li}^+ + \equiv\text{SEI} \rightleftharpoons \text{Li}_{\text{SEI}}^+$	Equation 1.11
Junction Formation	$\text{Li}_{\text{SEI}}^+ + \equiv\text{NiO-NiO} + e^- \rightleftharpoons \equiv\text{NiO-NiO-Li}$	Equation 1.12
Displacement	$\equiv\text{NiO-NiO-Li} \rightleftharpoons \equiv\text{NiO-Ni}_{\text{ads}}^+ \text{LiO}_{\text{ads}}^-$	Equation 1.13
Li ₂ O Formation	$\equiv\text{NiO-Ni}_{\text{ads}}^+ \text{LiO}_{\text{ads}}^- + \text{Li}_{\text{SEI}}^+ \rightleftharpoons \equiv\text{NiO-Ni}_{\text{ads}}^+ + \text{Li}_2\text{O}$	Equation 1.14
Ni nucleation	$\equiv\text{NiO-Ni}_{\text{ads}}^+ + e^- \rightleftharpoons \equiv\text{NiO-Ni}$	Equation 1.15

\equiv Denotes bulk material

In addition, during charge/discharge cycling electrochemical Ostwald ripening can result in the formation of larger crystals, which can lead to the growth of particles and a decrease in charge carriers at the electrochemically active sites.³⁹ The Ni-core of large crystals can therefore become electrically and ionically isolated (via a large Li₂O and NiO shell) and lead to trapped Ni metal within the bulk material.⁴⁰ Furthermore, the destabilized oxygen balance due to the spontaneous phase segregation of Li₂O leads to higher interfacial oxygen content within the Ni agglomerates, and promote the evolution to higher oxidation states (Ni²⁺ → Ni³⁺) during the discharge (oxidation)^{34,41,42}. When the electron flow switches during charge (reduction), the unstable higher oxidation states (Ni³⁺) can react with the SEI and/or electrolyte resulting in exposed reactive sites or irreversible consumption of active components.

Spinner et al.⁴⁰ were one of the first groups to use identical-location transmission electron microscopy (IL-TEM) to explore how degradative processes evolve over the course of a few cycles and found that untailed NiO undergoes rapid structural degradation. Pre/post cycled X-ray diffraction (XRD) studies suggest that on a bulk-scale, the severe performance loss is attributed to NiO becoming trapped in the charged state. The

study continued to probe the interface of NiO via IL-TEM, and found that the structural degradation resulted in continuous merging and growth of active particles. Also, small and low/dark transmission particles (Z contrast) were discovered inside the SEI. The SEI is known to have electronic insulating properties, which can fully disconnect a NiO/Ni particle from the current collector, leading to loss of active material. As a result, severe capacity loss over limited cycles (<20 cycles) was observed. In another study with *in-situ* TEM, Su et al.⁴³ found two dominant modes for MOs, 1) a violent reaction mode where agglomeration of small particles happens very fast (1-2mins), and 2) a gradual reaction mode where phase separation of MOs form core-shell like particles with multiple domains consisting of M, MO, and Li₂O – which expands the discoveries of Spinner et al.⁴⁰

Another concern of conversion electrodes is the large voltage hysteresis (i.e. the gap between the charge-to-discharge voltage), which ranges between several hundreds of mV to ~2 V,⁴⁴ which limits the energy efficiency of the system. Li et al. ⁴⁴ used a combination of X-ray absorption spectroscopy (XAS), TEM, density functional theory (DFT), and galvanostatic intermittent titration technique (GITT) to elucidate the root cause of large voltage hysteresis in conversion-based materials and found that FeF₃ in a 1M LiPF₆ EC/DMC (1:1 volume ratio) electrolyte exhibits a fairly low iR drop but the overpotential required for nucleation, growth of phases, mass transport, and charge transfer between the Fe/LiF phases is quite large (spans up to 300mV for the FeF₃→Fe/LiF charge and ~70mV for the Fe/LiF →FeF₃ discharge). Another consideration that was proposed is the spatial distribution of each phase, which either facilitates or restricts access to Li⁺ and e⁻. In their observation from *in-situ* TEM, a core-shell behavior was found for the active material during lithiation (i.e. intermediate FeF₂ core with a Fe/LiF shell in contact with the

electrolyte and conductive agents. During the delithiation, the core-shell reaction proposed by Li et al.⁴⁴ reverses with intermediate FeF₂ covering the reaction surface, which is electrically and ionically insulating. Their conclusion for the large voltage hysteresis for conversion based FeF₃ is based on comparing similar SOCs, and how an intermediate FeF₂ surface (Li-poor) and a Fe/LiF surface (Li-rich) will set the electrochemical system to different potentials vs Li/Li⁺ (i.e. compositional inhomogeneity can result in ~400 mV).⁴⁴

Next, the evolution to higher oxidation states is an intrinsic barrier to conversion-based transition metals. Transition metals can occupy multiple oxidation states (+1, +2, +3, +4, +7, etc.), which can either alter the system chemistry (i.e. destabilizing the counter-ion balance in the system) or introduce instability to the system (i.e. decomposition of SEI or electrolyte). Palmieri et al.^{41,45} discovered the effects of higher oxidation states, by using a Mn-based oxide (Mn_xCo_{1-x}O) as the system of interest and conducting cyclic voltammetry (CV) for different oxidation states of Mn-oxides. First, the CV study found mixed cathodic peaks that are present and ascribable to Mn₃O₄. Second, pre- and post-cycled X-ray photoelectron spectroscopy (XPS) was used to corroborate the electrochemical data and found that the deconvolution of the Mn 2p region, resulted in peaks that are attributed to Mn₃O₄ (mixed oxidation state of +2 and +3) and MnO (+2). The study proposed three possible root causes: 1) Mn₃O₄ formation coupled with the emergence of oxygen vacancies⁴⁶; 2) MnO reacts with oxygen-species (e.g. SEI components, electrolyte) to either attack the SEI and form reactive pockets or direct facilitation of the SEI growth; and 3) the reactant dynamics are very high leading anisotropy in local stoichiometries and kinetically favoring the formation of higher oxidation states.

Cumulatively, the performance limitations of conversion-based materials can be broken down into four key mechanisms:

1. Metal (charge) trapping within the SEI causes rapid loss of active material
2. Particle agglomeration and compositional inhomogeneity results in larger overpotentials that limits accessible capacity within a fixed voltage range
3. Destabilized oxygen balances and the reaction with the electrolyte or SEI leads to uncontrolled growth of the SEI and impacts the coulombic efficiency
4. The transition of active material to higher oxidation states reduces the coulombic efficiency

Much effort has been devoted to either eliminating the root cause or controlling the effects of degradation. One of which is regulating the key conductance parameters (interparticle and intraparticle conductivity), which has been proposed in the literature to have numerous benefits including: 1) minimization of the resistive losses within the cell, which enables higher achievable energy-densities and faster rate-capabilities; and 2) strategic control of ions and electrons that can minimize degradative processes within a cell (i.e., uniform ion flux and current densities can result in more homogenous reaction fronts). Inter-particle conductivity via the addition of either carbon black, graphene or carbon nanotubes has been shown to drastically improve the performance of MO anodes. Palmieri et al^{34,42} found that there is a direct correlation between the inter-particle electronic conductivity and the stable capacity (log-log linear relationship), a correlation between the enhancement of the intra-particle electronic conductivity to the evolution to higher oxidation states (i.e. attenuation of large particle-level polarizations), and more stable cycle performance.

These degradative processes that are intrinsic to conversion-based materials are further investigated in Chapter 5, and methods to circumvent these them are studied in Chapter 6 for the development of next-generation LIBs.

1.6 THEORETICAL FRAMEWORK FOR UNDERSTANDING THE PERFORMANCE AND LOSS MECHANISMS OF LI-ION BATTERIES

The electrochemical mechanisms for the materials in the LIB anode and cathode were discussed in the previous sections. However, that alone does not describe the behavior of the electrochemical system as a whole. In this section, fundamental relationships describing the thermodynamics, kinetics, and mass transfer of species in an operating Li-ion battery are discussed. The goal here is to develop a framework that will be used in Chapters 3 and Chapter 4 to understand the cell-level and material-level properties, performances, non-idealities, and loss mechanisms.

1.6.1 NONEQUILIBRIUM THERMODYNAMICS OF A CONCENTRATED SOLID SOLUTION

Nonequilibrium thermodynamics⁴⁷ captures the evolution of energy states with the assumption that the system proceeds through small perturbations from equilibrium, such that the changes can be linearized, and requires the system to be a reversible process. The chemical potential defines the differential energy of the system for a given change in the number of particles and can be defined in terms of state variables of the system by a Legendre transformation of the Gibbs-Duhem equation (e.g. internal energy, Helmholtz free energy, enthalpy, and internal energy).⁴⁸

$$\mu_i = \left(\frac{\partial G}{\partial n} \right)_{T,P,n_j \neq n_i}$$

Equation 1.16

Therefore, the chemical potential (μ_i) relates the change in energy of the system to the change in the number of the specified species, and when the other species within the system remains constant. In other words, the transition from one state to another at equilibrium must have an energy change of zero - the definition must hold for the rate equation. The chemical potential of a species in a solid solution is defined as:

$$\mu_i = k_B T \ln a_i + \mu_i^0 \quad \text{Equation 1.17}$$

where the activity can be further broken down via:

$$a_i = c_i \gamma_i \quad \text{Equation 1.18}$$

Here, c_i denotes concentration, γ_i represents the activity coefficient for additional non-ideal effects, μ_i^0 is defined as the reference chemical potential where $\gamma_i = 1$; k_B is Boltzmann constant; T is temperature. The activity considers the concentration effects and non-ideality.

1.6.2 DIFFUSIVITY: MODIFIED FICK'S LAW

Using the definition of the chemical potential, along with the general state energy diagram in **Figure 1.8**, random walk diffusivity of a species diffusing through a medium can be expressed as⁴⁹:

$$D_i = \frac{(\Delta x)^2}{2\tau_0 \exp\left(\frac{(\mu_{i,TS} - \mu_i)}{k_B T}\right)} = \frac{(\Delta x)^2}{2\tau_0} \frac{\gamma_i}{\gamma_{i,TS}} = D_0 \frac{\gamma_i}{\gamma_{i,TS}} \quad \text{Equation 1.19}$$

Here, Δx is the average step length (i.e. the distance of one diffusive hop); τ_0 is the time between barrier-less transitions; $\gamma_i = \exp\left(\frac{\mu_i - \mu_i^0}{k_B T}\right)$ and $\gamma_{i,TS} = \exp\left(\frac{\mu_{i,TS} - \mu_{i,TS}^0}{k_B T}\right)$ are the activity coefficients of the diffusing particle in the inactivated and the transition (activated) states, respectively. Essentially, the excess chemical potential drives the random walk

diffusion (making it not just dependent on temperature and entropic effects), which can be determined by equating the squared distance of a diffusive hop to the probability for a particle to translate in the positive direction (factor of two) and the mean time for each transition. The diffusion flux of a species can then be calculated by⁴⁷:

$$F_i = -D_i \frac{c_i}{k_B T} \frac{\partial \mu_i}{\partial x} = -D_0 \frac{\gamma_i}{\gamma_{i,TS}} \left(1 + \frac{\partial \ln \gamma_i}{\partial \ln c_i} \right) \nabla c_i \quad \text{Equation 1.20}$$

Equation 1.20 can subsequently be further generalized as,

$$F_i = -D_{chem} \nabla c_i \quad \text{Equation 1.21}$$

where D_{chem} is referred to as the chemical diffusivity and decomposed as⁴⁹:

$$D_{chem} = D_0 A_D \quad \text{Equation 1.22}$$

Here, pre-factor A_D is defined, which collectively includes all the terms related to activity coefficient,

$$A_D = \frac{\gamma_i}{\gamma_{i,TS}} \left(1 + \frac{\partial \ln \gamma_i}{\partial \ln c_i} \right) \quad \text{Equation 1.23}$$

For a dilute solution, Fick's Law can be recovered from **Equation 1.20** when the activity approaches the actual concentration ($a_i \rightarrow c_i$), the activity coefficient of the transition (activated) state approaches one ($\gamma_{TS} \rightarrow 1$), and the pre-factor is equal to one ($A_D = 1$). For Li-ion diffusion in the solid electrode, Fick's Law has been widely used, where D_{chem} is assumed to be a constant. However, as reported from experimental results⁵⁰, the diffusivity obtained using Fick's Law varies significantly as a function of SOC. Since the Li-ion concentration x_{Li} changes substantially over the SOC range during charge/discharge, the dilute solution assumption breaks down, especially at high Li-ion concentration⁵¹. Therefore, the inclusion of the activity coefficient term A_D becomes critical in correlating the diffusivity of Li-ion with SOC.

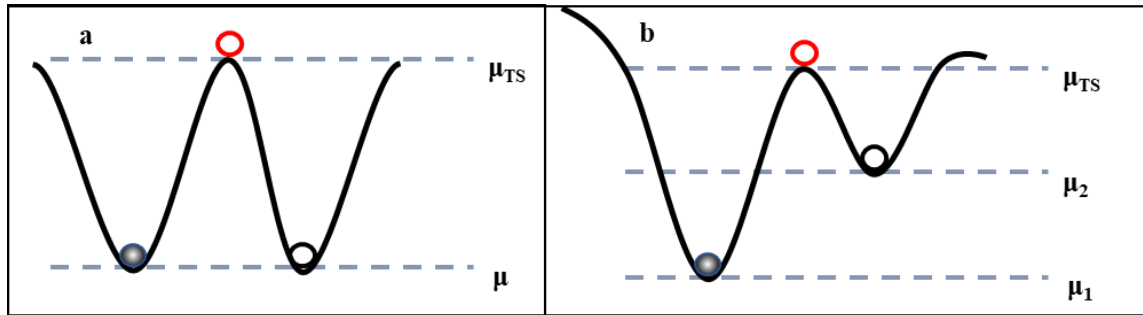


Figure 1.8. | Typical energy landscape (a) diffusion; (b) reaction.⁴⁹

1.6.3 REACTION KINETICS: MODIFIED BUTLER-VOLMER EQUATION

For the charge transfer reaction at the interface between the liquid electrolyte and solid electrode:



The electrochemical potentials of each species are represented as:

$$\mu_{Li^+} = \mu_{Li^+}^0 + k_B T \ln a_{Li^+} + e\phi_i \quad \text{Equation 1.25}$$

$$\mu_{Li} = \mu_{Li}^0 + k_B T \ln a_{Li} + e\phi_s \quad \text{Equation 1.26}$$

$$\mu_e = \mu_e^0 - e\phi_s \quad \text{Equation 1.27}$$

where, i and s denote liquid phase and solid phase; e is the elementary charge on an electron, $1.6 \times 10^{-19} \text{C}$; ϕ is the electric potential. At equilibrium, the sum of the chemical potentials on each side of **Equation 1.24** are equal, and:

$$\mu_{Li^+} + \mu_e = \mu_{Li} \quad \text{Equation 1.28}$$

The equilibrium potential, $\Delta\phi_{eq}$, between the Li^+ and Li ($\Delta\phi_{eq} = \phi_s - \phi_i$) can be related to the activity of the reacting species by the Nernst Equation:

$$\Delta\phi_{eq} = V_0 + \frac{k_B T}{e} \ln \frac{a_{Li^+}}{a_{Li}} \quad \text{Equation 1.29}$$

where $V_0 = \frac{-\mu_{Li^+}^0 + \mu_{Li}^0 + \mu_e^0}{e}$. To model the charge transfer reaction for a nonideal solution, the activity of the reactants and products needs to be accounted for, and the transition state needs to be considered. Here, state 1 is Li^+ and an electron, and state 2 is the Li in the active material. The potential of the transition state is the linear combination of the two present potentials,

$$\mu_{TS} = \mu_{TS}^0 + k_B T \ln \gamma_{TS} + \alpha e \phi_s - (1 - \alpha) e \Delta \phi \quad \text{Equation 1.30}$$

The coefficient α denotes the symmetry of the transition state. A general reaction rate for species proceeding between two states, denoted 1 and 2, can be represented by:

$$r = -k_0 \left[\exp \left(-\frac{(\mu_{TS} - (\mu_{Li^+} + \mu_e))}{k_B T} \right) - \exp \left(-\frac{(\mu_{TS} - \mu_{Li})}{k_B T} \right) \right] \quad \text{Equation 1.31}$$

where the reaction rate is defined in units of t^{-1} , attempt frequency is k_0 , μ_1 is the chemical potential of state 1, μ_2 is the chemical potential for state 2, $\mu_{TS} - (\mu_{Li^+} + \mu_e)$ is the forward reaction energy barrier, and $\mu_{TS} - \mu_{Li}$ is the reverse reaction energy barrier.

Defining another pre-factor, A_k and expressed as,

$$A_k = \frac{\gamma_O^{(1-\alpha)} \gamma_R^\alpha}{\gamma_{TS}} \quad \text{Equation 1.32}$$

After plugging in μ_{TS} and $\Delta \phi_{eq}$ from **Equation 1.30** and **Equation 1.29**, the reaction rate equation becomes⁴⁹:

$$r = k^0 c_O^{(1-\alpha)} c_R^\alpha A_k \left[\exp \left(\frac{(1-\alpha)e\eta}{k_B T} \right) - \exp \left(-\frac{\alpha e \eta}{k_B T} \right) \right] \quad \text{Equation 1.33}$$

where $k^0 = k_0 \exp \left(\frac{(1-\alpha)(\mu_{Li^+}^0 + \mu_e^0) + \alpha \mu_{Li}^0 - \mu_{TS}^0}{k_B T} \right)$, $\eta = \Delta \phi - \Delta \phi_{eq}$, and $\Delta \phi = \phi_s - \phi_i$; k_0 is the attempt frequency. The reaction rate **Equation 1.33** recovers the Butler-Volmer Equation in Newman's model for dilute solutions with $\gamma_O = \gamma_R = \gamma_{TS} = 1$ and $A_k = 1$.

The pre-factor A_k affects the interfacial reaction rate constant for concentrated solutions over the whole SOC range.

As a result, a modified porous electrode theory for a LIB is presented in this section, which combines the Butler-Volmer equation with concentrated solution theory and standard porous electrode theory equations. The derivation here will later be used in Chapter 3 for studying non-ideality in electrochemical impedance spectroscopy (EIS) data for a $\text{Li}(\text{Ni}_{0.5}\text{Mn}_{0.3}\text{Co}_{0.2})\text{O}_2$ system at various SOC.

CHAPTER 2: DECONVOLUTION OF THE THERMODYNAMIC, KINETIC, AND TRANSPORT PROPERTIES FROM COMMERCIAL LARGE FORMAT LI-ION BATTERIES

Multi physics-based Li-ion battery models, developed by Newman's group, use partial differential equations (PDEs) to describe the interfacial transport of charge carriers (e.g. electrons, ions, holes) and reactants across the solid/liquid interfaces of LIB cells.^{52,53} In addition, LIBs under different operating conditions (e.g. high current, temperature variations) and cell configurations (e.g. 18650 cylindrical, prismatic, coin cell) lead to anisotropic distributions of voltage, temperature, and concentration.^{54,55} Newman's pseudo-2D (P2D) models can describe complex behaviors inside LIBs. However, solving the P2D model equations requires complex mathematical solvers. In addition to the electrochemical model, a generic thermal model was proposed by Bernardi et.al that utilized a general energy balance to determine the heat generation and temperature distribution within battery systems. Electrochemical-thermal coupled (ECT) models⁵⁶⁻⁵⁹ have been developed to predict temperature effects on the capacity fade, performance, and the dynamic response of LIBs (e.g. pulse charge/discharge driving cycles). In general, ECT models follow two primary approaches: discrete or homogenous.⁶⁰ The main tradeoffs between the two ECT approaches are accuracy and speed (i.e. discrete ECT has greater temperature accuracy but homogeneous ECT has faster computational speed). Furthermore, the parameters that describe the multi-dimensional and multi-physics

behavior inside LIBs need to be extracted experimentally⁶¹, fitted empirically⁶², or determined by *ab initio* calculation⁶³. Approximately 40 parameters need to be determined, which decreases the model flexibility when considering one LIB chemistry versus another. There are modeling strategies in the literature for reducing P2D models to a model that consists of only ODEs.⁶⁴ However, many of these reduced-order models (ROMs) consist of overly complex mathematical artifices and transformations (i.e. parabolic profile estimation^{65,66}, state-space⁶⁷, Padé approximation^{68,69}, orthogonal decomposition⁷⁰), which require further development and optimization to convert into code for BMS implementation.⁶⁷

At low-to-moderate current densities, the current distribution throughout the LIB electrodes is essentially homogenous and the reactant concentration gradients are negligible. Under these conditions, the P2D model can be simplified to a single particle model (SPM), which idealizes the respective electrodes as a single porous and spherical particle.^{54,71} Both P2D and SPM models need many parameters (P2D $\simeq 40$ and SPM $\simeq 22$) to describe the electrodes, separator, and electrolyte properties, which can either be obtained from experiments or data fitting. The key problem in experimentally derived parameters is the destructive and invasive nature of the extraction procedure (e.g. cell-teardown and reassembly). The experimental determination of model parameters can be very complex, and hence there have been very few studies focusing on combined modeling and experimental work of full-cells.^{72,73} It has been shown that it is possible to measure and combine the properties of each electrode and compare with the measurements performed on the full cell, which opens a new way of modeling Li-ion cells, without the need for complex experimentation. Verma et. al⁵⁰ was able to use galvanostatic

intermittent titration technique (GITT) to characterize the kinetic and transport properties of NMC532 and coupled the results with both SPM and P2D models. A surface roughness factor was incorporated to model the alterations in electrode/electrolyte interfacial area, diffusion coefficients, and exchange current densities. However, the computational load of P2D and SPM models, with a large number of parameters, can be exhaustive and require fine meshes to predict the concentration and voltage gradients.⁷⁴ Therefore, alternative modeling strategies that require fewer parameters and computational load are more advantageous for a BMS. Lower-dimensional or nondimensional models are traditionally evaluated with equivalent circuit models (ECM) (e.g. resistors, capacitors, inductors), which cannot be directly linked to any specific chemical/physical process inside a LIB. Hence, SPMs are preferred over ECMs in situations where computation power is limited, such as in a BMS, though a model that can capture the battery behavior with few parameters without losing connection to the physical world is much preferred. It would also be advantageous if the experimental parameters could be determined without being destructive to the cells/stacks.

To model a full-cell without the invasiveness of disassembling a full-cell and without needing to know the chemistry, a simplified numerical electrochemical-thermal battery model is presented in this section. The model requires only four parameters that need fitting/experimental measurements (later extracted in Section 2.2 and will be implemented in Section 2.3.2): the exchange current (i_0S), the diffusion time constant (τ), the internal resistance (R_{IR}), and the entropic heat coefficient ($dUdT^{-1}$). The model is semi-empirical and based on a lumped model developed by Ekström et al⁷⁴ using the diffusion time constant (τ). The model presented consists of one PDE which solves the SOC equation

for the LIB full-cell, but in this section, the State Space approach is used to further reduce the PDEs to ODEs for rapid model calculation. The higher computational speed and model simplification to ODEs makes implementation in BMS chips more facile. In addition to this mathematical reduction, a thermal model is also coupled to the lumped model for evaluating the temperature and heat generation. For simplicity, the new model is defined as the tau lumped model (TLM). The calculation time of the TLM is reduced even further, but still requires physical interpretation, which an experimental methodology is developed to find the fitting bounds. Detailed experimental determination of the critical modeling parameters is reported in this section to accentuate the extremely high accuracy of the model in predicting the voltage and temperature profiles of a commercial 50Ah Samsung NCM532/Graphite Li-ion battery cell, using the simplified reduced electrochemical-thermal lumped model.

2.1 EXPERIMENTAL

2.1.1 CELL TEARDOWN AND PHYSICAL CHARACTERIZATION

Thermodynamic, kinetic, and transport properties for commercial LIBs were extracted from Samsung large-format 50Ah prismatic cells (refer to **Figure 2.1a**). These cells were assembled with a $\text{LiNi}_{0.5}\text{Mn}_{0.3}\text{Co}_{0.2}\text{O}_2$ (NMC532) cathode and a graphite anode. There were two jelly rolls inside the casing (refer to **Figure 2.1b**). Most of the experiments focused on full-cell-level properties, while electrode-level experiments were also done to enhance interpretation and discussion. To obtain the electrode-level properties, it was necessary to tear down the cells. This allowed both physical characterizations to be performed and for individual electrodes to be rebuilt as half cells – where one electrode was paired with a Li foil counter/reference electrode.

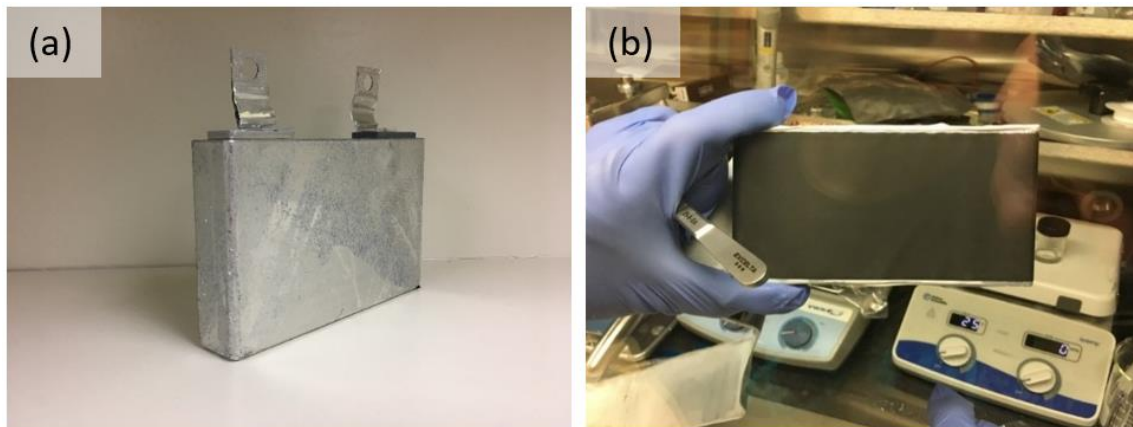


Figure 2.1 | Photograph of (a) the large format 50 Ah prismatic cell and (b) one of two jelly rolls

Cell teardown was conducted following complete discharge to a lower voltage bound of 2.8V, following a 24 hr relaxation time to reach electrochemical equilibrium. During the cell teardown process, the tabs were wrapped with electrical tape to prevent short-circuiting and transferred inside an argon-filled (Ar, UHP Praxair) MBraun Glovebox (H_2O and O_2 levels $< 0.1\text{ppm}$). First, two parallel lines separated by 1 mm were drawn 2 mm below and above the edge of the casing with a scalpel. A hydraulic prismatic cell opener was used to remove the casing on the drawn lines. The tabs and busbar were separated from the two jellyrolls for half-cell and electrode-level characterization purposes.

Energy-dispersive X-ray Spectroscopy (EDX) and Scanning Electron Microscopy (SEM) were performed on a Zeiss Ultraplus Field Emission Scanning Electron Microscope. X-ray photoelectron spectroscopy (XPS) measurements were conducted on a Kratos AXIS Ultra DLD XPS system. Atomic ratios of Ni, Co, and Mn in the cathode active material were determined using a Perkin-Elmer Inductively Coupled Plasma Optical Emission Spectroscopy (ICP-OES). Electrodes that were salvaged from the 50Ah prismatic cells for chemical analysis were first cut into 1.76 cm^2 disk electrodes and stored in EMC

(Ethyl-Methyl Carbonate) for 30 minutes to remove residual salts. Afterwards, the electrodes were transferred to an Ar-filled Kratos AXIS Ultra multipurpose transfer vessel and finally removed from the glovebox for physical characterization.

Inductively coupled plasma optical emission spectroscopy (ICP-OES) was used to confirm the atomic ratios of Ni, Co, and Mn in the cathode material (**Table 2.1**). In accordance with the linearity and sensitivity of the instruments, standard solutions of Li, Mn, Cobalt, and Ni have been prepared for the analysis. The cathode samples were digested in nitric acid and diluted as needed to match the standard solution concentrations. It was found that the cathode composition was $\text{Li}_{0.978}(\text{Ni}_{0.48}\text{Mn}_{0.28}\text{Co}_{0.20})\text{O}_2$. ICP-OES analysis of the anode found minor indications that possible Ni, Co, and Mn dissolution from the cathode occurred and subsequently redeposited on graphite. X-ray photoelectron spectroscopy (XPS) was also used to confirm cell chemistry.

Table 2.1. | Table showing the atomic ratio of Li, Co, Ni, Mn in the cathode and anode obtained by ICP-OES. The cathode was found to be $\text{Li}_{0.98}\text{Ni}_{0.48}\text{Mn}_{0.28}\text{Co}_{0.20}\text{O}_2$ and minor transition metal dissolution at the graphite anode.

	Li 610.37 nm	Co 238.89 nm	Ni 230.29 nm	Mn 257.60 nm
Cathode Intensity	69595	120889	290719	155454
Relative Cathode Composition	0.98	0.20	0.48	0.28
Anode Intensity	20840	136	290	195

2.1.2 ELECTROCHEMICAL AND THERMAL CHARACTERIZATION

LIB half-cells were assembled in an argon-filled MBraun glovebox at 5-8 psig to determine the electrochemical behavior of the cathode and anode independently with respect to a Li/Li^+ reference state. The electrochemical tests were performed in CR2032

coin cells (Hohsen Corp.) – which had 1.76 cm² lithium metal (99.9%, Alfa Aesar) counter/reference electrodes, 2320 Celgard tri-layer PP/PE/PP separators, and 1.2M lithium hexafluorophosphate (LiPF₆, Acros 98%) salt in EC: EMC (3:7 by wt.%) electrolytes. Full-cell-level properties (voltage window: 2.8-4.25V) and electrode-level properties (anode voltage window: 0.001-1V vs. Li/Li⁺; cathode voltage window: 3-4.4V vs Li/Li⁺) were extracted through galvanostatic intermittent titration technique (GITT), 1000Hz AC impedance, and constant current–constant potential (CC-CP) charge/discharge in a Tenney Temperature Control Chamber (temperature range of -15 to 45°C) with a Biologic MPG-205 Battery Tester. The protocol for extracting the Open Circuit Potential (OCP) was outlined in Verma et al.⁵⁰, but in short, the OCP was determined from the steady-state voltage during the relaxation period of the GITT experiment that will be discussed next. For the GITT experiments, two pre-conditioning full charge/discharge CC-CP cycles were performed at C/3 (15A) before the repetitive pulse-rest GITT protocol. After the CP stage, the 50Ah cell was discharged at current pulses of C/10 (5A) for 1 hour followed by a relaxation period of 30 minutes. A total of 50 pulses were used in the GITT protocol.

Entropic heat coefficient ($dUdT^{-1}$) measurements were carried out by first fully charging the 50Ah cell at 45°C with the constant current-constant potential (CC-CP) procedure on an Arbin MSTAT battery cycler inside a Tenney T6S-1 Temperature Control Chamber. In a typical setup, four K-type thermocouples were attached to the 50Ah NMC532/graphite Li-ion battery body with heat-shrink skin, the body without skin, positive terminal, and ambient interior of the chamber. A Graphtec GL240 datalogger with

pre-calibrations for K-type sensors were tested in ice water ($T = 0\text{ }^{\circ}\text{C}$) to ensure the reliability of the measurements.

The 50Ah cells were placed inside the chamber on a Teflon mat to insulate the cell from the metallic body of the thermal chamber. The cell was set in the upright position to minimize high surface area heat transfer for high fidelity modeling. The 50Ah cell was relaxed at OCP for 4 hours to reach thermal and electrochemical equilibrium. After relaxation, the temperature was reduced to $30\text{ }^{\circ}\text{C}$ and held for 4 hours until thermal equilibrium was reestablished. The same procedure was repeated for experiments conducted at $20\text{ }^{\circ}\text{C}$, $10\text{ }^{\circ}\text{C}$, $0\text{ }^{\circ}\text{C}$, and $-15\text{ }^{\circ}\text{C}$. After completion, the cell was reheated to $45\text{ }^{\circ}\text{C}$ for 4 hours and pulsed for 30 minutes at C/5 (10A), and allowed to relax for an additional 4 hours to reach equilibrium. The same temperature cycling procedure from $45\text{ }^{\circ}\text{C}$ to $-15\text{ }^{\circ}\text{C}$ was used for every decrement in SOC.

The EIS experiments were conducted using an Autolab PGSTAT302N potentiostat for an NMC532/Li metal half-cell. In a typical procedure, the Li-ion half-cell was pulsed 12 times with a current of C/20 for 2 hours. After each pulse, the cell was given time to reach electrochemical equilibrium (i.e. until open circuit voltage (OCV) reach ($\frac{dOCV}{dt} \leq 1 \frac{\mu\text{V}}{\text{s}}$) before an EIS measurement was taken. EIS was conducted at a frequency range of 20kHz – 0.01Hz with a sinusoidal voltage amplitude of 10mV in a Tenney T10RS climate control chamber set to $25\text{ }^{\circ}\text{C}$.

2.2 EXTRACTED COMMERCIAL BATTERY PARAMETERS

Particle size and electrode thickness for both the anode and cathode were determined by creating a statistical distribution on 100 particles from SEM. **Figure 2.2a**

shows that the cathode consisted of spherical NMC cathode particles with a range of particle sizes between 0.129-24.89 μm , with an average of 6.32 μm . **Figure 2.2** (a,b) shows a typical cross-sectional image of the cathode with an average thickness of ca. 50 μm . The deconvolution of the GITT dataset, by taking the steady-state voltage during the relaxation period, yielded the OCP as a function of lithiation state for NMC532 as shown in **Figure 2.2c**. The OCP for the lithiated and delithiated state for NMC532 overlaps from the state of charge (SOC) = 20-70% and diverges slightly outside of that range.

Figure 2.2d shows that the anode consisted of irregular shaped graphite particles with a range of sizes between 2.78-20.04 μm with an average particle size of 9.93 μm . **Figure 2.2e** shows a characteristic cross-sectional SEM image of the anode with an average electrode thickness of 68.77 μm . **Figure 2.2f** shows the OCP at various SOC, with the thermodynamically favored phases LiC_{32} , LiC_{12} , and LiC_6 labeled as well. It should be noted that minor voltage hysteresis that is ascribed to phase transitions or order-disorder transitions can be observed in both the OCP vs SOC for NMC532 and graphite⁷⁵⁻⁷⁷. The diameter and the thicknesses of the electrodes were useful for estimating the diffusion length, which can be used to estimate a range for the time diffusion constant in the model (Refer to **Table 2.2**).

Table 2.2. | List of parameters measured experimentally.

Parameter	Value	Unit
Diameters of NMC532 cathode - d_p	6.32	μm
Diameters of LiC_6 anode - d_n	9.93	μm
Thickness of NMC532 cathode - l_p	50.27	μm
Thickness of LiC_6 anode - l_n	68.77	μm

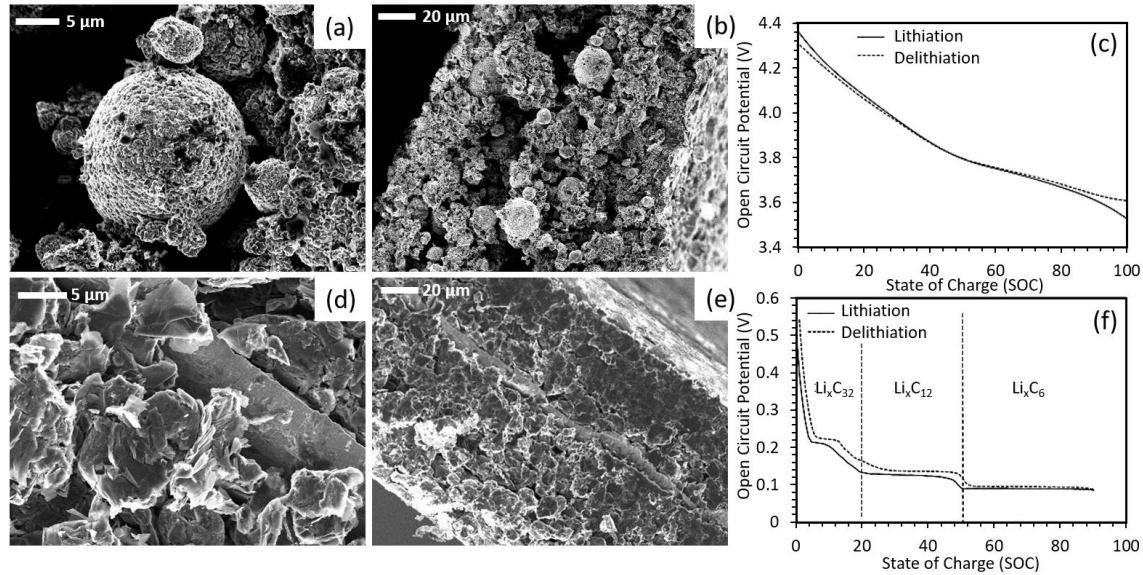


Figure 2.2 | Physical and Electrochemical Characterization. Field-emission scanning electron microscope (FE-SEM) of (a,b) NMC532 cathode, and (c) galvanostatic intermittent titration technique (GITT) for the open circuit potential (OCP) of the cathode. (d,e) FE-SEM images of graphite anode and (f) GITT for the OCP of the anode. Reproduced with permission from Elsevier.⁷⁸

For the full-cell analysis, the entropic heat coefficient ($dUdT^{-1}$) measurements were extracted from the OCP and temperature-vs-time plots at various SOC from 100% charge to complete discharge in increments of 10% SOC.

Figure 2.3(a-d) shows the characteristic OCP measurements as a function of temperature at various SOC. Across a wide SOC range (100% to 30%), the OCP decreases in a staging fashion similar to that of the temperature loss. Also, from 100% to 30% SOC, the differential OCP (dU) ranges from 2 mV to 9 mV and then transitions to an inverse relationship (i.e. OCP increases as the temperature of the cell drops). At SOC < 20%, dU ranges from -6 mV to -4 mV. The average OCP at electrochemical and thermal equilibrium was chosen for the entropy calculation.

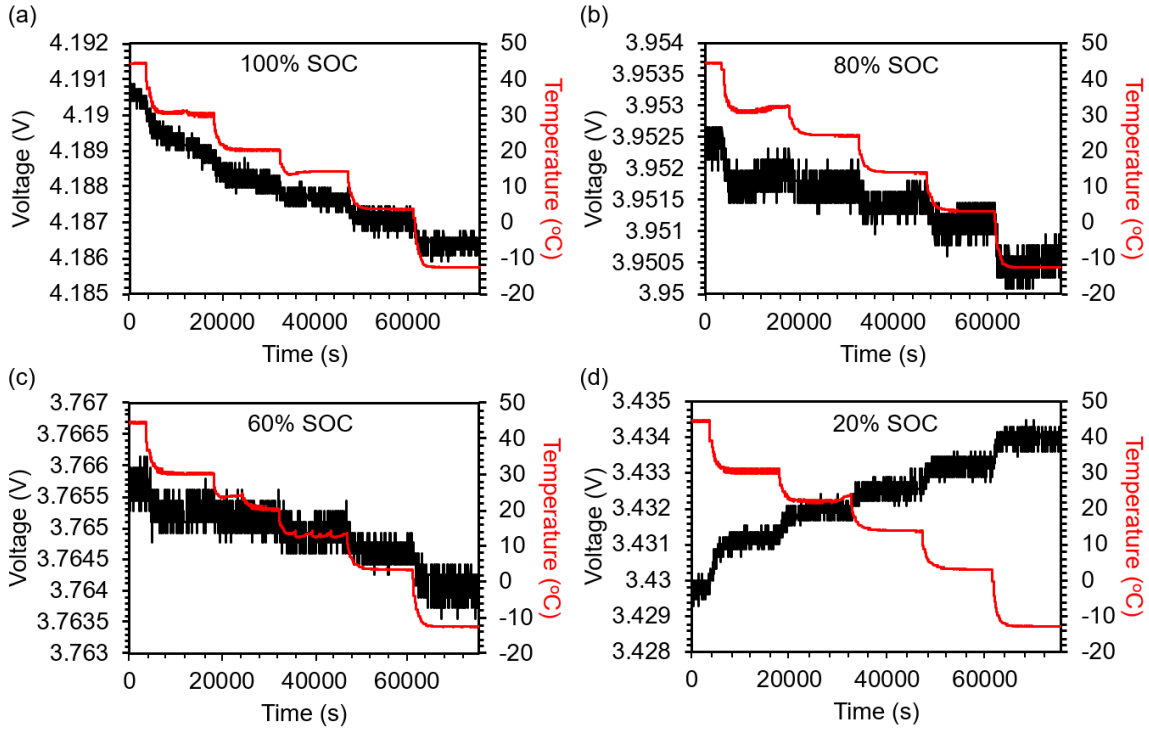


Figure 2.3 | Entropic Heat Coefficient Calculations. Open circuit potential (OCP) changes due to temperature (T) for the calculation of $dUdT^{-1}$ at various state of charge (SOC). Reproduced with permission from Elsevier.⁷⁸

In electrochemical systems, lowering the temperature does more than simply slightly modify the cell voltage. The lower temperature also leads to a reduction in the conductance of charge carriers (e.g. ions, electrons), impedes Li^+ ion migration within the SEI, elevates charge transfer resistance, and introduces diffusional limitations, which leads to large drops in cell-level voltage and capacity loss. Also, anodic overpotentials can reach the Li^+/Li redox couple for Li-plating.⁷⁹ To better understand these effects, the large format cells were charged at 25°C with CC-CP and relaxed at OCP at different iterations in temperature (-15°C, 10°C, 25°C, 45°C) to reach electrochemical and cell-level thermal equilibrium.

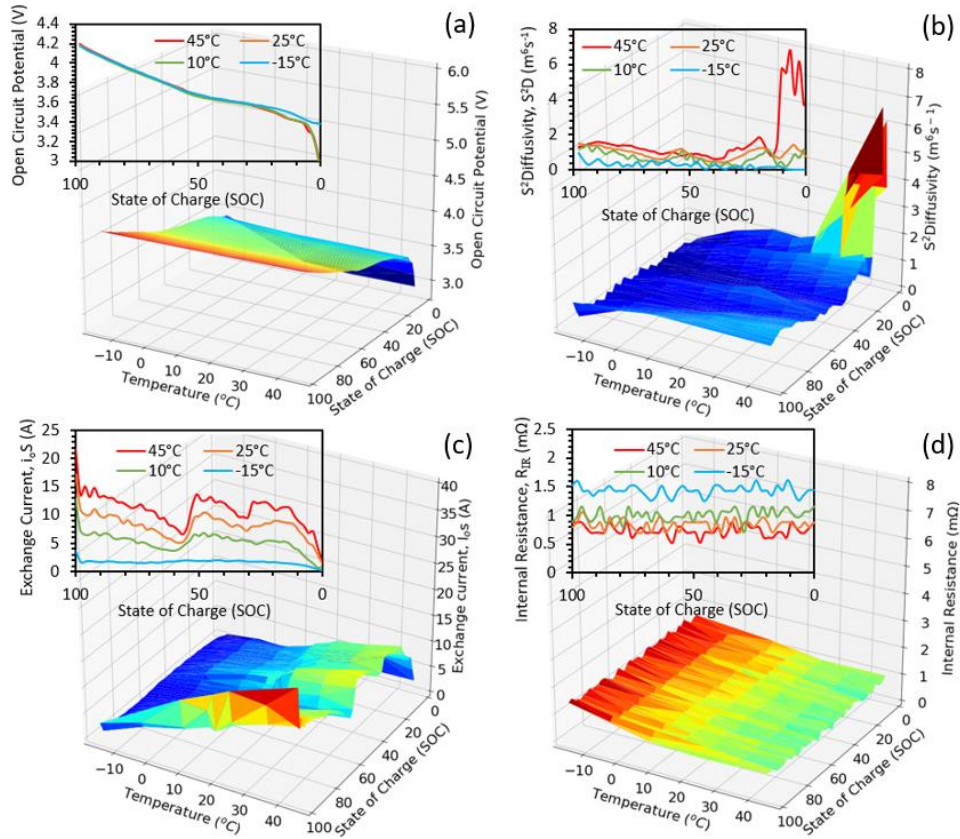


Figure 2.4 | Extracting Modeling Parameters at Different SOC and Temperatures. (a) Open circuit potential, (b) Area independent diffusivity (S^2D), (c) exchange current (i_0S), and (d) internal resistance (R_{IR}) for 50Ah cells at different SOC (100% to 0%) and at varying temperatures (-15°C to 45°C). Reproduced with permission from Elsevier.⁷⁸

The OCP of the 50Ah cells at different temperatures and SOC is plotted in **Figure 2.4a**. The OCP for 100% to 40% SOC from -15°C to 45°C follows a similar trend (i.e. temperature and OCP decreases in tandem) but then diverges at $\text{SOC} < 30\%$. The divergence in OCP is proposed to be due to the onset of the next lithiation phase of graphite, LiC_{12} ⁸⁰. The first inflection point at 3.7V in the OCP of the 50Ah cell corresponds well with the NMC half-cell inflection point at 3.8V. Overall, the end-of-discharge capacity was determined to be 52.54Ah ($T = 45^\circ\text{C}$), 51.81Ah ($T = 25^\circ\text{C}$), 51.41, ($T = 10^\circ\text{C}$), and 47.41 Ah ($T = -15^\circ\text{C}$).

Figure 2.4b shows the effective area independent diffusivity (S^2D) of the 50Ah cells and reflects the limiting diffusional process for the entire system during discharge (i.e. NMC532, graphite). It should be noted that the N/P ratio was determined to be approximately 1.24. The electrochemically active surface area (S) for both NMC and graphite varies with temperature and SOC, which makes the determination of the limiting S^2D difficult. The effective chemical diffusion coefficient or diffusion time constant of Li^+ ions change with SOC. During charge, the anode undergoes various degrees of lithiation to the thermodynamic stable phases LiC_{32} , LiC_{12} , and LiC_6 , and, due to an increase in electrostatic repulsive forces, the diffusion coefficient of the anode will decrease as a function of increased lithiation.⁸¹ On the other hand, the cathode exhibits opposite trends as the delithiation of Li^+ from the bulk NMC crystal leads to more facile pathways for diffusion and leads to higher diffusion coefficients as the amount of Li in the crystal decreases.⁸² The non-destructive extraction of the effective diffusion coefficient (D) was obtained by GITT. In the GITT method, the Li-ion cell system is perturbed by an applied constant current (I) for a specified pulse time (t) and relationships from the relaxation period to the pulse time give the chemical diffusion coefficient⁸³.

$$D = \frac{4}{\pi} \left(\frac{IV_m}{zFS} \right)^2 \left[\frac{dU/dSOC}{dV/d\sqrt{t}} \right]^2 \quad \text{Equation 2.1}$$

where V_m is the molar volume of the active material, F is Faraday's constant ($F = 96485.3 \text{ C mol}^{-1}$), z is the charge number of the carrier ion, S is the electrochemical active surface area, U is the open circuit potential (OCP), V is the measured voltage, SOC is the state-of-charge, and $dU/dSOC$ or $dV/d\sqrt{t}$ were calculated from the linear regression of each pulse. During the pulsation period, the voltage will exhibit a pseudo-instantaneous jump

when current is applied, followed by a steady increase in the voltage. These two regions can then be deconvoluted to express the ohmic plus the kinetic overpotentials ($\eta_{IR} + \eta_{CT}$) and the concentration overpotential η_C , respectively. The ohmic resistance as calculated is negligible to that of the kinetic contributions. Because of this, the ohmic overpotential is subsequently neglected.

Table 2.3 | Table showing the dimensions of the 50Ah cell and the 1000Hz AC ohmic resistance measurement.

Length [mm]	Width 1 [mm]	Width 2 [mm]	Width 3 [mm]	Height [mm]	AC Resistance at 1000 Hz [mΩ]
147.8	27.21	26.64	27.14	91.21	0.783089

By applying GITT relations for diffusivity and keeping S independent for parameter estimation, S²D shows a decreasing trend when the temperature drops from 45°C to -15°C and as SOC goes from 100% to 0%. However, at 45°C the diffusivity spikes towards low SOC (15% to 5%), which is attributed to the phase transition from graphite and seen as an additional plateau at 3.26V (i.e. phase transition from the thermodynamic stable phase LiC₁₂ to LiC₃₂) in the OCP vs SOC plot for the 50Ah cell. The phase transition is consistent with the entropic heat coefficient measurement,⁸⁰ where at higher temperatures, the differential OCP between LiC₁₂ and LiC₃₂ shrinks and gives rise to the LiC₃₂ plateau. Also, lower overpotentials in graphite at both elevated temperatures and low SOC simultaneously lead to more cell-level capacity.

The electrochemical kinetics of the cell can be represented by the Butler-Volmer (BV) current density formulation shown in **Equation 2.2**, followed by the linearized BV expression (which assumes low kinetic overpotentials) as shown in **Equation 2.3**.⁵⁰:

$$i = \frac{I}{S} = i_0 \left[\exp \frac{\alpha_a z F}{RT} \eta_{CT} - \exp \frac{\alpha_c z F}{RT} \eta_{CT} \right] \quad \text{Equation 2.2}$$

$$i = \frac{I}{S} = \frac{i_0(\alpha_a + \alpha_c)F}{RT} \eta_{CT} = \frac{i_0 F}{RT} \eta_{CT}; i_0 S = \frac{RT}{F} \frac{I}{\eta_{CT}} \quad \text{Equation 2.3}$$

where i is the current density, i_0 is the exchange current density, α is the transfer coefficient, z is the number of electrons participating in the electrode reaction ($z = 1$), R is the universal gas constant ($R = 8.314 \text{ J mol}^{-1} \text{ K}^{-1}$), T is the temperature ($T = 293.15 \text{ K}$), and η_{CT} is the charge transfer overpotential.

The charge transfer resistance, R_{CT} , can be deconvoluted from the 50Ah full-cell GITT measurements by applying the linearized Butler-Volmer equation and extracting the exchange current ($i_0 S$) as given in **Equation 2.2** and **Equation 2.3**. It should be noted that the extraction of the electrochemical active surface area (S) is difficult for LIB electrodes due to faradaic processes buried inside the double-layer response in cyclic voltammetry and also varies depending on the volumetric expansion/contraction of the electrode active material at different temperatures due to thermal expansion, lithium-induced expansion (13.2% volume expansion from LiC_{12} to fully lithiated LiC_6),⁸⁴ and/or lifetime history (particle detachment⁸⁵, graphite exfoliation⁸⁶). Therefore, neither the experiments nor the model attempt to decouple exchange current density and the electrochemical surface area ($i_0 S$). **Figure 2.4c** shows the extracted value for the effective $i_0 S$ in the 50Ah full-cell. The $i_0 S$ decreases at lower temperatures and the $i_0 S$ vs SOC oscillatory behavior shrinks. The $i_0 S$ behavior indicates sluggish kinetics at low temperature (-15°C) and the typical increase

at near 50% is not apparent when compared to the other temperatures (10°C, 25°C, 45°C). During the NMC half-cell inflection at 3.8V or full cell inflection at 3.7V, the exchange current of the cell drops, which shows that the number of reactions is controlled by the cathode. **Figure 2.4d** represents the internal resistance R_{IR} of the cell and shows an increasing trend at lower temperatures.

Table 2.4 | Table showing the method used to measure the average active material loading of the anode and the cathode.

Anode	Initial Mass	Mass of Electrode	Mass of Particles
Average	59.44	16.27	12.27 mg/cm ²
StDev	2.27	0.70	1.99
Cathode	Initial Mass	Mass of Electrode	Mass of Particle
Average	88.40	9.11	22.53 mg/cm ²
StDev	1.00	0.65	1.10

Based on the results above, estimates for the various parameters needed to be made as a function of temperature. These are summarized in **Figure 2.5(a,b)**. The average exchange current (i_0S), area independent diffusivity (S^2D), and internal resistance (R_{IR}) across 0% to 100% SOC are plotted in **Figure 2.5a**. There is an increasing trend for i_0S and S^2D at increasing temperatures (-15 °C to 45 °C), which corresponds to improved kinetics and mass transfer. Additionally, the internal resistance of the cell decreased at elevated temperatures. **Figure 2.5c** shows 2 cycles of constant current-constant potential (CC-CP) with the temperature measurements on the 50Ah cell terminal and casing body. The parameters extracted from **Figure 2.5 (a,b)** will be implemented into the model and used to validate **Figure 2.5c** for model fidelity.

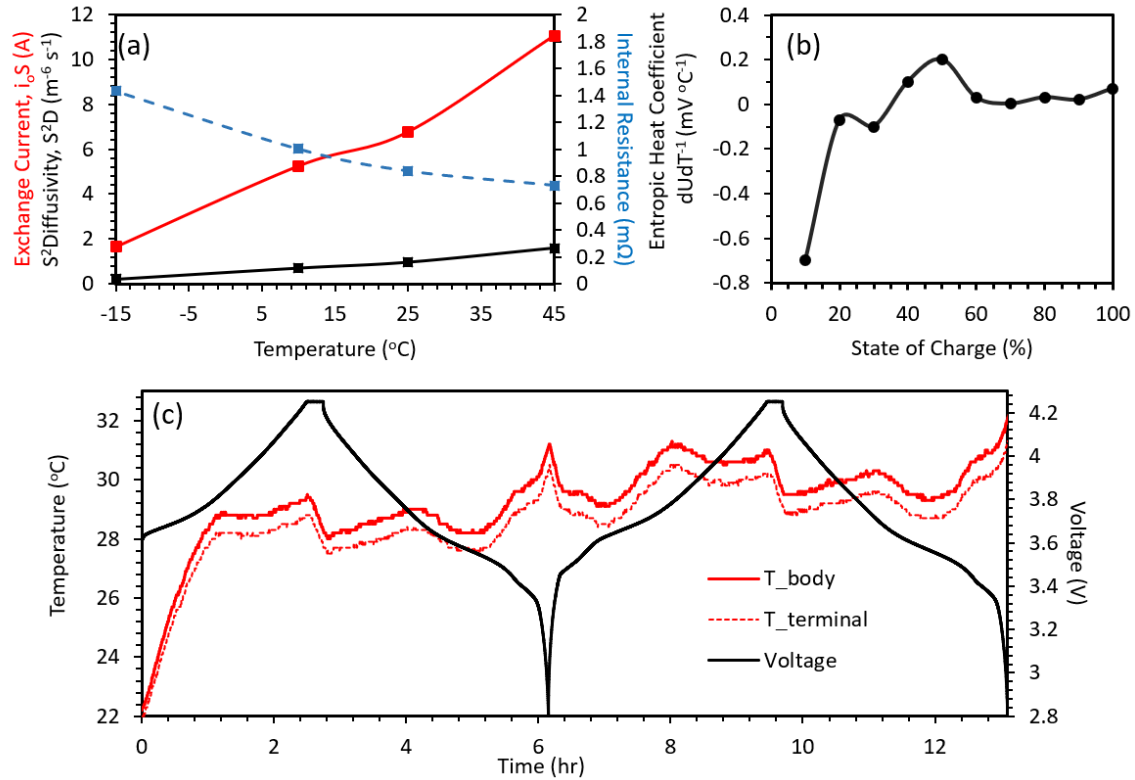


Figure 2.5 | Modeling Parameters and Cycling Profile. (a) Represents the average exchange current (red line), area independent diffusivity (black line), and ohmic resistance (blue line), (b) entropic heat coefficient at different state of charge, and (c) CC-CP charge-discharge profile with temperature measurements on the 50Ah cell terminal and casing body. Reproduced with permission from Elsevier.⁷⁸

2.3 ELECTROCHEMICAL-THERMAL MODEL: PERFORMANCE PREDICTIONS OF COMMERCIAL LI-ION BATTERIES

2.3.1 REDUCED ORDER LUMPED MODEL (TLM-MODEL)

The tau lumped model presented by Ekström et al.⁷⁴ provides the possibility to model a full cell and consists of the equations presented in **Table 2.5**.

Table 2.5 | Table showing the equations in the lumped model from Ekström et al.⁷⁴

Model	Equations
SOC estimation	$\tau \frac{\partial SOC}{\partial t} + \nabla \cdot (-\nabla SOC) = 0$ Equation 2.4
	BC: $\nabla SOC _{x=1} = \frac{\tau I_{cell}}{3Q_{cell,0}}$ Equation 2.5
	BC: $\nabla SOC _{x=0} = 0$ Equation 2.6
	IC: $\nabla SOC _{t=0} = SOC_{cell,0}$ Equation 2.7
	$\overline{SOC} = 3 \int_0^1 SOC x^2 \partial x$ Equation 2-8
Overpotential calculations	$V_{cell} = U(\overline{SOC}, T) + \eta_{ir} + \eta_{act} + \eta_{conc}$ Equation 2.9
	$\eta_{ir} = I_{cell} R_{cell}$ Equation 2.10
	$\eta_{act} = \frac{2RT}{F} \operatorname{asinh} \frac{I_{cell}}{2i_0 S}$ Equation 2.11
	$\eta_{conc} = U_{cell}(SOC _{x=1}, T) - U(\overline{SOC}, T)$ Equation 2.12
	$U(\overline{SOC}, T) = U_{ref}(SOC, T) + (T - T_{ref}) \frac{dU(SOC)}{dT}$ Equation 2.13

In this section, the notations were slightly modified to introduce the temperature dependency of the open circuit potential. The equations from **Table 2.5** can predict the voltage profiles for a driving cycle with relatively high precision.⁷⁴ Two main advantages make this model reliable: it is fast and requires no knowledge of cell chemistry. Even though it is a relatively fast model, it still contains one PDE (Partial Differential Equation), which requires a one-dimensional meshed domain, making it difficult to implement in the chipsets of a BMS, for example. In this study, the PDE shown in **Equation 2.5** was reduced to a series of ODEs given in **Equation 2.15** to **Equation 2.17**:

$$\tau \frac{\partial SOC}{\partial t} + \nabla \cdot (-\nabla SOC) = 0 \quad \text{Equation 2.14}$$

$$\frac{\partial SOC_{average}}{\partial t} = \frac{3I}{3Q_0} \quad \text{Equation 2.15}$$

$$SOC_{surface} = SOC_{average} + \sum_{i=1}^{N=4} Q_i \quad \text{Equation 2.16}$$

$$\frac{dQ_i}{dt} = \frac{a_i Q_i}{\tau} + \frac{b_i I}{3Q_0} \quad \text{Equation 2.17}$$

$$SOC_{average}(t = 0) = SOC_0 \quad \text{Equation 2.18}$$

Equation 2.15 - Equation 2.17 were used to model the average SOC and the SOC at the surface. In addition to this simplification, a heat generation term was also added to the model for calculating the temperature (**Equation 2.19**):

$$\dot{Q}_{gen} = I \left(V_{cell} - U(SOC_{average}) + T \frac{dU(SOC_{average})}{dT} \right) \quad \text{Equation 2.19}$$

where I is the current applied to the cell, U is the open circuit potential, V_{cell} is the potential of the cell, calculated with **Equation 2.9**, T the temperature of the cell, and the last term represents the variation of the OCP with the temperature, which in the heat generation term represents the reversible heat generation due to the displacement of the lattice during the intercalation/de-intercalation. While the cell potential was calculated with the model, the reversible term requires time-consuming experiments.

The Biot number was calculated to check if the cell can be modeled as a lumped capacitance model (**Equation 2.20**):

$$Bi = \frac{hL_c}{k} \quad \text{Equation 2.20}$$

where h is the heat transfer coefficient, L_c is the characteristic length and k is the effective thermal conductivity of the cell. The heat transfer coefficient is calculated using the Nusselt correlations considering natural convection for a vertical block with the dimensions

provided and the thermal conductivity derives from Lundgren et al⁸⁷. For both thermal conductivities (in-plane and through-plane), the Biot number is smaller than 0.1, which means that that cell can be modeled using the lump capacitance model⁸⁸ using **Equation 2.21**:

$$m_{cell}C_p \frac{dT}{dt} = \dot{Q}_{gen} - hA(T - T_{amb}(t)) \quad \text{Equation 2.21}$$

The mass of the cell (m_{cell}) was measured experimentally, while the specific heat (C_p) was taken from Schmalstieg et al⁷². The ambient temperature increases slowly with time and was extracted from the data logger. The final TLM consists of **Equation 2.9** to **Equation 2.21**. The time diffusion constant (τ) from **Equation 2.17**, the exchange current (i_0S) from **Equation 2.11**, and the ohmic overpotential (η_{IR}) from **Equation 2.10** are the unknowns that require fitting or experimental determination. The complete list of parameters can be found in the next section, in **Table 2.7**. Calculating or measuring these parameters using experimental data is a challenging task since the model was used for modeling a full-cell and not for separate electrodes.

2.3.2 APPLICATION OF EXPERIMENTAL BATTERY PARAMETERS INTO THE MODEL

The Levenberg-Marquardt nonlinear optimization method was used for fitting the three parameters during a discharge process for the 50Ah cells at a constant current (CC) of 15A (0.3C) in ambient conditions. After the optimization, the fitted values were extracted and inserted into the final model. The TLM model showed an excellent agreement with the experimental data when comparing the potentials, as seen in **Figure 2.6**.

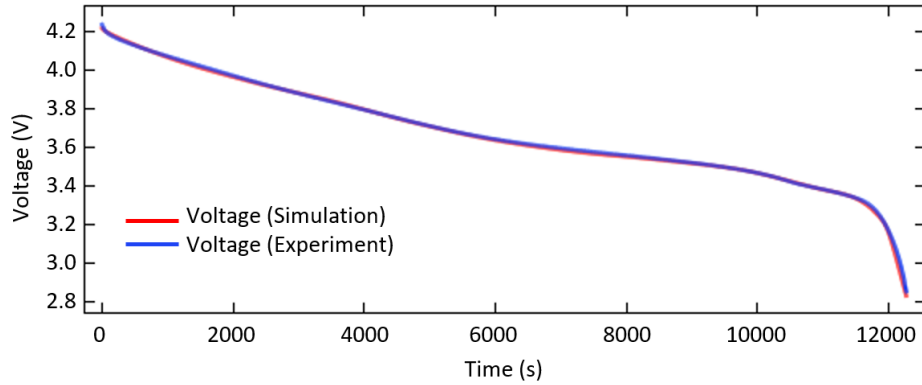


Figure 2.6. | Plot showing the cell potential calculated using the TLM and the potential measured experimentally for a discharge process of 0.3C. Reproduced with permission from Elsevier.⁷⁸

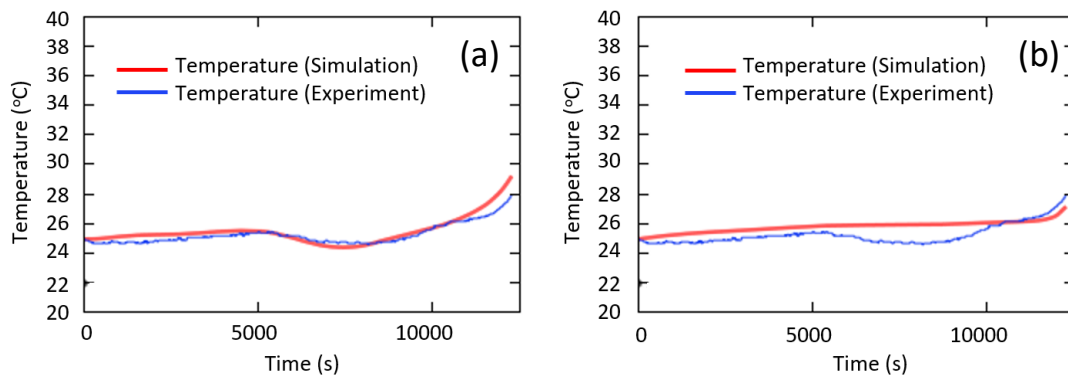


Figure 2.7. | Plots showing the cell temperature calculated using the TLM and the potential measured experimentally for a CC discharge process of 0.3C when a) the reversible term is included and b) when the reversible term is neglected. Reproduced with permission from Elsevier.⁷⁸

The difference between the experiment and the model is less than 7 mV on average over the entire discharge time. The temperature calculated using **Equation 2.11** also shows good agreement with the experimental data, as seen in **Figure 2.7**. The temperature calculated with the model not only shows a good agreement with experimental data, but it also follows the phase changes within the cell and the subsequent alterations in the entropic

heat coefficient ($dUdT^{-1}$) at different SOCs. When the $dUdT^{-1}$ term is neglected in **Figure 2.7b**, the temperature differences are still small, but the model does not capture the influence of phase changes within the cell. The fitted parameters used for getting the data in **Figure 2.6** and **Figure 2.7** are given in **Table 2.6**.

Table 2.6 | Model parameters calculated using the Levenberg-Marquardt optimization method.

i_0S [A]	τ [s]	η_{IR} [V]
6.808	1716	0.0028

The exchange current (i_0S) has the electrochemical active area (S) embedded in the term for the entire cell as it is exceedingly difficult to deconvolute. The exchange current was measured experimentally at different temperatures for the entire cell (**Figure 2.5**), but at 25°C, the average value over the entire discharge time was around 6.8 A, which is very close to the value obtained using the Levenberg-Marquardt optimization method. This observation shows that it is possible to measure this parameter for a full-cell, reducing the number of unknowns that require fitting. The time diffusion constant (τ) can be calculated analytically using the following equation⁸⁹:

$$\tau = \frac{l^2}{D} \quad \text{Equation 2.22}$$

where l is the electrochemical diffusion length, which can be the thickness of the electrode in thin-film electrodes or the particle radius, and D is the diffusion coefficient. For this section, the diffusion length was assumed to be the radius of the particles, for finding the fitting bounds. Because the study was focused on a full-cell rather than on individual electrodes, it is important to find which radius can be used, the cathode or the anode. Taking the constant value for the graphite anode diffusion coefficient from Sikha et al⁹⁰, the

diffusion time constant was found (τ) to be a value of 630.8 s, which is lower than the one predicted by the model. When considering the diffusion coefficient from Yang et al⁹¹ and the measured radius of the cathode, the time diffusion constant yields values between 64 s and 12,948 s, which is extremely wide. However, the value given by the fitting process falls in between this range and it can give the bounds for the parameter estimation process.

The ohmic overpotential (η_{IR}) is calculated using the internal resistance of the cell and the discharge current. For a CC discharge process of 15A and a resistance of 0.79 m Ω at 25°C, the ohmic overpotential gives 0.012 V, which is higher than the value fitted in the model. By using the values of the exchange current ($i_0S = 6.8$ A), the time diffusion of the anode ($\tau = 630.8s$) and the internal resistance at 25°C ($R_{cell} = 0.79$ m Ω), the model still shows a good agreement with the experimental data, as seen in **Figure 2.8**, which indicates that the values for the TLM can be obtained experimentally. The exchange current can be measured using the GITT method for a full-cell and the internal resistance can be directly measured for a full-cell using the AC resistance at 1kHz. However, the diffusion coefficient term for the entire cell contains the electrochemical area, which requires additional deconvolution. \

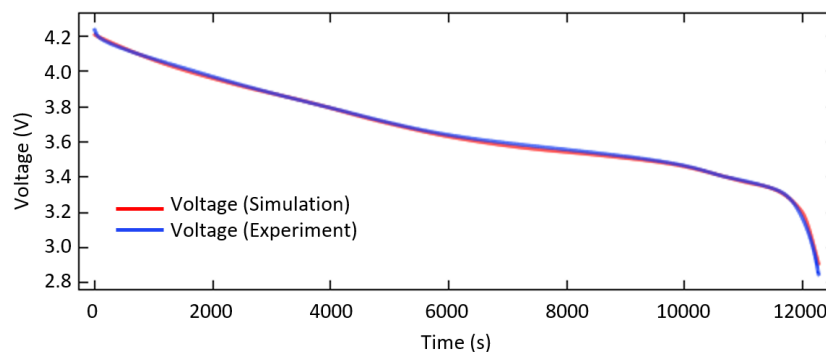


Figure 2.8. | Plot showing the cell potential calculated using the TLM and the potential measured experimentally for a discharge process of 0.3C using the measured internal resistance and the exchange current at 25°C. Reproduced with permission from Elsevier.⁷⁸

An exceptionally good agreement between the model and the experiment can be observed when increasing the discharge current to 25 A (0.5C) as seen in **Figure 2.9a**. When increasing the discharge current to 50A or 1C (**Figure 2.9a**), the model still shows a good agreement for almost the entire discharge process, with the exception that at the end of discharge (EOD), the model predicts a slightly lower capacity. This indicates that at rates that are higher than 0.5C, the parameters should be set to be dependent on the C-rate or the temperature (e.g. such as an Arrhenius dependency), considering that the measured parameters depend on the temperature, but this is beyond the scope of this work.

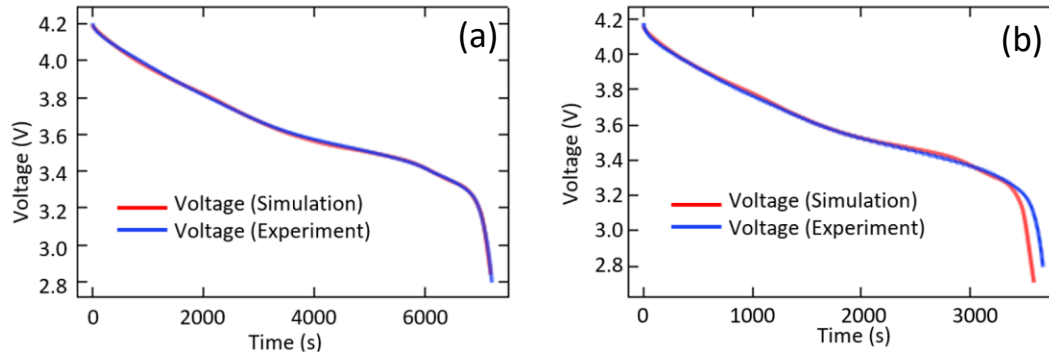


Figure 2.9. | Plots showing the cell potentials calculated using the TLM and the potential measured experimentally for a) a discharge process of 0.5C and for b) a discharge process of 1C, using the measured internal resistance and the exchange current at 25°C. Reproduced with permission from Elsevier.⁷⁸

Table 2.7 | Parameters used for model.

Symbol	Description	Value	Unit	Source
SOC_0	Initial state of charge	1	-	Estimated
I	Applied current	15/25/50	A	Measured
Q_0	Cell capacity	50	Ah	Estimated
C_p	Specific heat of the entire cell	937.5	$J\ kg^{-1}\ K^{-1}$	[⁸⁷]
h	Heat transfer coefficient	4.5	$W\ m^{-2}\ K^{-1}$	Calculated [⁸⁸]
A	Surface of cell exposed to convection	0.0359	m^2	Measured
m_{cell}	Mass of the cell	0.875	kg	Measured
T_{ref}	Reference temperature	298.15	K	Measured
T_{amb}	Ambient temperature	294.15	K	Measured

2.4 SUMMARY

Non-destructive experimental extraction of parameters through a pulse-relaxation GITT method can map the temperature and SOC dependent parameter surface for the OCP, exchange current (i_0S), diffusion time constant (τ), internal resistance (R_{IR}), and the entropic heat coefficient ($dUdT^{-1}$). Also, the reduced order Lumped electrochemical-thermal model (TLM) is fully capable of utilizing the extracted parameters to obtain fast calculation times for voltage and temperature predictions that are consistent with the experimental measurements. The TLM model deviates at high current densities ($>1C$) from cell-level SOC $< 5\%$; however, LIB packs typically operate within the voltage plateau (SOC = 10% to 100%) and BMS discharge cutoffs occur at a specified $dV dt^{-1}$ to ensure pack longevity.

In summary, the State Space approach (PDE to ODE transformation) is an effective method to greatly enhance the calculation time for BMS applications, and the non-destructive GITT measurement for four cell-level parameters (i_0S , τ , R_{IR} , $dUdT^{-1}$) is directly relatable to mathematical quantities in the reduced order-TLM. In a world that requires faster calculations/computational time, a novel method to extract parameters non-destructively can be implemented as initial guesses to increase the convergence time and approach higher-fidelity voltage and temperature predictions.

CHAPTER 3: INVESTIGATION OF THE KINETIC AND TRANSPORT NON-IDEALITIES IN COMMERCIAL LI-ION ELECTRODES - DECONVOLUTING COMPLEX ELECTROCHEMICAL IMPEDANCE SPECTROSCOPY DATA

Chapter 2 explored cell-level properties (OCV , i_0S , τ , R_{IR} , $dUdT^{-1}$) for large 50Ah commercial cells and applied those parameters into a Lumped reduced-order model that utilized a State Space transformation for order reduction. The full cell model in Chapter 2 plays a significant role when fast computational speed, low processing power, and minimal/nondestructive parameter extraction is needed. However, the model cannot capture a necessary-level of fidelity at high C-rates, nor any information at the electrode-level. Therefore, this chapter uses a modified version of the porous electrode theory to investigate the impedance response of a LIB at a higher level of fidelity and complexity.

Electrochemical impedance spectroscopy (EIS) is widely considered to be a powerful characterization tool for separating individual electrochemical processes by their timescales and enabling quantitative analysis of electron transport, interfacial reaction mechanisms, and Li-ion intercalation processes. EIS has been widely used to estimate the diffusivity (D) of Li-ions in the solid active materials and the reaction rate constant (k) at the electrolyte/electrode interface. The quantitative analysis of EIS data is highly complementary to the development of physics-based models (PBMs)^{92,93}. Macroscopic

PBMs of Li-ion cells and batteries began with a relatively simple Fick's law governed solid-phase Li-ion diffusion model, extended from Atlung et al.'s⁹⁴ work in 1979 and named by Santhanagopalan et al.⁹⁵ as the single-particle (SP) model in 2006. Another dominant Li-ion cell full-order model (FOM), commonly referred to as the "pseudo-2D model (P2D)", was developed in 1994 by Fuller et al.⁹⁶, who represented a dual foil Li-ion cell by a pseudo-two-dimensional domain.

Even though PBMs contain most battery physics that represent the key electrochemical processes, it is possible that some important physics-based phenomena are neglected. For example, in a general PBM of LIBs, Li-ion diffusion is governed by Fick's law in a dilute solution, which neglects the thermodynamic nonideality of the solid active material, which experiences large concentration variation during charge/discharge. Although both k (solid/liquid interface reaction or Li-ion intercalation rate) and D (diffusivity of Li-ion in a solid phase) have exhibited correlations with Li-ion content x_{Li} (equals 1-SOC, state of charge), especially at the end of discharge, they have been assumed to be constants over the entire range of SOC⁶⁸. Likely because of this, their values reported from different experimentalists show a wide variation spanning two-to-five orders of magnitude⁹⁷. With this large variation, both battery SOC and State-of-Health (SOH) will remain unpredictable, which means that, ultimately, true battery management and diagnosis remains uncertain.

In the existing literature, the occurrence of nonideality of mixed conducting materials has been widely reported when the charge carrier concentration comprises a significant percentage of the total lattice sites. Concentrated solution theory, with the inclusion of the activity coefficient of the transporting ion, has generally been employed to

account for the nonideal portions of the thermodynamic properties. This chapter seeks to understand the nonideality of a solid Li-ion active material using nonequilibrium thermodynamics in a concentrated solution to correlate k and D with the activity coefficient of the solid solution (γ). These new correlations are then paired with deconvoluted EIS experimental data, where regression is done to determine the experimental γ . This research provides theoretical explanations of the governing mechanisms for such nonlinear interrelationships and a mathematical methodology is developed to obtain such correlations by parameter estimation with experimental data.

The model was developed for a Li-ion half-cell with the geometry illustrated in **Figure 3.1**. This cell includes a porous cathode consisting of solid particles, a polymer separator, and a lithium metal foil that acts as both the counter and reference electrode. The governing equations for this half-cell model are like Newman's pseudo-2D model, including the solution phase Li-ion diffusion, charge conservation in the electrolyte, charge conservation in the cathode, and Li-ion diffusion in the cathode particle.

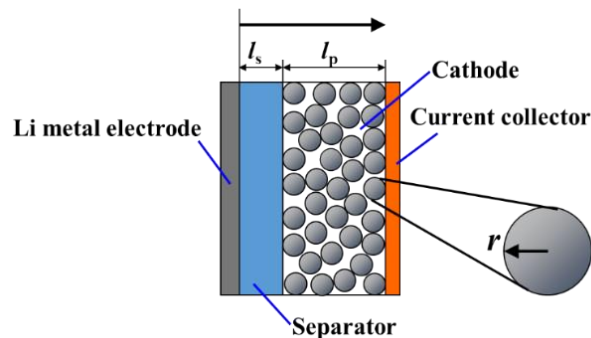


Figure 3.1. | Schematic of a Li-ion half-cell PBM. The porous electrodes are formed by spherical insertion particles. Reproduced with permission from IOP Publishing.⁹⁸

3.1 EXPERIMENTAL EXTRACTION OF ELECTRODE-LEVEL PARAMETERS

There are around 40 parameters that are needed from experimental measurements to run the PBM model. To characterize the anode and cathode separately, Samsung prismatic 50Ah cells were dissected, and then electrodes were cut from each side to construct coin cells in a half-cell configuration. By doing this, the number of parameters can be reduced to 20. These cells had an NMC532 cathode, resulting in half-cells containing the commercial cathode and a Li metal anode/reference. Several material characterization methods were used to deduce chemical and structural information that can be correlated to the information gained from EIS studies. These studies are also designed to provide essential input for the new physics-based EIS model.

3.1.1 MATERIAL CHARACTERIZATION

The microstructure, composition, and electrical conductivity of the extracted NMC532 cathodes were characterized by scanning electron microscopy (SEM), mercury intrusion porosimetry (MIP), X-ray photoelectron spectroscopy (XPS), and four-terminal Linear Scan Voltammetry (LSV). Detailed descriptions of each method are given in the supplementary material. Surface and cross-sectional SEM images were taken to create a statistical distribution of the particle diameter and electrode thickness using ImageJ so that the electrode active area (S) could be assessed. Further, MIP was used to determine the electrode porosity and provide complementary information about the electrode active area. Specifically, the electrodes were cut into 1.76 cm² disk electrodes and then massed. Then, they were delaminated from the current collector using a scalpel. Each component was massed to determine its loading and weight. Ten trials were done for each sample. The samples were then cut into 2mm squares and placed into a holder. The active material mass

was used for porosimetry measurements. XPS and four-terminal LSV measurements were conducted to confirm the elemental composition of the active material and determine the electrical conductivity, respectively.

3.1.2 CELL TEARDOWN AND COIN CELL ASSEMBLY

Samsung prismatic 50 Ah cells purchased from the market were disassembled to make CR2032 coin cells in the half-cell configuration, as shown in **Figure 3.2**. In a typical cell disassembly, the cell was fully discharged to the lower voltage bound (2.8V) and allowed to stabilize for 24 hours. The cell tabs were taped with electrical tape to prevent any abrupt short-circuiting upon transfer. After transferring the cell into the glovebox, a scalpel was used to draw 2 parallel lines 1 mm apart and 2 mm from the top and bottom on the face of the cell. A total of 8 lines were drawn on the casing. A diagonal plier was used to remove the casing at the previously drawn lines. Upon removal of the casing, the tabs and busbar were removed to separate the two jellyrolls (**Figure 3.2b**). Jellyroll 1 was unraveled, measured with a Fisher Scientific Traceable® caliper, and then discarded. Jellyroll 2 was sealed away for coin cell assembly.

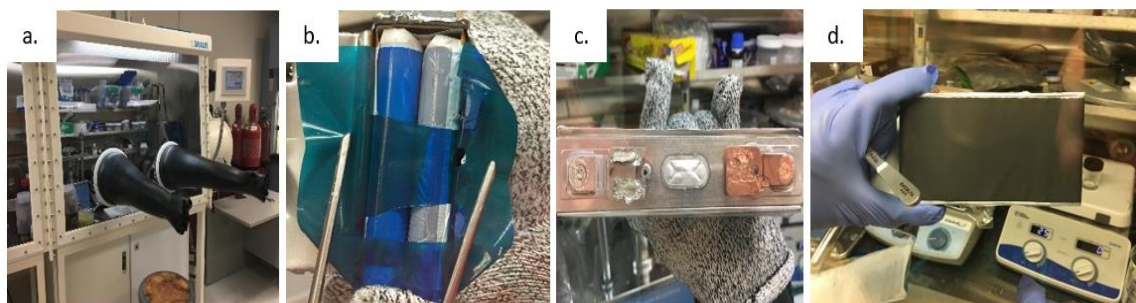


Figure 3.2. | Images depicting the teardown process with (a) Ar-filled MBraun glovebox <math><0.1\text{ ppm H}_2\text{O}</math> and

3.1.3 PHYSICAL CHARACTERIZATION

Scanning Electronic Microscopy (SEM) was conducted on a Zeiss Ultra Plus Field-emission Scanning Electron Microscope. In typical sample preparation, the electrode was cut with a scalpel and placed vertically onto the stage. Several images were captured (representative image of the NMC532 cathode in **Figure 3.3a**) to create a statistical distribution.

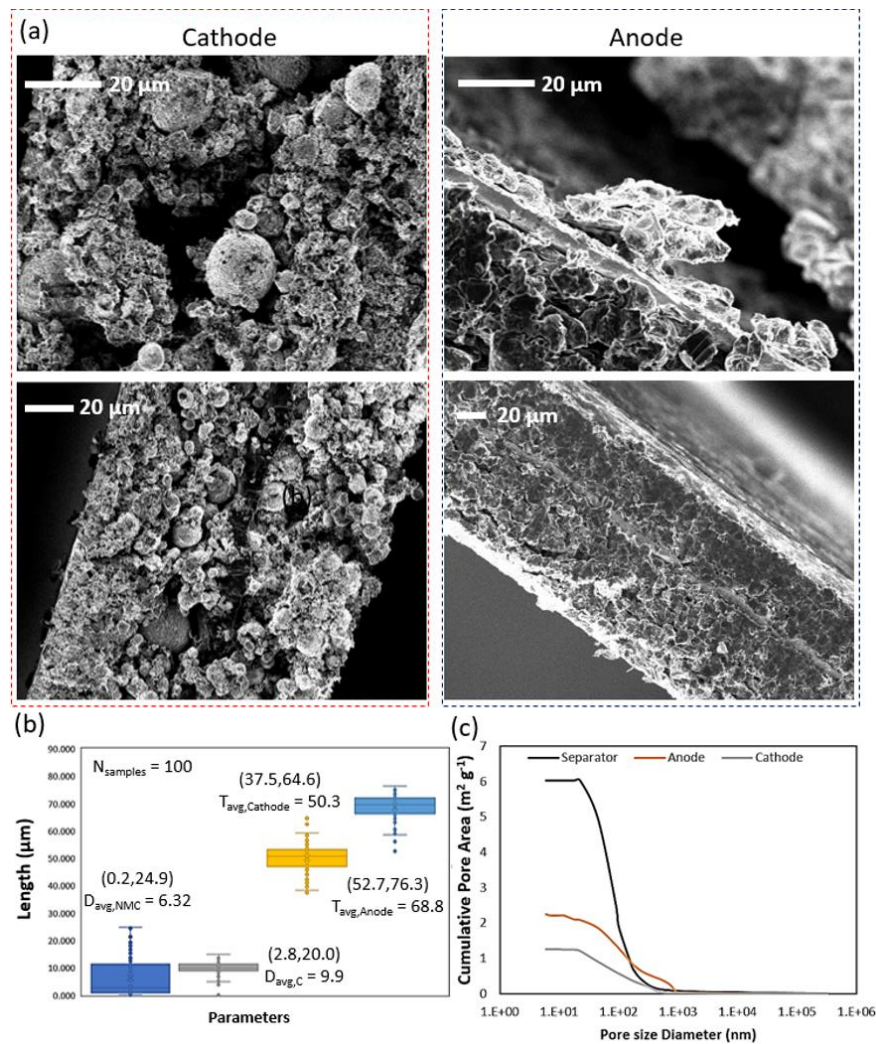


Figure 3.3. | a) SEM images of electrode cross-sections; b) the box and whisker graph of particle size and one side electrode thickness; (c) the cumulative pore area and porosity distribution of cathode, anode, and separator calculated from mercury intrusion porosimetry.

The particle size and electrode thickness were determined to be an average of 100 samples and were calculated with ImageJ. **Figure 3.3a** are the SEM images of both NMC532 cathode and Graphite anode. In **Figure 3.3b**, their particle sizes were collected statistically, and are 6.32 for NMC532 and 9.93 μm Graphite; their electrode thicknesses are 50.27 for the cathode and 68.77 μm for the anode.

Mercury porosimetry was conducted on the anode and cathode by first passivating the current collector in an oven at 100°C for 24 hours. The electrodes were cut into 1.76 cm^2 disk electrodes and massed. The electrodes were then delaminated from the current collector by using a scalpel. The separate components were massed to determine the loading and the weight of the current collector. Ten trials were done for each sample. The samples were then cut into 2mm squares and placed into the holder. The active material mass was used for porosimetry. **Figure 3.3c** shows the pore area versus the pore size diameter, together with the measurements for porosity. The dimension, porosity, and particle size will be used in the Physics-based EIS model later.

3.1.4 ELECTRONIC CONDUCTIVITY OF ELECTRODES

In a typical electronic conductivity measurement, the active electrode material was removed from the current collector with a scalpel then pressed into a pellet with an MTI hydraulic press. Silver wires and silver paste were used to decrease contact resistance between the bipotentiostat and the pellet. **Figure 3.4** shows the electronic conductivity determined for the NMC532 cathode.

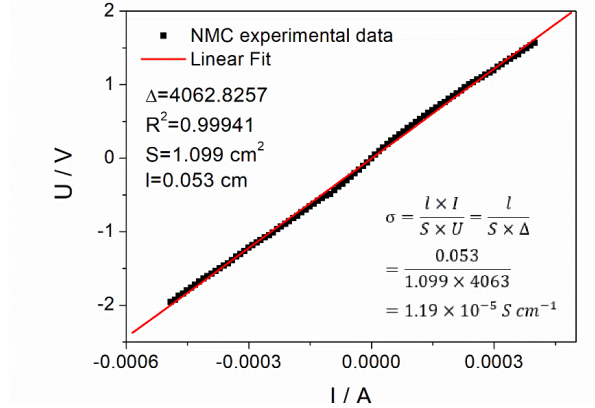


Figure 3.4. | Potential vs current experimental data and fitting of the electronic conductivity of NMC532.

3.1.5 EIS MEASUREMENTS

The EIS experiments were conducted using an Autolab PGSTAT302N potentiostat for an NMC532/Li metal half-cell. In a typical procedure, the Li-ion half-cell was pulsed 12 times with a current of $C/20$ for 2 hours. After each pulse, the cell was given time to reach electrochemical equilibrium (i.e. until open circuit voltage (OCV) reach ($\frac{dOCV}{dt} \leq 1 \frac{\mu V}{s}$) before an EIS measurement was taken. EIS was conducted at a frequency range of 20kHz – 0.01Hz with a sinusoidal voltage amplitude of 10mV in a Tenney T10RS climate control chamber set to 25°C.

3.1.6 GALVANOSTATIC INTERMITTENT TITRATION TECHNIQUE (GITT)

GITT measurements were performed on the assembled coin cell (NMC532/Li metal half-cells) during both charging and discharging cycles to determine the OCV of the NMC532 cathode. The cells were conditioned for 2 cycles with constant current charge-discharge at $C/10$. Then 25 intermittent pulses were applied at $C/20$ for 2 hours until the

upper or lower voltage bound was met. The rest period was over 30 minutes to ensure equilibrium conditions are reached between adjacent pulses.

Table 3.1 | Perturbation form of the Lithium-Ion battery P2D model

Model	Equations
Solution phase diffusion	$\varepsilon_1 i \omega \Delta c_1(x, \omega) = D_{1, \text{eff}} \frac{\partial}{\partial x} \left(\frac{\partial \Delta c_1(x, \omega)}{\partial x} \right) + a(1 - t^+) \frac{\Delta j_s(x, \omega)}{F}; D_{1, \text{eff}} = D_{1, \text{bulk}} \varepsilon_1^{1.5}$ $\left. \frac{\partial \Delta c_1(x, \omega)}{\partial x} \right _{x=0} = 0; \left. \frac{\partial \Delta c_1(x, \omega)}{\partial x} \right _{x=l_n+l_2+l_p} = 0$ $\Delta j_s(x, \omega) = 0 \text{ in the separator region } (0 < x < l_s)$
Charge conservation in the electrolyte	$\frac{\partial}{\partial x} \left(\kappa_{\text{eff}} \frac{\partial \Delta \phi(x, \omega)}{\partial x} - \kappa_d \frac{\partial \Delta c_1(x, \omega)}{\partial x} \right) + a \Delta j_s(x, \omega) = 0$ $\Delta j_s(x, \omega) = 0 \text{ for } 0 < x < l_s$ $\left. \frac{\partial \Delta \phi_1(x, \omega)}{\partial x} \right _{x=0} = 0; \left. \frac{\partial \Delta \phi_1(x, \omega)}{\partial x} \right _{x=l_n+l_1+l_p} = 0$ $K_{\text{eff}} = \kappa_{\text{bulk}} \varepsilon_1^{1.5}; \quad \kappa_d = \kappa_{\text{eff}} \frac{2RT}{Fc_1} (1 - t^+) \left(1 + \frac{d \ln f_{\pm}}{d \ln c_1} \right)$
Charge conservation in solid phase	$\frac{\partial}{\partial x} \left(\sigma_{\text{eff}} \frac{\partial \Delta \phi_s(x, \omega)}{\partial x} \right) - a \Delta j_s(x, \omega) = 0 \quad \sigma_{\text{eff}} = \sigma \varepsilon_s^{1.5}$ $\Delta \phi_s(x, \omega) _{x=0} = 0 \quad \left. \frac{\partial \Delta \phi_s(x, \omega)}{\partial x} \right _{x=l_n} = 0 \quad \left. \frac{\partial \Delta \phi_s(x, \omega)}{\partial x} \right _{x=l_n+l_s} = 0$ $\text{Not applied in the separator region } (0 < x < l_s)$
Butler-Volmer equation for electrochemical reactions	$\Delta j_s(x, \omega) = j_0 \left[\left(\frac{0.5F}{RT} + \frac{0.5F}{RT} \right) \Delta \eta(x, \omega) \right]$ $+ i \omega \Delta \eta(x, \omega) C_{dl} \quad \text{Not applied for } 0 < x < l_s$ $\Delta \eta(x, \omega) = \Delta \phi_s(x, \omega) - \Delta \phi_1(x, \omega) - \Delta U(x, \omega) - \Delta j_s(x, \omega) R_{fitm}$ $j_0 = A_k F k_r c_1^{0.5} (c_{s, \text{max}} - c_s _{r=R_s})^{0.5} (c_s _{r=R_s})^{0.5}$ $\Delta U(x, \omega) = \frac{dU}{d\theta} \Delta \theta(x, \omega)$
Solid-phase diffusion	$i \omega \Delta c_s(r, \omega) = A_D D_s \frac{1}{r^2} \frac{\partial}{\partial r} \left(r^2 \frac{\partial [\Delta c_s(r, \omega)]}{\partial r} \right)$ $- D_s \left. \frac{\partial \Delta c_s(r, \omega)}{\partial r} \right _{r=0} = 0 - D_s \left. \frac{\partial \Delta c_s(r, \omega)}{\partial r} \right _{r=R_s} = \frac{\Delta j_s(r, \omega)}{F} \Delta \theta^*$ $= \frac{\Delta c_s _{r=R_s}}{c_{s, \text{max}}} \quad \text{Not applied in the separator region } (0 < x < l_s)$
Impedance	$Z = \frac{\Delta V}{\Delta I(x, \omega)} = \frac{\Delta V}{\sigma_{\text{eff}} \left. \frac{\partial \Delta \phi_s(x, \omega)}{\partial x} \right _{x=l_s+l_p}}$

3.2 PERTURBATION FORM OF PSEUDO-2-DIMENSIONAL MODEL

A Physics-based P2D Impedance model including **Equation 1.23** and **Equation 1.32**, as shown in **Table 3.1**, was built to simulate the impedance spectra. A periodic 10mV voltage perturbation with a small stimulus is applied to the system at the steady-state. The corresponding current response is then calculated to yield the impedance Z. Then, a nonlinear regression (described in the next section) was carried out using MATLAB LSQNONLIN to fit the EIS spectra with the model by varying k and D, as well as $\frac{Y_i}{Y_{i,rs}}$.

3.3 PARAMETER ESTIMATION

A nonlinear regression algorithm was utilized to estimate the parameters. Here, the sum of squares (Objective function, *Obj*), **Equation 1.33**, was minimized.

$$Obj = \sum_{n=1}^N \left[\sqrt{\left(\frac{Z'_{m,n} - Z'_{exp,n}}{Z'_{exp,n}}\right)^2} + \sqrt{\left(\frac{Z''_{m,n} - Z''_{exp,n}}{Z''_{exp,n}}\right)^2} \right] \quad \text{Equation 3.1}$$

In **Equation 3.1**, Z' and Z'' represent the real and imaginary parts of the impedance; the subscripts m and exp stand for the model and experiment, respectively; N is the number of impedance data points, corresponding to the number of frequencies (ω). The uncertainty of the obtained parameters was obtained by a numerical Jacobian matrix with the finite difference method:

$$J_{ij} = \frac{\Delta Obj_i}{\Delta x_j} \quad \text{Equation 3.2}$$

The standard deviation was related to the residuals and Jacobian matrix by:

$$\sigma = \sqrt{\frac{(y_m - y_{exp})'(y_m - y_{exp})}{n-k} \text{diag}((J'J)^{-1})} \quad \text{Equation 3.3}$$

Moreover, according to Student's t inverse cumulative distribution function,

$$p = F(t | \nu) = \int_{-\infty}^t \frac{\Gamma(\frac{\nu+1}{2})}{\Gamma(\frac{\nu}{2})} \frac{1}{\sqrt{\nu\pi}} \frac{1}{\left(1+\frac{t^2}{\nu}\right)^{\frac{\nu+1}{2}}} dt \quad \text{Equation 3.4}$$

where p is the desired probability and lies on the interval $[0, 1]$; t values fall into 95% probability. The confidence interval (CI) of a parameter was determined by:

$$CI = x \pm t \cdot \sigma \quad \text{Equation 3-5}$$

3.4 EIS MODEL PARAMETERS

As discussed, the parameters used in the Physics-based impedance model are listed in **Table 3.2**. Most of the parameters used in the model were determined from the experimental measurements. A few were taken from the literature and the remaining six were estimated by the non-linear regression described above. In the optimization process, initial constants were taken from the literature, as shown in **Table 3.2**.

Table 3.2 | Parameters used in the EIS Model.

Variable	Value	Source
Initial electrolyte concentration $c_{e,0}$	2000 [mol/m ³]	69
Maximum Li capacity C_{spmax}	48230 [mol/m ³]	50
Radius of particle R_{sp}	3.16 μ m	SEM
Thickness of components $L_s/L_n/L_p$	20/50.27/68.77 μ m	SEM
Porosity of electrode ϵ_{ls}	0.67	MIP
Porosity of electrode ϵ_{lp}	0.42	MIP
Volume fraction of active material ϵ_{sp}	0.7	MIP
Li-ion diffusivity D_{Spref}	$8.5966e-15[m^2/s]*A_{D,cathode}$	PBM
Interface reaction rate i_{enref}	$496.11[A/m^2]*A_{k,anode}$	PBM
Interface reaction rate i_{epref}	$2.24[A/m^2]*A_{k,cathode}$	PBM

Interface capacitance Cd_{In}	$0.2393[F/m^2]* A_{c,cathode}$	PBM
Interface capacitance Cd_{Ip}	$0.2393[F/m^2]* A_{c,anode}$	PBM
Contact resistance R_{cur}	$0.0013[\Omega m^2]* A_R$	PBM
Electronic conductivity σ_{pos}	$8.27 \cdot 10^{-3}[S/m]$	Four-terminal LSV
Maximum SOC $SoC_{max,pos}$	0.997	GITT
Minimum SOC $SoC_{min,pos}$	0.305	GITT
Open circuit voltage OCV_{pos}	Variable of x_{pos}	GITT
Li-ion conductivity in electrolyte κ_l	Variable of c_e ,	67

In total, there are six pre-factors in the optimization procedures and they are associated with six parameters: $A_{k,cathode}$ (the reaction rate at the cathode/electrolyte interface), $A_{k,anode}$ (the reaction rate at the Li-metal foil/electrolyte interface), $A_{c,cathode}$ (the capacitance at the cathode/electrolyte interface), $A_{c,anode}$ (the capacitance at the Li-metal foil/electrolyte interface), $A_{D,cathode}$ (the Li-ion diffusivity in the cathode particles), and A_R (the current collector/electrode contact resistance).

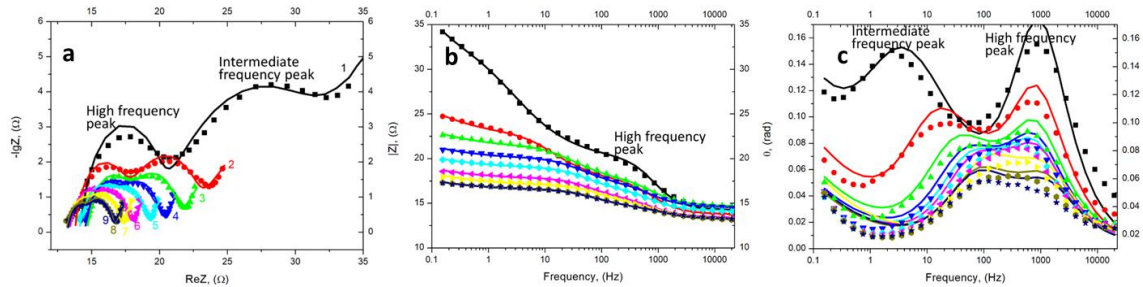


Figure 3.5. | Model and Experimental data comparison in (a) complex plan (Nyquist) plot, (b) magnitude of impedance ($|Z|$), and (c) phase angle (θ). Reproduced with permission from IOP Publishing.⁹⁸

As shown in **Figure 3.5**, nine impedance spectra were collected, each tested at a different cathode x_{Li} . The x_{Li} are listed in **Table 3.3**. Good agreement between the experimental data (symbols) and model predictions (lines) was reached for all the impedance spectra. Generally, each of the impedance spectra contained two overlapping arcs and a long Li-ion diffusion tail. The intermediate frequency peak is associated with Butler-Volmer reactions at NMC532/electrolyte interface; the high-frequency peak is related to the reaction at the Li-metal/electrolyte interface.

Table 3.3 | Optimized parameters

Curve No.	x_{Li}	OCV	A_k	A_D
1	0.96	3.63	3.63	0.01
2	0.89	3.68	6.97	0.04
3	0.81	3.72	9.30	0.10
4	0.74	3.75	10.98	0.19
5	0.66	3.79	13.23	1.15
6	0.59	3.86	15.05	4.92
7	0.52	3.96	17.94	12.39
8	0.47	4.06	20.42	17.49
9	0.40	4.18	19.79	22.65

Table 3.3 also lists the optimized $A_{k,cathode}$ and $A_{D,cathode}$ to make the predictions in **Figure 3.5**. **Figure 3.6** shows the model prediction with a 95% model Confidence Interval (CI) using the optimized parameters. The calculation of the model CI was detailed in the Parameter Estimation Section. The model predictions fall between the 95% confidence interval for all nine curves. The sensitivity of different portions of the curves to the parameters varies with OCV.

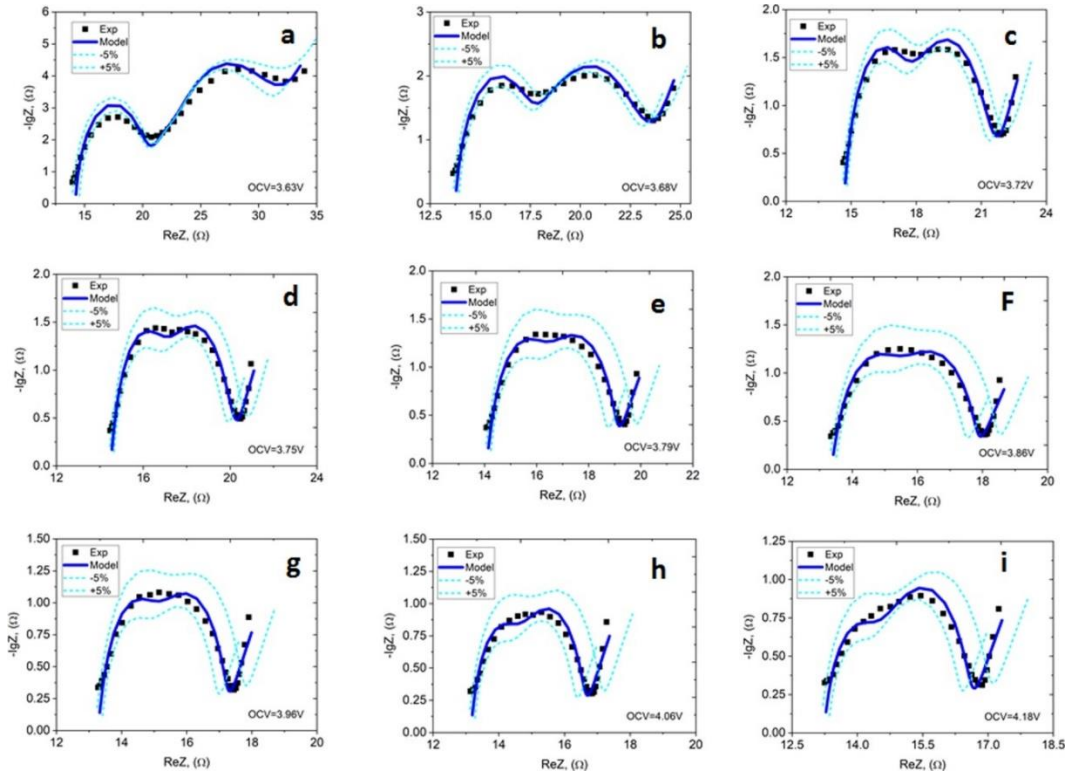


Figure 3.6. | Comparing the Nyquist plots from model and experimental data with 95% Confidence Intervals under different x_{Li} of the cathode: a) $x_{Li} = 0.96$, b) $x_{Li} = 0.89$, c) $x_{Li} = 0.81$, d) $x_{Li} = 0.74$, e) $x_{Li} = 0.66$, f) $x_{Li} = 0.59$, g) $x_{Li} = 0.52$, h) $x_{Li} = 0.47$, and i) $x_{Li} = 0.40$. Reproduced with permission from IOP Publishing.⁹⁸

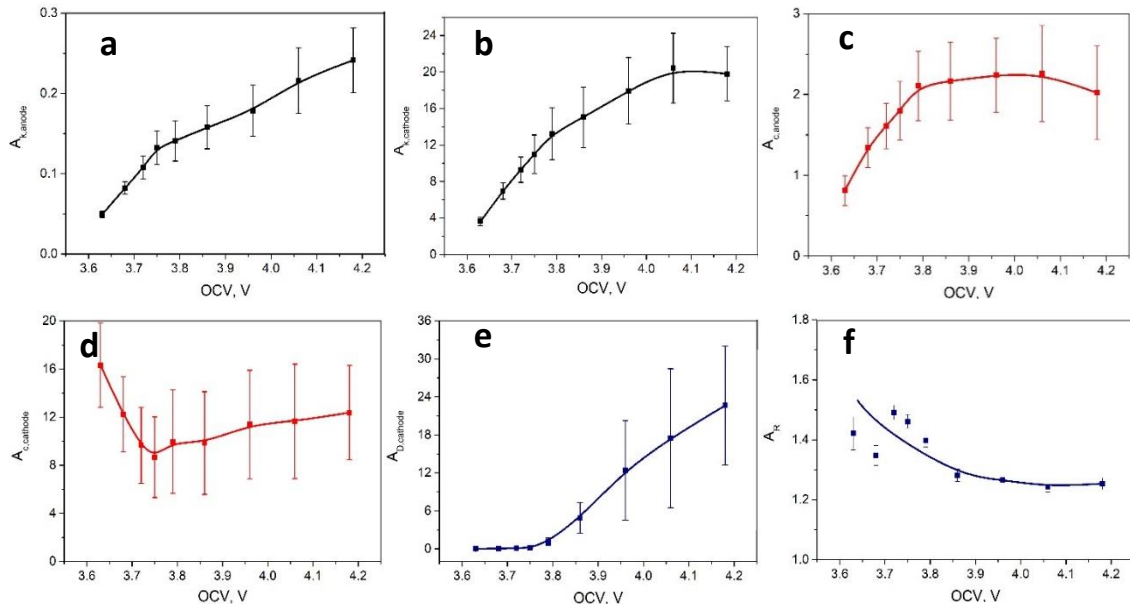


Figure 3.7. | Optimized Parameters as a function of OCV for (a-f) $A_{k,cathode}$, $A_{k,anode}$, $A_{c,cathode}$, $A_{c,anode}$, $A_{D,cathode}$, and A_R . Reproduced with permission from IOP Publishing.⁹⁸

Figure 3.7 shows the correlation between x_{Li} and the optimized parameters. For $A_{k,cathode}$ and $A_{k,anode}$, the uncertainties in the parameters are higher at higher OCVs. While both pre-factors increases vs OCV, the magnitude of $A_{k,anode}$ is more than one order of magnitude lower than $A_{k,cathode}$. Besides, combining with the baseline parameters in **Table 3.2**, the order of magnitude of exchange current density in both electrodes are similar. For $A_{c,cathode}$ and $A_{c,anode}$, the capacitance at the NMC/electrolyte interface first decreases with the OCV, and then reaches a plateau. The uncertainty in $A_{c,cathode}$ is almost 50%; the magnitude of $A_{c,anode}$ (high-frequency arc) is around one order of magnitude smaller than $A_{c,cathode}$; $A_{c,anode}$ increases first and then reaches a relatively stable value. For $A_{D,cathode}$, the diffusion coefficient in NMC particles increases nonlinearly with the OCV. However, the uncertainty in $A_{D,cathode}$ can be 100%, especially at higher OCV. For A_R , the current collector/electrode interfacial resistance does not appreciably vary, though it does decrease with the OCV. The sensitivity of each of the estimated parameters is shown in **Figure 3.8**. The sensitivity of $A_{D,cathode}$ varies significantly in the OCV range.

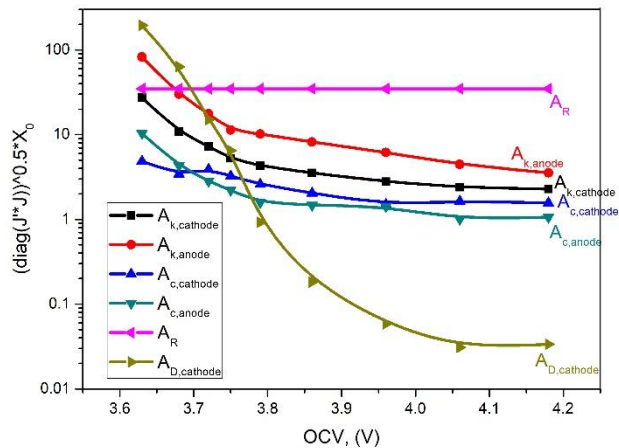


Figure 3.8. | Sensitivity of each parameter. Reproduced with permission from IOP Publishing.⁹⁸

Therefore, there might be relatively larger uncertainty in this parameter. The uncertainty of the parameters was obtained by the numerical Jacobian matrix with the finite difference method, as given in the Parameter Estimation Section. Processing the data A_D and A_k in **Table 3.3** by dividing their counterparts at the lowest x_{Li} (0.4, curve 9), their relative values can be obtained as $\bar{A}_D = \frac{Y_i}{Y_{i,0.4}} \left(1 + \frac{\partial \ln Y_i}{\partial \ln c_i}\right) / \left(1 + \frac{\partial \ln Y_{i,0.4}}{\partial \ln 0.4}\right)$ and $\bar{A}_k = \left(\frac{Y_i}{Y_{0.4}}\right)^\alpha$, which are plotted versus x_{Li} in **Figure 3.9**. Also, D varies over 3 orders of magnitude, and k changes by 1-2 orders of magnitude. Both pre-factors were fit by a lognormal function $\bar{A} = y_0 + \frac{B}{\sqrt{2\pi}\omega x} e^{\left(-\ln\left(\frac{x}{x_c}\right)^2 / 2\omega^2\right)}$ with a Levenberg-Marquardt iteration algorithm. The parameters are given in **Table 3.4**.

Table 3.4 | Parameters used in Fitting of A in **Figure 3.9**

Pre-factor	y_0	B	w	x_c
\bar{A}_D	-0.0085	0.22746	0.21916	0.42365
\bar{A}_k	-0.05953	0.68552	0.53641	0.54787

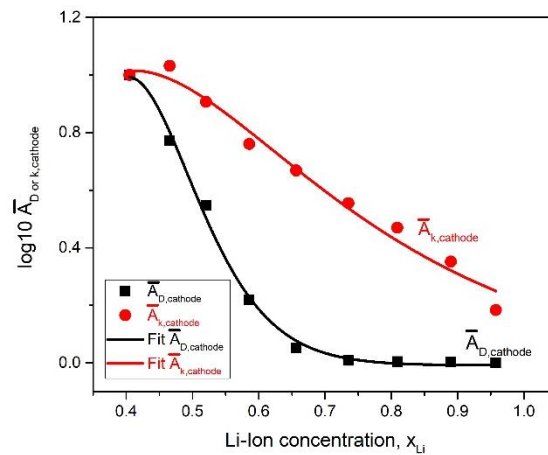
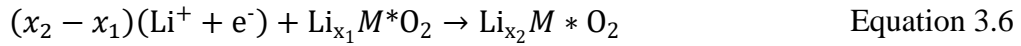


Figure 3.9. | Relative pre-factors for k and D for the cathode. Reproduced with permission from IOP Publishing.⁹⁸

3.5 THERMODYNAMIC NONIDEALITY

As discussed in Section 1.6, the transport and kinetic nonideality (diffusion or reaction) of a Li-ion electrode is closely correlated to its thermodynamic non-ideality (chemical potential). The variation of the latter can be described by the open circuit voltage of the electrode mathematically. For an electrode reaction (where M = Ni, Mn, Co, or mixed), the intercalation/deintercalation energy of Li-ion can be calculated as,



The Li-ion content, x_{Li} , was varied between 0.4 and 1 according to the experimental section. The thermodynamic equilibrium of the system can be expressed as:

$$\mu_{\text{Li}_{x_2}\text{M}^*\text{O}_2} - (x_2 - x_1)\mu_{\text{Li}} - \mu_{\text{Li}_{x_1}\text{M}^*\text{O}_2} = -e(x_2 - x_1)E \quad \text{Equation 3.7}$$

where E is the open circuit voltage at a given x_{Li} ; e is the magnitude of the elementary electrical charge of an electron with a value $1.6 \times 10^{-19}\text{C}$; μ_{Li} , the chemical potential of Lithium metal is not a function of x_{Li} and therefore equals μ_{Li}^0 . Plugging **Equation 1.17** and **Equation 1.18** into **Equation 3.7**, and with further derivation, the following relationship can be obtained:

$$\frac{d \ln \gamma}{dx_{\text{Li}}} = -\frac{eE_{x_{\text{Li}}} - \mu_{\text{Li}}^0}{k_B T} - \frac{1}{x_{\text{Li}}} \quad \text{Equation 3.8}$$

In **Equation 3.8**, E versus x_{Li} can be obtained by GITT measurements, as shown in **Figure 3.11**; $\mu_{\text{Li}}^0 = -eE_{\text{Li}} = 3.04[\text{eV}]$ can be determined by the chemical potential of Li-metal versus Standard Hydrogen electrode reported in the literature. With the two terms on the right-hand side of **Equation 3.8** known, the first-order derivative of the logarithm of the activity coefficient towards x_{Li} , $\frac{d \ln \gamma}{dx_{\text{Li}}}$, can be calculated. If the solid electrode particles

are dilute solutions, the activity coefficient γ equals 1, so $\frac{d \ln \gamma}{dx_{Li}}$ should be 0; on the contrary, if nonideal effects exist in the particles during charge/discharge cycles, $\frac{d \ln \gamma}{dx_{Li}}$ will be a function of x_{Li} . Based on the available experimental data, $\frac{d \ln \gamma}{dx_{Li}}$ is contrived in the following plot, shown in **Figure 3.10**.

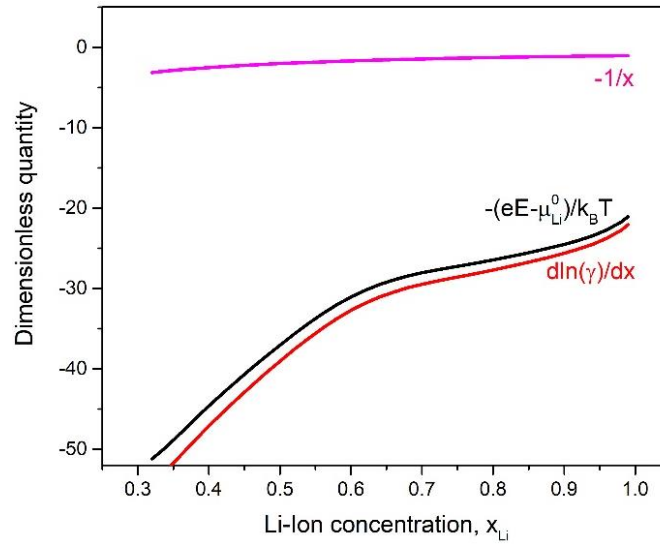


Figure 3.10. | $\frac{d \ln \gamma}{dx_{Li}}$ as a function of x_{Li} obtained from Equation 3.8. Reproduced with permission from IOP Publishing.⁹⁸

In **Figure 3.10**, obviously, $\frac{d \ln \gamma}{dx_{Li}}$ is a strong function of x_{Li} , and γ is cannot be a constant. Such a correlation is consistent with the nonlinear profiles of pre-factors \bar{A} shown in **Figure 3.9**. It also illustrates that the variation in the activity coefficient contributes to a significant portion of the chemical potential change $-\frac{eE_{x_{Li}} - \mu_{Li}^0}{k_B T}$, whereas the change of chemical potential that resulted from x_{Li} variation can almost be neglected. Such predictions further confirm that significant thermodynamic nonideality exists in the solid

cathode material during charge/discharge cycles and it will lead to substantial transport and kinetic nonideality in the electrode material.

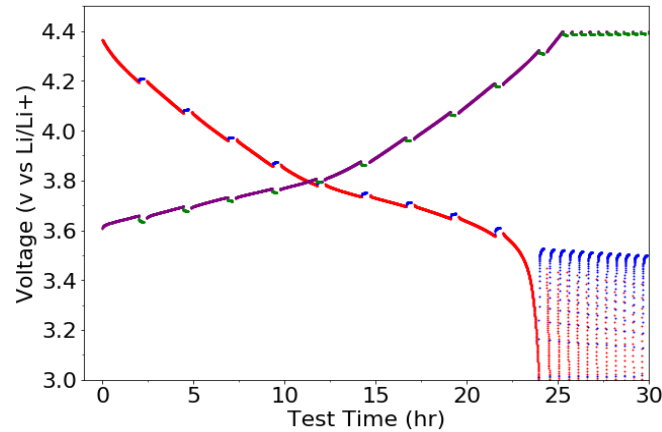


Figure 3.11. | GITT measurement of NMC532 half-cell during the charging/discharging cycles Reproduced with permission from IOP Publishing.⁹⁸

3.6 IMPORTANCE OF INTEGRATING NONIDEALITY INTO PHYSICS-BASED MODELS

Li-ion batteries are not only energy conversion devices but also a proxy to store energy in the form of chemical potential in electrodes. For such energy storage materials, both the transport and kinetic properties of electrodes will affect the overall cell performance. Especially, when the Li-ion concentration becomes close to 1, the diffusivity and reaction kinetics reduces exponentially with respect to x_{Li} . Therefore, significant overpotential is likely to occur, which is the root of degradation from undesirable parasitic reactions. As shown in **Figure 3.12**, there are three discharge profiles predicted by models with different pre-factors. For the black curve, \bar{A}_D and \bar{A}_k are both 1. In other words, the diffusivity D and reaction kinetics constant k are assumed to be the same as those with $x_{Li}=0.4$. For the green curve, it is predicted by the model with functions $\bar{A}_D(x_{Li})$ and

$\bar{A}_k(x_{Li})$ shown in **Figure 3.9**. For the red curve, \bar{A}_D and \bar{A}_k are optimized to be 0.06 and 1 to regress the best fit with the green curve. There are no equivalent constants for \bar{A}_D and \bar{A}_k , which can lead to a same discharge profile as that with functions $\bar{A}_D(x_{Li})$ and $\bar{A}_k(x_{Li})$. On the contrary, the discharge profile with the pre-factors in **Figure 3.12** deviates substantially from that obtained with constant pre-factors. Adjusting the two constant pre-factors does not necessarily provide the same discharge profile.

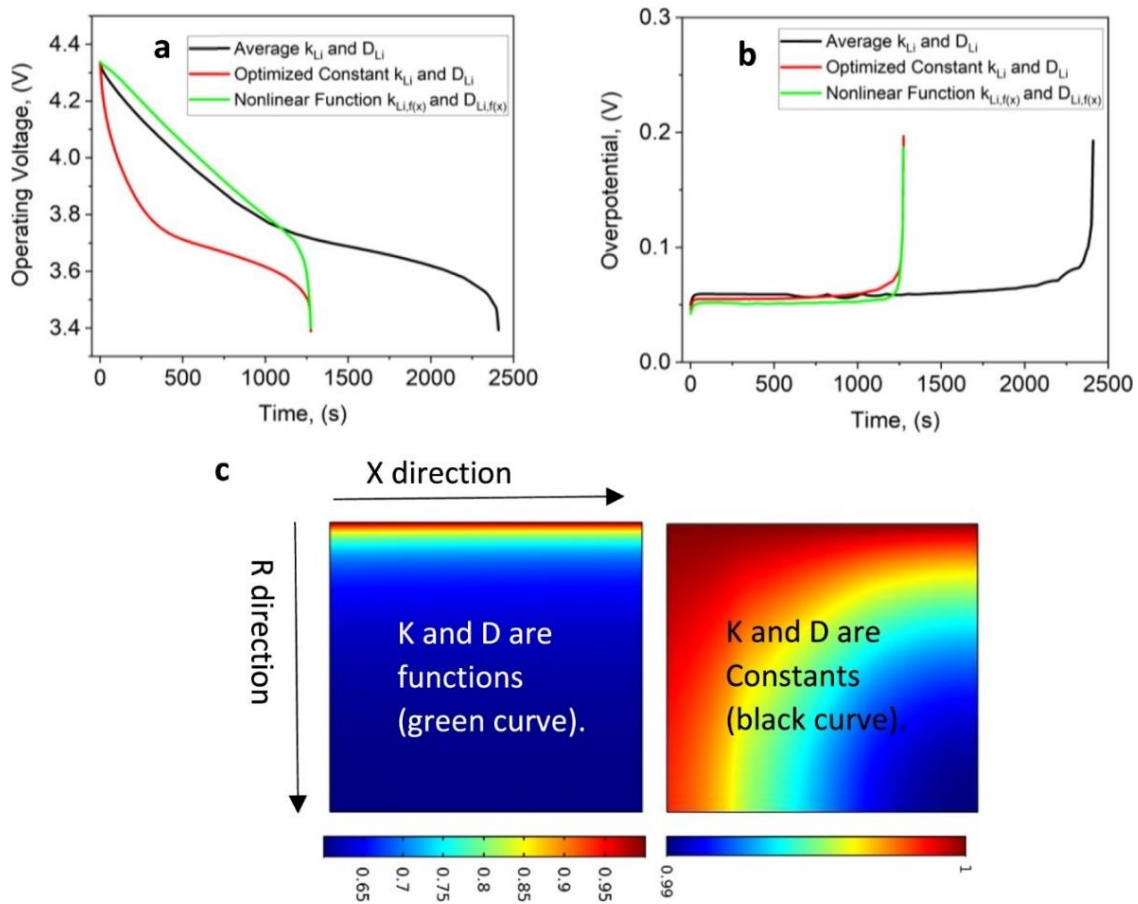


Figure 3.12. | Comparison between different pre-factors: (a) discharge profiles (Current=1C); (b) overpotentials; (c) xLi concentration profiles in active particles at the end of discharge. Reproduced with permission from IOP Publishing.⁹⁸

In practice, additional parameters will be augmented to fit the experimental curve, so the obtained parameters do not represent the true properties of the cell. Only functions $\bar{A}_D(x_{Li})$ and $\bar{A}_k(x_{Li})$ can reveal the true physical properties of the cell and equivalent constants of them could lead to significant deviations in the electrochemical performance predictions of the batteries. **Figure 3.12b** shows the overpotential profiles with different k and D . The green (A_D and A_k are constants) and red ($A_D=0.06$ and $A_k=1$) curves reach higher overpotentials much earlier than the black curve ($A_D=1$ and $A_k=1$) due to the different diffusivity into the cathode particles. As shown in **Figure 3.12c**, the Li-ion concentration gradient at the end of discharge is much higher for the green curve than that for the black curve. Therefore, the large diffusion resistance will lead to a significant loss in capacity, which is the major reason for the shorter discharge time shown in **Figure 3.12a**.

3.7 SUMMARY

New pre-factors were derived that accurately describe the diffusivity and interfacial reaction rate constant of a Li-ion battery cathode under the framework of concentrated solution theory. To do this, electrochemical impedance spectra were fit by a physics-based model through nonlinear optimization. The optimized pre-factors show significant variation as a function of the SOC. Therefore, large nonideality exists in the solid Li-ion active materials during the intercalation/deintercalation process. In the application of BMS, especially for degradation prognosis through parameter estimation, it is important to include such nonlinear pre-factors to achieve high fidelity prediction.

In summary, the work presented in this chapter is a corollary to Chapter 2, which for recollection, applied experimental parameters from 50Ah full-cells to a reduced-order Lumped model and prioritized rapid computation for BMS applications. The speed,

fidelity, and limitations can be seen in **Table 3.5**, which compares various model complexities (e.g. standard pseudo-2D (P2D), pseudo-2D reduced order model (P2D ROM), single particle model (SPM), Lumped model, and Lumped reduced-order model). In essence, Chapter 2 showed the successful implementation of the State Space approach to transform the PDEs in the Lumped model for order reduction and as a result, decreased the computational time for 1 charge/discharge cycle by 50%. The Lumped reduced-order model in Chapter 2 shines when computation speed, processing power, and parameter extraction is the limiting factor (i.e. standard BMS), but the modified P2D model in this Chapter explains the system at a much higher level of fidelity and is capable of capturing non-ideality and describing the loss mechanisms on an electrode-level.

Table 3.5 | Advantages and Disadvantages of different model techniques

MODEL *	P2D ⁵³	P2D ROM ⁶⁴	SPM ⁷¹	Lumped ⁷⁴	TLM
# of parameters	~40	37	~22	4	4
Calculation time (single cycle)**	~73 s	~5 s	~6 s	~2 s	<1 s
Model complexity	Moderate-to-high	High	Moderate	Easy	Easy
Ability to model high C-Rates	Yes	Yes	Works well for moderate-to-low rates (<1.5C)	Works well for low rates (<1C), but with fitting, it can go to >1C	Works well for low rates (<1C), but with fitting, it can go to >1C
Current distribution	Yes	Yes	No	No	No
Need for measurements/experimental difficulty	Yes/Complex	Yes/Complex	Yes/Moderate	Minimal (Discharge profiles and OCV is all)	No
Needs parameter fitting	Yes	Yes	Yes	Yes	Yes

*The other models (P2D, P2D ROM, SPM and Lumped) were developed using other experimental measurements that were not presented in this section.

**The calculations were performed using COMSOL Multiphysics 5.4 on a Precision WorkStation T7500 with Intel® Xenon® 12-core CP, 48Gb of RAM and NVIDIA Quadro 4000 video card.

CHAPTER 4: EXTREME OPERATION OF LI-ION BATTERIES

The experiments and models in Chapters 2 and 3 described commercial LIBs under stable operating conditions, but nowadays LIBs are widely-integrated into advanced applications (e.g. satellites, electric cars), which can be subjected to extreme conditions. This chapter was created out of urgency and deals with the effect of low-temperature operation of commercial LIBs, and seeks to answer questions about how rapid degradation occurs and what are the root-cause and effects from a multi-scale perspective (e.g. chemistry-level, particle-level, electrode-level, and cell-level). The U.S. Advanced Battery Consortium (USABC) has established targets for deployed LIB packs, including 1) stable operating temperatures from -40°C to $+66^{\circ}\text{C}$, 2) lifespan of 15 years, and 3) 350 mile drivable distance per full charge.⁹⁹ For next-generation LIBs to achieve longer driving ranges, it is imperative to extend the reversible energy density of operating cells, but this typically comes with a tradeoff in safety and pack cycle life. The safe operation of high energy density LIBs is a prerequisite of government regulations and it requires the mitigation of thermal runaway. Extreme conditions and discrepancies in Li-ion battery operating conditions (i.e. oscillations in temperatures, current, and depth-of-discharge)^{4,100–102} and chemistry (i.e. additive engineering, fluorination, electrolyte, anodes/cathodes)^{42,103–109} have led to unpredictable variations in the onset for catastrophic cell-failure (i.e. rapid performance degradation, abrupt cell death, thermal runaway)^{110–114}. In particular, electrified transportation (e.g. electric cars, electric trucks, aircraft)^{5,115–117} are

on the precipice of extreme operating conditions, which include repetitive fast-charge/fast-discharge in a matter of seconds (i.e. effect of acceleration and regenerative braking in **Figure 4.1**)^{118–120} and possible exposure to extreme temperatures on Earth ranging from -29°C (e.g. mountainous regions, troposphere for commercial airplanes) to +52°C (e.g. desert regions, hotter areas)⁹⁹ or abusive cold-mission space temperatures down to -20°C to -40°C with thermal regulators (e.g. exploration rovers, spacecraft).¹²¹ Also, thermal expansion and contraction due to temperature oscillations can lead to thermal shock and mechanical failures, including active material delamination and current collector cracking. The state-of-charge (SOC) of both the anode and cathode drifts due to parasitic Li-losses either from kinetically governed solid-electrolyte interphase (SEI) formation at elevated temperatures or thermodynamically forced irreversible Li deposition followed by SEI passivation on the reactive Li surface at low temperatures or high C-rates.

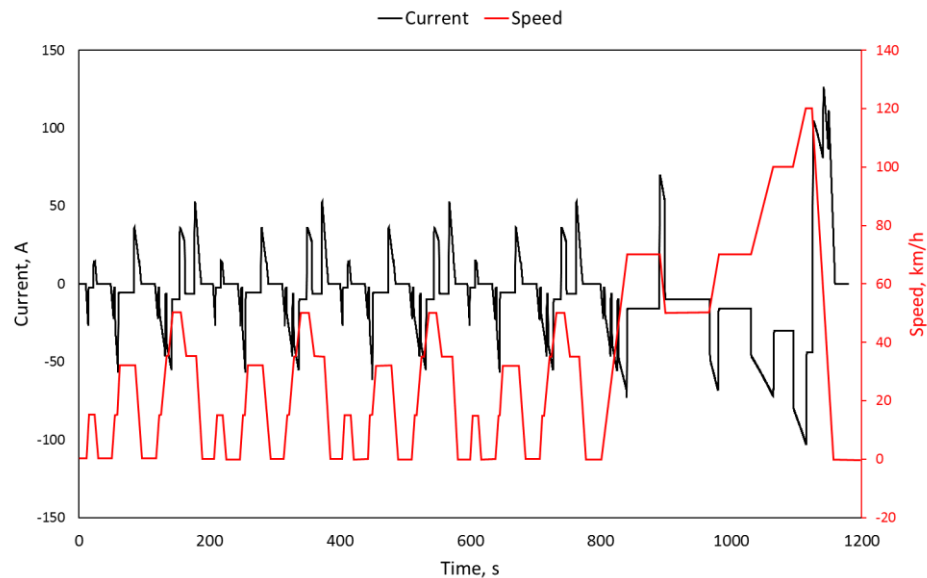


Figure 4.1. | New European Driving Cycle (NEDC) speed correlations to current for a given 1200s experiment.

4.1 FAILURE MODES

High-rate charging is highly desirable – especially in the electric vehicle sector that is looking to compete with the timescale for refueling both gasoline and H₂-fueled cars (~5 min, a battery charging rate ~10 C). During rapid charging of existing Li-ion batteries (LIBs), either from fast-charging stations or regenerative braking, over polarization at the anode drives Li deposition and dendrite formation, which can cause internal short-circuiting leading to thermal runaway (TR) and catastrophic failure of the battery pack.^{5,122} Wide temperature operation for Li-ion batteries is also desirable – especially for electric vehicles that operate in regional locations that are colder or hotter than usual.

Generally, TR initiates through a series of exothermic runaway reactions that build upon each other (i.e. resulting in a cyclic pathway: heat enables reaction, reaction generates heat) and can result in both cell-temperatures that far-exceed 600°C and complete release of hot, toxic, and combustible gases (e.g. H₂, O₂, CO, CO₂, CH₄, C₂H₄, C₂H₆, HF).^{123,124} Generally, the electrolyte consisting of lithium hexafluorophosphate (LiPF₆) dissolved in ethylene carbonate (EC) and dimethyl carbonate (DMC) are employed and also have combustible characteristics that can fuel the propagating flame (**Figure 4.2**). Furthermore, hazardous gases like carbon monoxide (CO) are toxic and preferentially attacks hemoglobin to form the deactivated oxygen carrier carboxyhemoglobin, resulting in tissue hypoxia (acute CO toxicity = 1000 ppm).¹²⁵

The evolution of other toxic fluorinated-gases (e.g. HF, POF₃, PF₅) is primarily the direct result of the hydrolysis reaction of LiPF₆, which under USA's Protective Action Criteria (PAC), gaseous HF is incredibly toxic and has irreversible/serious health effects at 24 ppm, poses life-threatening risks at 44 ppm,¹²⁶ and displays high corrosivity. The

resulting fire, gas emissions, and/or explosion due to thermal runaway are spotlight hazards that result in the catastrophic failure of the entire application system.¹²⁷ Real-world implications have severe consequences such as events involving thermal damage of Li-ion batteries on the Boeing 787 Dreamliner¹²⁸ or the Samsung Galaxy Note 7 where welding burrs or design flaw and deflected electrodes can result in high local mechanical and/or thermal stress that eventually compromises the separator and causes thermal runaway.¹²⁹

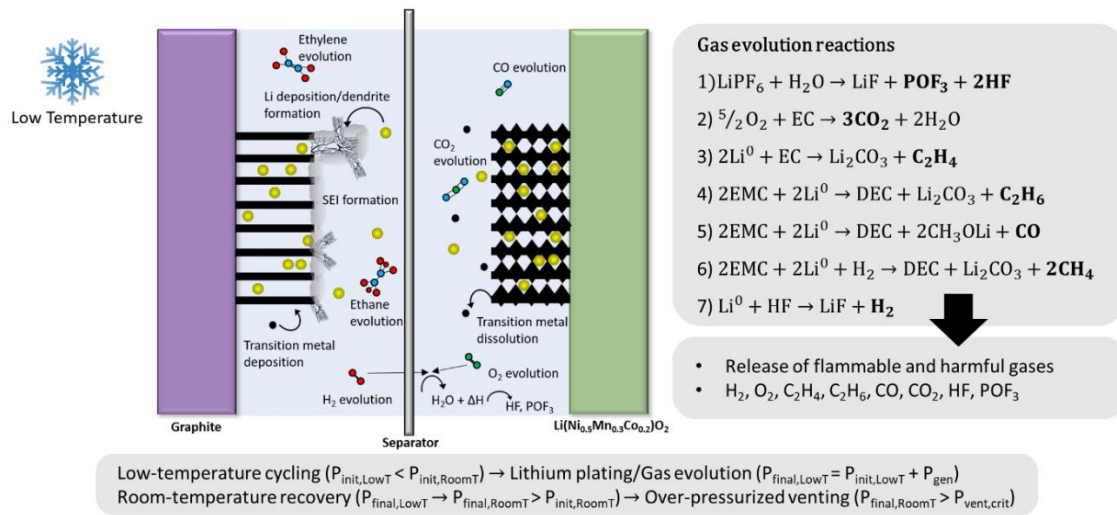


Figure 4.2 | Schematic of low-temperature Li⁰ plating and gas generation over repetitive cycling and subsequent over-pressurized venting after room-temperature recovery. Reproduced with permission from American Chemical Society.¹³⁰

4.2 LITHIUM PLATING MECHANISM AND RAPID BATTERY DEGRADATION OF COMMERCIAL LI-ION BATTERIES UNDER LOW TEMPERATURE

Fast charge and/or low-temperature operation of Li-ion batteries at a relatively high state of charge (SOC), can result in anode overpotentials that well-exceed the Li/Li⁺ redox couple, resulting in Li⁰ deposition, which is widely debated in the literature to be a trigger

for thermal runaway. Therefore, an extensive suite of characterization techniques was used to study how rapid battery degradation occurs due to severe Li^0 plating. First, the electrocrystallization of Li^0 onto a nucleation seed depends largely on the crystallization surface and the facet orientation of Li^0 seeds. Determining the facet where Li^0 preferentially deposits is extremely difficult due to poor interaction with X-ray sources and high reactivity in many testing environments. Steiger¹³¹ was able to deposit well-faceted Li^0 particles potentiostatically at -0.1V vs Li/Li^+ for 100s, and found due to interfacial interaction of Li^0 -SEI interface, that Li^0 deposition preferentially occurs on the lowest interfacial energy plane, $\{110\}$. It should be noted that the electrolyte, additives, and SEI composition will create inherent differences in the electrodeposition process. Steiger also found whisker formation after a set termination-size of the particle, and then homoepitaxial elongation of the same facet occurs to form whiskers. The preferential growth of electrodeposits is also compounded with non-homogenous current densities, which causes non-uniform Li^0 deposition. The growth of high surface area and high reactivity Li^0 electrodeposits, results in further electrolyte reduction, depletion of Li^+ , and uncontrolled growth of a resistive SEI layer. Also, Li^0 dendrites can grow within the pores of the polymeric separator that result in internal short circuits and aggressive thermal runaway.

4.3 EXPERIMENTAL

4.3.1 EXTREME BATTERY OPERATION AND ELECTROCHEMICAL TESTING

Low-temperature gas generation experiments were conducted on as-received 50Ah NMC532/graphite large-format prismatic cells with two jellyrolls inside. The cycle performance of these cells is evaluated by low-temperature constant current-constant potential (CC-CP) cycling and 1000Hz AC impedance inside a Tenney T6S-1 temperature

control chamber ($T = -29^{\circ}\text{C}$ or 0°C) with an Arbin MSTAT battery cycler. Each NMC532/graphite large-format prismatic cell was equipped with three K-type thermocouples (thermocouple 1: terminal, thermocouple 2: in-between clamps and cell, thermocouple 3: ambient). Both -29°C and 0°C temperature experiments were carried out on cells that were cycled at 0.3C (15A) from 2.8-4.25V with a CP tapering constraint of $<0.05\text{C}$ (2.5A).

To understand the effects of low-temperature cycling on the structure of the electrodes and cells, both tested and fresh cells were disassembled. Cell teardown was done at complete discharge to the lower voltage bound (2.8 V) and relaxed at open circuit potential (OCP) for 24 hours to reach electrochemical equilibrium. These fully discharged cells were securely insulated with electrical tape and transferred inside an argon-filled (Ar, UHP Praxair) MBraun Labmaster SP glovebox (H_2O and O_2 levels < 0.1 ppm). Two parallel breaching lines separated by 1 mm were etched 2 mm from the top and bottom of the casing with a scalpel and acted as guides for cell opening. Next, a hydraulic cell opener was used to remove the casing. Upon complete removal of the cell casing, the tabs and busbar were mechanically separated from the jellyrolls and used for further electrochemical and physical characterization. Each jellyroll was examined carefully to distinguish flat vs. curved locations, edge vs. center, and tab proximity.

4.3.2 COIN-CELL TESTING

From some of the electrodes, 1.5 cm^2 disks (cathode: NMC532, anode: graphite) were cut from the jellyrolls with a Precision Disc Cutter (MTI Corporation). Each disk was placed into its own glass vial (labeled to indicate anode vs. cathode, location on the jellyroll, etc.) containing dimethyl carbonate (DMC, 99.9% purity, Sigma Aldrich Fine

Chemicals Biosciences) for 30 minutes and dried under vacuum for 30 minutes. Some of the disks were transferred to an Ar-filled Kratos AXIS Ultra multipurpose transfer vessel and removed from the glovebox for characterization. Other disks were used to assemble a three-electrode split cell (MTI Corporation, equipped with a pressure gauge). To do this, the active material was removed from one side of the current collector foils by exposing the electrode to N-methyl-pyrrolidone (NMP, 99.5% Extra Dry, Acros). The reference electrode was a lithium metal (Li, 99.9%, Alfa Aesar) ring (outer diameter = 24 mm, inner diameter = 15 mm). The electrolyte was 1.2M lithium hexafluorophosphate (LiPF_6 , 99.9%, TCI America) salt dissolved in ethylene carbonate (EC, 99%, ACROS Organics) and dimethyl carbonate (DMC, 99.9% purity, Sigma Aldrich Fine Chemicals Biosciences) at 3:7 EC: DMC mass ratio. The three-electrode cells were tested at both -29°C and 0°C at a rate equivalent to 0.3C from 2.8-4.25V with a CP tapering current equivalent to $<0.05\text{C}$. The anode potential was measured vs Li/Li^+ reference electrode in the three-electrode setup.

4.3.3 PHYSICAL CHARACTERIZATION

An extensive array of physical characterization tools was also used to understand cell behavior. Energy-dispersive X-ray spectroscopy (EDS) and scanning electron microscopy (SEM) were conducted with a Zeiss Ultraplus Field Emission Scanning Electron Microscope (FE-SEM). X-ray photoelectron spectroscopy (XPS) wide scan and high-resolution measurements were performed on a Kratos AXIS Ultra DLD XPS system. The cathode composition and metal deposition (e.g. Li, Ni, Mn, Co) on the anode electrode were evaluated by inductively coupled plasma optical emission spectroscopy (ICP-OES) using a Perkin-Elmer 2100DV Spectrometer. To analyze the gaseous species in the cells

after cycling, the gas products were first collected in a syringe and fed to a customized, multi-detector Agilent 7890B-5977B GC-MSD instrument. Carbon dioxide and carbon monoxide were detected with a flame ionization detector (FID) and ethylene, methane, hydrogen, nitrogen, and oxygen were detected with a thermal conductivity detector (TCD). The GC response was calibrated by standard gases before the analysis. Multi-location liquid nitrogen (N₂) Raman Spectroscopy was conducted with a 633nm laser source set to 0.1% intensity, 1025 μ m hole size, 300 μ m width, grating 950. Raman samples were first treated with liquid nitrogen(N₂) to prevent material degradation due to the laser source. The calibration of the spectrometer was done before the samples with a $\lambda = 520.7\text{cm}^{-1}$ silica standard at a tolerance of $\pm 1.0\text{cm}^{-1}$.

4.4 RESULTS AND DISCUSSION

4.4.1 ELECTROCHEMICAL-THERMAL RESPONSE UNDER EXTREME OPERATION (THERMAL RUNAWAY AND OVER-PRESSURIZATION)

Low temperature (LT) cycling experiments on 50Ah NMC532/graphite large format cells were found to undergo two primary life-limiting processes: 1) non-thermal runaway venting process (i.e. over-pressurization) or 2) thermal runaway venting with ejecta products (e.g. Cu/Al shreds, carbon, cathode material) after room temperature recovery from repetitive cycling at $T = -29^{\circ}\text{C}$ (thermocouple temperature) at a current of 15A (C-Rate = 0.3C). As shown in **Figure 4.3a**, the characteristic average discharge capacity (over 5 cycles) was 50.85 Ah. Transitioning from room temperature to low temperature (LT, $T = -29^{\circ}\text{C}$) immediately caused the discharge capacity to drop to 36.72 Ah (Cycle 6), a loss of 28%, as expected.

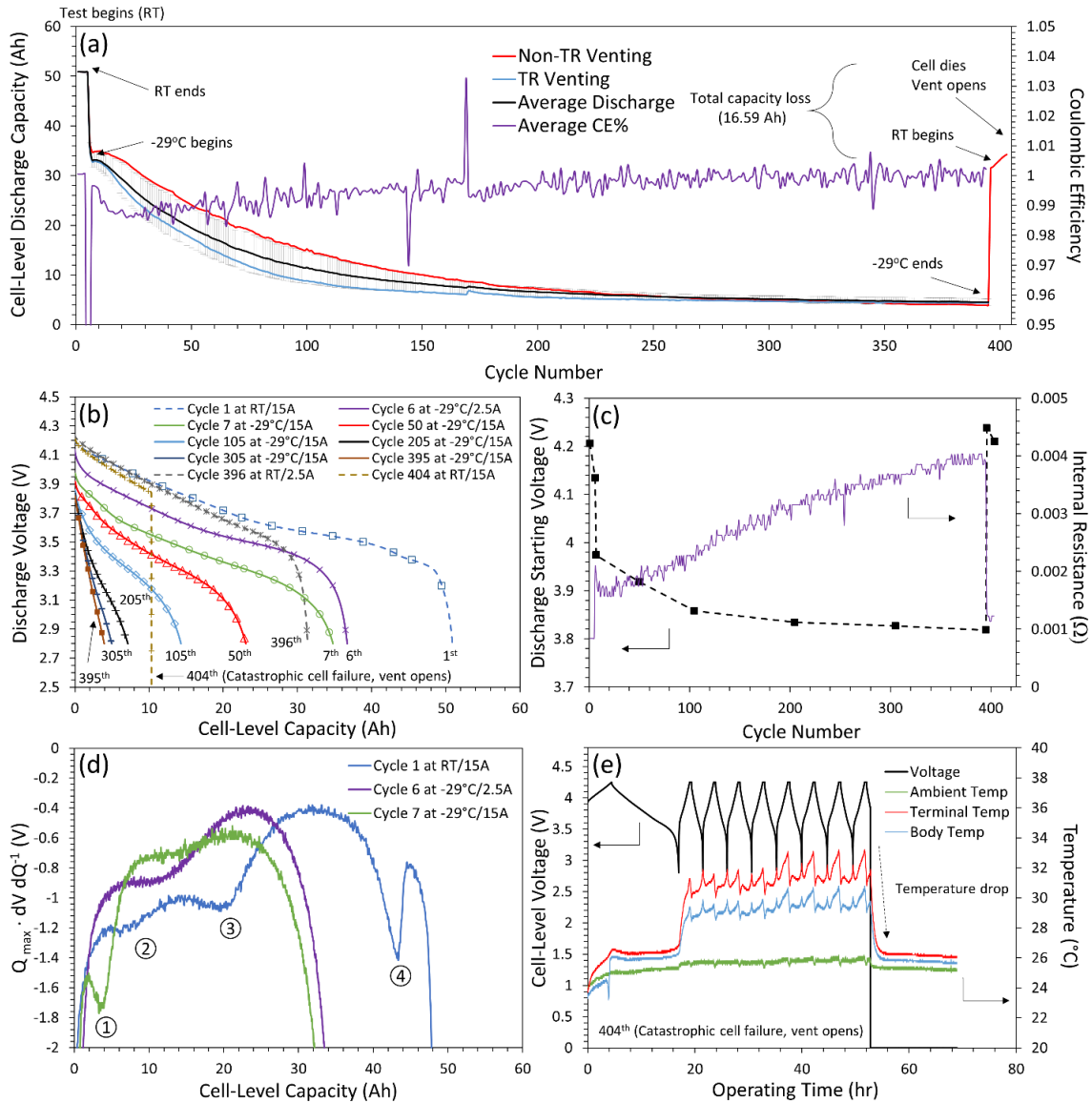


Figure 4.3. | Low temperature electrochemical and thermal analysis on the effects of Li^0 plating and gas generation. (a) Cycle performance and coulombic efficiency during temperature transitions (RT \rightarrow -29°C \rightarrow RT), (b) charge-discharge profile highlighting the temperature transitions and charge/discharge currents (i.e. characteristic no plating curve at 2.5 A and other plating curves at 15A), (c) internal resistance measured by AC-1000Hz method and relaxation voltage before discharge, (d) Q_{max} normalized differential capacity analysis to decouple the no Li^+ stripping characteristic curve and identify Li^+ stripping peaks⁷⁹ under the more extreme charge/discharge current (15A), and (e) temperature recovery back to RT and cycling results catastrophic venting that causes the cell to internally shutdown. Reproduced with permission from American Chemical Society.¹³⁰

Over 390 cycles of low-temperature CC-CP cycling, the final discharge capacity was found to be 3.96Ah, only 11% of the original low-temperature capacity. The coulombic efficiency at 25°C was near 1.00, but significantly dropped initially, and was only 0.988 over the first 100 cycles. Coulombic efficiencies less than 1.00 are typically attributed to irreversible parasitic reactions (i.e. irreversible Li^0 plating/stripping, SEI formation, electrolyte oxidation). After room temperature recovery and cell-relaxation to electrochemical and thermal equilibrium, the discharge capacity was 31.37 Ah (Cycle 396), showing that some of the capacity loss was due to parasitic reactions that consume charge, but some can also be ascribed to higher electrode overpotentials during cell aging. After 8 additional cycles at 25°C (Cycle 404), one 50Ah cell (red curve in **Figure 4.3b**) underwent non-thermal runaway venting during the discharge process (~3.8V).

Figure 4.3b takes a closer look at the cycling behavior of the cell that experienced non-thermal runaway. Discharge profiles at various operating conditions and cycle number (note the temperature and current applied in the legend) are presented. The characteristic discharge profile at room temperature (1st cycle) displays characteristics that are consistent with NMC532 and graphite full cells (i.e. transition at ~50% SOC attributed to NMC532 and phase transitions at lower SOC to graphite). After transitioning from RT to LT in Cycle 6 (0.05 C), the most notable change in the discharge profile is the disappearance of the phase change region attributed to graphite at low SOC. This is due to a drastic increase in the ohmic and kinetic overpotentials, which drives the voltage to the end-of-discharge voltage prematurely (which manifests as a loss in capacity). Upon recovery to room temperature (396th cycle), the discharge follows a similar trend to that of the (1st cycle) but diverges significantly with the loss of the inflection point attributed to NMC532. The

discharge profile is also completely devoid of the phase change response for graphite (refer to my archival publications on the same 50Ah cells for delineation)^{78,98}. As mentioned above, after 8 RT cycles, this particular cell underwent catastrophic cell failure by non-thermal runaway and venting. Operationally, this meant that the pressure valve opened, and the safety fuse was triggered, which led to the instantaneous drop in voltage. As shown in **Figure 4.3c**, the average starting discharge voltage at LT increased nearly linearly with cycle number (slope ~ 1.2 mV/cycle) over the first 100 cycles, then tapering off at 0.13 mV/cycle for the remaining cycles. After recovery to room temperature (RT), the voltage was 32 mV higher than the 1st cycle, which indicated a mixed potential between Li⁰ and Li_xC₆. Also, the ohmic resistance at RT was 0.839 mΩ, which more than doubled to 2.08mΩ at -29°C. By the end of LT cycling, the ohmic resistance had doubled to 4.03 mΩ. The increase in ohmic resistance during the transition from RT to LT is attributable to the decrease in charge carrier mobility in the electrolyte. The cycling-induced ohmic resistance can originate from multiple factors including Li⁰ plating/SEI formation which decreases the ionic conductivity of the electrolyte due to electrolyte reduction(anode) or oxidation(cathode).

Figure 4.3d presents the differential voltage analysis normalized to Q_{\max} (for comparison of different capacities).⁷⁹ $Q_{\max}dV dQ^{-1}$ is capable of differentiating potential plateaus, even in narrow voltage regions where a competing reaction is occurring and can be used to interrogate peaks associated with Li-stripping.¹³² The characteristic $Q_{\max}dV dQ^{-1}$ at room temperature/0.3C (labeled: RT/15A) and low temperature/0.05C (labeled: LT/2.5A) confirms the hypothesis that Li-stripping does not occur under mild conditions and will be used as characteristic curves. Peak 2, 3, and 4 in $Q_{\max}dV dQ^{-1}$ at room

temperature/0.3C is consistent plateaus/peaks ascribed to NMC532/graphite cells. In contrast, the $Q_{\max}dV dQ^{-1}$ for LT/0.3C (labeled: 29°C/15A in **Figure 4.3d**) shows the occurrence of an inflection at the beginning of discharge which indicates a plateau/peak for Li-stripping (indicated as peak 1). At the end of LT/0.3C experiments, the cells recovered from LT to RT after a 24-hour relaxation period to reach thermal and electrochemical equilibrium. **Figure 4.3e** shows the temperature and voltage profile for the cell after equilibration back to 25°C, which starts with a low 0.05C charge. The temperature profile during the venting event drops to 25°C, the cell shuts down as indicated by the drop-in voltage and referred to as non-thermal runaway overpressurized venting.

4.4.2 SEVERE GASSING AND ELECTRODE CHARACTERIZATION

The electrolyte and active material (NMC532/graphite) decomposition are exacerbated under abuse conditions and results in severe gas evolution. Postmortem gases were evaluated by GC-MS and represented in **Figure 4.4a**. The presence of carbon dioxide (CO₂) and carbon monoxide (CO) was detected by flame ionization detector (FID). Additional gases including ethylene (C₂H₄), methane (CH₄), hydrogen (H₂), and oxygen were detected by thermal conductivity detector (TCD). It is important to note, GC-MS has limitations in deconvoluting multicomponent mixtures and detecting trace quantities of short-lived reactive chemicals (e.g. HF, PO₂F₂, etc.). Besides the gas evolution reactions listed in **Figure 4.2**, which are the more common gassing reactions, additional side reactions can occur during extreme conditions. The proposed gas generation reaction mechanism is illustrated in **Figure 4.4b**. The combination of Li⁰ deposition and the large electrochemical polarization at low temperatures can drive further electrolyte decomposition. The formation of ethane (C₂H₆) proceeds via Li⁰ corrosion and attack on

dimethyl carbonate (DMC), to cause the cleaving of two C-O bonds, then dimerization, and subsequent formation of Li_2CO_3 . Also, steric hindrance can prevent significant ethane evolution from the cleavage of the methyl groups on DMC and the subsequent dimerization reaction. The hydrogenation reaction of the cleaved methyl group can evolve methane. The decomposition of ethylene carbonate (EC) via Li^0 corrosion and electron propagation causes the EC ring-opening mechanism to form ethylene and Li_2CO_3 . Significant release of the gases during -29°C cycling, in combination with the shift in equilibrium vapor pressure of the electrolyte and gas expansion when the cell was brought back up to 25°C , significantly increased the internal pressure – leading to valve rupture and failure.

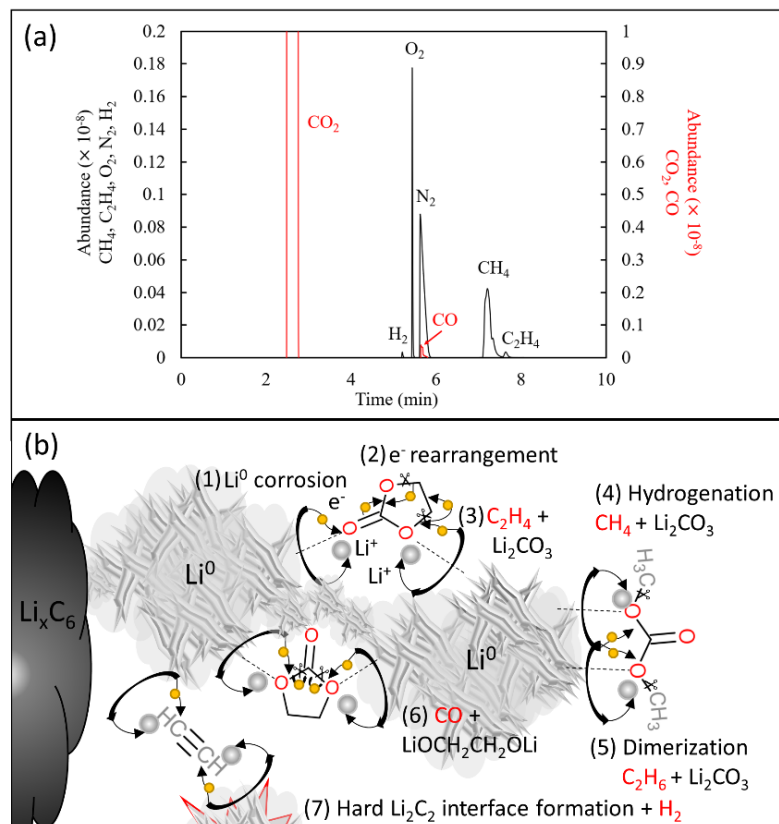


Figure 4.4. | Plot showing (a) the gases accumulated during cycling, as detected by the Gas chromatography-Mass spectrometry (GC-MS) analysis of post-mortem electrodes and (b) proposed Li^0 corrosion reaction mechanism for gas generation. Reproduced with permission from American Chemical Society.¹³⁰

Electrode samples were collected from the non-thermal runaway vented cell inside the MBraun glovebox (H₂O and O₂ levels < 0.1 ppm) with a hydraulic prismatic cell opener. **Table 4.1** reveals significant variations from the “initial-to-final layers” (that is, the first unravel of jellyroll to final unravel). The initial layers (outermost) were found to have a greater degree of particle delamination from the current collector. Also, there’s significant warping at the “curved regions” of the jellyroll. The most likely explanation for this originates from the volumetric expansion/contraction during charge/discharge, such that the outermost layers experience the cumulative expansion/contraction of all the subsequent layers. Subsequently, the outermost layers stretch more, and microfractures in the active layer propagate after repetitive cycling, which results in particle delamination. Graphite was much more extensively detached from the current collector surface than NMC532, which is potentially due to Li⁰ deposition and gas evolution that leads to drastic volumetric expansion.¹³³ Most notably, the curved areas of the jellyroll shows a tendency for warping and significant fractures. Also, there was significant color anisotropy from the “tab edge to the center” of each layer (RT vs LT cycling). In fact, a ripple-type structure propagated from the electrode edge towards the center.

Table 4.1. | Presents the spatial heterogeneity of both the Li(Ni_{0.5}Mn_{0.3}Co_{0.2})O₂ cathode and graphite anode for the full jellyroll analysis.

Electrode Designations	Description
Initial-to-final layers	Initial layers have a greater degree of particle delamination from the current collector and displayed high warping at the curved regions compared to the final layers at the interior of the jellyroll
Flat-to-curved regions	Curved regions appear extremely brittle in comparison to flat regions
Tab edge-to-center	Ripple distribution from edges to center region and from tab to curved regions

Figure 4.5 explores the spatial morphological inhomogeneity of the outermost anode of the jellyroll. This analysis looked at the electrode in 8 distinct locations. SEM images of the near-tab edge (Location 1) found gas pockets in the vicinity of particles that are fused together (that is, indistinguishable boundaries between particles) as well as Li^0 deposits. Furthermore, the gas evolution and transformation of the electrode morphology is intensified in immediate proximity to the tab (Location 2). Severe gas evolution at Location 2 seems to have caused the significant displacement of the graphite particles, indicated by a random distribution of peaks and valleys. Also, large quantities of voids are present.

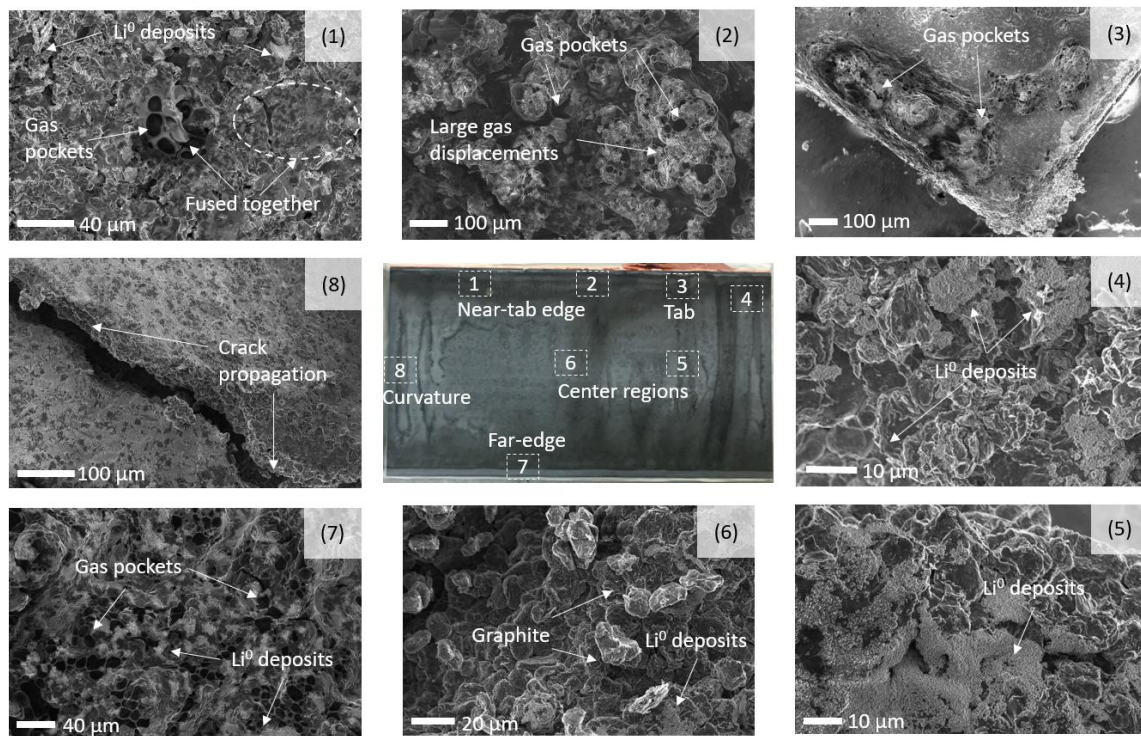


Figure 4.5. | SEM images of different areas on the surface of the anode reveal high spatial anisotropy of low-temperature Li^0 plating/gas generation and the sample collection regions on the Li_xC_6 negative electrode at the center with near-tab, center, far-edge, and curvature designations. Reproduced with permission from American Chemical Society.¹³⁰

However, the severity of displaced particles due to gas evolution at the tab itself (Location 3) was found to be less severe than that of Location 2. Negligible gas pockets were found at Locations 4, 5, and 6 which correspond to regions away from the electrode edge. At higher magnifications, Li deposits were observed on top of graphite. The Li deposits in Locations 1, 2, 3, and 4 appear mossy-like and agglomerated in comparison to Locations 5 and 6, where Li covers the surface semi-uniformly. Large electrochemical polarization during low-temperature cycling can exacerbate highly stressed areas, and cause voltage spikes at the edges, which promotes dendritic whiskers and/or mossy Li^0 .^{134,135} At the far edge (Location 7), the combination of Li deposits and severe gassing were observed similar to that of Locations 1-3. Micro-fractures and cracks were found at the curved area of the jellyroll (Location 8). In addition to the micro-fractures, severe Li plating was apparent from the SEM and indicated by the lighter deposits on top of graphite in every Location.

In general, SEM analysis suggests large discrepancies in the degree of Li deposition, gas evolution, and morphological changes, and can be isolated into 3 primary regions. At the electrode edges, there was significant Li deposition in combination with severe gassing (indicated by gas pockets and lighter deposits on the surface of graphite). The center region of the electrode had less gassing, reduced Li deposition on the surface, and graphite agglomeration. At the curved region of the jellyroll, the cumulative expansion/contraction of the subsequent layers during cycling led to significant fracturing and particle delamination from the current collector. Also, the spatial dependence of Li^0 plating and gas generation was elucidated and provides probable cause for the non-thermal runaway venting.

4.4.3 VARIABLE STATE OF CHARGE (SOC) IDENTIFICATION

To better show how the LT abuse cycling impacted electrode morphology, **Figure 4.6** presents enhanced optically filtered images (EOFI) of $\text{Li}(\text{Ni}_{0.5}\text{Mn}_{0.3}\text{Co}_{0.2})\text{O}_2$ (**Figure 4.6a**) and Li_xC_6 (**Figure 4.6b**) from both a cell that was cycled under non-abuse conditions as well as one that experienced non-thermal runaway venting. Non-abuse cycled cells (RT/0.3C and no extreme conditions) had fairly uniform electrodes from the tab to the region of high curvature (note, the tab indication is for the anode because +/- tabs alternate between full revolutions). The deviations in intensity in the EOFI relates to the deformity of the electrode. By interrogating the EOFI, rippling contours can be accentuated in the abuse conditions (i.e. electrode warping) in comparison to the non-abuse conditions (i.e. uniformity in electrodes). Analysis of the EOFI shows post-mortem electrodes (i.e. vented cell) with high anisotropy and significant warping, which is consistent with the severe gassing and bloating of the cell. Most notably, the electrodes display a ripple-type distribution that propagates from the “edge-to-center” and “tab-to-high curvature”.

During repetitive charge/discharge at low temperature, current distributions tend to follow a ripple-type behavior (i.e. indicated by peaks and troughs of Li^0 deposits), which is potentially due to warping of the electrodes under high electro-mechanical stress conditions. Multi-location liquid N_2 Raman spectroscopy was performed on $\text{Li}(\text{Ni}_{0.5}\text{Mn}_{0.3}\text{Co}_{0.2})\text{O}_2$ and Li_xC_6 . Essentially, NMC532 has $R\bar{3}M(D_{3D}^5)$ space group tendencies that produce A_{1g} and E_g in all regions (e.g. curvature, ripples, center, and bottom) in **Figure 4.6a**. The A_{1g} and E_g correspond to M-O (M = Ni, Mn, Co) out of plane stretch at $\sim 595 \text{ cm}^{-1}$ and the O-M-O in-plane bend at $\sim 474 \text{ cm}^{-1}$. Therefore, the relative

intensities of A_{1g} for M-O and E_g for O-M-O vibrations can be used to determine the spatial Li distribution.

The high-resolution metal-oxygen vibrations at bands between 300-750 cm^{-1} for the cathode change significantly based on locations, which indicates different lithiated states of NMC532 lattice across the electrode. At a lower degree of lithiation ($x < 0.4$) or subject to higher local voltages, the Raman peak shifts from 595 cm^{-1} to values greater than 600 cm^{-1} and become a merged-broad peak. However, when the Raman A_{1g} and E_g bands are well resolved, NMC exists at higher state of charges and experienced lower voltages. The Raman spectra at several locations on the anode and cathode are shown in the bottom portions of **Figure 4.6** and **Figure 4.6b**, respectively. Qualitatively, well-resolved A_{1g} and E_g bands are observed for NMC electrodes at high curvature, which indicates higher degrees of lithiation ($I_{595}/I_{474} \sim 1.81$). When correlating this region with graphite (**Figure 4.6b**), a pronounced Raman peak at 1837 cm^{-1} was observed and was attributed to vibrations from Li-carbide (Li-C \equiv C-Li) bonds.⁴⁶

To form Li_2C_2 , the Li^0 corrosion reaction can facilitate neighbor-neighbor EC reduction to adsorbed acetylene and further reaction to Li_2C_2 . The same 1837 cm^{-1} peak can be observed at various locations on the graphite electrode including regions of high curvature, ripple-peaks near the edge, and the bottom edge. By focusing the Raman laser source on the striation lines (ripple-peaks) and at the negative lines (ripple-troughs), an 1837 cm^{-1} high-intensity peak trend can be observed. Li-carbide was found to preferentially form on ripple-peaks and absent at the troughs. Therefore, regions of high stress (e.g. high curvature, ripple peaks, edges) exacerbate Li^0 deposition and subsequently results in the conditions that favor the formation of Li-carbides. Also, the degree of lithiation after low-

temperature repetitive cycling varies spatially in parallel with the counter graphite electrode. High lithiation states for NMC was found in the highly stressed regions, which corroborates the finding that under low-temperature cycling, severe gradients cause preferential Li residence.

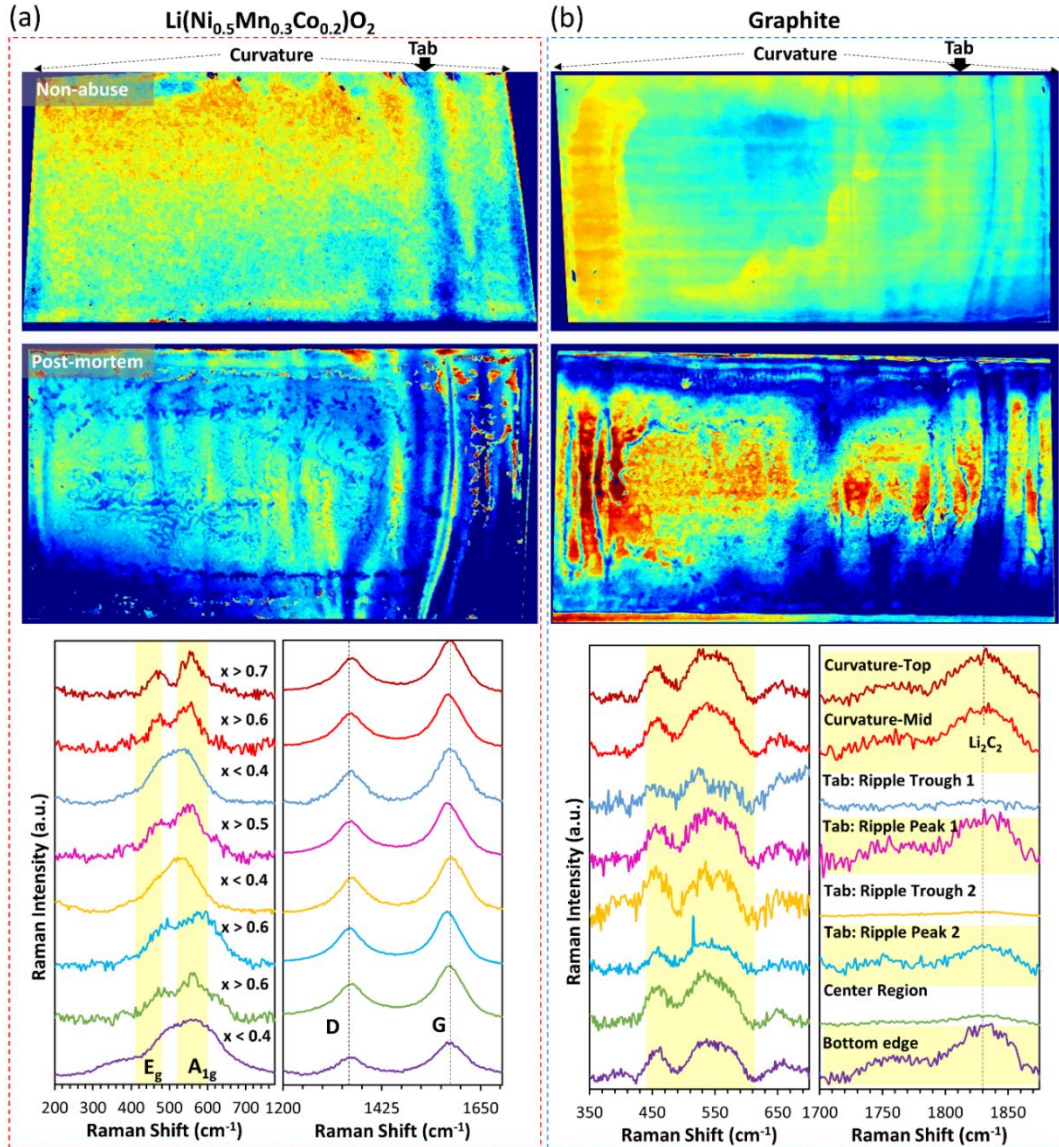


Figure 4.6. | Enhanced optically filtered images of (a) $\text{Li}(\text{Ni}_{0.5}\text{Mn}_{0.3}\text{Co}_{0.2})\text{O}_2$ and (b) Li_xC_6 , and multi-location liquid nitrogen Raman spectroscopy of the respective electrodes after non-abuse conditions (room temperature) and post-mortem (low temperature) to analyze spatial distribution of chemical species, state of charge, and electrolyte degradation products. Reproduced with permission from American Chemical Society.¹³⁰

4.4.4 CHEMISTRY ANALYSIS OF LIB FAILURE MODES UNDER EXTREME OPERATION

Finally, XPS was used to understand the chemical transformations of NMC532 after low-temperature cycling and to find the causes for the over-pressurization of the cell without thermal runaway. XPS spectral analysis and deconvolution is shown in **Figure 4.7** for NMC532 and **Figure 4.7b** for graphite. XPS results for uncycled NMC532 showed the presence of NiO (Ni2p peak 854.9 eV), CoO (Co2p peak 780.2 eV), and MnO₂ (Mn2p peak 642.5 eV). Of course, even electrodes that were cycled under non-abuse conditions (e.g. RT/0.3C discharged to 2.8V) showed deviations in the chemical species and oxidation state from the undischarged cell. The speciation of NMC532 electrodes found Ni₂O₃ (855.8 eV), CoO (780.2eV), Co(OH)₂ (782.0eV), MnO₂ (642.4 eV), and MnF_x (644.4eV).

For cells discharged at LT, there were significant deviations in the chemical species present on the anode, such as the presence of NiF_x/Ni₂O₃ (857 eV), NiO (854.6 eV), and Ni-carbides (849.9 eV). This is shown in the deconvoluted Ni 2p, Mn 2p, O 1s, and C 1s spectra in **Figure 4.7a**. The existence of two valence states for Ni (Ni²⁺ and Ni³⁺) also shows that the material degree of lithiation is not homogeneous. For Mn, cells cycled at LT showed the presence of MnF_x(643.5 eV), Mn₂O₃ (641.5 eV), and Mn-carbides (638.0 eV). A prominent peak for metal oxides is observed in the O1s for the non-abuse cycled electrodes but a significant depression in the metal oxide 529.5 eV peak was observed in the cells cycled at LT. Therefore, significant oxygen loss from NMC532 can be inferred and is also confirmed by the speciation of Ni/Mn/Co fluorides and carbides in Ni2p, Mn2p, and Co2p. The oxygen-associated species on the surface layer indicates the presence of C-O bonds (peak at 531.0eV) and C=O bonds (peak at 532.0eV), which are the expected spectra for Li₂CO₃ and lithium alkyl carbonates.^{136,137}

Furthermore, the cathode electrolyte interphase (CEI) formed at low temperatures can be probed in **Figure 4.7a**. The presence of carbon bonded to one oxygen (C-O) at 286.1eV, to two oxygens (O-C=O) at 288.2 eV, and three oxygens (carbonate-type) at 290.1eV was found. The bond formations reveal the CEI contains lithium carbonate (Li_2CO_3) and possibly lithium alkyl (that is, methyl or ethyl) carbonates ($\text{R-CH}_2\text{O}(\text{C}=\text{O})\text{OLi}$), which corroborates the O 1s spectrum analysis. Also, the spectrum suggests the ring-opening mechanism for EC, which can lead to the formation of $\text{LiO}(\text{C}=\text{O})\text{OCH}_2\text{CH}_2\text{O}(\text{C}=\text{O})\text{OLi}$ (it is important to note that the decomposition product can be formed during manufacturing or induced by harsh low-temperature conditions).¹³⁸

The metal carbide peak at 283.0eV confirms the degradation of NMC532. The phosphorus content in the sample is only 1.2 by mass or 0.6 by atomic percentage. The P2p spectra indicate the presence of phosphates (133.2 eV), which are LiPF_6 decomposition products such as LiPOF_2 or Li_2PFO_3 , and are typically given a generic formula as $\text{Li}_x\text{PF}_y\text{O}_z$. Overall, the electrolyte decomposition products on NMC532 consist of primarily Li_2CO_3 , lithium alkyl carbonates ($\text{CH}_3\text{O}(\text{C}=\text{O})\text{OLi}$, $\text{CH}_3\text{CH}_2\text{O}(\text{C}=\text{O})\text{OLi}$ and/or $\text{LiO}(\text{C}=\text{O})\text{OCH}_2\text{CH}_2\text{O}(\text{C}=\text{O})\text{OLi}$), phosphates (LiPOF_2 and/or Li_2PFO_3) (Note: further deconvolution of the actual species require more information than C1s and O1s). There is significant anisotropy in the electrolyte and/or active material decomposition products across the electrode (i.e. tab, center, and high curvature regions), which indicates high spatial dependence in the capacity fade and failure mechanisms of the cell.

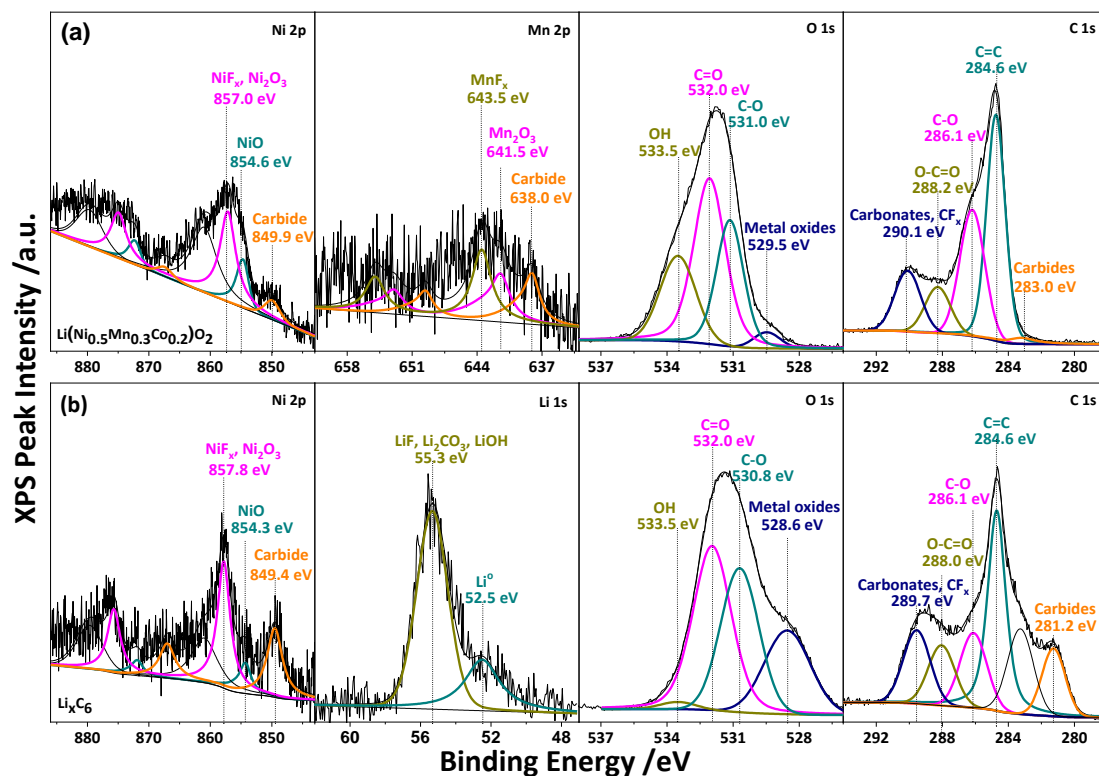


Figure 4.7. | X-ray photoelectron spectroscopy analysis of (a) Ni 2p, Mn 2p, O 1s, C 1s for $\text{Li}(\text{Ni}_{0.5}\text{Mn}_{0.3}\text{Co}_{0.2})\text{O}_2$, and (b) Ni 2p, Li 1s, O 1s, C 1s for graphite electrodes after -29°C cycling and non-thermal runaway over-pressurization and venting. Reproduced with permission from American Chemical Society.¹³⁰

Multiple-location XPS was very useful for developing a firm understanding of the degradation processes at the anode. The Ni2p, Li 1s, O 1s, and C 1s spectra at the curved region of the anode are given in **Figure 4.7b**. Spectral peaks were discovered in the Ni2p region for all three anode regions (tab, edge, high curvature), which indicates Ni as the primary transition metal that is dissolved and redeposited on the anode at LT. Furthermore, in the Ni2p spectra, Ni exists in a mixed oxidation state with $\text{NiF}_x/\text{Ni}_2\text{O}_3$ (857.8 eV), NiO (854.3eV), and Ni-carbide (849.4eV) species. In addition, by probing the Li1s spectrum a muddled peak at 55.3eV attributes the solid electrolyte interphase (SEI) with LiF, Li_2CO_3 and LiOH species. Also, the shoulder peak protruding out at lower binding energies

indicates the presence of metallic Li^0 at a binding energy of 52.5 eV, which confirms low-temperature plating and irreversibly trapped Li^0 , even after room temperature recovery and cycling. The quantity of Li also varies spatially along the electrode, which leads to significant gradients in the concentration, potential, and current during operation as well as uneven Li deposition at LT. In the O1s spectrum for Li_xC_6 , there is a prominent metal oxide peak at 528.6eV which is ascribed to Li_2O and $\text{Ni}^{2+}/\text{Ni}^{3+}$ species in the form of NiO and Ni_2O_3 . Also, similar C-O (530.8eV), C=O (532.0eV), and OH (533.5eV) peaks can be deconvoluted from the broad main peak and ascribed to the SEI. In the C1s spectra, similar bonds are observed for carbonates/ CF_x (289.7eV), O-C=O (288.0eV), C-O (286.1eV), C=C (284.6eV), and metal carbide (281.2eV). The metal carbide peak shoulder extends further out and displays significantly greater electron intensity in comparison to NMC532. Surface Ni/Mn speciation of the NMC532 electrode indicates 18.3%/35% carbides near the tab, 54.4%/34.6% near the center, and 11.4%/32.7% near the region of high curvature. The low Li atomic percentage near the center exacerbates the degradation of the cathode via metal carbide formation. Therefore, the net flux of Li repetitively migrating towards areas of high stress during cycling leads to over-exhaustion of NMC532 surfaces and results in severe degradation.

Overall, one of the key findings of this work is that the degradation processes for large jellyroll electrodes were highly spatially heterogeneous, where the degradation process was found to be exacerbated at highly stressed regions (e.g. high curvature, ripple-peaks, edges). SEM analysis discovered severe gassing and pocket formation near regions of high mossy-like Li^0 deposits. Also, the complete destruction of the graphite particle morphology was observed and realized by the large-scale fusing of graphite particles (i.e.

indistinguishable boundaries that potentially originate from degradation residuals due to Li^0 plating) that span for $>500\mu\text{m}$. At the center regions, Li^0 plating still occurs but follows a relatively more uniform deposition process. Also, negligible gassing was observed at the center regions. At the electrode curvature, cumulative volumetric expansion/contraction of every layer during cycling led to micro-fractures and large-scale cracks. Furthermore, XPS revealed severe cathode degradation and indicated by oxygen release and subsequent M-carbide ($\text{M} = \text{Ni}, \text{Co}$) degradation product. Low-temperature cycling appears to exacerbate the cathode electrolyte interphase (CEI) formation due to large electrochemical polarization, and XPS reveals the chemistry consists of significant quantities of Li, C, and O elements that encompasses Li_2CO_3 , lithium alkyl carbonates ($\text{CH}_3\text{O}(\text{C}=\text{O})\text{OLi}$, $\text{CH}_3\text{CH}_2\text{O}(\text{C}=\text{O})\text{OLi}$ and/or $\text{LiO}(\text{C}=\text{O})\text{OCH}_2\text{CH}_2\text{O}(\text{C}=\text{O})\text{OLi}$), phosphates (LiPOF_2 and/or Li_2PFO_3). Metallic Li^0 and carbide formation at the anode was found to be severe. By using Raman spectroscopy, a ripple-type behavior was observed for large jellyroll electrodes. Also, Li-carbide ($\text{Li-C}\equiv\text{C-Li}$) 1837 cm^{-1} high-intensity band was observed at ripple-peaks and absent at ripple-troughs. Lastly, highly stressed regions during low-temperature cycling were found to have severe gassing, mossy-like Li^0 plating, morphological changes, and Li-carbide formation.

The speciation of Ni-species (**Table 4.2**) and the atomic ratio of Ni in the anode:cathode is 1.1:2.5 (**Table 4.3**), which means that the high-intensity peak from metal carbides (C1s peak at 281.eV) is attributed to a different metal-substitution (that is, lithium). Therefore, one possible explanation for the high-intensity peak is the formation of lithium carbides (Li_2C_2) from the corrosion of irreversibly trapped Li^0 that is deposited during plating at low temperature. Li_2C_2 is the most thermodynamically stable state out of

the possible lithium carbides (including LiC_6 , Li_4C_2 , Li_4C_3), and exist with C_2^{2-} as the backbone tethered to two alkali metals in the form of $\text{LiC}\equiv\text{CLi}$. Li-carbides have similar applications as diamonds,¹³⁹ and exhibit physical properties of extreme hardness, toughness, and excellent electrical conductivity, which can harden soft Li^0 deposits.

Table 4.2 | Transition metal speciation for various regions (e.g. edge, center, curvature) of surface $\text{Li}(\text{Ni}_{0.5}\text{Mn}_{0.3}\text{Co}_{0.2})\text{O}_2$ and Li_xC_6

Transition metal speciation	NMC532 Near-tab	NMC532 Center	NMC532 Curvature	Li_xC_6 Near-tab	Li_xC_6 Center	Li_xC_6 Curvature
Ni_xC_y	18.3%	54.4%	11.4%	33.9%	26.7%	27.3%
NiO	39.7%	-	25.3%	14.0%	35.3%	28.5%
NiF_x , Ni_2O_3	42.0%	45.6%	63.3%	52.1%	38.0%	44.2%
Mn_xC_y	35.0%	34.6%	32.7%	-	-	-
MnO_2	65.0%	65.4%	35.3%	-	-	-
Mn_2O_3	-	-	32.0%	-	-	-

Table 4.3 | Mass and atomic percentages (%) of the elements Li, P, C, O, F, Mn, Co, and Ni at different regions for $\text{Li}(\text{Ni}_{0.5}\text{Mn}_{0.3}\text{Co}_{0.2})\text{O}_2$ and Li_xC_6 from XPS spectra analysis after non-thermal runaway venting

Species	$\text{Li}(\text{Ni}_{0.5}\text{Mn}_{0.3}\text{Co}_{0.2})\text{O}_2$			Li_xC_6		
	Edge	Center	High Curvature	Edge	Center	High Curvature
	Atomic %	Atomic %	Atomic %	Atomic %	Atomic %	Atomic %
Li	15.1	7.3	11.1	30.8	16.5	23.6
P	1.3	1.0	0.6	0.7	0.9	1.1
C	43.2	52.6	48.0	28.0	40.9	34.8
O	21.0	18.5	22.0	30.8	28.3	26.9
F	16.7	16.3	14.6	8.9	11.8	12.5
Mn	0.3	0.6	0.3	-	0.2	-
Co	0.1	0.8	0.9	-	-	-
Ni	2.3	2.9	2.5	0.8	1.4	1.1

4.5 SUMMARY

Overall, one of the key findings of this work is that the degradation processes for large jellyroll electrodes were spatially heterogeneous, where the degradation processes were found to be exacerbated at highly stressed regions (e.g. high curvature, ripple-peaks, edges). SEM analysis discovered severe gassing and pocket formation near regions of high mossy-like Li^0 deposits. In addition, the complete destruction of the graphite particle morphology was observed and realized by the large-scale fusing of graphite particles (i.e. indistinguishable boundaries that potentially originate from degradation residuals due to Li^0 plating) that span for $>500\mu\text{m}$. At the center regions, Li^0 plating still occurs but follows a relatively more uniform deposition process. At the electrode curvature, cumulative volumetric expansion/contraction of every layer during cycling led to micro-fractures and large-scale cracks. Furthermore, XPS revealed severe cathode degradation and indicated by oxygen release and subsequent M-carbide (M = Ni, Co) degradation product. Low-temperature cycling appears to exacerbate the cathode electrolyte interphase (CEI) formation due to large electrochemical polarization, and XPS reveals the chemistry consists of significant quantities of Li, C, and O elements that encompasses Li_2CO_3 , lithium alkyl carbonates ($\text{CH}_3\text{O}(\text{C}=\text{O})\text{OLi}$, $\text{CH}_3\text{CH}_2\text{O}(\text{C}=\text{O})\text{OLi}$ and/or $\text{LiO}(\text{C}=\text{O})\text{OCH}_2\text{CH}_2\text{O}(\text{C}=\text{O})\text{OLi}$), phosphates (LiPOF_2 and/or Li_2PFO_3). Metallic Li^0 and carbide formation at the anode was found to be severe. By using Raman spectroscopy, a ripple-type behavior was observed for large jellyroll electrodes. In addition, Li-carbide ($\text{Li}-\text{C}\equiv\text{C}-\text{Li}$) 1837 cm^{-1} high-intensity band was observed at ripple-peaks and absent at ripple-troughs. Lastly, highly stressed regions during low-temperature cycling were found to have severe gassing, mossy-like Li^0 plating, morphological changes, and Li-carbide formation.

CHAPTER 5: STRATEGIC DESIGN OF DURABLE, SAFE, ENERGY

DENSE LIB ANODES

The demands of emerging portable electronics, electric vehicles (EVs), and space technologies have ushered in a new paradigm for engineers and scientists to develop safe, durable, and lightweight rechargeable batteries.^{2,4,140,141} Commercial LIBs, which were discussed in Chapters 1-4, have become the backbone of our electrified and interconnected society, and have allowed device manufacturers to push the performance boundaries of cell phones, laptops, and other devices. However, the emergence of enhanced capabilities (e.g. GPS, music players, web browsing, video chats) and processing power (e.g. emerging 5G networks, cloud computing) is expected to drain existing onboard batteries at an alarming rate – thereby creating an urgency for Chapter 5 to discuss the development of advanced next-generation, high energy density, and safe LIB materials.^{116,142} Also, high-rate charging is highly desirable – especially in the electric vehicle sector that is looking to compete with the timescale for refueling both gasoline and H₂-fueled cars (~5 min, a battery charging rate ~10 C). During such rapid charging of existing Li-ion batteries (LIBs), over polarization at the anode drives Li deposition and dendrite formation, which can cause internal short-circuiting leading to thermal runaway and catastrophic failure of the battery pack.^{5,122} Therefore, new LIB anode materials are needed that are safer (no Li plating during fast charging), have higher capacities (> 600 mAh g⁻¹), and are durable (> 1000 deep cycles).^{42,55,143}

5.1 MATERIAL SELECTION AND DESIGN STRATEGIES

One pathway to achieve high-rate charging at lower overpotentials (reducing the driving force for Li-plating) is to create nano-sized electroactive materials. Small particle sizes allow for enhanced reaction kinetics and rapid diffusion.^{117,144} Small size can simultaneously enhance the ability of active particles to accommodate strain, as well as significantly increase the number of charge carriers near the electrode-electrolyte interface. However, batteries employing nano-sized active materials are typically penalized with increased irreversible capacity loss, as well as decreased stability and reversibility. The result is typically electrodes with low coulombic efficiency (CE), mediocre capacity, and limited cycle life.

A second pathway to avoiding Li plating is to search for materials with a reversible potential substantively higher than the Li/Li⁺ redox couple to provide a buffer in its operating potential. Though materials with higher anode potentials might have lower operating voltages, materials with much higher theoretical capacity than commercial graphite will more than compensate for any energy density concerns, and the ability to safely operate at higher discharge rates can also result in comparable or superior power density. The desire to have nanostructured active materials with a higher anode potential during charge/discharge leads to the consideration of a whole new set of chemistries that have never before been deployed in commercial LIBs such as metal hydrides, nitrides, oxides, fluorides, phosphides, and sulfides^{33,44,145-149} – each of these conversion materials has its advantages and challenges, but the most widely studied family of conversion anodes is metal oxides (MOs). Recall in Chapter 1, the primary advantages that MO materials have over the standard graphite intercalation compounds (GICs) are: 1) multiple electrons per

repeat unit (e.g. $2 e^-/\text{NiO}$, resulting in a theoretical capacity of 718 mAh g^{-1}) compared to one electron per six carbons (372 mAh g^{-1} theoretical capacity) – giving MO-anode LIBs a higher theoretical energy density than graphite-anode LIBs; and 2) a redox potential approximately 1 V greater than Li/Li^+ redox couple, which makes Li plating thermodynamically unfavorable.

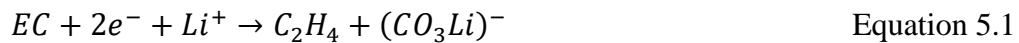
MOs also have advantages over the most widely touted graphite alternative, Si: 1) MOs can be operated between 0-100% state of charge at high rates with as little as 5-10 wt% carbon added to the electrode³⁴, where Si electrodes typically have nearly 50% added carbon¹⁵⁰⁻¹⁵³ to achieve high performance and employ voltage cutoff strategies. In combination, these significantly limit the achievable capacity of Si-based anodes; 2) the volumetric expansion of MOs is much less than Si, typically ~60%, versus ~300% for Si;¹⁵⁴⁻¹⁵⁶ and 3) MOs are air-stable and easy to process, unlike Si (and other more widely discussed anode replacements, such as Li metal).

5.2 THE STRUCTURE AND CHEMISTRY OF THE SOLID ELECTROLYTE

INTERPHASE

As higher energy density materials are developed to enable such next-generation Li-ion batteries, their interfacial interaction with the electrolyte and reaction mechanism might be expected to be different than existing materials. This will be particularly important at the anode, where the formation of the solid electrolyte interphase (SEI) from electrolyte decomposition at low potentials is one of the most important phenomena that allow for conventional graphite anodes to be chemically stable over long-duration cycling and/or storage. The SEI and its formation is well-characterized for graphite, and even on some alternative materials such as Si.^{36,157,158} **Figure 5.1a** shows the electrode/electrolyte

interface immediately after cell assembly, but before charge has been passed, where a non-faradaic electric double layer formation (via specific and non-specific adsorption/desorption) and faradaic electrochemical reactions (facilitated by the reversible transfer of electrons at open circuit) occur.¹⁵⁹ The thermodynamic potential gap between the electrode and electrolyte (**Figure 5.1b**) determines the initial specific adsorption behavior, solvation-shell near the interface, and the electrochemical reaction (e.g. intercalation/conversion/alloying, electrolyte decomposition, Li plating, etc.). The SEI is formed during initial charging where the anode potential is driven negative of its open-circuit value (**Figure 5.1c**). Electrolyte instability at these potentials leads to electrolyte reduction to more stable compounds – both organic and inorganic. One of the most pervasive components of modern electrolytes is ethylene carbonate (EC), and it is known to play an important role in SEI formation. Aurbach et al.^{19,160} proposed a general reaction pathway for EC reduction on carbon-based anodes.



Experimentally, it has been shown that EC reduction occurs at potentials around 0.8-1.4V vs. Li/Li⁺, which is in reasonable agreement with theoretical calculations that fall between 0.48 – 0.96V.^{19,160} EC undergoes a 2-electron reduction, though the reaction pathway can vary based on the EC concentration. At high EC concentrations, the 1st electron transfer destabilizes a Li⁺-EC moiety, causing the carbonate anion to attack a neighboring Li⁺-EC to form Li⁺(CO₃)R(CO₃)Li⁺ (where R can be methyl, ethyl, butyl, etc.).

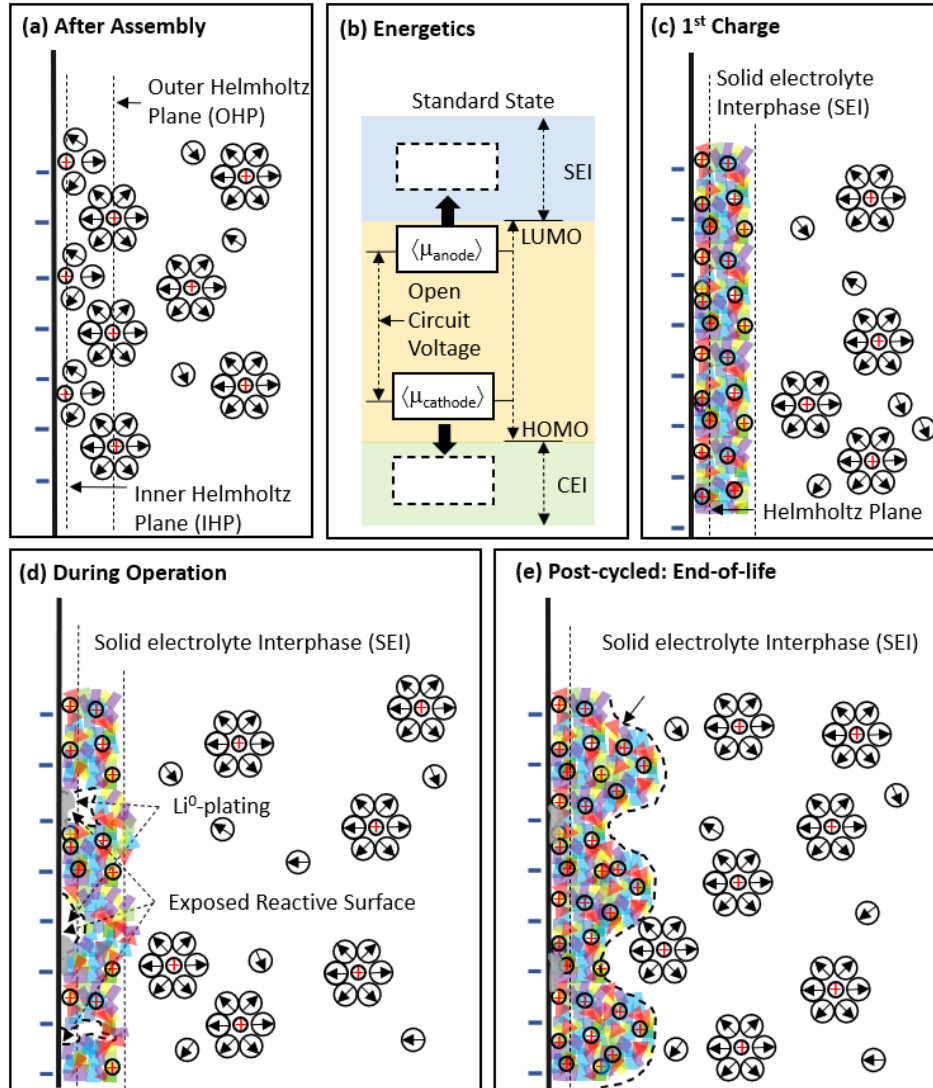


Figure 5.1 | Energy diagram of a Li-ion battery and reaction mode inside the electric double layer (pre-cycled) and the solid electrolyte interphase (post-cycled). The schematic captures the interfacial dynamics in the inner/outer Helmholtz plane (I/O-HP) and shows desolvated Li⁺ transport through the SEI. Adapted from ^{165,166} Reproduced with permission from The Royal Society of Chemistry.¹⁶⁷

At low EC concentrations and potentials closer to Li/Li⁺ redox couple, the carbonate anion will instead abstract a Li⁺ to form Li₂CO₃.¹⁹ The more stable compounds become an electronically insulating shield (typically 10-40nm for graphite-based electrodes²², ~0-50nm for metal oxide based electrodes¹⁶¹, and non-observable for titanate-based electrodes¹⁶²) that naturally prevents the high energy electrode surface from further

reaction, and enhancing long-term durability and capacity retention.¹³³ Depending on the electrolyte the SEI is considered to finish after 1-5 cycles¹⁶³, however different stress factors (e.g. volumetric expansion, gas formation, Li-plating, external impact) can expose reactive surfaces that allow additional SEI to grow during operation (**Figure 5.1d**). The continual build-up and consumption of the electrolyte increase the internal resistance of the cell, leading to performance loss (**Figure 5.1e**), which can eventually include battery failure. Though the SEI formation on carbon/graphite has been extensively studied, very little information exists in the literature regarding SEI formation on promising next-generation anode materials with high capacity, which are expected to be vital to device design and operation in the near future as the demand to increase the energy density of Li-ion batteries for commercial devices intensifies.¹⁶⁴

By leveraging the breakage of bonds, both alloying materials (e.g. Si, capacity up to 4200mAh g⁻¹)¹⁵² and M-X conversion materials (capacity ~ 700-1200 mAh g⁻¹, where M = V, Cr, Mn, Fe, Co, Ni, Cu, W, Mo, Ru, and X = H, N, O, F, P, or S)³⁷, can store significantly more electrons per unit mass than intercalation compounds. Alloying materials undergo several crystallographic phase changes to accommodate the inclusion of Li, which results in a tradeoff between the desire for high energy density and the need to avoid catastrophic volumetric expansion and material fracture. When the latter occurs, the original solid-solid interfaces (active material-binder-conductive carbon) break down, and contact resistance increases, or, worse yet, delamination (electrode particles becoming fully detached from the current collector) occurs. The most common characteristic of alloying materials in Li-ion batteries is rapid capacity loss (some <10 cycles)¹⁶⁸. Conversion materials, on the other hand, operate under a similar bond-breaking principle, but the

reaction also involves the displacement of the counter-ion (X) from the parent host (M). This helps to limit volumetric expansion. Recall, the conversion-based reactions follow the generalized reaction depicted below and in Chapter 1,³⁷



Also unlike Si, M-X conversion-based materials have a higher reversible redox potential than graphite (~1V vs Li/Li⁺)¹⁶⁹. Though at first, this may seem like a negative, because it does slightly lower the operating voltage in practical batteries, it is actually an advantage because high potentials offer significantly increased protection from thermal runaway by avoiding Li plating and dendrite formation. Additionally, it should be noted that the much higher capacity for M-X materials more than compensates for the reduced operating voltage from an energy density perspective. Though M-X materials do show promise, they are still relatively understudied, particularly when it comes to their long-term stability and operation in LIBs. That being said, researchers^{33,34,170-172} have started to understand and control the in-cell M-X degradation pathways, including 1) metal (charge) trapping, 2) transition of the MO to higher oxidation states, 3) exposed reactive sites for electrolyte decomposition, and 4) agglomeration-induced loss of electrochemically active sites, which causes capacity fade and oscillations/low coulombic efficiency. The various methodologies that have been proposed in the literature to improve the cyclability of these M-X electrodes (encapsulation, nanoconfinement, etc.)^{173,174}. One of the M-X materials that have particularly shown high performance recently is NiO. In fact, NiO-based anodes have boosted their cycle performance from <25 cycles³⁰ a decade ago to >2000 deep cycles in 2020 at a 1C rate^{175,176}. These promising results have increased interest in this family of materials for commercial applications, which makes further studies regarding their

reactivity and long-term stability an important endeavor, including developing a better understanding of the formation of the SEI on these materials.

Therefore, the overarching goal of this section is to electroanalytically decouple the multi-step SEI reaction mechanism from the conversion reaction at the Ni-O/electrolyte interface. A multitude of electroanalytical techniques, such as galvanostatic intermittent titration technique (GITT) and transient voltammetry were performed. The resulting data was analyzed using kinetic relationships derived from electron transfer theory (Marcus-Hush-Chidsey, Butler Volmer). Diffusivity (S^2D) and apparent exchange current (i_0S) measurements at different states of charge (SOC) were calculated to elucidate the complex mesostructural changes of the conversion reaction. The effective transfer coefficient (α_{eff}) was used to provide a mechanistic understanding of EC activation at the M-X/electrolyte interface. The combined electroanalytical techniques and theory are combined to fundamentally deconvolute the complex growth mechanism of the SEI on conversion-based electrodes.

5.3 EXPERIMENTAL AND THEORETICAL FRAMEWORK

5.3.1 REAGENTS

Pluronic P123 triblock copolymer (poly(ethylene glycol)-block-poly(propylene glycol)-*block*- poly(ethylene glycol), $M_n \sim 5800$, CAS#9003-11-6), tetraethyl orthosilicate (TEOS, >99.0%, CAS#78-10-4), hydrochloric acid (HCl, ACS reagent grade 37%, CAS#7647-01-0) were purchased from Sigma Aldrich. Nickel (II) nitrate hexahydrate ($Ni(NO_3)_2 \cdot 6H_2O$, 99%, CAS#13478-00-7) and potassium hydroxide (NaOH, Certified ACS, CAS#1310-58-3) were purchased from Fisher Scientific. Vulcan XC-72R was

purchased from Cabot. All water used in the synthesis processes uses ultrapure deionized water (18.2 MΩ cm) from a lab-scale Millipore Milli-Q Integral system with E-POD. All chemicals were used as received with no further purification.

5.3.2 SYNTHESIS OF HIGHLY ORDERED MESOPOROUS NICKEL OXIDE (NiO)

Highly ordered mesoporous NiO was produced via a mesoporous silica (SBA-15) template-assisted synthesis. The SBA-15 template was synthesized in accordance with a similar procedure in previous publications.^{33,177,178} Typically, 6g of Pluronic P123 triblock copolymer and 13.6 mL tetraethyl orthosilicate was dissolved in 180mL of concentrated (2M) HCl solution, heated to 45°C for 20 hours, and then heated to 100°C for an additional 24 hours. The product was washed with a 50:50 vol.% DI water/ethanol mixture, dried in a Fisherbrand Isotemp Model 281A vacuum oven (~ -30in.Hg, 50°C) for 12 hours and calcined at 500°C for 3 hours in air.

Next, an aqueous 0.5M Ni(NO₃)₂ solution was added dropwise to a beaker containing the synthesized SBA-15 until 6.3 mL/g_{SBA-15} was achieved. The resulting gel was magnetically stirred under ambient conditions and then calcined at 400°C for 3.5h in air. After calcination, the template was removed by immersion in a 5M KOH solution for 12 hours at 100°C. Finally, the remaining solids were rinsed with three rounds of excess deionized water, centrifuged at 4500rpm, and dried under vacuum at 70°C for 8 hours.

5.3.3 ELECTRODE FABRICATION AND COIN CELL ASSEMBLY

Anodes were created using either the highly ordered mesoporous NiO anodes or Vulcan XC-72R carbon. Vulcan XC-72R carbon black was chosen in this study as a control material since it does not store charge significantly via intercalation; this allows the

reaction plateaus to be dominated by electrolyte decomposition and not muddled with intercalation-based phase changes. NiO-based anodes were prepared with a ratio of 95:5 active material to polyvinylidene fluoride binder (PVDF, Kynar Blend). Vulcan-based anodes were prepared with a 90:10 carbon:PVDF ratio. The change in the active material:PVDF ratio between the two types of electrodes considers the differences in their surface area (conductive carbon > NiO) and the amount of binder required to maintain sufficient particle-particle contact. In a typical setup, 400 μL of N-methyl-pyrrolidone (NMP, Acros, 99.5% Extra Dry) solvent was micropipetted into a vial containing a total of 100 mg of total solids to obtain an ink with moderate viscosity. The ink was homogenized via 3 successive rounds of sonication (20 mins) and magnetic stirring (8 hrs). The ink was sprayed onto a 50 μm thick Cu current collector (Alfa Aesar, Catalog No. AA42972FI) with an Iwata-Medea Eclipse HP-CS. The electrodes were then dried at 75°C for 24 hours under vacuum. Then, to minimize particle-particle contact resistance, the electrodes were hydraulically pressed at 1500 lbs (MTI 5T Max. Manual Mechanical Press) and calendared (MTI Electric Roller-MSK-MR100DC) to a specified gap of 60 μm . The final active loading target was 1 mg cm^{-1} .

Coin cell assembly was done inside of an argon-filled (Ultra-high purity 5.0 Argon, Airgas) MBraun Labmaster SP glove box (O_2 and H_2O < 0.1 ppm). All coin cells were assembled in a half cell configuration using CR2032 coin cells (Hohsen Corp.). The counter/reference electrode was a 1.5 cm diameter lithium metal foil (99.9%, Alfa Aesar). In a typical procedure, the Li foil was polished, positioned at the center of the coin cell base, and then flattened to ensure minimal contact resistance. Then, 15 μL of electrolyte (1M lithium hexafluorophosphate (LiPF_6 , Acros 98%) in a 1:1:1 volumetric mixture of

ethylene carbonate (EC, Acros 99+%): dimethyl carbonate (DMC, Acros 98+%): diethyl carbonate (DEC, Acros 99+%) was injected uniformly onto the Li-metal. A Celgard 2320 tri-layer PP/PE/PP separator was centered on top of the Li-metal/electrolyte surface. Next, an additional 15 μL of electrolyte was injected uniformly onto the separator. The gasket was placed along the outer diameter of the coin-cell base to ensure proper centering of the working electrode and sealing of the cell. A spacer disk and spring was used to ensure uniform distribution of pressure and electrical continuity in the cell. Finally, the cap of the coin cell was used to seal the cell with an MTI hydraulic press (MSK-110) at a pressure of 750 PSI.

5.3.4 CHEMICAL AND STRUCTURAL CHARACTERIZATION

Pre-/post-cycled transmission electron microscopy (TEM) was performed on electrodes of interest by a similar procedure that was outlined in a previous publication.³⁰ To preserve the region of interest during microscopy, a Cu TEM finder grid (3mm diameter, 100 mesh, Ted Pella, Inc) was used. First, 1 μL of diluted active material slurry (1:10 dilution ratio) was deposited onto the grid and capillary drained via light application of a lint-free laboratory cloth (KimwipesTM). The procedure was repeated three times and fully-dried before TEM. After microscopy, the TEM grid, loaded with the active material, was mounted into a custom-designed electrode fixture between a Teflon shroud and a cylindrical Cu current collector. The assembly was electrochemically cycled (details in the following section) in a 3-electrode cell inside of an Ar-filled Mbraun glovebox. After the electrochemical experiments, the TEM grid with active material removed from the assembly was submerged in excess DMC for 30 minutes and dried inside the glovebox for 24 hours prior to additional microscopy. All microscopy was performed either using a FEI

Talos scanning transmission electron microscopy (S/TEM) and a Hitachi H8000 TEM with integrated energy-dispersive x-ray spectroscopy (EDS). In addition, X-ray Photoelectron Spectroscopy (Kratos AXIS Ultra DLD XPS System) was used to determine the elemental composition on the surface, chemical state, and electronic structure of the active material.

5.3.5 ELECTROCHEMICAL TESTING

Three electrochemical methods were primarily used in this work. Current-pulse relaxation, via the galvanostatic intermittent titration technique (GITT), was done using an Arbin MSTAT battery cyclers under pseudo-isothermal conditions inside a Tenney T6S-1 climate-control chamber at 25°C. The method involves 100 intermittent current pulses at $C/10$ for a time that satisfies $t \ll L^2/D$, followed by a relaxation time (i.e. no current) to electrochemical equilibrium. In addition to a time constraint (i.e. satisfies $t \ll L^2/D$), the voltage window was specified to be 0.001-3.0V. The GITT data allowed for the apparent diffusion coefficients and apparent exchange current densities to be extracted as a function of the state of charge (SOC). The other method used in this work was linear sweep voltammetry (LSV), which was done using the Arbin MSTAT battery cyclers. LSV was used to determine the effective transfer coefficient as a function of the SOC during a parallel GITT test. The scan rate was 1mV s^{-1} and the upper/lower cutoff voltage was $\pm 100\text{mV}$ vs. the open circuit voltage (OCV). A 30-minute relaxation time was given between the positive and negative scan. Finally, the samples deposited on the TEM grid for pre-post imaging were exposed to cyclic voltammetry (CV) at a 0.1mV/s scan rate over the same potential window as the GITT measurements (0.001- 3.0 V).

5.3.6 ELECTROKINETIC FRAMEWORK

The electrokinetics for complex heterogeneous reactions (combinations of multi-step electrochemical and/or chemical reactions) are developed to understand current-potential (i-E) relationships. The i-E relationship can be rigorously derived by applying Dirac's time-dependent perturbation theory to Schrodinger's wavefunction (Ψ) of an electron and integrating the density of states for the electrolyte (detailed proof can be found in Fletcher et al.¹⁷⁹). For most reactions, the reaction rate is expressed in the Butler-Volmer (BV) formulation, given as **Equation 5.5**⁴⁷:

$$i = i_0 [e^{-\alpha_{eff} f(E-E^0)} - e^{(n-\alpha_{eff}) f(E-E^0)}] \quad \text{Equation 5.5}$$

where i_0 is the exchange current density, α_{eff} is the transfer coefficient, $f = F/RT$, n is the number of electrons, $E - E^0$ is the overpotential. If all of the electrochemical steps can be assumed to be reversible, the overall effective transfer coefficient is represented as:¹⁸⁰

$$\alpha_{eff} = \frac{\vec{\gamma}}{\upsilon} + \rho\beta \quad \text{Equation 5.6}$$

in which $\vec{\gamma}$ is the number of electrons prior to the rate-determining step, υ is the number of times the rate-determining step occurs, ρ is either 0 (if the rate-determining step, RDS, is a chemical step) or 1 (if the RDS is an electrochemical step), and β is 0.5. The Butler-Volmer electrokinetic expression is typically valid in a very narrow regime where the free energy curves for oxidation and reduction are linear. However, the potential energy surface based on Marcus theory is represented by intersecting parabolas that account for the cumulative coordination energy between the initial and final states of the electrolyte. This model results in the Marcus-Hush-Chidsey (MHC) relationship between the current and overpotential, which is given below:¹⁸¹

$$i_{\text{ox/red}}^{\text{MHC}}(\lambda, \eta) = A \int_{-\infty}^{\infty} \exp\left(-\frac{(x-\lambda \pm e\eta)^2}{4\lambda}\right) \frac{dx}{1 + \exp(x)} \quad \text{Equation 5.7}$$

In **Equation 5.7**, λ is reorganizational energy normalized to the thermal voltage, and $\eta = e(E - E^0)/k_B T$. The Fermi distribution of the electronic energy upon an applied potential is accounted for in the MHC framework by integrating $x = (\epsilon_{e1} - eE)/k_B T$. The pre-exponential factor (A) accounts for the strength of the electronic coupling and density of states. Previous studies¹⁸² found that the Fermi distribution in the MHC is negligible ($x = (\epsilon_{e1} - eE)/k_B T$), resulting in the low overpotential approximation for the Marcus-Hush-Chidsey kinetic expression. Therefore, the MHC breaks down to a modified transfer coefficient to the Butler-Volmer expression and can be represented as a potential-dependent property and as a function of the electrolyte reorganizational energy, **Equation 5.8**.¹⁸²

$$\alpha_{\text{eff}} = \frac{\vec{\gamma}}{v} + \rho \left[\beta + \frac{e(E - E_{\text{eq}})}{4\lambda} \right] \quad \text{Equation 5.8}$$

5.4 RESULTS AND DISCUSSION

5.4.1 MECHANISTIC FRAMEWORK – KNOWN EC REACTIONS ON CARBON BASED ANODES

The effective transfer coefficient can help researchers to elucidate the mechanistic pathway of the reaction and it is capable of decoupling multi-step reactions because it elucidates the nature of the RDS. For a generalized multi-step reaction that follows the form of $A + ne^- \rightleftharpoons Z$, the RDS plays an essential role in the rate of reaction. Therefore, a multi-step reaction can be broken down into the number of electrons prior to the RDS and the number of electrons after the RDS to give a cumulative number of electrons of n . By

writing out every rate expression for every step of the pathway, the effective transfer coefficient can be derived and used for mechanistic insight (**Table 5.1**).

Table 5.1. | Hypothetical generalized mechanism where n is the total number of e^- , $\vec{\gamma}$ is the number of e^- before RDS, $\tilde{\gamma}$ is the number of e^- after RDS, and ρ is either 0 (chemical) or 1 (electrochemical) ^{180,183}

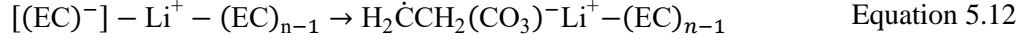
Generalized Reaction for:	# of electrons
$A + ne^- \rightleftharpoons Z$	
$A + e^- \rightleftharpoons B$	1
$B + e^- \rightleftharpoons C$	2
$\downarrow \quad \dots \quad \downarrow$	\downarrow
$M + e^- \rightleftharpoons N$	$\vec{\gamma}$
$N + \rho e^- \rightleftharpoons O$	$\tilde{\gamma} + \rho \leftarrow \text{RDS}$
$O + e^- \rightleftharpoons P$	$\tilde{\gamma}$
$\downarrow \quad \dots \quad \downarrow$	\downarrow
$X + e^- \rightleftharpoons Y$	$n-1$
$Y + e^- \rightleftharpoons Z$	n

With the present theoretical framework for multi-step reactions, electroanalytical techniques can be applied to study the activation of EC on conversion electrodes. Numerous studies have applied high-level density functional theory (DFT) calculations for the reduction pathway of EC, which is the dominant reactant participating in the SEI formation step on carbon/graphite (**Equation 5.9** to **Equation 5.17**).^{160,184,185} First, supermolecules of $(EC)_n$ and Li^+ are formed during the electrolyte preparation step.



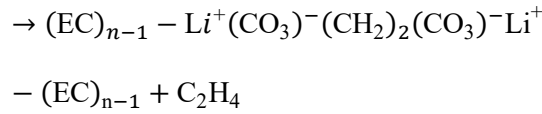
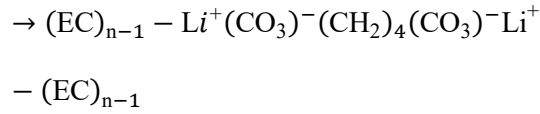
The supermolecules of $Li^+(EC)_n$ then undergo a 2-electron decomposition reaction at the electrified surface. The 1st electron transfer step destabilizes the system to an ion-pair intermediate via homolytic C-O bond cleavage:



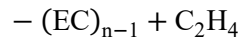
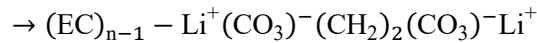
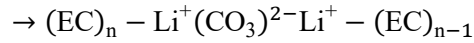
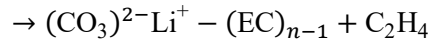


From here, the EC can further decompose to a lithium organic(R) dicarbonate (ROCO₂Li)₂

where R can either be ethylene or butylene:



An alternative decomposition reaction can occur at low EC concentrations via the formation of an unpaired carbonate nucleophile (LiCO₃⁻), which can react after the 1st electron transfer to either Li₂CO₃ or (CH₂OCO₂Li)₂:



Despite the plethora of experimental data that corroborates the EC reaction mechanism above for carbon (a detailed DFT study can be found in Wang et al.¹⁸⁶), there is a demand to generalize the reaction mechanism on developmental-stage electrodes with higher energy densities or phenomenal reversibility. Therefore, this section attempts to bridge this gap by providing a systematic approach to deconvoluting the SEI reaction

mechanism on M-X anodes. First, SEI formation is summarized on Vulcan XC-72R carbon. Vulcan XC-72R provides a control case for SEI formation that is well-studied (i.e. carbon) where the result is well known – without interference from intercalation. This is meant to validate the overall methodology, which is then extended to a representative M-X material, NiO. To my knowledge, this study contains the most comprehensive dataset and analysis for the SEI formation on M-X anodes, which has resulted in a much more complete understanding of the reaction mechanism as a function of SOC on this family of materials as well as a framework for others to apply to similar systems in the future.

The SEI reaction mechanism and location of the electrolyte decomposition (inner or outer-sphere reaction) primarily occurs during the first charge. The charge curve for the first charge of Vulcan XC-72R (carbon control) is shown in **Figure 5.2a**. The curve can be split into 3 regions (Arabic numerals: 1, 2, 3). In Region 1, the charge is primarily stored via electric double layer (EDL) capacitance, though some of the current passed also contributes to electrolyte decomposition/SEI formation. In Region 2, the behavior is dominated by charging the EDL. Finally, Region 3 shows both EDL charge storage as well as extended capacity from electrolyte reduction. The diffusional transport properties extracted from galvanostatic intermittent titration technique show a stepwise decrease in the apparent diffusion coefficient (S^2D) and are represented as the solid/dashed black lines in **Figure 5.2a**. Region 1 shows a gradual decrease in the apparent diffusion coefficient from 10^{-13} to 10^{-14} $\text{cm}^6 \text{s}^{-1}$. The electrolyte reduction process and formation of the SEI impede Li^+ diffusion, resulting in an average diffusion coefficient that decreases as a function of the SEI film growth. The transition from Region 1 to Region 2 is reflected by a stabilization of the apparent diffusion coefficient, which corresponds well with the

inflection point of the OCP (i.e. transition from an electrochemical reaction (EC) that forms the SEI to a purely capacitive behavior). The transition between Region 2 to Region 3 is marked by a comparative extension in the capacity in the low potential range and the increase in the diffusional barrier. The stage-wise decrease in the diffusion coefficient captures a two-stage SEI formation process and this phenomenon elucidates some of the previous SEI-related literature (i.e. a porous SEI near the electrolyte interface and densification near the electrode surface).²² The apparent exchange current in **Figure 5.2b** captures the kinetics at different SOC. The V-shape curve for i_0S is consistent with the potential response and delineation of Region 1-3. Region 1, which shows tendencies that are consistent with an electrochemical reaction with EDL charge storage. The delineation is reflected in the form of a higher exchange current in-comparison to Region 2, which comparatively shows similarities to subsequent cycles. The steep drop in the apparent exchange current in the transition from Region 1 to Region 2 marks the near completion of the first SEI formation process. At low potentials vs Li/Li⁺ the apparent exchange current increases significantly, which is a corollary to a secondary plateau or more specifically a secondary reaction.

Linear sweep voltammograms taken in Region 1 and Region 3 during the first charge are plotted in **Figure 5.2c**. In **Figure 5.2c**, experimental data are represented by semi-transparent dots, while Tafel curves are indicated by straight dashed lines and the low overpotential approximated MHC analysis is indicated by solid lines. The highlighted colors and labels in **Figure 5.2c** also show the constituent physical and/or chemical processes that primarily contribute to the LSV behavior in various potential regimes.

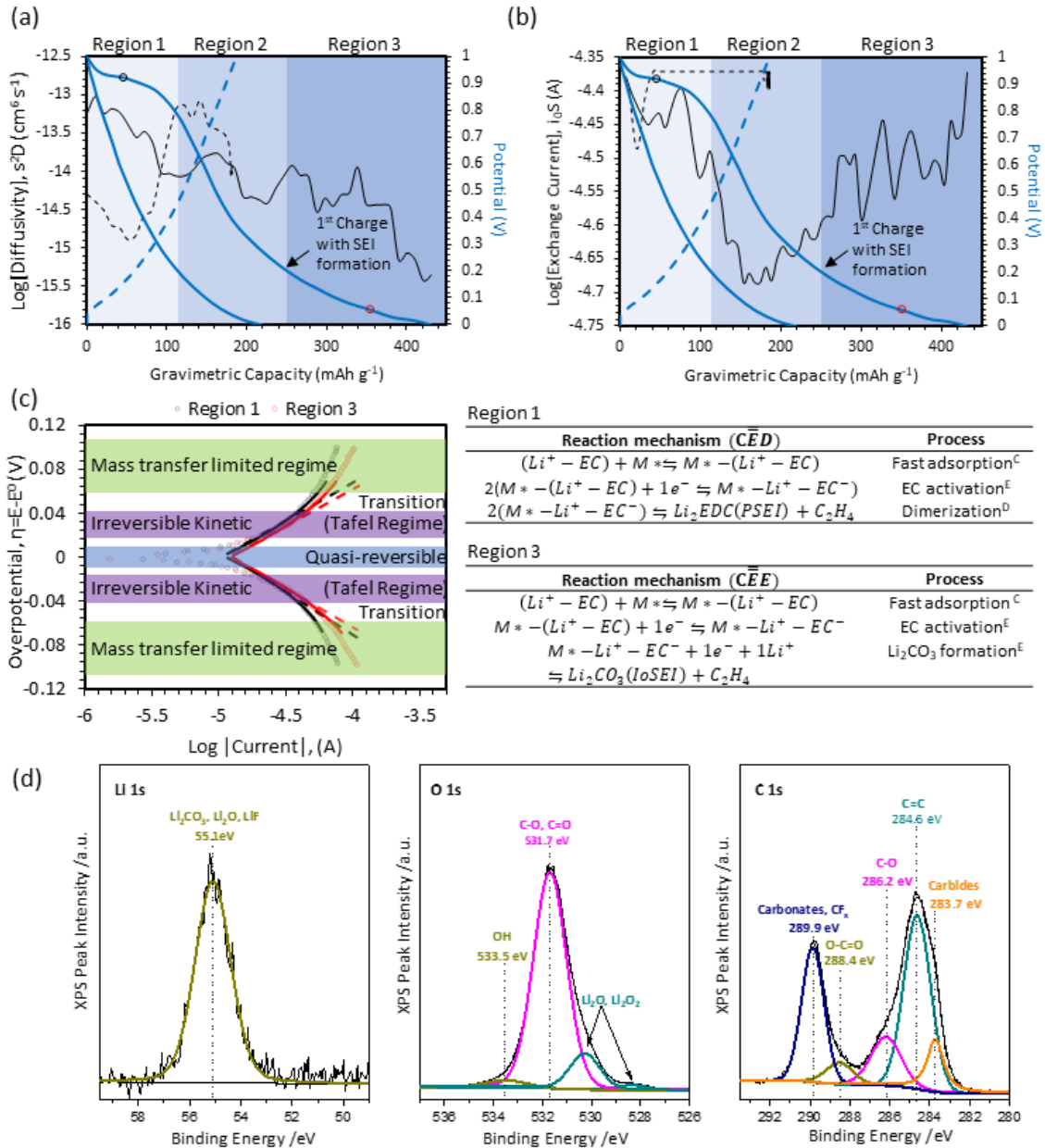


Figure 5.2. | Represents (a) charge/discharge curves for Vulcan XC-72R carbon black, (b) Tafel-like plots with Butler-Volmer (solid line) and Marcus-Hush-Chidsey (dashed lines) models on-top of experimental data (dots), and (c) illustration of the interfacial structure of carbon during initial charge stages and reaction mechanism as proposed by (Wang et al.¹⁸⁶). The reaction mechanism designations are C = chemical step, E = electrochemical step, D = dimerization reaction, and a double line highlight the rate-determining step. Reproduced with permission from The Royal Society of Chemistry.¹⁶⁷

At low overpotentials, the quasi-reversible regime near the equilibrium potential is highlighted in blue. In this regime, reversible interfacial charge transfer occurs. At moderate overpotentials, highlighted in purple, linear Tafel behavior can be observed. At high overpotentials, highlighted in green, mass transfer limitations take over as the log(i) response deviates significantly from linearity^{181,182,187}. Calculations of α_{eff} and low overpotential MHC calculations of the reorganization energy (λ) for Vulcan XC-72R carbon black are provided in **Table 5.2**. First, the reorganizational energy for Region 1 and Region 3 were found to be $\lambda = 0.33 \text{ eV} \pm 0.01$ and $0.37 \text{ eV} \pm 0.01$, respectively. The small reorganizational energy suggests that electrolyte reduction is controlled by electron transfer and not solvation/desolvation ion transport mechanisms that typically exhibit reorganizational energies above 0.5 eV. The good agreement of the experimental data to the MHC model, combined with low reorganization energies, indicates that the SEI formation on carbon in this region is an outer-sphere electron transfer process.¹⁸⁸

Table 5.2. Tafel calculations of α_{eff} for Vulcan XC-72R carbon black.

	Region 1	Region 3
α_{eff}	0.43 ± 0.01	0.47 ± 0.01
λ	$0.33 \text{ eV} \pm 0.01$	$0.37 \text{ eV} \pm 0.01$

5.4.2 MECHANISTIC ASSESSMENT OF EC ACTIVATION AND ORGANIC SEI FORMATION

(REGION 1)

As shown in **Table 5.2**, kinetic deconvolution of the LSV data yielded an α_{eff} of 0.43 in Region 1. From this value, it can be surmised that $\vec{\gamma} = 0$ and $\rho = 1$, meaning that the rate determining step is the first electron transfer step. To ascertain the number of times

the RDS occurs, additional information is needed. Wang et al.¹⁸⁶ proposed the reaction mechanism in **Figure 5.2c** for Region 1, which indicates a fast adsorption step followed by an activation step and a dimerization reaction to form organic Li₂EDC and ethylene (translates to a $\nu = 2$). From their DFT calculations, they also proposed the 1st electron transfer step to be the rate-determining step. In this region, the SEI formation is dominated by organic species formation because the bulk EC concentration (~7M) makes it highly available, with high surface coverage as well. Even though surface mobility of activated EC is low due to steric hindrance, there is a boundless supply of EC in Region 1 prior to SEI formation. In this region, the simultaneous ethylene evolution and Li₂EDC formation enable the formation of the porous, organic portion of the SEI.

5.4.3 MECHANISTIC MODEL FOR EC ACTIVATION TO INORGANIC SEI (REGION 3)

During the first charge, Region 3 has an α_{eff} of 0.47, which again suggests that $\vec{\gamma} = 0$ and $\rho = 1$. However, by the time that the charge has reached Region 3, the surface is much different than it was in Region 1 since a significant portion of the porous, organic SEI (Li₂EDC) has already been formed as discussed above. The existence of this porous layer, as opposed to a flat, open surface, also means that the reaction likely becomes EC mass transport limited¹⁸⁴. Because the surface mobility of activated EC is low, the lower concentration of EC results in severely hindered dimerization due to lack of proximity between active species¹⁸⁴. Also, in Region 3, the anode potential is lower than it was in Region 1. The combination of a high driving force and low EC concentration results in nucleophilic attack of neighboring Li-species, as shown in **Figure 5.2c**, which changes the formed reduction products from organic species to inorganic compounds such as Li₂CO₃.

In addition to the electroanalytical analysis, XPS was used to corroborate the reaction mechanism for SEI formation on carbon. High-resolution Li 1s, O 1s, and C 1s for post-SEI formation on carbon are presented in **Figure 5.2d**. The Li 1s high-resolution spectrum captures one broad peak at 55.1 eV, which is difficult to deconvolute but characteristic of Li_2CO_3 ($E_b \sim 55.2$ eV), Li_2O ($E_b \sim 53.8$ eV), LiF ($E_b \sim 55.6$ eV), and ROCO_2Li ($E_b \sim 54.7$ eV).¹⁸⁹⁻¹⁹¹ A deconvolution of the O 1s high-resolution spectrum indicates the presence of C-O, C=O functionalities ($E_b \sim 531.7$ eV), and possible O-H ($E_b \sim 533.5$ eV). Also, a shoulder corresponding to the formation of Li_2O is observed at 528.5 eV. The C 1s spectrum contains a convoluted set of peaks that are consistent with carbonate/ CF_x ($E_b \sim 289.9$ eV), O-C=O ($E_b \sim 288.4$ eV), C-O ($E_b \sim 284.6$ eV), and carbide-related species ($E_b \sim 283.7$ eV). The observed CF_x binding energies are expected and related to the PVDF binder. The remaining peaks correspond to compounds in the SEI and conductive carbon and are consistent with the known products for SEI formation on carbon, including lithium alkyl carbonates (e.g. ROCO_2Li) in Region 1 and Li_2CO_3 in Region III.

5.4.4 SUMMARY OF SEI FORMATION ON CARBON

The potential and concentration dependence of the SEI formation process can therefore be broken down into three primary regions on the carbon control. In Region 1, the extended reaction plateau at 0.93V and the non-existent reaction plateau in the subsequent cycles can be used to decouple the two charge storage mechanisms, EDL charging and SEI formation. The SEI formation process can then be further deconvoluted via electron transfer theory to yield an effective transfer coefficient ($\alpha_{\text{eff}} = 0.43$) that corroborates the reaction pathway of highly concentrated EC to the organic-phase SEI (either $(\text{CH}_2\text{CH}_2\text{OCO}_2\text{Li})_2$ or $(\text{CH}_2\text{OCO}_2\text{Li})_2$). In Region 2, the potential profile resembles

characteristics of subsequent cycles and indicates charge storage that is consistent with EDL storage (i.e. no definitive reaction plateau). As the charging reaches Region 3, an extended reaction plateau at $<0.3V$ is observed and corroborates the widely accepted 2nd reaction pathway of the SEI. A further deconvolution of Region 3 reveals an effective transfer coefficient of 0.47, which leads to the observation that the 1st electron transfer step is the rate-determining step. These findings agree with the widely-accepted literature pathway for SEI formation, where EC reduction leads to the Li_2CO_3 -rich^{19,160,184} Though this first section is a validation of already-published work, it is included here to provide a baseline for comparison with the true system of interest in this work: M-X species. The results above show that the mechanistic framework shown here is fully capable of deconvoluting the complex multi-step reaction pathway of the primary active electrolyte species (EC) – meaning that it can be extended to M-X species with a high chance for success.

5.4.5 SOLID ELECTROLYTE INTERPHASE ON CONVERSION METAL OXIDE

After confirming the plausibility for the DFT-proposed reaction mechanisms by Wang et al.^{192,193} and the experimental observations by Aurbach et al.¹⁸⁴ for SEI formation on the control-carbon electrodes in this study, the methodology was then extended to M-X conversion anodes, specifically using NiO as a representative material. **Figure 5.3a** shows the galvanostatic intermittent titration technique (GITT) results for the open circuit potential (OCP) and diffusivity (S^2D) for NiO as a function of the state of charge (SOC) during the initial charge (solid lines) and discharge (dashed lines). The apparent exchange current as a function of SOC during the initial charge (solid line) and discharge (dashed line), also from GITT, is shown in **Figure 5.3b**. Because SEI formation occurs during the

1st charge, that will be the focus of the discussion. From the trends in the data, four regions (denoted by Roman numerals: I, II, III, IV) could be identified.

In Region I (OCP > 1 V), the initial reaction occurs at the solid/liquid interface, which is indicated by a high apparent diffusion coefficient ($10^{-8} - 10^{-9} \text{ cm}^6 \text{ s}^{-1}$) and the lowest exchange current, ca. $2 \times 10^{-5} \text{ A}$. By the end of Region 1, the apparent diffusion coefficient decreased to $10^{-10} \text{ cm}^6 \text{ s}^{-1}$, while the apparent exchange current increased slightly to ca. $2.5 \times 10^{-5} \text{ A}$. In Region II ($0.7 < \text{OCP} < 1 \text{ V vs. Li/Li}^+$, $72 < Q < 610 \text{ mAh g}^{-1}$), the apparent diffusion coefficient was fairly stable ($\sim 10^{-11} \text{ cm}^6 \text{ s}^{-1}$) and its magnitude is characteristic of solid-state diffusion, most likely lithium ions through the porous SEI and active metal oxide particles. Concurrently, the apparent exchange current continuously increased to ca. $5.0 \times 10^{-5} \text{ A}$. In Region III ($0.5 < \text{OCP} < 0.7 \text{ V vs. Li/Li}^+$, $610 < Q < 790 \text{ mAh g}^{-1}$), there was an increase in the apparent diffusion coefficient from $\sim 10^{-11}$ to $\sim 10^{-9}$, which indicates a possible transition in the diffusion mechanism from purely solid-state diffusion back to a combination of solid-state + liquid-state phase diffusion. The most likely reason for this phenomenon can be attributed to slight volumetric expansion as well as the phase segregation of Ni-metal + Li_2O domains, which exposes the additional active material surface to the electrolyte (visual evidence will be discussed later along with **Figure 5.3c**). However, the exchange current was not changed in this Region. In Region IV ($0 < \text{OCP} < 0.5 \text{ V vs. Li/Li}^+$, $Q > 790 \text{ mAh g}^{-1}$), there was a rapid drop in the apparent diffusion coefficient from (10^{-9} to 10^{-12}), suggesting a transition from a mixed solid-state/liquid-state diffusion back to a purely solid-state mechanism.

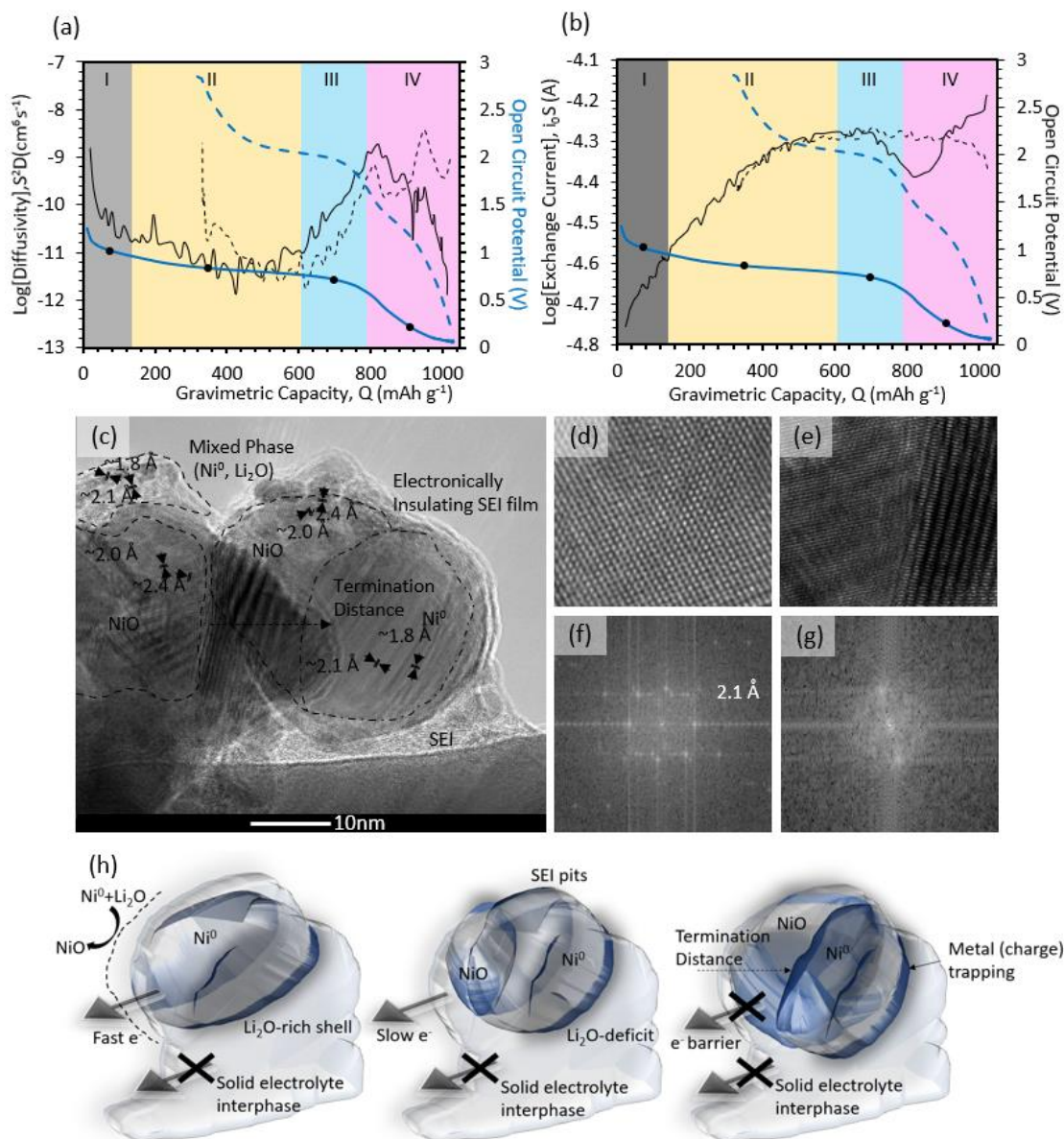


Figure 5.3. | Depicts galvanostatic intermittent titration technique for the parameter extraction of (a) apparent diffusion coefficient and (b) the apparent exchange current. Both plots contain the open circuit potential of NiO marked in (blue). Each section contains a dot that indicates locations where linear sweep voltammetry is done. Four sections are broken down (I, II, III, IV) to delineate dominant mechanisms. Also, high-resolution transmission electron microscopy is depicted as (c) TEM of post-cycled NiO. The atomic resolution HRTEM is depicted in (d) for the Ni domain ($\sim 2.1\text{\AA}[111]$, $\sim 1.8\text{\AA}[200]$) and (e) for the NiO domain ($2.4\text{\AA}[111]$, $2.0\text{\AA}[200]$). The Fast Fourier Transform (FFT) analysis of the HRTEM (f) for Ni and (g) for NiO. (h) Depicts the schematic for NiO particle transformation and showing the conversion reaction front propagation for the particle-level HRTEM image in **Figure 5.3c** (i.e. lithiation propagates from the bulk electrode until the reaction front stops due to high local polarization (i.e. the electrical losses generate a termination distance) and resulting in trapped charge). Reproduced with permission from The Royal Society of Chemistry.¹⁶⁷

The rapid drop in the diffusion coefficient in combination with an overpotential in-proximity to Li/Li^+ is consistent with the 2nd stage of SEI formation in carbon electrodes, which included densification and a transition from organic to inorganic electrolyte decomposition products. A HRTEM image of a partially charged NiO particle is shown in **Figure 5.3c**. The image captures a moving phase boundary between the charged state and the discharged-state that does not begin homogeneously at the surface and move inward, a so-called shrinking core model, as might be initially expected. Instead, evidenced by a distinct lateral phase boundary in the particle, the particles begin their charge from the side of the particle closest to the current collector/substrate and the reaction plane moves from that side of the particle to the other. By zooming in at higher magnification, atomic resolution images are captured for both the charged Ni (**Figure 5.3d**) and discharged NiO (**Figure 5.3e**) domains within the particle. The corresponding fast Fourier transform (FFT) is also shown below the HRTEM images for both phases. The FFT deconvolution shows two distinct lattice fringes neighboring the phase boundary with lattice constants of 2.0 \AA [200] and 2.4 \AA [111] corresponding to planes of NiO in **Figure 5.3f**, and 2.1 \AA [111] and 1.8 \AA [200] corresponding to Ni-metal in **Figure 5.3g**. The anisotropic lithiation/delithiation behavior of the conversion reaction suggests that the reaction front is controlled by electronic conductance (the charge does result in the formation of metallic Ni particles, which have high conductivity). This seems to confirm previous work showing that the charge/discharge efficacy of metal oxide anode materials is strongly dependent on the intra-particle and inter-particle conductivity.^{34,45}

Figure 5.4 applies Tafel and MHC electrokinetic models to LSV data taken in each Region during the first charge, as was done for carbon in the previous sections, to better

understand the reaction mechanism during SEI formation. In all Regions, the Tafel and MHC descriptions capture the near linear $\log(i)$ response with reasonable agreement, and the resulting effective transfer coefficients and reorganizational energies are shown in **Table 5.3**. Even with the simplification of the MHC used here, the model is in good agreement with the data, suggesting that the Fermi distribution and EDL have a negligible contribution to the kinetic behavior in this system. Also, symmetry in the data indicates that an electron transfer step is rate-limiting, and not ion transport through the EDL or the prematurely formed SEI, even though some studies have suggested that desolvation of Li^+ from the electrolyte into the SEI may be rate-limiting.¹⁹⁴ Typically, desolvation requires reorganizational energies greater than 0.5 eV.

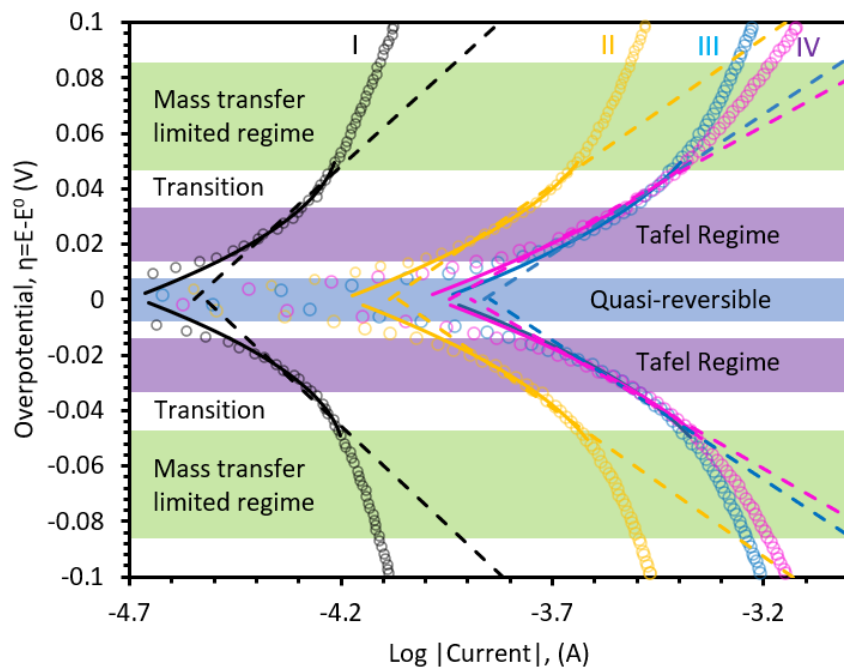


Figure 5.4. | Represents Tafel-like plots for Butler-Volmer (solid line) and Marcus-Hush-Chidsey (dashed lines) models on-top of experimental data (dots). Reproduced with permission from The Royal Society of Chemistry.¹⁶⁷

Table 5.3. | Effective transfer coefficient calculated by Tafel slope and reorganizational energy calculated by the low overpotential approximation for the Marcus-Hush-Chidsey theory

	I	II	III	IV
α_{eff}	0.41 ± 0.01	0.55 ± 0.02	0.58 ± 0.01	0.67 ± 0.02
λ	$0.23 \text{ eV} \pm 0.01$	$0.28 \text{ eV} \pm 0.01$	$0.30 \text{ eV} \pm 0.01$	$0.38 \text{ eV} \pm 0.01$

Since Marcus theory¹⁸⁸ was originally derived for outer-sphere electron transfer reactions, the reorganizational energy indicates the reduction of EC at the outer Helmholtz plane. The interfacial interaction of the electrolyte and the electrode can be deconvoluted from the reorganization energy in the MHC model and studied at different SOC to provide a temporal view of the electrode/electrolyte interaction across the entire reaction coordinate. From the beginning to the end of the first charge, Region I→II→III→IV, λ continuously increased from 0.23 to 0.38. Since λ is an indicator of the energy required to reorganize the electrolyte, differences in this value can elucidate surface interactions. The fact that electrolyte reorganization energy increased from low SOC to high SOC suggests that the interface is altered by the SEI formation and it is likely that the ion-pairing between Li^+ and solvent dipoles or PF_6^- anions become stronger at higher SOC (i.e. the coordination level increases or ion-pairing changes). In comparison, the reorganizational energy on carbon is higher than on NiO at low SOC ($\lambda_{\text{C}} = 0.33 \text{ eV} \pm 0.01$ in Region 1 vs $\lambda_{\text{NiO}} = 0.23 \text{ eV} \pm 0.01$ for Region I), which means the transfer of charge on an oxide surface is initially more facile on NiO. This could be due to a catalytic effect, since the surface area of C (250 m^2/g) vs. NiO (80.4 m^2/g) is drastically different, though this needs to be probed more deeply in the future. However, as the electrolyte decomposition proceeds to a more mature stage, the reorganization energies (and hence the electrolyte-SEI interaction) become

statistically identical ($\lambda_C = 0.37 \text{ eV} \pm 0.01$ in Region 3 vs $\lambda_{\text{NiO}} = 0.38 \text{ eV} \pm 0.01$ for Region IV), which suggests that the advanced SEI/electrolyte interfaces are likely similar.

5.4.6 MECHANISTIC ASSESSMENT OF EC ACTIVATION ON CONVERSION MATERIALS

(REGION I)

Because two processes are occurring simultaneously during the first charge, both the conversion reaction and SEI formation, isolating the process of interest can be difficult and requires several pieces of experimental data to be systematically pieced together to generate a full understanding. Based on the effective transfer coefficient in Region I, and the consistency to Region 1 in carbon, the analysis strongly suggests that the reaction pathway for the reduction of EC to $(\text{ROCO}_2\text{Li})_2$ also occurs on NiO. The effective transfer coefficient results are also fully consistent, with the value of the α_{eff} indicating that the reaction is again rate-limited by the 1st electron transfer ($\vec{\gamma} = 0$, $\rho = 1$). Here, $\text{Li}^+(\text{EC})_n$ supermolecules are rapidly adsorbed onto the active material, followed by activation and dimerization to Li_2EDC and ethylene. Again, the lower reorganization energy for this initial process does suggest possible catalytic decomposition in the early stages of SEI formation on the NiO surface, which requires future study.

5.4.7 BEHAVIOR IN REGIONS II AND III

The effective transfer coefficient in Regions II and III were very similar ($\alpha_{\text{eff}} = 0.55$ for Region II and $\alpha_{\text{eff}} = 0.58$ for Region III). In-combination with the behavior of the apparent diffusion coefficient as discussed above and the apparent exchange current density, the behavior in these two Regions appears to correspond primarily to the conversion reaction $(\text{Ni}^{2+}\text{O}^{2-} + \text{Li}^+ \rightarrow \text{Ni}^0 + \text{Li}_2\text{O})$, not SEI formation. Palmieri et al.

proposed a reaction mechanism based on thermodynamic arguments and behaviors consistent with the observations here.³⁴ Because it is not expected that significant SEI formation occurs in Regions II and III, they will not be extensively discussed here as their dynamics fall outside of the focus of this work.

5.4.8 MECHANISTIC MODEL FOR EC ACTIVATION ON CONVERSION MATERIALS (REGION IV)

XPS chemical analysis was performed to guide the mechanistic deconvolution of Region IV, which also is comprised of responses from multiple reactions.

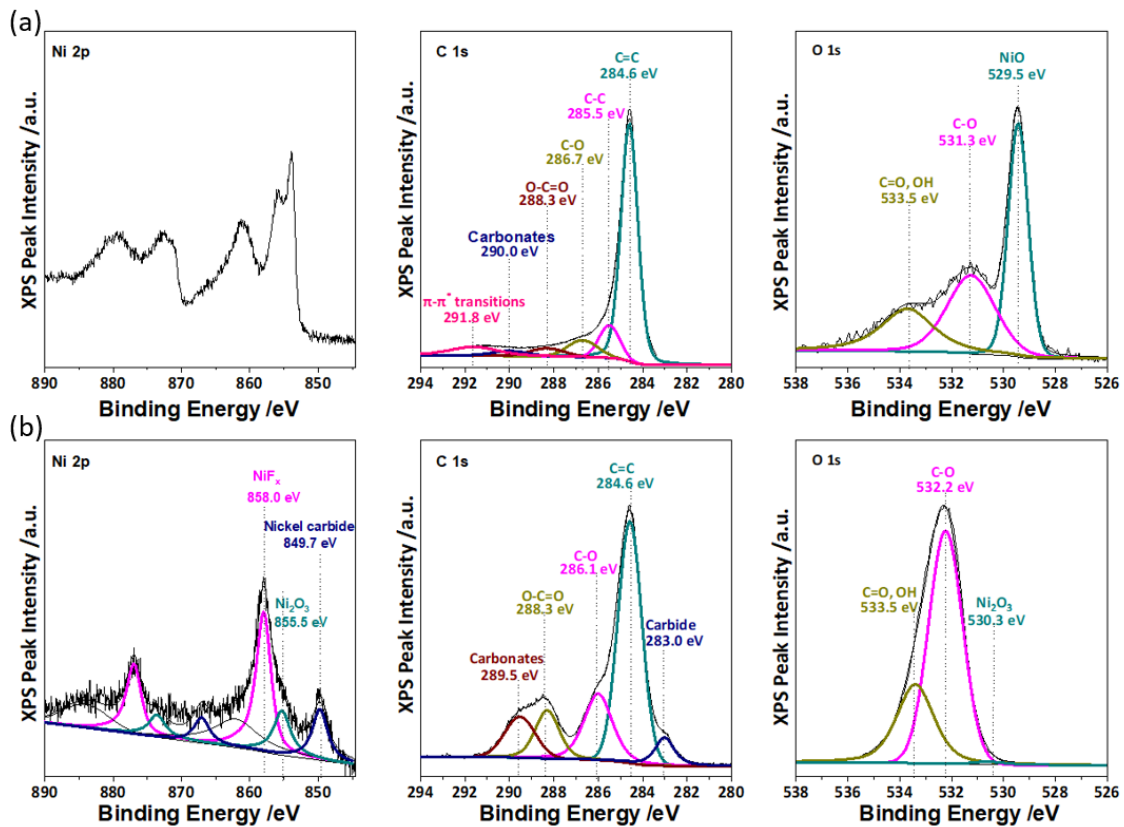


Figure 5.5. | High-resolution XPS spectra of (a) pre-cycled and (b) post-cycled NiO electrodes in the Ni 2p, C 1s, and O 1s spectra. Reproduced with permission from The Royal Society of Chemistry.¹⁶⁷

Figure 5.5a shows a high-resolution XPS spectrum for pre-cycled NiO in the Ni 2p spectra, which shows characteristic (872.5eV) $2p_{1/2}$ and (854.3eV) $2p_{3/2}$ with an 18.2 eV displacement from the split spin-orbit of nickel oxide (NiO). Satellite peaks for Ni $2p_{1/2}$ at 872 eV and Ni $2p_{3/2}$ at 862 eV can be observed as well. After being cycled (100x), the Ni 2p spectra (**Figure 5.5b**) indicates the presence of mixed oxidation states between Ni²⁺ and Ni³⁺ that is characteristic of Ni₂O₃, NiF₂, Ni carbide, and Nickel carbide species at Ni $2p_{3/2}$ binding energies of 858 eV, 855.5 eV, and 849.7 eV, respectively.

In the pre-cycled C1s spectrum, responses were observed from C=C ($E_b \sim 284.6\text{eV}$), C-C/C-H ($E_b \sim 285.5\text{ eV}$), C-O ($E_b = 286.7\text{eV}$), O-C=O ($E_b \sim 288.3\text{ eV}$), and -CO₃⁻ (or PVDF at $E_b \sim 290.0\text{ eV}$) species. In addition, the π - π^* shakeup satellites were observed at $E_b \sim 291.8\text{ eV}$. The high resolution pre-cycled C 1s spectrum shows functionalities for PVDF and carbon black. The post-cycled C 1s spectrum reveals a significant increase in -CO₃⁻ functionalities at $E_b \sim 289.5\text{ eV}$. O-C=O ($E_b \sim 283.3\text{ eV}$), C-O ($E_b \sim 286.1\text{ eV}$), and C=C ($E_b \sim 284.6\text{ eV}$) were also observed, which correspond to the typical SEI components discussed for carbon, including Li₂CO₃ and Li(CO₃)-R-(CO₃)Li. Finally, a noticeable shoulder peak was observed at $E_b \sim 283.0\text{ eV}$, which corresponds to the formation of carbides and corroborates the Ni 2p peak at 849.7 eV.

The pre- and post-cycled high-resolution XPS spectra for O 1s are also shown in **Figure 5.5**. The O1s XPS spectrum for the post-cycled electrode shows the presence of C=O ($E_b \sim 533.5\text{ eV}$) and C-O bonds ($E_b \sim 532.2\text{ eV}$), which corroborates the C1s spectrum for the formation of Li₂CO₃. Additional lithium alkyl carbonate species (R-CH₂O(C=O)OLi ($E_b \sim 532.2\text{ eV}$) and R-CH₂O(C=O)OLi ($E_b \sim 533.5\text{ eV}$) were also identified

during the deconvolution. A less pronounced peak for Ni_2O_3 ($E_b \sim 530.3$) was observed from the peak shoulder at 530.3 eV.

By coupling the XPS results with electroanalytical analysis of the RDS, it is possible to decouple the controlling processes in the reaction mechanism. There is a discrepancy in the effective transfer coefficient when comparing Region I to Region II/III and to Region IV. Like SEI formation on the carbon black control, α_{eff} was ~ 0.4 . For carbon, the transfer coefficient is almost independent of the SOC, but for NiO α_{eff} increased with the SOC from 0.41 to 0.67, suggesting a deviation in the reaction mechanism. More specifically, in Region IV the observed effective transfer coefficient is an amalgam of the competition between the SEI formation and the conversion. From previous work³⁴, it is known that the transfer coefficient for the conversion reaction is around 0.5. This means that the large positive deviation in the measured α_{eff} must come from a process whose transfer coefficient is > 0.5 and the only other process occurring is the latter stages of SEI formation, which is discussed below.

As the conversion and SEI formation simultaneously occur, there is likely depletion of Li^+ reactants near the anode surface. This phenomenon does not affect the conversion due to the fact that the Ni^+ transition state formed during the RDS is unstable and all the subsequent steps are relatively facile (i.e. the dissociation step and formation of Li_2O is highly thermodynamically favorable). However, electrolyte reduction in its latter stages, just like carbon, relies on the reaction of free electrolyte that is trapped inside of the pore space formed during reaction in Region I. When this happens, the reaction is not just limited by surface activated electrolyte species, it also encounters a deficiency in Li^+ ions that may be abstracted to form Li_2CO_3 . This abstraction is energetically uphill, and if it

becomes controlling, this chemical step would be the RDS and the resulting transfer coefficient would be 1 ($\bar{\gamma} = 1$, $\nu = 1, \rho = 0$) and fully consistent with all of the experimental observations in this work.

Table 5.4. | Mechanistic insight in the reaction pathway for Region IV ($2.2 < x < 2.8$), showing chemical (C) and electrochemical (E) steps.

MO Reaction mechanism (C\bar{E}C\bar{E}E)	Process
$SEI - Li^+ \rightleftharpoons SEI + Li^+$	Li ⁺ Dissociation from SEI ^C
$MO + Li^+ + e^- \rightleftharpoons MO - Li^+$	1 st electron transfer ^E
$MO - Li^+ \rightleftharpoons M^+ + LiO^-$	Dissociation ^C
$Li^+ + LiO^- \rightleftharpoons Li_2O$	Li ₂ O recombination ^C
$M^+ + e^- \rightleftharpoons M^0$	2 nd electron transfer ^E
EC Reaction mechanism (C$\bar{E}$$\bar{E}$E)	Process
$(Li^+ - EC) + M^* \rightleftharpoons M^* - (Li^+ - EC)$	Adsorption in open pore ^C
$M^* - (Li^+ - EC) + 1e^- \rightleftharpoons M^* - Li^+ - EC^-$	EC activation ^E
$SEI - Li^+ \rightleftharpoons SEI + Li^+$	Li ⁺ Dissociation from SEI ^C
$M^* - Li^+ - EC^- + 1e^- + Li^+ \rightleftharpoons M^* - Li_2CO_3(1oSEI) + C_2H_4$	Li ₂ CO ₃ formation ^E

5.4.9 PHYSICAL STRUCTURE OF THE SEI ON NiO

Figure 5.6a shows TEM images of the mesoscale-scale structure of the post-cycled NiO. Compared to pre-cycled NiO, significant structural changes were observed. Some were expected, such as particle agglomeration – leading to a loss of distinguishable boundaries between particles. Also observed was the non-uniform deposition of SEI components onto the surface of the active material. In fact, NiO and SEI components were found to preferentially cluster, leading to fully agglomerated regions and partial vacancies in the SEI that can be areas for high reactivity.

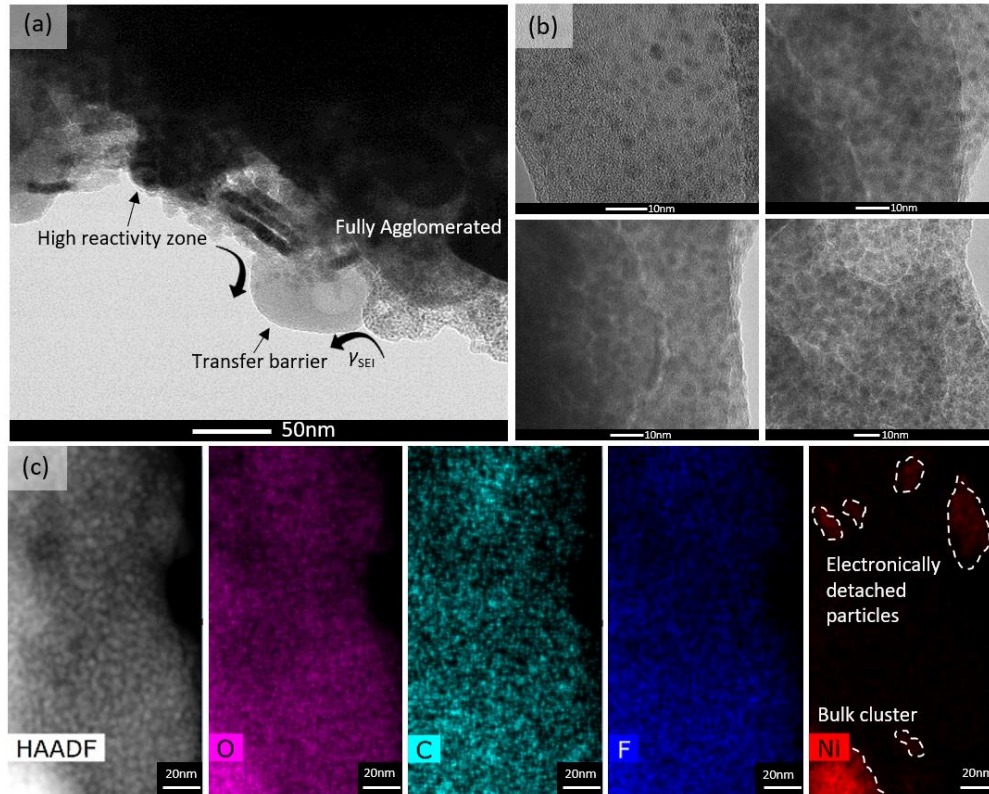


Figure 5.6. | Transmission electron microscopy was used in (c) which represents the post-cycle surface mesostructure and highlights high anisotropy in SEI formation, (d) high resolution of the SEI, (e) energy-dispersive X-ray spectroscopy, and elemental mapping of the SEI. Reproduced with permission from The Royal Society of Chemistry.¹⁶⁷

High-resolution TEM images in **Figure 5.6b** show two regions in the SEI with multiple particles embedded into the SEI matrix. HAADF and EDS elemental mapping in **Figure 5.6c** suggest that the SEI's elemental composition consists of C, O, F, P, and Ni, confirming constituents of Li_2CO_3 , $\text{Li}(\text{CO}_3)\text{R}(\text{CO}_3)\text{Li}$, LiF , trapped-Ni, etc. Also, from elemental mapping, Ni clusters appear to be enveloped inside of the electronically insulating SEI. This indicates a possible aging mechanism that involves metals becoming trapped and detached from the bulk electrode. This metal-trapping mechanism leads to the active material becoming stuck in the charged state, reducing the achievable capacity. It also can sacrifice the mechanical integrity of the SEI later itself, which relates back to the

GITT results, where the apparent diffusion coefficient increased near the end of Region III. What is likely occurring is that the volumetric changes from the conversion reaction, coupled with the formation of the SEI forcing some particles off the surface, temporarily increase the porosity of the newly-formed SEI, allowing a different mode of transport (fully solid-state to liquid phase diffusion) to be active.

5.5 SUMMARY

First, characteristic regions were isolated for conversion-based MOs anodes based on the thermodynamic, kinetic, and transport properties at different SOC. The reaction mechanisms were isolated for each region and revealed very similar characteristics to the SEI formation process in Region 1 on carbon and Region I on MO. Unlike carbon, where only SEI formation and EDL storage were observed, MOs store charge via bond-breakage, which dominated the response for Regions II and III. The conversion reaction mechanism also occurs extensively in Region IV; however, increased driving force for SEI formation (lower potential) leads to a competition between the two reactions that revolves around the Li^+ dissociation from the SEI. This results in a shift in the Tafel slope and the RDS for SEI formation from an electrochemical step to a chemical step with an $\alpha_{eff} = 1$. Cumulatively, it can be surmised that the SEI formation on M-X materials appears to initiate identically to carbon, though some surfaces may show a catalytic effect that needs to be studied further. However, the final stages of SEI formation, though they result in very similar inorganic products, appear to diverge mechanistically.

CHAPTER 6: AVOIDING THE SOLID ELECTROLYTE INTERPHASE

DEGRADATION MECHANISM IN NEXT GENERATION

CONVERSION ANODES

The fundamental reaction mechanism to the formation of the SEI and the conversion reaction has been discussed in depth in Chapter 5 and this Chapter will take the study one step further to study the long-term effects of conversion metal oxides (e.g. cyclability, reaction reversibility, coulombic efficiency, chemistry) and methods to bypass these degradative processes. Recall from Chapter 1, metal oxides (MOs) typically suffer from intrinsically low electronic conductivities ($10^{-8} - 10^{-3} \Omega^{-1} \text{cm}^{-1}$)¹⁹⁵ and display several degradation mechanisms that are inherent to their chemistry. First, if the structure and electronic conductivity of the local environment are not well controlled, the base metal (M) and Li_2O reaction products can phase separate, resulting in the trapping of the active material in the charged state, rapidly lowering the capacity during cycling¹⁹⁶⁻¹⁹⁸. Second, there is an entropic penalty associated with the repetitive restructuring and collapse of the parent host ($\text{MO} \rightarrow \text{M} + \text{Li}_2\text{O}$)¹⁹⁸⁻²⁰⁰, which can lead to the growth of larger particles and phase segregation to minimize surface free energy. Third, there can be the continued growth of the SEI due to physical changes in the electrode during charge/discharge,²⁰¹⁻²⁰⁵ which can reduce the electrode capacity during cycling through both increased irreversible capacity loss as well as particle detachment and metal trapping within the SEI^{85,189,206,207}. Finally, through reaction either with excess electrolyte or the SEI, MOs undergo a side

reaction that forces them to higher oxidation states during their lifetime – a reaction that lowers their achievable coulombic efficiency (but not their achievable capacity since the reaction does not consume Li)⁴². In combination, these four degradation mechanisms have often significantly limited the performance and lifetime of MO-based anode materials and have led to their exclusion from cells of commercial interest.

Therefore, Li-ion cells employing MO anodes must overcome the low (particle-level) and long-range (electrode-level) electronic conductivity problems, long-term phase segregation, and irreversible capacity loss due to uncontrolled overgrowth of the SEI. One possible approach is physically confining the MO from the electrolyte in a highly entangled, high-aspect-ratio conductive matrix (e.g. high crystallinity carbon nanotubes), which has the potential to significantly reduce the effects of all the “inherent” degradation mechanisms listed above – increasing their cyclability and coulombic efficiency – and limit irreversible capacity loss in the first cycle. Doing so with a low loading of the conductive material (~10%) can provide a practical pathway forward for these materials – resulting in a low cost, long-life, high-rate active material with no Li plating during fast charge, which would have a significant impact on the LIB technology. This chapter will provide the first steps in this direction – using NiO confined inside of carbon nanotubes (NiO@CNT) as a proof-of-concept. The physical and electrochemical properties of the NiO@CNT material will be investigated. It will be shown that nano-confinement is a convincing panacea to eliminate the existing degradation pathways, allowing for these materials to be extensively cycled with full material utilization and fast-charged.

6.1 EXPERIMENTAL

6.1.1 REAGENTS

Multi-walled carbon nanotubes (CNTs) (average $D = 10$ nm, P/N 412988 and average $D = 50$ nm, P/N 901002), Pluronic P123 triblock copolymer (PEG-PPG-PEG, $M_n \sim 5800$), tetraethyl orthosilicate (TEOS, >99.0%), hydrochloric acid (HCl, ACS reagent grade, 37%) and nitric acid (HNO_3 , ACS reagent grade, 70%) were purchased from Sigma Aldrich. Nickel (II) nitrate hexahydrate ($\text{Ni}(\text{NO}_3)_2 \cdot 6\text{H}_2\text{O}$, 99%) and potassium hydroxide (NaOH) were purchased from Acros Organics through Fisher Scientific. Vulcan XC-72R was purchased from Cabot. The CNTs were purified with an acid treatment and high-temperature defunctionalization (detailed in Section 2.2). $\text{Li}(\text{Ni}_{0.5}\text{Mn}_{0.3}\text{Co}_{0.2})\text{O}_2$ powder was purchased from MTI corporation. Ultrapure deionized water (18.2 $\text{M}\Omega$ cm) was supplied by a lab-scale Millipore Milli-Q Integral system with E-POD. All other chemicals were used as received.

6.1.2 SYNTHESIS OF NiO/C, ID-NiO/CNT, AND NC-NiO@CNT

Three unique NiO-carbon composite materials were synthesized: (1) unconstrained deposition of NiO on the surface of carbon black (Vulcan XC-72R), which will be denoted as NiO/C; (2) NiO indiscriminately deposited on both the inside and outside of CNTs, denoted as ID-NiO/CNT; and (3) NiO nano-confined exclusively on the inside of CNTs, denoted as NC-NiO@CNT_x (where x = the CNT diameter in nm).

NiO/C was synthesized through a mesoporous silica (SBA-15) template-assisted synthesis. First, the SBA-15 template was produced using the same procedure as previous publications.^{33,177,178} In a typical synthesis, 6g of Pluronic P123 and 13.6 mL TEOS was

first dissolved in 180mL of 2M HCl solution and successively heated at 45°C (20 hours) and 100°C (24 hours). The resulting SBA-15 template was washed with a DI water/ethanol mixture and dried under a vacuum. The dried SBA-15 was then calcined in air at 500°C for 3 hours. Next, 500 mg of nickel nitrate hexahydrate was dissolved to create an aqueous 0.5M Ni(NO₃)₂ solution. The solution was added dropwise to the SBA-15 until a ratio of 6.3 mL/g_{SBA-15} was obtained. The Ni(NO₃)₂/SBA-15 gel was magnetically stirred and then calcined in air for 3.5 hours at 400°C. The resulting powder was immersed into an aqueous 5M KOH solution for 12 hours at 100°C to etch away the SBA-15 template. The supernatant was disposed of, and the remaining solids were rinsed three times with excess DI water, centrifuged at 4500rpm using a Sorvall ST-8 centrifuge, and then dried for 8 hours at 70°C under vacuum. Finally, the templated NiO was added to a mortar along with Vulcan XC-72R in a 7:1 mass ratio and ground with a pestle for 30 minutes.

ID-NiO/CNT was synthesized by dispersing 200 mg of CNT₅₀ into 20 mL nitric acid with a magnetic stirring rod. The CNT₅₀ dispersion was refluxed at 120°C for 30 minutes to purify the CNTs, which also opened their closed-ends. Next, the CNT₅₀ dispersion was diluted slowly under magnetic stirring with a total of 80 mL of DI water. The diluted dispersion was then transferred to a 50 mL centrifuge tube and the solids were separated by centrifugation at 4500 rpm for 10 min. After decanting the liquid, an additional 40mL of DI water was added to the centrifuge tube, which was then sonicated and centrifuged (repeated three times with the liquid being decanted off each time). The solids were vacuum dried at 70°C for 24 hours and defunctionalized for 4 hours at 1500°C in a tube furnace under an Argon atmosphere to ensure high CNT crystallinity. Next, 30 mL of a 10M nickel nitrate hexahydrate (Ni (NO₃)₂ · 6 H₂O) in 70% nitric acid solution

was prepared by stirring for 1 h. 100 mg of the defunctionalized CNT₅₀ was added to the solution and refluxed at 120°C for 12 hours. The solid precipitate was vacuum filtered with a G2-grade glass fiber membrane (Fisherbrand) in a Büchner funnel, vacuum dried at 70°C for 24 hours, and then placed in a tube furnace and heated to 450°C for 4 hours under Argon atmosphere. The final ID-NiO/CNT was obtained after grinding with a mortar and pestle for 30 minutes to break up any agglomerates.

NC-NiO@CNT_x anodes were synthesized by dispersing 200 mg of CNT_x into 20mL of 70% nitric acid under continuous stirring. The CNT dispersion was refluxed at 120°C for 30 minutes. The temperature was reduced to room temperature and then slowly diluted with 80mL of DI water. The diluted dispersion was centrifuged at 4500 rpm for 10 minutes, then decanted and refilled with 40mL of DI water, and finally sonicated. The process was repeated three times. The supernatant was removed, and the remaining CNT_x solids were dried at 70°C for 24 hours under vacuum. The dried solids were thermally treated and defunctionalized for high CNT crystallinity in a tube furnace under continuous Argon flow for 4 hours at 1500°C. The samples were re-dispersed in a 30mL 70% nitric acid and 10M Ni(NO₃)₂ solution. Then, the 10M Ni(NO₃)₂-CNT_x solution was refluxed for 12 hours at 120°C to allow for complete permeation of the nickel precursor into the CNT_x. After filtration with a G2-grade glass fiber filter, the samples were dried under vacuum at 70°C for 24 hours and pyrolyzed at 450°C for 4 hours under continuous Argon flow. 300 mg of the pyrolyzed solids were dispersed in 50 ml of 0.25M nitric acid and stirred for 1 hour. The remaining solids were collected by vacuum filtration with G2-grade glass fiber circles in a Büchner funnel (the liquid filtrate was bluish-green), dried under vacuum at 70°C for 24 hours, and then heated in a tube furnace at 450°C for 2 hours in an Argon

atmosphere. The final NC-NiO@CNT₅₀ (i.e. CNTs with 50 nm diameter) and NC-NiO@CNT₁₀ (i.e. CNTs with 10 nm diameters) active materials were obtained after grinding with a mortar and pestle for 30 minutes.

6.1.3 ELECTRODE FABRICATION AND COIN CELL ASSEMBLY

NiO/C, ID-NiO/CNT, and NC-NiO@CNT_x anodes were prepared by mixing 95% active material with 5% polyvinylidene fluoride binder (PVDF, Kynar Blend). A transfer micropipette was used to measure 400 μL of N-methyl-pyrrolidone (NMP, Acros, 99.5% Extra Dry) solvent, which was used as a dispersing agent for 100 mg of total solids to obtain an anode ink with moderate viscosity. The final ink was obtained after homogenization by 3 rounds of sonication (20 minutes) and continuous stirring (8 hours). The homogenized ink was uniformly sprayed onto a 50 μm thickness Cu current collector (Alfa Aesar, Catalog No. AA42972FI) with an Iwata-Medea Eclipse HP-CS sprayer. The resulting electrodes were dried in a vacuum oven at 75°C for 24 hours, pressed at 1500 lbs with a hydraulic press (MTI 5T Max. Manual Mechanical Press), and calendared (MTI Electric Roller-MSK-MR100DC). Electrodes used in half-cell studies had an active loading between 0.5 and 1.5 mg cm^{-2} . Full cells had a higher target anode mass loading of 5 mg cm^{-2} and the cathode target mass loading was 18 mg cm^{-2} . (target N/P ratio \sim 1.1). The full cell cathode active material:carbon:binder ratio was 8:1:1.

Coin cells were assembled in an argon (Ar, UHP Praxair) filled glove box (O_2 and H_2O < 0.1 ppm, MBraun Labmaster SP) in a half cell configuration with a Li metal counter/reference electrode. All electrochemical tests were conducted with CR2032 coin cells (Hohsen Corp.), 1.5 cm diameter lithium metal (99.9%, Alfa Aesar) counter electrodes, Celgard 2320 tri-layer PP/PE/PP membrane separator, and 1M lithium

hexafluorophosphate (LiPF_6 , Acros 98%) salt in a 1:1:1 volumetric mixture of ethylene carbonate (EC, Acros 99+%): dimethyl carbonate (DMC, Acros 98+%): diethyl carbonate (DEC, Acros 99+%) electrolyte. A typical coin cell assembly began with a lithium counter electrode centered and flattened onto the coin cell base. A micropipette was used to transfer 15 μL of electrolyte to both sides of the Celgard separator, which was then placed, centered, onto the lithium electrode. The gasket was placed to position the working electrode (NiO/C , ID-NiO/CNT , NC-NiO@CNT_x) directly in the center of the assembly. The spacer disk, spring, and the anodic cap of the coin cell were placed on top and the cell was finished by crimping with an MTI hydraulic press (MSK-110) to a pressure of 750 PSI. All sealed coin cells were inspected and safely transferred out of the glove box for electrochemical testing.

To assemble the high loading full cells, the anodes were first prelithiated to control the state of charge of anode upon assembly and to avoid any irreversible capacity loss in the initial cycles. The anode electrode was prelithiated by first immersing the electrode in a 1:1:1 EC: DMC, DEC, 1M LiPF_6 electrolyte for 72 hours to allow for full electrolyte penetration. Then, the anode was cycled in the same electrolyte 10 times between 0.001 and 3.0 V versus a Li foil. The first cycle rate was C/20 and subsequent cycles were 1C. Then, the prelithiated anode (5.16 mg cm^{-2}) was paired with a $\text{Li}(\text{Ni}_{0.5}\text{Mn}_{0.3}\text{Co}_{0.2})\text{O}_2$ (18.23 mg cm^{-2}) cathode using the same procedure as the half-cell experiments. Before cycling, full cells were aged for 48-hours at 40°C inside a Tenney temperature control chamber to allow the electrolyte to fully permeate into the electrodes. After removal from the Tenney chamber, the cell was given an additional 8-hour relaxation to equilibrate to ambient temperature before testing.

6.1.4 CHEMICAL AND STRUCTURAL CHARACTERIZATION

An extensive suite of characterization tools was used to determine the structural and chemical state of the active materials before and after cycling. For materials characterized at the end of cycling, the Li-ion cells were disassembled in the MBraun Ar-filled glovebox detailed above. The electrodes were washed with dimethyl carbonate (DMC) to remove residual Li salts and dried for 1 hour under vacuum at room temperature. X-Ray Diffraction (XRD) patterns were collected between 10 and 90 2θ degrees at a scan rate of 0.0285 degrees s^{-1} using a Rigaku Miniflex II at room temperature equipped with a high sensitivity D/tex Ultra Si slit detector. The Miniflex II had a Cu K(α) radiation source ($\lambda = 0.15405$ nm) that was operated at 30 mA and 15kV. Thermo-gravimetric Analysis (TGA) was done using a NETZSCH STA 449. The TGA traces were collected from room temperature to 1000 °C. Each sample was purged of moisture for one hour at 120°C under UHP N₂. Scanning transmission electron microscopy (S/TEM) images were collected using a FEI Talos S/TEM and Hitachi H8000 TEM with integrated energy-dispersive x-ray spectroscopy (EDS). X-ray photoelectron spectroscopy (XPS) measurements were performed with a Kratos AXIS Ultra DLD XPS system.

Pre-/post-cycled TEM images were collected using the identical-location TEM technique from a previous publication.⁴⁰ Generally, a Cu TEM finder grid (3mm diameter, 100 mesh, Ted Pella, Inc) was dropped with 1 μ L of diluted active material ink (1:10 ratio), drained, repeated three times, and dried for 24 hours under ambient conditions. After TEM imaging, the TEM grid/active material was cycled with a custom-designed Teflon-shrouded Cu electrode with a Teflon cap that applies pressure to the outer ring of the Cu grid. A 3-electrode system was employed to ensure high-fidelity voltage measurements

(i.e. mitigate external factors that contribute to high overpotentials) inside the Ar-filled Mbraun glovebox. The 3-electrode system (working electrode: NiO/C, ID-NiO/CNT, NC-NiO@CNT; counter electrode: Li foil; reference electrode: Li foil) was separated with a Celgard separator inside a beaker and filled with 1M LiPF₆ in 1:1:1 volumetric mixture of EC/DMC/DEC. After electrochemical treatment, described in the next section, the working electrodes were rinsed with DMC by submersion for 30 minutes and dried under ambient glovebox conditions for 24 hours. Afterwards, the post-cycled electrodes were transferred to an Ar-filled Kratos AXIS Ultra multipurpose transfer vessel and removed from the glovebox for further characterization (e.g. XPS, TEM, SEM).

6.1.5 ELECTROCHEMICAL TESTING

Electrochemical measurements were done on both coin-cells and the identical location TEM working electrodes. For the coin cell experiments, chronopotentiometric charge/discharge experiments were performed using an Arbin MSTAT battery test station. The voltage window for half-cells charge/discharge measurements were 0.001-3.0V. The C-rates for the charge/discharge were determined based on the NiO mass, and all capacities are normalized to the total material mass (NiO + C + PVDF). The voltage window for full-cells was set to 0.001-4.0V at C/2 with respect to Li(Ni_{0.5}Mn_{0.3}Co_{0.2})O₂ and held at upper cutoff voltage until C/20 current taper. The coin cells were also exposed to cyclic voltammetry and Electrochemical Impedance Spectroscopy (EIS) using an Autolab PGSTAT302N Potentiostat (Metrohm USA). Cyclic voltammograms (CVs) were collected in the same voltage window as the charge/discharge experiments with a 0.1 mV s⁻¹ scan-rate. EIS experiments were done at open circuit with a 5mV amplitude after full discharge (3V) at multiple frequencies between 1 MHz and 0.01 Hz. The open circuit

potential assumed to be reached was reached when $dV dt^{-1} < 1\mu V s^{-1}$. All the electrochemical measurements were made at room temperature. The electrodes used for identical location TEM electrodes were exposed to either 10 or 100 CV cycles were performed between 0.001-3.0V at $0.8 mV s^{-1}$,

6.2 RESULTS AND DISCUSSION

6.2.1 BEHAVIOR OF NON-CONFINED METAL OXIDE NANOPARTICLES

Li-ion cells employing MO anodes must overcome the low (particle-level) and long-range (electrode-level) electronic conductivity problems, long-term phase segregation, and irreversible capacity loss due to uncontrolled overgrowth of the SEI. One possible approach is physically confining the MO from the electrolyte in a highly entangled, high-aspect-ratio conductive matrix (e.g. high crystallinity carbon nanotubes), which has the potential to significantly reduce the effects of all the “inherent” degradation mechanisms listed above – increasing their cyclability and coulombic efficiency – and limit irreversible capacity loss in the first cycle. **Figure 6.1a** is an SEM image of the NiO/C macrostructure, showing that the material synthesized consisted of large agglomerations of NiO nanoparticles with good porosity. **Figure 6.1b** presents transmission electron microscopy (TEM) images and energy-dispersive X-ray (EDS) spectroscopy of pre-cycled NiO/C and shows the successful synthesis of ordered mesoporous NiO via the SBA-15 template-assisted synthesis. The TEM images of NiO/C indicate highly distinctive boundaries between each NiO nanoparticle.

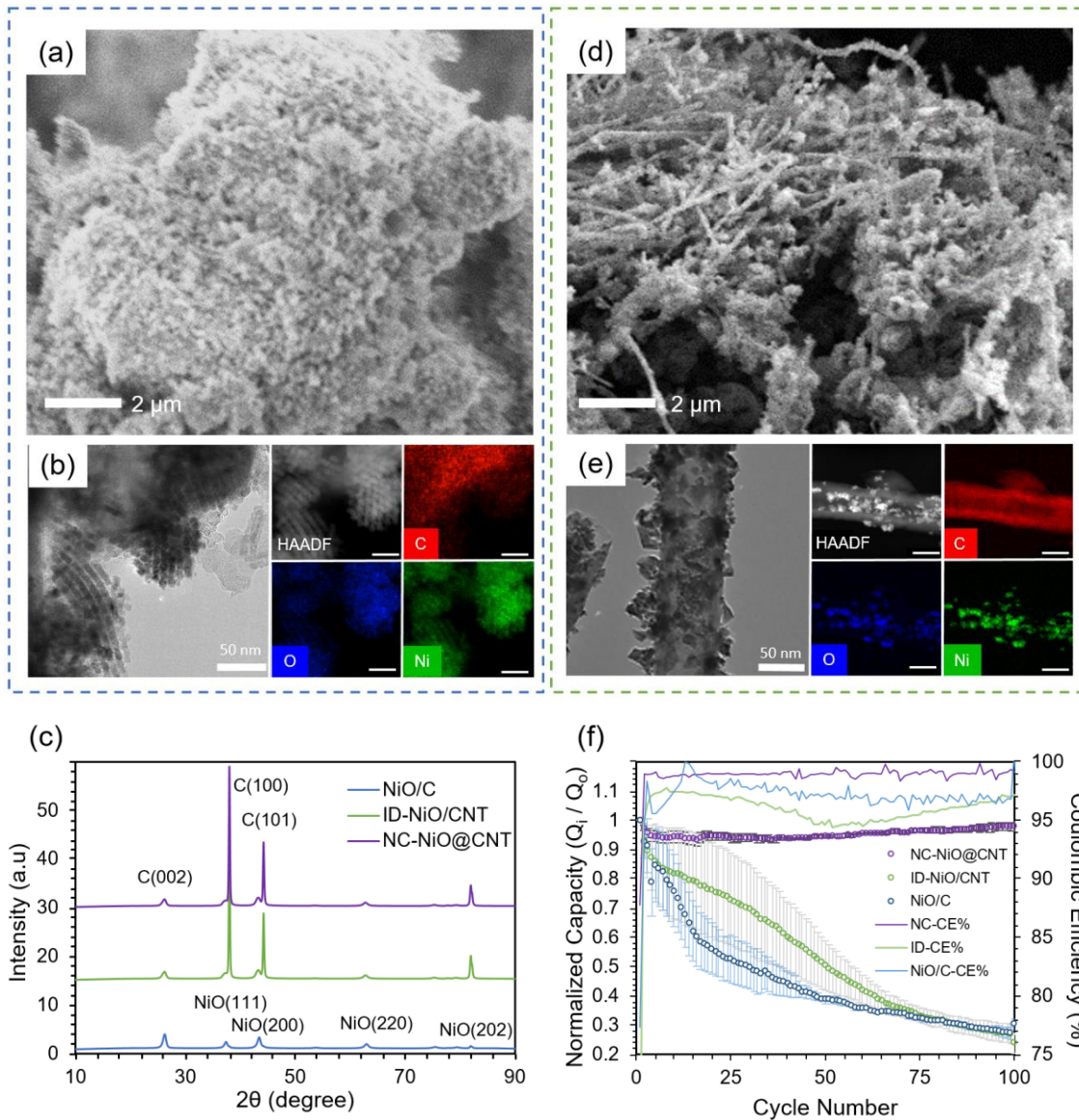


Figure 6.1. | Physical and Electrochemical Characterization. Depicts (a) scanning electron microscopy (SEM), (b) transmission electron microscopy and energy dispersive spectroscopy (TEM/EDS) of NiO/C. (c) X-Ray Diffraction (XRD) patterns comparing the crystallography (e.g. crystallite domain size, structure) of NiO/C (blue line), ID-NiO/CNT (green line), and NC-NiO@CNT₅₀ (purple line). (d) SEM and (e) TEM/EDS of ID-NiO/CNT. (f) Comparing the capacity retention of NiO/C (blue line), ID-NiO/CNT (green line), and NC-NiO@CNT₅₀ (purple line) at 1C charge/discharge rate to observe the reaction and cell-level reversibility. Reproduced with permission from The Royal Society of Chemistry.³⁷

High angle annular dark-field (HAADF) and elemental mapping of NiO shows the majority of the NiO is distributed on Vulcan carbon, though some NiO particles extend beyond the main carbon cluster. The images and EDS mapping shows that the MO particles were not chemically attached to the surface but existed as a physical mixture with the carbon. The X-ray diffraction (XRD) pattern for the NiO/C (blue line) is presented in **Figure 6.1c**. Characteristic peaks for NiO were observed at 37° , 44° , 63° , 75° , and 80° (2θ), corresponding to its (111), (200), (220), (311), and (222) Miller indices, respectively.²⁰⁸ Additionally, two carbon-related peaks were observed at 26° and 44° , which are associated with the graphitic (002) and C(100) Miller planes, respectively.²⁰⁹ No secondary phases or peaks ascribed to contaminants were observed. The Scherrer equation was applied to calculate the average crystallite domain size for NiO/C, 24.1 nm. **Figure 6.1d** is an SEM image of NiO indiscriminately deposited and anchored onto the surface of the 50 nm diameter CNTs, ID-NiO/CNT. The image clearly shows a semi-entangled carbon nanotube network with a high degree of surface NiO deposition. As shown in the SEM image, the MO particles are tethered to the CNT surface as both dispersed particles as well as larger agglomerates. Also, TEM and EDS in **Figure 6.1e**, were used to analyze the nanostructure and spatial arrangement of NiO and CNT in the ID-NiO/CNT material before any electrochemical testing. Since HAADF is able to contrast by atomic weight (high Z-contrasted material is ascribed to Ni, whereas the lighter Z-contrasted material is C), it was confirmed that the surface of the CNTs was covered extensively by NiO, though it should be noted that some NiO was also deposited inside of the CNTs. The XRD pattern for ID-NiO/CNT (green line) has similar characteristic peaks for NiO and C, NiO: 37° (111), 44° (200), 63° (220), and 75° (222); C: 26° (002) and 44° (100). The average

crystallite domain size for ID-NiO/CNT was found to be 16.6 nm, smaller than that of NiO/C.

Although their physical structures are different, one important similarity between the NiO/C and ID-NiO/CNT materials is that they are both comprised of NiO particles that are completely exposed to the electrolyte in operating cells. Therefore, it can be expected that all four of the degradation mechanisms discussed in the Introduction will be active for these materials and it is likely that their behavior in operating LIBs would be similar. **Figure 6.1f** presents the normalized capacity retention (Q/Q_0) plots for both NiO/C (blue line) and ID-NiO/CNT (green line) over 100 cycles at a 1C rate. Each experiment was repeated on three cells to confirm the repeatability of the electrochemical performance. Also, the reference point for the initial capacity (Q_0) was assumed to be the 2nd cycle to account for the irreversible capacity loss from SEI formation. The overall electrochemical cycling performance of NiO/C and ID-NiO/CNT showed similar capacity fade over 100 cycles – showing that the type of carbon is not an intrinsically determining factor when considering the onset of degradation. For NiO/C, the irreversible capacity loss in the first cycle was 23%. From the 2nd cycle to the 15th cycle, the rate of capacity fade was very high, and the NiO/C anode lost 41% of its capacity during this time. The average coulombic efficiency (CE) over the first 15 cycles was also low, only 97.4%. After cycle 15, the degradation rate for NiO/C was slowed, though still relatively severe and over 100 cycles; NiO/C lost 69.4% of its capacity and the average CE of a single cycle was 97.1%.

As an anode, ID-NiO/CNT (**Figure 6.1f** green line) experienced a similar trend in capacity fade to NiO/C. The SEI-related irreversible capacity loss for ID-NiO/CNT was 35.4%, which was higher than that of NiO/C, most likely due to the higher surface area of

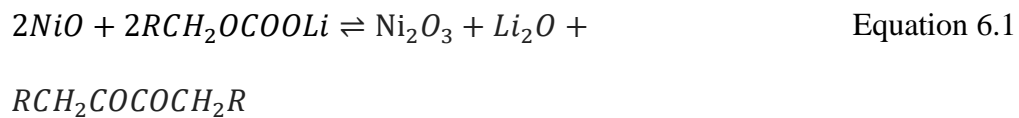
the smaller NiO crystallites in ID-NiO/CNT (16.6 nm) compared to NiO/C (24.1 nm). The total capacity loss of ID-NiO/CNT was 73.1% over 100 cycles whereas NiO/C was 69.4%, which shows a high degree of similarity in the onset of degradation and overall capacity loss. An important point related to the capacity retention plots in **Figure 6.1f** is that the data for both NiO/C and ID-NiO/CNT had seemingly large scatter, particularly at low cycle numbers. What this suggests is that MO degradation by metal (e.g. Li, M) trapping, SEI (re)formation, and/or transition to higher oxidation states is a complex series of events that can be triggered over the distribution of cycle numbers – though typically the onset of degradation will occur within the first 30 cycles, and the rate of initial degradation is rapid. Finally, the average CE for ID-NiO/CNT was also low, 95.8%, with a notable trend of CE loss over 50 cycles followed by a gradual recovery. The correlation between capacity loss and CE loss indicates that material is being trapped in the charged state repetitively after each cycle. This would result in larger Ni agglomerates, which were investigated by collecting TEM images of post-cycled materials and comparing them to **Figure 6.1b** and **Figure 6.1e**. Also, the low measured CE without catastrophic failure and loss of capacity is direct evidence of the conversion of the NiO to higher oxidation states during charge/discharge³⁴, which was further investigated by XPS before and after cycling.

Figure 6.2 shows post-cycle TEM images and pre/post-cycled XPS of NiO/C and ID-NiO/CNT. It is important to observe the evolution of the MO particle size, as this impacts the electrochemical behavior. As observed in **Figure 6.2** for NiO/C, even after 10 cycles the interfacial boundaries between each NiO nanoparticle appear to merge. After 100 cycles, the NiO agglomerates in NiO/C are so large that individual particles are almost indistinguishable. The repetitive restructuring and collapse of the MO active material

during the conversion reaction led to larger and larger phases each time it is reformed, causing a gradual decrease in the Ni/Li₂O interfacial contact area during discharge (oxidation) and trapping of material in the charged state. In other words, the NiO/C undergoes significant metal trapping during discharge and is likely the primary cause for capacity fade during cycling.

Figure 6.2(b-d) presents the pre- and post-cycle XPS analysis for NiO/C. **Figure 6.2 (b,c)** shows the Ni2p and O1s post-cycled XPS spectra for electrodes both before and after 100 cycles (the spectra were collected for materials in the discharged state). The high resolution Ni2p XPS spectrum before cycling (**Figure 6.2b**) shows characteristic Ni2p_{1/2} (872.5eV) and Ni2p_{3/2} (854eV) with a multiplet-split and displacement of 18.5 eV (from Ni2p_{1/2} to Ni2p_{3/2}), which is characteristic of NiO spin-orbital levels.³⁴ After 100 cycles, a peak at 859 eV emerged, which could be attributed to the formation of surface NiF₂ (a likely SEI product). In addition, a shoulder peak was found at a binding energy of 855.4 eV, which is characteristic of higher oxidation state Ni₂O₃, and indicates a pre-to-post cycle material transformation from (Ni²⁺→Ni³⁺). The O1s XPS spectrum (**Figure 6.2**) for the post-cycled NiO/C shows the presence of C=O, OH bonds at a binding energy of 533.0 eV and C-O bonds at 531.3 eV. Evidence for lithium alkyl carbonates, R-CH₂O(C=O)OLi was also found at O1s binding energies of 532.5 eV and 533.5 eV.²¹⁰ A less pronounced peak for the oxygen associated with metal oxides was observed from the peak shoulder at 530.1 eV. From the XPS results, the portion of the Ni in the active material in the 2+ (NiO) and 3+ (Ni₂O₃) oxidation states are summarized in **Figure 6.2d**. During cycling, the unconstrained NiO/C underwent a material transformation from 100% Ni²⁺ to a mixed oxidation state of 52% Ni³⁺ and 48% Ni²⁺, accounting for the low CE observed in **Figure**

6.1f. As stated in the introduction, the most likely cause for the transition of Ni²⁺ to Ni³⁺ is the reaction of NiO with oxygen-containing species in the SEI and/or the electrolyte. However, because there are several oxygen-containing species in the system, it can be difficult to determine which one is responsible for the transformation of NiO to Ni₂O₃ over time. Though there are many possible reactions, the O1s XPS spectra does provide evidence for at least one possible reaction, shown in **Equation 6.1**.



In the O1s XPS spectra for NiO/C (**Figure 6.2c**) and ID-NiO/CNT (**Figure 6.2c**) there is a clear asymmetry in the C-O peak where the peak shifts towards the left. The integrated area on either side of the peak suggests there are more C=O bonds than C-O bonds, which suggests that the alkyl carbonate SEI decomposition product R-CH₂O(C=O)OLi likely undergoes further decomposition. It is also noted that the asymmetry of this peak coincides well with the emergence of the Ni₂O₃ species, suggesting that these events are related; however, it is acknowledged that additional reactions are certainly possible, even likely. **Figure 6.2e** shows that after 10 cycles ID-NiO/CNT was able to retain its pre-cycled architecture with no observable deformation to the CNT. However, it was observed that some NiO agglomeration occurs and that some of the active material particles were detached and isolated from the CNTs as they were engulfed by the SEI. These particles remain trapped in the electronically insulating SEI and become deactivated. The SEI was found to grow similarly to that of graphite, where the SEI partially extends out of the CNT edge planes and caps. Also, SEI-clusters were found near large MO deposits.

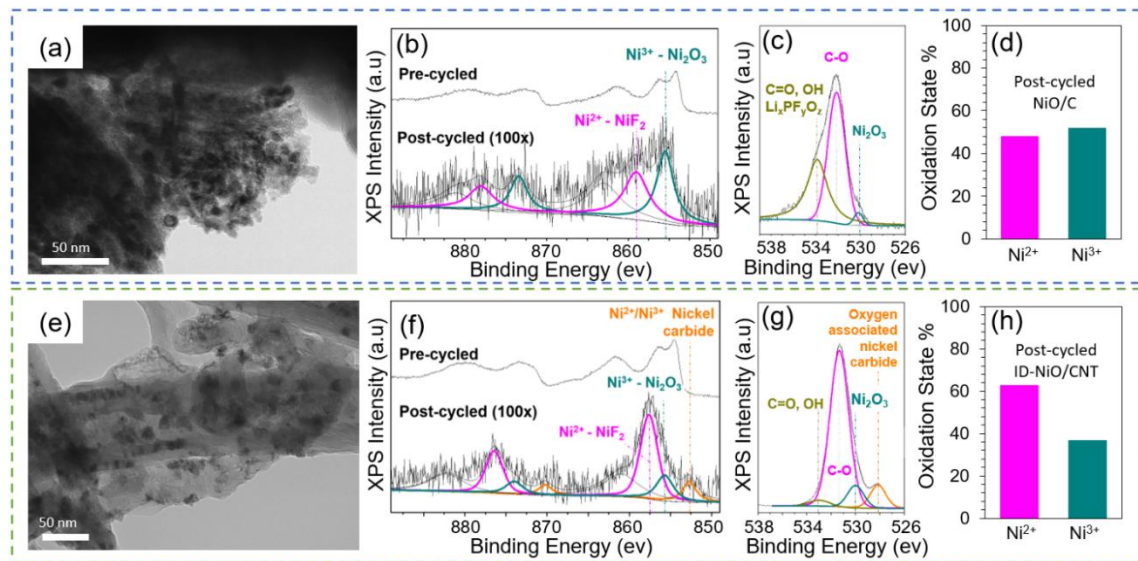


Figure 6.2. | Evaluation of Physical and Chemical Transformations. (a) TEM image of NiO/C after 10 electrochemical cycles. XPS spectra of NiO/C including (b) Ni₂p, (c) O1s, and (d) oxidation state percentages for NiO/C. (e) TEM images of ID-NiO/CNT after 10 electrochemical cycles. XPS spectra of ID-NiO/CNT including (f) Ni₂p, (g) O1s, and (h) oxidation state percentages for ID-NiO/CNT. Reproduced with permission from The Royal Society of Chemistry.³⁷

Figure 6.2 (f-h) presents the pre- and post-cycled XPS analysis of ID-NiO/CNT and the characteristic peaks in ID-NiO/CNT show the degradation pathway to form nickel carbides at 852.6 eV and Ni₂O₃ at 857.5 eV. **Figure 6.2f** shows the high-resolution Ni₂p XPS spectra for pre- and post-cycled ID-NiO/CNT. Prior to cycling, the XPS spectra were very similar to NiO/C, where Ni₂p_{1/2} (873eV) and Ni₂p_{3/2} (854.5eV) displayed an electron-spin difference of 18.5 eV. Also, like NiO/C, significant material transformation occurred after 100 cycles, and the presence of nickel fluorides (857.5eV), nickel oxide (855.6eV), and nickel carbides (852.8eV) were observed. The indiscriminately deposited ID-NiO/CNT post-cycled XPS analysis suggests similar chemical transformation of higher oxidation states (Ni²⁺→Ni³⁺) as that found in NiO/C, **Figure 6.2h**. Finally, **Figure 6.2g**

shows that the O1s spectrum for ID-NiO/CNT showed a similar presence of C=O, and OH bonds (533 eV) and C-O bonds (531 eV) as NiO/C.

In total, the observations in **Figure 6.1** and **Figure 6.2** suggest that the behavior of NiO/C and ID-NiO/CNT are very similar, though there were some subtle differences. For instance, the degradation rate of ID-NiO/CNT seems slightly slower and the transition to higher oxidation states is not quite as severe. These differences may be due to the partial confinement of NiO inside the CNT host, which might be able to minimize degradation of those particles, which are mostly isolated from the bulk electrolyte.

6.2.2 CNT-NANOCONFINED NiO

The proposed role of nanoconfinement to inhibit the dominant MO degradation pathways (in this case NiO) is illustrated in **Figure 6.3a**. When the MO particles are deposited solely inside the CNT, the CNT acts as an immobilization host that isolates MOs from the bulk electrolyte – which is expected to limit the extent to which the MO active material can react with the electrolyte, minimizing degradation. Also, the finite space within the CNT provides some elasticity for volumetric expansion, but limited opportunity for continuous SEI growth (i.e. CNT confinement can minimize particle detachment, isolation, and ripening/agglomeration). In addition, the CNT holds all reactants and products in one closed packet, which is hypothesized to minimize possible parasitic degradation reactions and increase the interaction area between reactants – increasing the material-level reaction reversibility and improving coulombic efficiency.

Therefore, to explore the realized effect of confinement on long-term reversibility and stability, NC-NiO@CNT₅₀ was synthesized. The SEM images in **Figure 6.3b** show that the synthesized material was nearly completely free of surface MO particles compared

to ID-NiO/CNT in **Figure 6.1d**. Not only is this expected to yield the advantages discussed above, it should also be noted that the resulting electrode would primarily consist of a highly conductive, interconnected carbon matrix that can freely transport electrons throughout the active layer^{211,212}. **Figure 6.3c** further shows the successful synthesis of the nanoconfinement concept presented in **Figure 6.3a**, providing a high-resolution view of the structure alongside EDS elemental mapping, which showed the presence and distribution of Ni, O, and C. Also, the NiO particles appeared to be tethered to the inner walls of the CNT, which physically restricts the MOs and their charge products (M and Li₂O) to a finite space, thereby suppressing movement.

The high-resolution TEM images (HR-TEM) in **Figure 6.3(c-1 to c-3)** shows the lattice fringes of NiO nanocrystallites with a d-spacing of 2.4 Å, which is ascribed to (111) plane of NiO. The interlayer separation of the CNT was determined to be 3.4 Å. Finally, XRD patterns for NC-NiO@CNT₅₀ (purple line) are shown in **Figure 6.1e**. The same characteristic peaks for NiO (at 37°, 44°, 63°, 75°, and 80°) and carbon (at 26° and 44°) were observed in NC-NiO@CNT₅₀ that were observed for NiO/C and ID-NiO/CNT. Application of the Scherrer equation yielded a calculated average crystallite domain size for NC-NiO@CNT₅₀ of 15.9 nm, similar to ID-NiO/CNT (16.6 nm).

After synthesis, the electrochemical response of NC-NiO@CNT₅₀ was investigated and its normalized capacity retention (Q/Q_o) over 100 cycles is shown in **Figure 6.1f**, alongside the data for NiO/C and ID-NiO/CNT for comparison. Unlike NiO/C and ID-NiO/CNT, the NC-NiO@CNT₅₀ retained essentially all its capacity over the first 100 cycles. Also positive, NC-NiO@CNT₅₀ had a much lower irreversible capacity loss than the other two NiO materials, only 12.2%. Because of this excellent initial performance,

the NC-NiO@CNT₅₀ could cycle for an additional 300 cycles. Over the 400 total deep charge/discharge cycles at 1C, the NC-NiO@CNT₅₀ retained 96.3% of its capacity with very little scatter over three repeated cells. In addition, the average coulombic efficiency of NC-NiO@CNT₅₀ was 99.2%.

Figure 6.3d shows post-cycle TEM images of NC-NiO@CNT₅₀, which shows that minimal structural changes occurred during charge/discharge, in stark contrast to NiO/C and ID-NiO/CNT (**Figure 6.2**). The NiO particle size distribution of confined MOs was very similar pre- and post-cycling. Also, there was no evidence of either particle detachment or migration that led to the formation of large M/MO agglomerates. Furthermore, the SEI appeared to remain confined within the interior of the CNT, which can effectively limit SEI growth during long-term cycling. Finally, XPS analysis showed that confinement also inhibited the transition of the nickel to higher oxidation states.

Figure 6.3e shows a similar pre-cycled high-resolution Ni2p XPS spectrum for NC-NiO@CNT to that of NiO/C and ID-NiO/CNT. Post-cycling (100 cycles), NC-NiO@CNT only showed the presence of NiF₂ (from SEI formation) and NiO, which suggests that after repeated charge/discharge cycles, Ni²⁺ → Ni²⁺ retention was achieved and that no measurable transformation to Ni³⁺ was observed (**Figure 6.3g**). Therefore, the possible reaction pathways for a constrained material appear to be limited to the reversible electrochemical reaction pathways – which should allow for long term operation. To better understand the electrochemical behavior of the NC-NiO@CNT₅₀, **Figure 6.4a** and **Figure 6.4b** shows charge/discharge and differential capacity analysis (dQ dV⁻¹) curves, respectively, during the 1st, 100th, 200th, 300th, and 400th cycle.

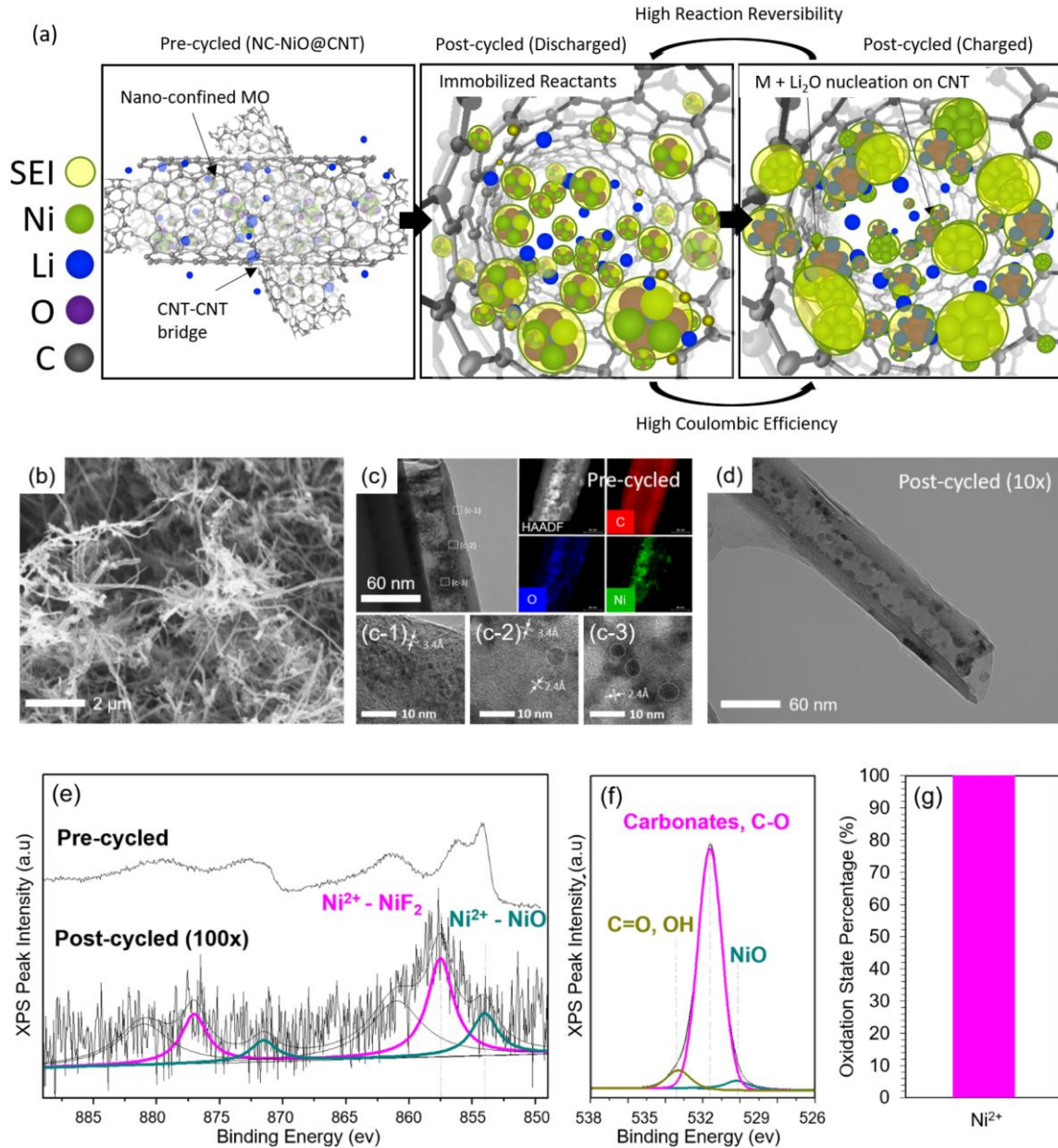


Figure 6.3. | Material Nanoconfinement. (a) Illustration of metal oxides spatial rearrangement during charge/discharge in the case of nanoconfinement, (b) SEM images of nano-confined NiO in NC-NiO@CNT₅₀, (c) TEM images and EDS mapping of NC-NiO@CNT₅₀, (c-1) interlayer spacing of CNT, (c-2) interface between MO-CNT, (c-3) lattice fringes of NiO, (d) TEM image of NiO@CNT₅₀ after 10 electrochemical cycles. XPS spectra of NC-NiO@CNT₅₀ including (e) Ni₂P, (f) O 1s, as well as (g) the percentage of active materials remaining in the 2+ oxidation state after cycling. Reproduced with permission from The Royal Society of Chemistry.³⁷

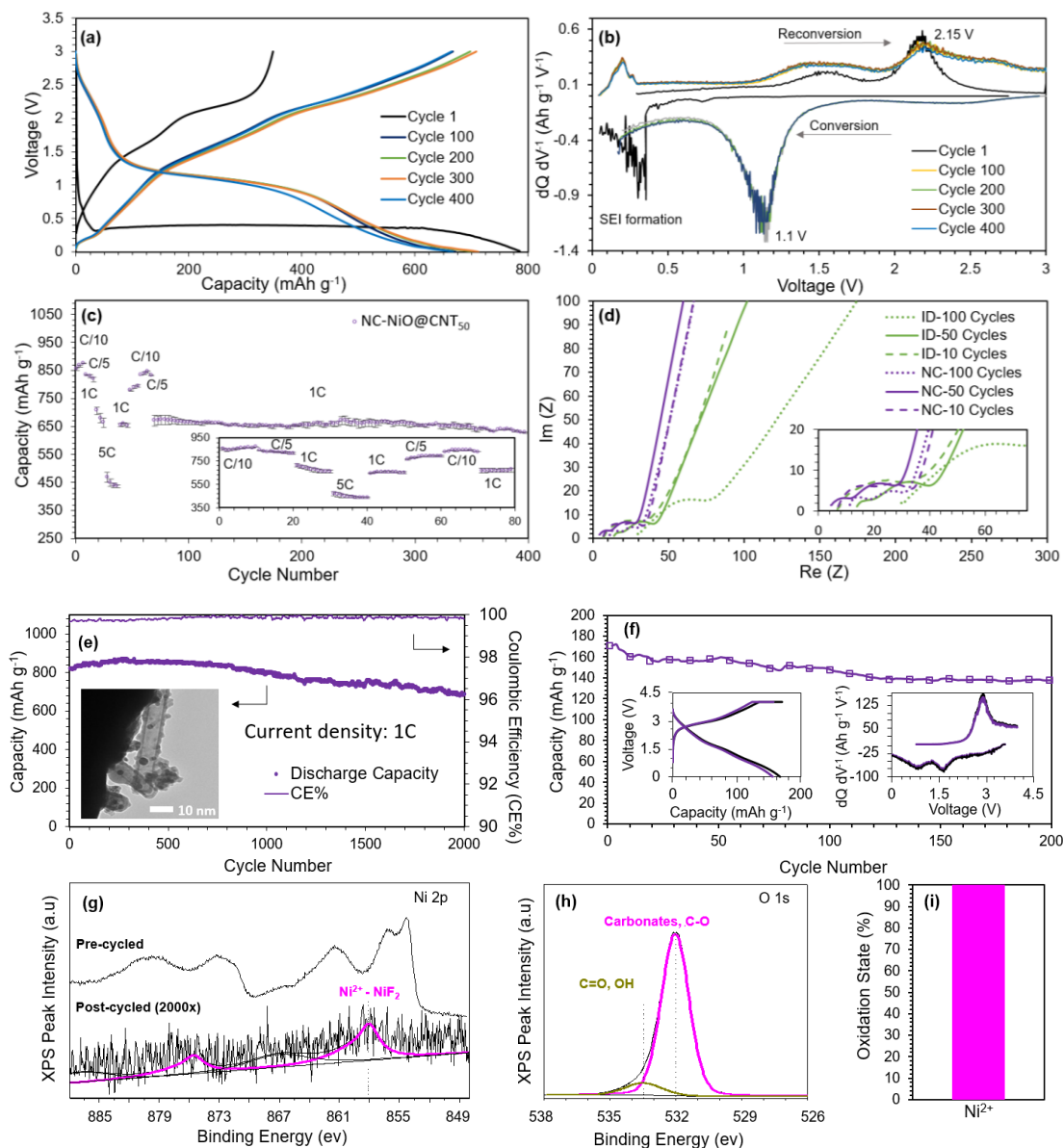


Figure 6.4. | Electrochemical performance. (a) The charge-discharge curves and (b) differential capacity analysis ($dQdV^{-1}$) of NC-NiO@CNT₅₀. (c) Rate capability evaluation for charge reversibility and rate-specific side reactions at different current densities for NC-NiO@CNT₅₀. (d) EIS spectra after 10, 50, and 100 charge/discharge cycles for ID-NiO/CNT and NC-NiO@CNT₅₀, showing the evolution of chemical and physical processes (e.g. diffusion, charge transfer, electrolyte conductivity, SEI resistance) during cycling. (e) Capacity retention over 2000 cycles for NC-NiO@CNT₁₀ at 1C (718 mAh g⁻¹). (f) Capacity retention, charge-discharge curves, and differential capacity analysis for high loading full cells made from NC-NiO@CNT₁₀ anodes and Li(Ni_{0.5}Mn_{0.3}Co_{0.2})O₂ cathodes (anode loading: 5.16 mg cm⁻²; cathode loading: 18.23 mg cm⁻²) full cell. XPS spectra for NC-NiO@CNT₁₀ before and after cycling including (g) Ni2p, (h) O1s, and (i) the percentage of NiO remaining in the 2+ oxidation post-cycling. Reproduced with permission from The Royal Society of Chemistry.³⁷

The conversion reaction and the SEI formation is shown in the 1st cycle at a mixed potential of 0.350V. The subsequent reduction plateau occurs at 1.15V and the oxidation plateau at 2.15V. Cycles 100, 200, 300, and 400 show minimal deviations in both the charge and discharge voltage plateaus/peaks, which indicates excellent reaction reversibility and active material utilization over time. Subsequent cycles result in a decoupled reduction plateau that is characteristic of the conversion reaction. It is noted that the CNT is a non-dilutive conductive carbon additive that also allows for some Li⁺ ion intercalation, which may contribute a little to the total capacity. During the oxidation, a Li de-intercalation peak was observed at 0.2 V and a metallic Ni reversion back to NiO at 1.5V and 2.15 V.

Electrodes made of well-embedded MOs in conductive carbon matrices will exhibit less contact resistance at the MO/Carbon interface. Therefore, it might also be possible that these confined, nano-sized MOs will exhibit enhanced reaction kinetics and rapid diffusion of Li ions compared to other structures. This was explored through experiments at several charge/discharge rates. **Figure 6.4c** shows the rate capability of NC-NiO@CNT₅₀ and shows a capacity of 460 mAh g⁻¹ at 5C. Even after alternating among various C-rates, the cell capacity retention after 400 cycles was at 627 mAh g⁻¹ at 1C, which was 94% of the original capacity.

EIS measurements (**Figure 6.4d**) can be used to explain the evolution of the physical and chemical processes because each of the characteristic phenomena (diffusion, reaction, etc.) have their time constants and relaxation times, which hence can be probed at different frequencies. It was observed that unlike ID-NiO/CNT, where the evolution of the R_{ohmic} increased over 100 cycles, the nano-confined NC-NiO@CNT₅₀ showed a

negligible increase in charge transport impedance. NC-NiO@CNT₅₀ also had a lower charge transfer resistance than ID-NiO/CNT and the charge transfer resistance was unaffected by cycling.

The combination of cycling performance, pre-/post-cycled TEM/XPS, and EIS analysis suggest that the degree of confinement and isolation from the bulk electrolyte might play a pivotal role in concomitantly increasing the MO reaction reversibility and minimizing the side reactions responsible for the change in Ni oxidation state and long-term SEI growth. Therefore, a version of the NC-NiO/CNT_x anode was synthesized with the specific goal of providing even less void space (i.e. less volume for excess electrolyte exposure) and more rapid Li⁺ diffusion. This was accomplished by using CNTs with a small diameter, 10 nm versus 50 nm. The total active loading of NiO was determined to be 89.9% through thermogravimetric analysis (TGA).

Figure 6.4e shows the capacity retention of NC-NiO@CNT₁₀ over 2000 charge/discharge cycles at 1C. It was found that this material was highly reversible, showing an achievable capacity 686 mAh g⁻¹ after 2000 cycles (initial capacity = 824 mAh g⁻¹, retention = 83.3%). Also, a coulombic efficiency greater than 99.9% was measured (to be more quantitative would require High Precision Coulometry measurements, which is beyond the scope of this study). Additionally, **Figure 6.4** (f-h) shows the pre- and post-cycle XPS spectra after 2000 cycles for the highly-constrained NC-NiO@CNT₁₀. In short, it was found that all of the nickel after 2000 cycles was in the 2+ oxidation state, suggesting that the confined MO in NC-NiO@CNT₅₀ is highly stable and highly reversible.

6.3 SUMMARY

The main descriptor for whether high capacity and capacity retention was achieved was whether or not the MO was exposed to (NiO/C and ID-NiO/CNT) or isolated from (NC-NiO@CNT_x) the electrolyte. As summarized in **Figure 6.5**, MOs undergo four types of physical processes that influence their behavior in operating LIBs: uncontrolled growth of the SEI, a transition to higher oxidation states, metal agglomeration, and metal trapping. These processes directly impact the coulombic efficiency, capacity retention, and onset of degradation. Randomly dispersed MOs on conductive carbon (whether its carbon black or advanced carbon) are susceptible to continuous uncontrolled growth of the SEI, and this phenomenon is primarily found to be caused by the repetitive expansion/contraction of MOs during phase separation/recombination that exposes the highly reactive surfaces of the MO nanoparticles. Without a proper barrier, the SEI grows onto the highly exposed surface and uncontrollably dislodges particles from the conductive medium in the electrode. These electronically isolated particles become electrochemically deactivated, and with the loss of active material, results in capacity fade. Also, the destabilized oxygen balance and local overpotentials due to elevated internal resistance drive the evolution to higher oxidation states. The reactions that guide the transformation of the MO to higher oxidation states do not consume Li, but they do consume oxygen in the system and change the number of electrons transferred per metal atom. This results in lower coulombic efficiencies but does not result in capacity loss.

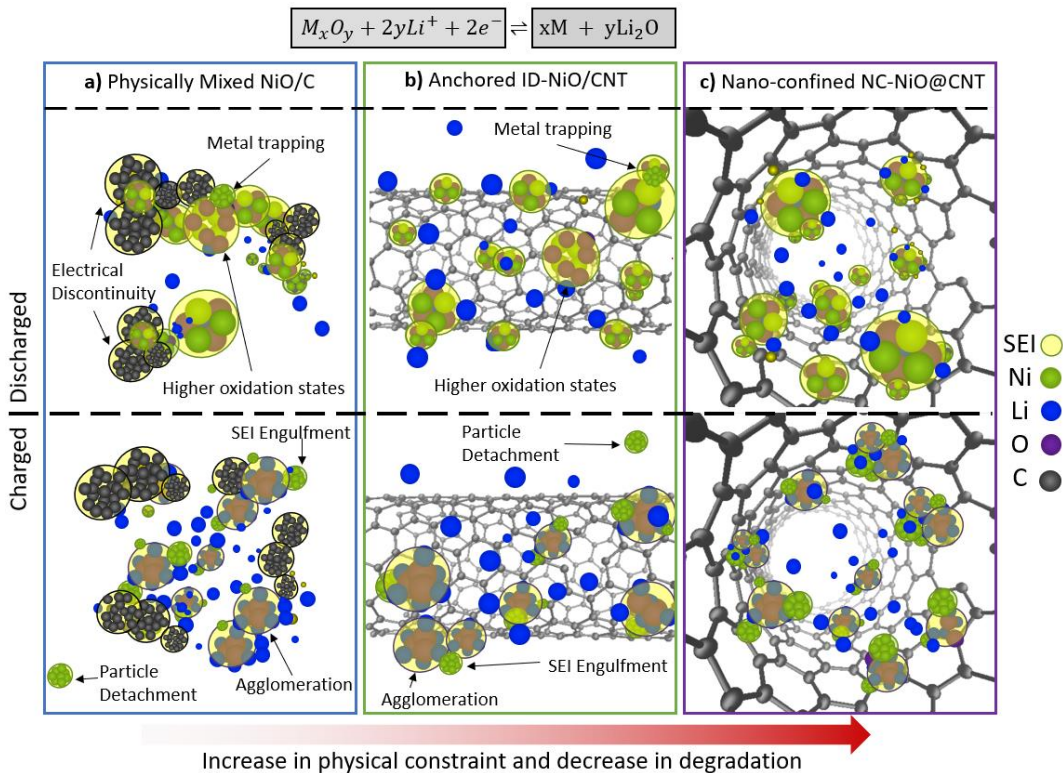


Figure 6.5. | Phase Separation and Degradation Pathway. Identifying the degradation pathways in conversion MOs (e.g. M/MO agglomeration, metal trapping, electrical detachment, SEI engulfment of MO, particle delamination) caused by fluctuations in the local e^- , Li^+ , oxygen, and metal balance during phase separation for (a) physically mixed NiO/C, (b) anchored ID-NiO/CNT, and (c) nano-confined NC-NiO@CNT. Reproduced with permission from The Royal Society of Chemistry.³⁷

The SEI reactions and the reactions associated with coulombic efficiency loss in operating cells are summarized in **Table 6.1**. The MO particles were always contained inside the CNT-matrix, which enabled it to obtain a very high reaction reversibility. In other words, the Ni atoms in the fully discharged state remained in the 2+ oxidation state. NiO was extremely stable over a large number of cycles with high coulombic efficiency. Therefore, it appears that constraint-based synthesis routes minimize the degradation pathways associated with MOs and such nano-confinement represents a very promising strategy to increase the adoption and practicality of MO-based anodes for Li-ion batteries.

Table 6.1. | Evaluation of Oxidation States. The overall reaction pathways associated with various degrees of constraints of confinement of metal oxides.

Case Study	Pre-Cycled	Post-Cycle	Possible Reaction Pathway	Results
Control (NiO/C) 100 cycles	100% Ni ²⁺	48% Ni ²⁺ 52% Ni ³⁺	2LiF + Ni \rightleftharpoons NiF ₂ + 2Li ⁺ + 2e ⁻ (SEI) 2NiO + 2RCH ₂ OCOOLi \rightleftharpoons Ni ₂ O ₃ + Li ₂ O + RCH ₂ COCOCH ₂ R (HOS)	Resulted in the formation of higher oxidation states (HOS) 3+ oxidation state
Indiscriminately Deposited (ID-NiO/CNT) 100 cycles	100% Ni ²⁺	63% Ni ²⁺ 37% Ni ³⁺	2LiF + Ni \rightleftharpoons NiF ₂ + 2Li ⁺ + 2e ⁻ (SEI) 2NiO + 2RCH ₂ OCOOLi \rightleftharpoons Ni ₂ O ₃ + Li ₂ O + RCH ₂ COCOCH ₂ R (HOS) Li _x C _y O _z + Ni \rightleftharpoons NiC _y O _z + xLi ⁺ + xe ⁻ (SEI)	Similar results to control the Formation of higher oxidation states (HOS) and NiC_yO_z species
Nanoconfined (NC-NiO@CNT _x) 2000 cycles	100% Ni ²⁺	100% Ni ²⁺	2LiF + Ni \rightleftharpoons NiF ₂ + 2Li ⁺ + 2e ⁻ (SEI)	NiO transformed to NiF₂ and remained in the 2+ oxidation state

CHAPTER 7: CONCLUSIONS

Li-based batteries play a pivotal role in enabling of all the luxuries of our electrified society and are here to stay. This thesis fostered a better understanding of the complex thermodynamics, kinetics, and transport properties of current-generation graphite/NMC532 cells. A non-destructive parameter extraction via a pulse-relaxation GITT method was used to map the exchange current (i_0S), diffusion time constant (τ), internal resistance (R_{IR}), and the entropic heat coefficient ($dUdT^{-1}$) as a function of temperature (-30°C to 45°C) and SOC (0% to 100%). The extracted parameters were later used in a reduced order lumped electrochemical-thermal model (TLM) to capture the voltage and temperature profiles, which is consistent with the experimental validation in Ng et al⁷⁸. The TLM model deviates at high current densities ($>1C$) from cell-level SOCs $< 5\%$; however, LIB packs typically operate within the voltage plateau (SOC = 10% to 100%) and BMS discharge cutoffs occur at a specified $dV dt^{-1}$ to ensure pack longevity. The state space transformation of the PDEs used in this lumped model was able to decrease the computational time for 1 charge/discharge cycle by 50% (~2s to less than 1s). The state space approach (PDE to ODE transformation) is an effective method to greatly enhance the calculation time for BMS applications, and the non-destructive GITT measurement for four cell-level parameters (i_0S , τ , R_{IR} , $dUdT^{-1}$) and is directly relatable to mathematical quantities in the reduced order TLM. In a world that requires faster calculations and reduced computational time, a novel method to extract parameters non-destructively can

be implemented as initial guesses to increase the convergence time and approach higher-fidelity voltage and temperature predictions.

The next section of this thesis focused on studying the effects of the extreme operating conditions that are expected to be experienced in multiple applications (e.g. satellites, UUV, electric aircraft, cold-climate EVs, etc.) on LIBs. Low-temperature cycling at low rates were found to catastrophically compromise the cell, and the electrode (NMC532/Li_xC₆) morphology, by a combination of Li⁰ deposition and severe gassing. The morphology of Li⁰ deposits was found to vary spatially on an electrode, where mushroom-shaped and/or mossy-like Li⁰ grows near electrode edges but near-uniform Li⁰ deposition occurs towards the electrode center. The anisotropy in the Li⁰ growth mechanism indicates severe (voltage, current, concentration) gradients within the electrode from tab-to-center, flat-to-curved, and initial-to-final layers. First, Li⁰ deposition exacerbates the formation of gases, which was found to result in a chemical reaction that causes particles to fuse together and form numerous gas pockets that drastically alter the porosity and volume of the electrode. Gas formation was also found to occur preferentially near the anode edge. Furthermore, severe volumetric expansion/contraction during LT cycling causes high warping of the curved regions of each jellyroll and can cause electrode buckling fractures and complete breakage of the electrode. Therefore, next-generation battery electrode design should incorporate reinforced anodes and/or cathodes that mechanically strengthen regions where high-stress is expected. Most notably, this study showed that there exists two catastrophic failure pathways for large format LIBs under low-temperature cycling: 1) non-thermal runaway from pressurized venting and 2) thermal runaway.

The last portion of this thesis dealt with NiO as a possible safe, high energy density anode material. The next-generation of Li-based batteries must balance the safety, energy density, and durability trilemma that plagues material development. It is well known and further elucidated in this thesis that the pursuit of high energy density materials (e.g. Si, Li, conversion metals) usually leads to poor cyclability or compromised safety. Conversion-based materials, such as MOs, can be a promising alternative to commercialized intercalation chemistries. Although conversion-based metal oxides have high gravimetric capacities, it was shown that a complex series of degradation mechanisms can be active, even over a very limited number of cycles. MO-based anode materials undergo four primary degradation pathways that limit their achievable capacity, coulombic efficiency, and long-term stability. When the MO particles are fully exposed to the electrolyte in networks with insufficient electronic conductivity, all the degradation pathways are active, and the MO anode can undergo rapid material degradation.

SEI formation on NiO was found to be broken down into four Regions. At the beginning of SEI formation on NiO, the results were very consistent to those observed during early-stage SEI formation on carbon, suggesting that SEI formation begins very similarly from a mechanistic perspective. After the early stages of SEI formation, the behavior is dominated by the conversion reaction itself with little contribution to the SEI formation. The conversion reaction did result in some volumetric expansion and some particle detachment from the surface, with some of the detached particles being embedded in the SEI. In the final stages, a densified SEI layer is formed, just like on carbon-based materials, but the mechanism for its formation is different. On carbon-based materials, the formation of the dense SEI is limited by the electrochemical activation of low concentration

EC-intermediates on the surface. For NiO, the nature of the RDS to form the dense SEI is consistent with Li^+ abstraction from the SEI. In the future, these new insights can help battery manufacturers to engineer appropriate environments and pre-treatment protocols to build robust SEI layers on this family of materials, enabling long-life, stable, high-capacity Li-ion batteries.

It is additionally shown that nano-confinement of MO nanoparticles can significantly reduce the rate of some degradation mechanisms and eliminate others – extending the achievable lifetime of LIBs with MO anodes significantly. In fact, the top-performing material in this study, NC-NiO@CNT₁₀, was able to cycle for more than 2000 deep charge/discharge cycles at 1C while retaining > 80% of its initial capacity (824 mAh g⁻¹) with a coulombic efficiency > 99.9%. Nanoconfined NiO was also able to support a very high capacity of 460 mAh g⁻¹ at 5C, a rate that is very relevant for fast-charging and high-power applications. Also, high loading full metal oxide Li-ion cells (prelithiated NC-NiO@CNT₁₀/LiNi_{0.5}Mn_{0.3}Co_{0.2}O₂) were assembled and tested. The MO/LMO full cell confirmed the hypothesis that confinement inhibits anode degradation (increasing the coulombic efficiency) and the long-range conductive CNT networks helps electrons percolate through thick, high loading electrodes (boosting material utilization). Finally, the discovery that nanoconfinement can improve the reaction reversibility and longevity of conversion metal oxides can likely also be applied to other conversion-based chemistries as well (e.g. metal hydrides, nitrides, oxides, fluorides, phosphides, and sulfides). Therefore, the findings of this work help represent one promising pathway to find a safe, high capacity, fast-charge, and highly reversible anode that may one day enable LIBs for applications that require high-energy density and/or high-power density and long life. One reasonable

question that remains from this work is the practicality of using CNTs in commercial cells, which have historically been thought of as cost-prohibitive. There are some CNTs available today that have lower aspect ratios and/or increased defect density that are relatively inexpensive; these may be viable options, though the ramifications of their use need to be further investigated. Also, it may be possible to implement lower-cost solutions for nanoparticle confinement that are yet to be discovered.

CHAPTER 8: RECOMMENDATION FOR FUTURE WORK

The future for battery technology is bright, filled with opportunity, and ever-changing. As a result, there are still many questions left unknown. Four main recommendations are presented here. First, new batteries are being rolled out since there is a paradigm shift towards higher energy density batteries that are extremely durable. Batteries like the million-mile battery chemistry²¹³ ($\text{Li}(\text{Ni}_{0.5}\text{Mn}_{0.3}\text{Co}_{0.2})\text{O}_2/\text{Li}_x\text{C}_6$) or secondary Li/FeS_2 are of high interest²¹⁴ and the parameterization of these next-generation Li-ion batteries can be highly beneficial from an optimization and safety standpoint. The next recommendation takes a bigger leap beyond Li-ion batteries. In particular, Li/S batteries have very attractive properties including very high energy densities and low cost, but are limited by how long these systems last (i.e. poor cycle life). A detailed study on the fundamental parameters (thermodynamics, kinetics, and transport) of Li/S batteries can help battery researchers isolate and develop strategies to circumvent the degradative processes inherent to sulfur and Li^0 metal. The third recommendation is built on the second and explores various ion-exchange trapping agents as a method to stop the polysulfide shuttle problem. Finally, *operando* optical/spectroscopic studies are proposed as a viable method to study the corrosion of Li^0 metal and the polysulfide shuttle problem. The inclusion of Li_2S on the anode is known to drastically alter the SEI film and change the deposition/stripping process but how does the reaction mechanism change is left unknown.

8.1 PARAMETERIZATION OF NEXT-GENERATION LI-ION BATTERIES

Li-ion batteries or Li-related batteries are the most promising energy storage devices for the adoption of new technologies. Also, EVs are still in their infancy and still require years before full maturation. The adoption of the million-mile battery chemistry²¹³ ($\text{Li}(\text{Ni}_{0.5}\text{Mn}_{0.3}\text{Co}_{0.2})\text{O}_2/\text{Li}_x\text{C}_6$) in later-generation EVs will require full parameterization of that system to aid in the predictive analytics and wide-scale distribution of the technology. The principles in this thesis can be used for that specific cell chemistry and design. The extracted parameters can in-turn be used in the standard P2D, SPM, or Lumped model. Model-driven design provides invaluable information in R&D and helps researchers develop a fundamental framework to optimize the system of interest. In the case of batteries, near-theoretical limits to energy density, cyclability, and total performance of the system can be targeted (i.e. as an objective) to tease out optimal operating conditions, geometry, chemistry, etc. Also, degradative processes, and loss mechanisms (e.g. electrical conduction, lithium diffusion, electrolyte diffusion, and charge transfer kinetics) can be deconvoluted into fundamental principles that limit the battery. In combination with the macroscale models (P2D, SPM, lumped), mesoscale models that apply similar physics-based principles to real cross-sectional images of battery electrodes can prove to be invaluable in engineering design. A similar method is currently being used for secondary Li/FeS₂ batteries in nonaqueous or polymer electrolytes (e.g. LiTFSI in DOL/DME or ionic liquids) that have high energy density (>300 Wh/kg) and cyclability. Unlike LiCoO₂ or graphite (standard electrodes for Li-ion batteries), whose reactions are based on highly reversible intercalation/deintercalation, FeS₂ leverages a two-stage reaction mechanism that intercalates/deintercalates ($0 < x < 2$ for Li_xFeS_2) and then bond-breaks (conversion

reaction) in the presence of Li^+ ions to form Fe^0 -metal and Li_2S ($x > 2$). A two-stage physics-based reaction mechanism (**Figure 8.1**) was implemented in COMSOL Multiphysics® via an interfacial reaction of $\text{Li}^+|\text{FeS}_2$ coupled to solid-state diffusion (intercalation reaction) and a shrinking core phase separation reaction mechanism of $\text{LiFeS}_2 | \text{Fe}^0 + \text{Li}_2\text{S}$ (conversion reaction). Below contains the design equations and simulation domain for the 3D mesoscale model.

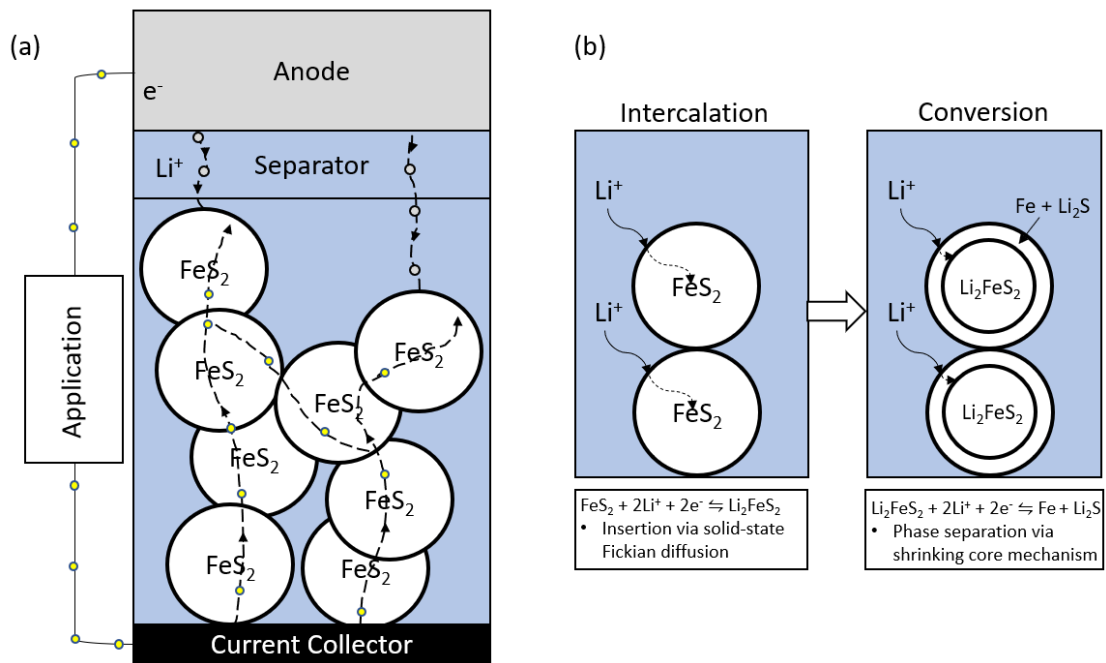


Figure 8.1. | Illustration of the simulation domain and geometry

Ion transport in the electrolyte of an electrochemical system (i.e. a battery) is coupled with electron conduction in the electrode domain. The electron conduction within the FeS_2 cathode particles can be modeled using charge conservation of Ohm's law, and expressed as,

$$\nabla \cdot i_s = \nabla \cdot (-\sigma_s \nabla \phi_s) = 0 \quad \text{Equation 8.1}$$

where σ_s denotes the electrical conductivity and ϕ_s represents the solid phase potential of the particle. The material balance of species within the cathode and separator is represented as,

$$\frac{\partial (C_i)_d}{\partial t} = -\nabla \cdot J_i + R_i \quad \text{Equation 8.2}$$

where C_i is the concentration of species i ($i = \text{Li}^+$, TFSI) [mol m^{-3}] and the index d represents the individual domain (separator, cathode, electrolyte). The intercalation of Li^+ into the FeS_2 particle is described by Fick's second law of diffusion and represented as,

$$J_{Li} = -D_{Li} \nabla c_{Li} \quad \text{Equation 8.3}$$

where D_i is the solid-phase diffusion coefficient for lithium and c_{Li} is the concentration of lithium in the intercalating particle. The conversion reaction of fully intercalated Li_2FeS_2 is converted to Fe^0 and Li_2S via a level-set field function that moves an interface between the shell ($\text{Fe}^0/\text{Li}_2\text{S}$, $\xi = 1$), the core phase (fully intercalated Li_2FeS_2 , $\xi = 0$), and represented as,

$$\frac{\partial \xi}{\partial t} + \mathbf{u} \cdot \nabla \xi = \gamma \nabla \cdot \left(\varepsilon \nabla \xi - \xi(1 - \xi) \frac{\nabla \xi}{|\nabla \xi|} \right) \quad \text{Equation 8.4}$$

where the ε parameter is proportional to the element size, γ is the reinitialization parameter that accounts for the conversion reaction rate. The interfacial velocity of $\text{Li}_2\text{FeS}_2 | \text{Fe} + \text{Li}_2\text{S}$ core-shell is calculated based on the expression below,

$$\mathbf{u} = n \cdot \left(-\frac{i_{\text{loc}} M_P}{nF \rho_P} \right) \quad \text{Equation 8.5}$$

where i_{loc} is the local current density, n is the number of electrons, M_P is the molar mass and ρ_P is the density of $\text{Fe}^0/\text{Li}_2\text{S}$, and the interface normal is defined as $\mathbf{n} = \frac{\nabla \xi}{|\nabla \xi|}$. The source

and consumption terms are implemented into the mass balance to simultaneously produce the Fe⁰/Li₂S and consume the Li₂FeS₂ phase.

The flux term J_i is expressed as the diffusion and migration term in the Nernst-Planck expression,

$$J_{i,m} = -D_{i,m} \nabla C_i - z_i \frac{D_{i,m}}{RT} F C_i \nabla \phi_l \quad \text{Equation 8.6}$$

where $D_{i,d}$ is the diffusion coefficient for the domain d and species i , z_i is the valence state, F is Faraday's constant (96,485 C mol⁻¹), R is the gas constant (8.314 J mol⁻¹K⁻¹), and ϕ_l is the liquid-phase potential. The reaction rate is modeled by the Butler-Volmer kinetic expression,

$$i = i_0 \left[\exp\left(\frac{\alpha_a F \eta}{RT}\right) - \exp\left(\frac{-\alpha_c F \eta}{RT}\right) \right] \quad \text{Equation 8.7}$$

where α_a/α_c is the anodic/cathodic transfer coefficient, η is the overpotential for the electrochemical reaction ($\eta_j = \phi_s - \phi_l - \phi_{eq}$), and i_0 is the exchange current density and represented as,

$$i_{0,i} = k_i c_{s,max,i} c_l^{0.5} \left(1 - \frac{c_{s,i}|_{r=R_{s,i}}}{c_{s,max,i}} \right)^{0.5} \left(\frac{c_{s,i}|_{r=R_{s,i}}}{c_{s,max,i}} \right)^{0.5} \quad \text{Equation 8.8}$$

where k_i is the reaction rate constant.

The temperature dependency of important kinetic and transport parameters was investigated for the intercalation/conversion hybrid chemistry model. Parameters such as diffusion coefficients, reaction rate constants, and electrical conductivity are temperature-dependent and their values as a function of temperature can be expressed via an Arrhenius formulation.

$$D_{s,j}(t) = D_{s,j,ref} \exp\left[\frac{E_{a,dj}}{R} \left(\frac{1}{T} - \frac{1}{T_{ref}}\right)\right] \quad \text{Equation 8.9}$$

$$k_j(t) = k_{j, \text{ref}} \exp \left[\frac{Ea_{r,j}}{R} \left(\frac{1}{T} - \frac{1}{T_{\text{ref}}} \right) \right] \quad \text{Equation 8.10}$$

$$\sigma_j(t) = \sigma_{j, \text{ref}} \exp \left[\frac{Ea_{d,j}}{R} \left(\frac{1}{T} - \frac{1}{T_{\text{ref}}} \right) \right] \quad \text{Equation 8.11}$$

where T_{ref} represents the reference temperature, $D_{s,j, \text{ref}}$ is the solid-state diffusion coefficient at reference state, k_j is the reaction rate constant of reaction j (intercalation or conversion), σ_j is the electrical conductivity, and $Ea_{d,j}$ is the activation energy of the parameter.

Figure 8.2a shows the open circuit potential (OCP) curves (blue dots) and charge/discharge profile (black dots) for a solid-state Li/FeS₂ battery that undergoes a four-electron transfer process. The first two electrons transferred from FeS₂ to form Li₂FeS₂ is an intercalation reaction (**Equation 8.14**) and the reaction of Li₂FeS₂ to Li₂S and Fe⁰ follows a conversion-type reaction (**Equation 8.15**). The simulation profile shows model fidelity to a multi-plateau and multi-reaction process. **Figure 8.2b** shows the particle reaction dynamics. At 100% SOC the interfacial reaction of Li and FeS₂ particles is facilitated by the solid-state diffusion of Li into the particle which generates the concentration gradient within the particle. Next, the Li₂FeS₂ undergoes a conversion reaction at the interface to form a shrinking core type reaction mode. The process in **Figure 8.2b** resembles the *in-operando* TEM experiments of FeS₂ by Yersack et al²¹⁵



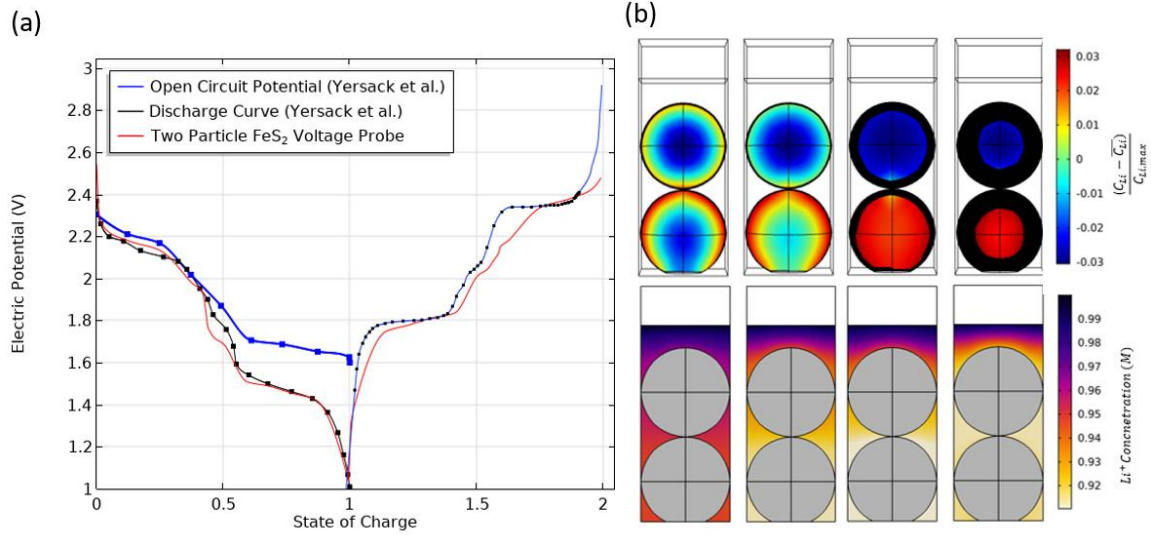


Figure 8.2. | Prototype model of a two-particle Intercalation/Conversion (2P-I/C) hybrid FeS₂ chemistry for secondary battery purposes, where (a) represents the model simulation for the discharge/charge reaction with multiple reaction plateaus, and (b) contains the particle-level reaction modes and electrolyte loss.

The remaining goals of this project is to convert the prototype model into the full-3D mesoscale model using the X-ray computed tomography of FeS₂ electrodes (XCT and 3D mesoscale simulation from the previous project²¹⁶ and represented in **Figure 8.3**). In short, the futures tasks required in converting the prototype 2-particle model into the full 3D XCT mesoscale model includes:

- 1) Full implementation of hybrid chemistry (intercalation/conversion) into the 3D XCT mesoscale model and capture snapshots of $\Delta C_{Li}/C_{Li,max}, Li^+(M), I/I_{app}, \Delta V (V), \sigma(S cm^{-1}), vonMisesStress(GPa)$
- 2) Calculate per-particle reaction rates which are classified based on whether it is the near binder or electrolyte surfaces for various depths of discharge
- 3) Re-simulate the hybrid chemistry charge/discharge curves using the 3D XCT mesoscale model

- 4) Determine the mechanical effects due to expansion/contraction of FeS_2
- 5) Isolate the loss mechanisms that are inherent to the FeS_2 electrode design (i.e. electrical conduction, lithium diffusion, electrolyte diffusion, and charge transfer resistance) and at different SOC.

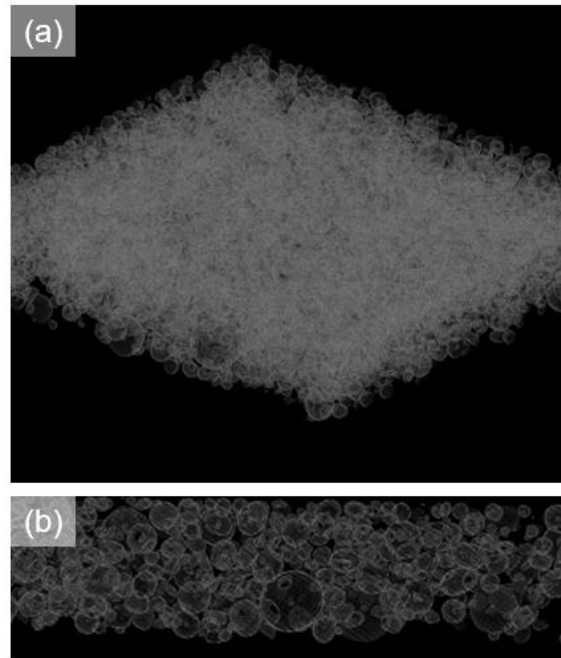


Figure 8.3. | Reconstruction of X-ray computed tomography (XCT) of NMC from Ebner et al.²¹⁷

8.2 LI-SULFUR BATTERIES

Lithium-sulfur (Li-S) batteries that operate based on a series of complex dissolution/precipitation reactions benefit from a high theoretical energy density (~600 Wh/kg – which is 4x greater than standard Li-ion batteries). Also, Li-S systems exhibit good performance under low-temperature operation and the materials are abundant, non-toxic, low cost, and highly sustainable – which makes the system a promising future alternative to the current Li-ion battery technologies. Several hurdles hinder wide-scale

adoption of Li-S batteries: 1) the complex dissolution and diffusion/migration of polysulfides from the cathode to the anode, which causes severe active material loss and impedance build up at the anode, and 2) the high-capacity results in large volumetric variations and morphological degradation, which leads to interfacial instability (S/carbon, S/binder, etc).

Li-S batteries are still under development but typically consist of a Li-metal anode paired with a sulfur/carbon (thermodynamically stable state cyclo-S₈ rings) composite cathode. The electrolyte consists of 1M LiTFSI in 1:1 volumetric ratio of 1,3-dioxolane (DOL) and 1,2-dimethoxyethane (DME). During discharge, the Li-metal oxidizes to release electrons and Li⁺ into the electrolyte. The Li⁺ migrate from the cathode to react with the sulfur. At the same time, sulfur undergoes a complex series of dissolution/precipitation reactions. Cyclo-S₈ rings solubilize during the reduction process to produce lithium polysulfide species as depicted in **Table 8.1**. Typically, higher-order chains are soluble (>S₄) whereas low orders polysulfide chains are not.

Table 8.1 | Reactions in Li/S batteries

Dissolution Reactions	Precipitation Reactions	
$Li \rightleftharpoons Li^+ + e^-$		Equation 8.14
$S_{8(s)} \rightleftharpoons S_{8(l)}$		Equation 8.15
$\frac{1}{2}S_{8(l)} + e^- \rightleftharpoons \frac{1}{2}S_8^{2-}$	$2Li^+ + S_8^{2-} \rightleftharpoons Li_2S_{8(s)}$	Equation 8.16
$\frac{3}{2}S_8^{2-} + e^- \rightleftharpoons 2S_6^{2-}$	$2Li^+ + S_6^{2-} \rightleftharpoons Li_2S_{6(s)}$	Equation 8.17
$S_6^{2-} + e^- \rightleftharpoons \frac{3}{2}S_4^{2-}$	$2Li^+ + S_4^{2-} \rightleftharpoons Li_2S_{4(s)}$	Equation 8.18
$\frac{1}{2}S_4^{2-} + e^- \rightleftharpoons S_2^{2-}$	$2Li^+ + S_2^{2-} \rightleftharpoons Li_2S_{2(s)}$	Equation 8.19
$\frac{1}{2}S_2^{2-} + e^- \rightleftharpoons S^{2-}$	$2Li^+ + S^{2-} \rightleftharpoons Li_2S$	Equation 8.20

Experiments should be designed and performed to obtain different parameters and provide validation data for the models. One of the most important sets of parameters is the design parameters (e.g. thickness of electrodes, particle size, etc.), diffusion coefficients, and exchange currents densities, which can be determined experimentally.

As with a typical coin cell assembly, a 1.76 cm² lithium reference/counter should be centered on the cathodic side of the case. A micropipette can be used to transfer 30 μL of 1M LiTFSI in 1:1 volumetric ratio of 1,3-dioxolane (DOL) and 1,2-dimethoxyethane (DME) onto the lithium reference/counter electrode. The separator should be cut to 1.96 cm² and placed on top of the lithium foil. Another 30 μL of 1M LiTFSI in DOL/DME can be deposited onto the separator. A gasket should be put on the outer casing to prevent short-circuiting. The working electrode (Sulfur-graphene oxide nanocomposite) should be placed facedown onto the electrolyte wetted separator. The spacer disk, wave washer, and cap should be placed on top and then crimped at 750 PSI with an MTI hydraulic press.

A current-pulse relaxation method via galvanostatic/potentiostatic intermittent titration technique (GITT/PITT) on an ARBIN battery cycler can be used to extract the diffusion coefficient (D_{Li+}) as a function of the state of charge (SOC) and operating temperature. The temperature of each cell can be controlled inside a Tenney climate-control chamber. A typical procedure can include 100 current pulses at C/10 for a designated time that satisfies $t \ll L^2/D$, followed by a relaxation period (i.e. no current) that lasts until electrochemical equilibrium. In accordance with Fickian diffusion, the diffusion coefficient can be extracted from the equation⁵⁰:

$$D = \frac{4}{\pi} \cdot \left(\frac{iV_M}{S \cdot F \cdot n} \right)^2 \cdot \left[\left(\frac{dE}{d\delta} \right) / \left(\frac{dE}{d\sqrt{t}} \right) \right]^2 \quad \text{Equation 8.21}$$

where V_M is the molar volume (cm^3/mol), i is the pulsing current (A), S is the electrochemically active surface area (cm^2), F is Faraday's constant (96485 C/mol), n represents the charge number, δ is the titration step, and t is the pulse time duration (s).

The steady-state potential response during the relaxation period of the GITT/PITT protocol can also reveal the open circuit potentials (OCP) of the electrodes. In addition to D_{Li^+} and the OCP, the exchange current density and the reaction rate constant can also be extracted at low overpotentials via the Taylor series expansion of the Butler-Volmer (BV) equation to the Linearized form of the BV equation,

$$i = i_o \frac{(\alpha_a + \alpha_c)F}{RT} \eta_s \quad \text{Equation 8.22}$$

where $(\alpha_a + \alpha_c)$ is the anodic and cathodic transfer coefficient, R is the ideal gas constant, T is temperature, and η_s is the overpotential. In addition to the diffusion coefficient and exchange current density, the reaction rate constant can also be measured at various states of charge following the equation below,

$$kS = \frac{e_0 S}{F c_s^{\text{max}} c_e^{0.5} (1 - \theta_{\text{surf}})^{0.5} \theta_{\text{surf}}^{0.5}} \quad \text{Equation 8.23}$$

in which c_s^{max} is the maximum Li solid-phase concentration (mol/m^3), c_e is the electrolyte concentration, θ_{surf} is $c_s(r=R)/c_s^{\text{max}}$. The electrochemical properties of different polysulfides are convoluted but are important parameters to develop a high-fidelity model. In order to extract the diffusion coefficient, exchange current density, and reaction rate constant, a binary solution at various concentrations should be procured. The samples should contain stoichiometric amounts of lithium, sulfur, and LiTFSI. The mixture should be rigorously stirred for 4 days via magnetic agitation and the procedure should create a

binary electrolyte containing LiTFSI and Li₂S_n (n = 6, 4) in DOL/DME. The fundamental diffusion coefficient can be realized by the equation below for ternary electrolytes,

$$D_{ij}^0 = \frac{F^2}{\kappa} \sum_{k=1}^3 \sum_{w=1}^3 \frac{z_k z_w}{g_{i-1,2} \theta_{j-1,a}} (l_{ij}^0 l_{kw}^0 - l_{in}^0 l_{kj}^0), i, j = 2, 3 \quad \text{Equation 8.24}$$

where $\kappa = F^2 \sum_{k=1}^3 \sum_{w=1}^3 z_k z_w l_{kw}^0$, l_{ij}^0 is the fundamental transport coefficients for irreversible processes, $g_{i-1,2}$ is the stoichiometries of the ions, and z is the charge number.

Additional electrode properties can be extracted from several methods including scanning electron microscopy (SEM), mercury intrusion porosimetry (MIP), and Brunauer Emmett Teller (BET). The particle size can be collected from a statistical distribution of multiple SEM images at different locations (sample size = 100) for the sulfur/graphene nanocomposite cathode. The microscopy can be performed on a field emission scanning electron microscope (Zeiss Ultraplus field emission SEM) that is equipped with energy-dispersive X-ray spectroscopy (Oxford Instruments). Pre-/post-mortem SEM analysis can be done at different cycles to provide a temporal view of the morphological changes in the particle and mesostructural changes of the electrode. Sulfur-based conversion reactions coupled with dissolution effects can drastically change over time.

In addition, porosity, pore size distributions, and pore volume measurements can be evaluated from mercury intrusion porosimetry (MIP). In a typical procedure, the mercury penetrometer is filled with electrode materials with passivated current collectors (prevent amalgamation effects) and sealed. The porosimeter utilizes a pressure vessel to incrementally step the pressure such that mercury can fill the pore spaces of the porous electrode. The Washburn Equation can be used to relate the incremental pressure to extract a pore size distribution. The surface area can be extracted from the nitrogen (N₂) adsorption

Brunauer Emmett Teller (BET) method. Applied principles of gas adsorption can be applied on pre-/post-cycled electrodes to determine the dynamics of surface area due to sulfur-conversion. In a typical procedure, the sample is immersed into a bath of liquid nitrogen followed by injection of nitrogen gas at a given partial pressure. The relationship between the amount of gas required to reach a designated partial pressure is related to the amount of monolayer adsorption of gases to the substrate. In other words, more surface area translates to more gas required to reach the designated partial pressure.

The electrochemical performance of a Li/S cell (formula: 50wt%-Sulfur, 40wt%-Carbon, 10wt%-PVDF) based on 1M LiTFSI in DOL/DME is presented in **Figure 8.4**. The high carbon content is designed to alleviate the low electronic conductivity ($5 \times 10^{-14} \text{ S m}^{-1}$) and provide additional surface area/void space for the precipitation of lithium polysulfides. Since conductive carbon hardly stores charge at this voltage window (1V – 3V), the majority of the charge/discharge capacity performance is attributed to sulfur itself and nears the theoretical capacity. However, the coulombic efficiency which reflects the amount of charge extracted vs. the amount of charge applied is relatively low (80% to 90%). The low coulombic efficiency indicates partial loss of active material during the charge/discharge process.

In general, Li-S batteries are widely touted as the next-generation Li-based chemistry. Researchers that can carve up a piece of this topic either in modeling (e.g. P2D, 3D-mesoscale, machine learning) or in advanced material design for ultra-stable performance (i.e. capacity retention, coulombic efficiency, energy density) can reap the benefit for years to come.

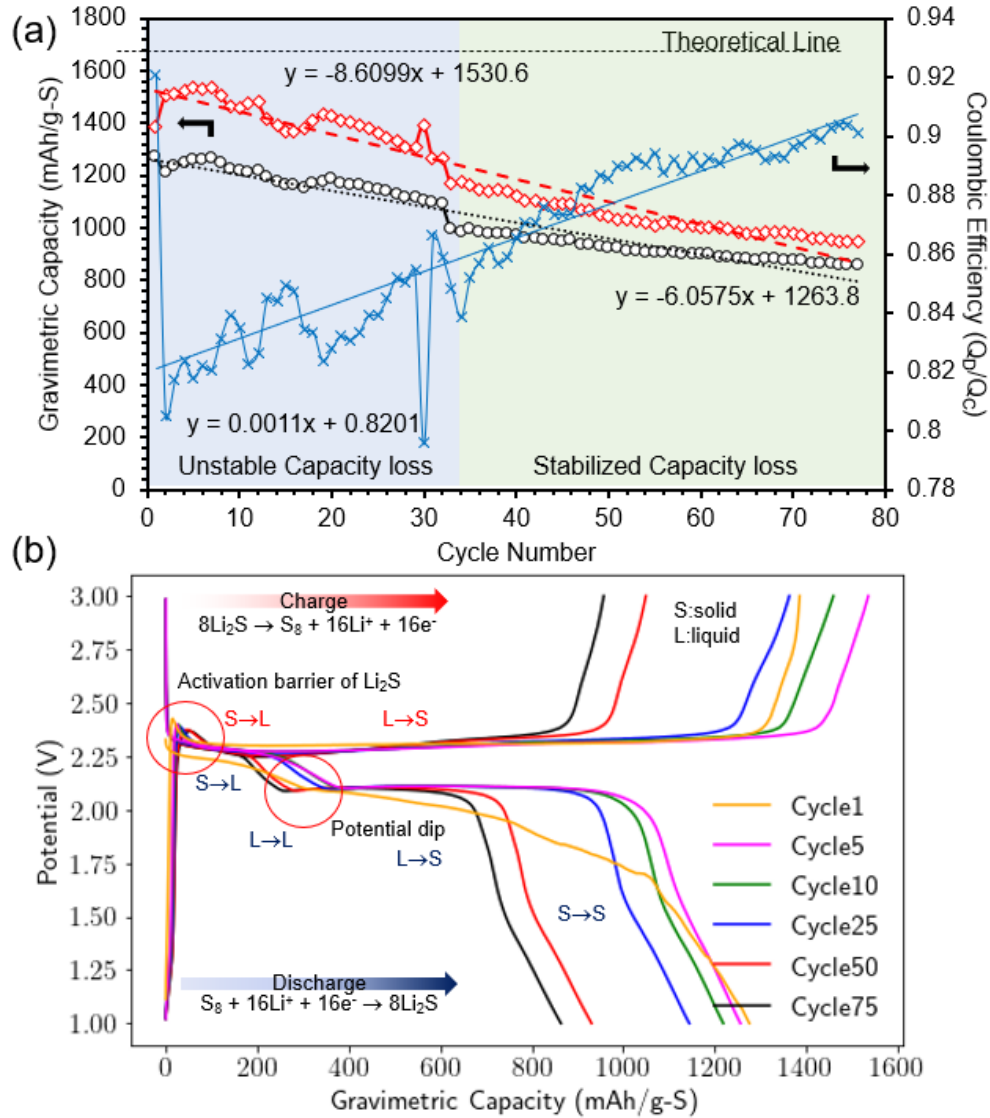


Figure 8.4. | Next-generation conversion electrodes based on energy-dense Li-Sulfur technologies where (a) is the cycle performance plot, and (b) shows the charge-discharge profile

8.3 IMPLEMENTING AN ION-EXCHANGE TRAPPING AGENT TO STOP THE POLYSULFIDE DEGRADATION PROCESS

As discussed above, several challenges hinder the practical deployment of Li-S based batteries.²¹⁸ Below are the main detrimental factors of ‘sulfur cathodes’:

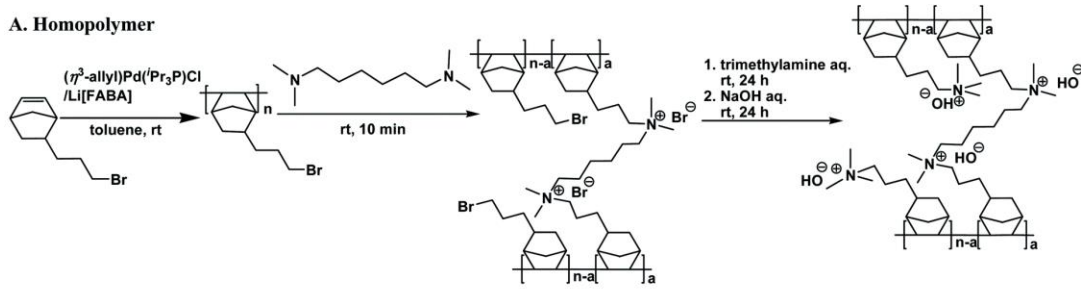
- (1) Polysulfide shuttle effect – The higher-order lithium polysulfide species readily dissolve into the electrolyte, resulting in a continual active material loss to the electrolyte. During this process, the solubilized polysulfides can transport from the cathode through the electrolyte to the anode and then partially undergo a return trip. During the transport process, the solubilized polysulfides that interact with the Li anode can become reduced to shorter chain Li_2S_2 or Li_2S . The precipitation of Li_2S_2 or Li_2S on the anode is trapped and results in severe active material loss. On a cell-level, the polysulfide shuttle effect results in poor coulombic efficiency and rapid performance loss.
- (2) Poor utilization of Sulfur – The low electronic conductivity of cyclo- S_8 ($\sim 5 \times 10^{-14} \text{ S m}^{-1}$) results in poor utilization of the active material. This effect is exacerbated during the precipitation event of Li_2S_4 to Li_2S_2 and Li_2S as well. The deposition increases the impedance and results in poor reaction kinetics, high polarization, poor sulfur utilization, and low-rate performance.
- (3) Catastrophic change in the cathode structure – The repetitive dissolution/precipitation event during discharge/charge results in severe mesostructural changes. First, the density of cyclo- S_8 vs. the end-form Li_2S is very different ($2.03 \text{ vs. } 1.66 \text{ g cm}^{-3}$),²¹⁸ resulting in hydrostatic stress from the volumetric expansion/contraction. The precipitation event is not well-controlled in these systems and results in a very transient and unstable cathode structure.

One method to circumvent the degradative processes of sulfur is to control the effects of the polysulfide shuttle. Pham et al.²¹⁹ utilized a cationic polymer, poly[2,2' -

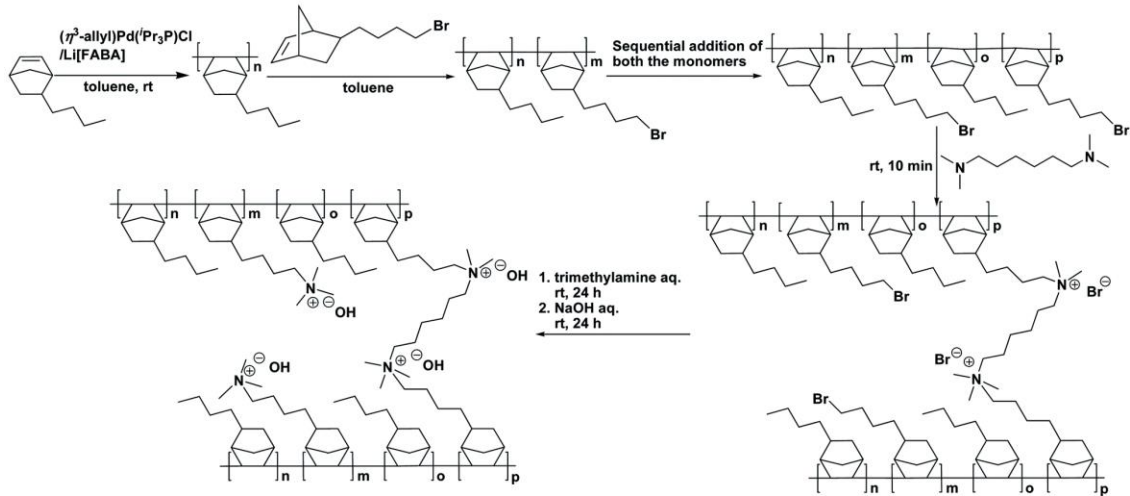
(2,2'',4,4''',6,6''-hexamethyl-p-terphenyl-3,3''-diyl)-5,5' -bibenzimidazolium iodide] (HMT-PMBI(I)), to preferentially increase the residence of polysulfides at the cathode. The HMT-PMBI(I) serves as a binder and the active benzimidazolium cation couples with polysulfides, which prevents polysulfides from escaping the cathode. The HMT-PMBI(I) binder enabled >440 cycles at a loading of 3-4 mg cm⁻² with an electrolyte/sulfur (E/S) ratio of 6 $\mu\text{L mg}_s^{-1}$.

A similar principle can be applied with ionomers based on highly tunable poly(norbornene) tetrablock copolymers in the form of homopolymers, block copolymers, or random copolymers with high ion-exchange capacities (**Figure 8.5**). Various cross-linking of the polymer can be tested to explore the effects of the electrolyte uptake vs mechanical properties, effects on polysulfide shuttle, and impacts on reaction kinetics. The poly(norbornene) polymer at various cross-linkings was tested as a potential candidate for regulating the polysulfide shuttle effect. The sulfur electrode formula was based on 50wt%-Sulfur, 38wt%-Carbon, 2wt% active ionomer, and 10wt%-PVDF. At small quantities of ionomer, the gravimetric capacity of sulfur is relatively low (~700-900 mAh g⁻¹), but shows characteristics of typical sulfur charge-discharge profiles. By comparison, the S₈ → Li₂S₈ reactions for both GT-32 and GT-72 are well-defined but GT-72 displays a narrower gap between subsequent cycles, whereas GT-32 has a sparser distribution for the first plateau (i.e. potential direction). The transition from Li₂S₈ to Li₂S₆ shows negligible change but GT-72 does spread more in the gravimetric capacity direction. The conversion from Li₂S₄ to Li₂S₂ primary region is captured in **Figure 8.6(a,b)** by an extended reaction plateau at ~2.15V.

A. Homopolymer



B. Block copolymer



C. Random copolymer

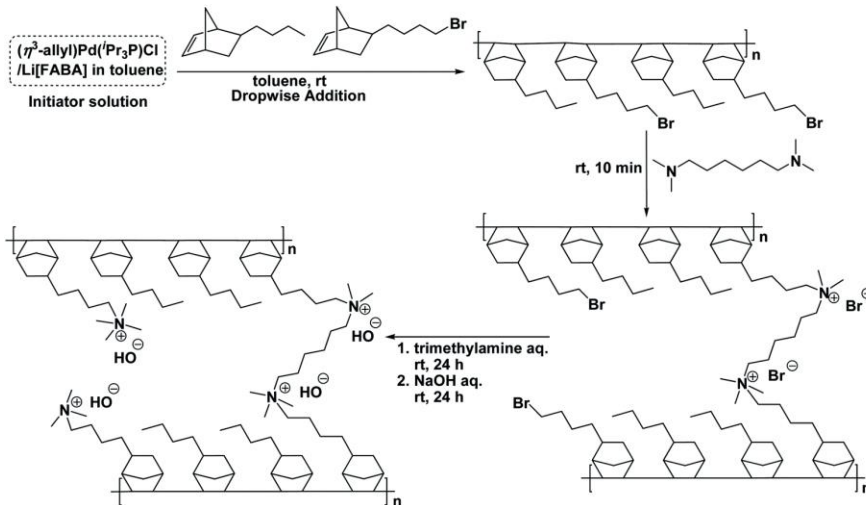


Figure 8.5. | Homopolymer based on (a) block, (b) random, (c) casting membranes. Reproduced with permission from The Royal Society of Chemistry.²²⁰

The typical profile for (Li_2S_2 to Li_2S) is realized towards the end of discharge. The most likely cause for the relatively moderate capacity and well-defined plateaus/peaks is due to the combination of LiTFSI and LiNO_3 which can limit the solubility of S_8 and the 1.8V cutoff voltage. Also, the coulombic efficiency ranges between $>98\%$ - which means the irreversible losses associated with S-reaction with Li-metal at the anode is inhibited. The preliminary results confirm active polymers as a potential candidate to mitigate the degradation processes of Li-S batteries. It is recommended that tuning the ion exchange capacity and/or the amount of ionomer can help in boosting the performance, cyclability, and columbic efficiency of Li-S batteries.

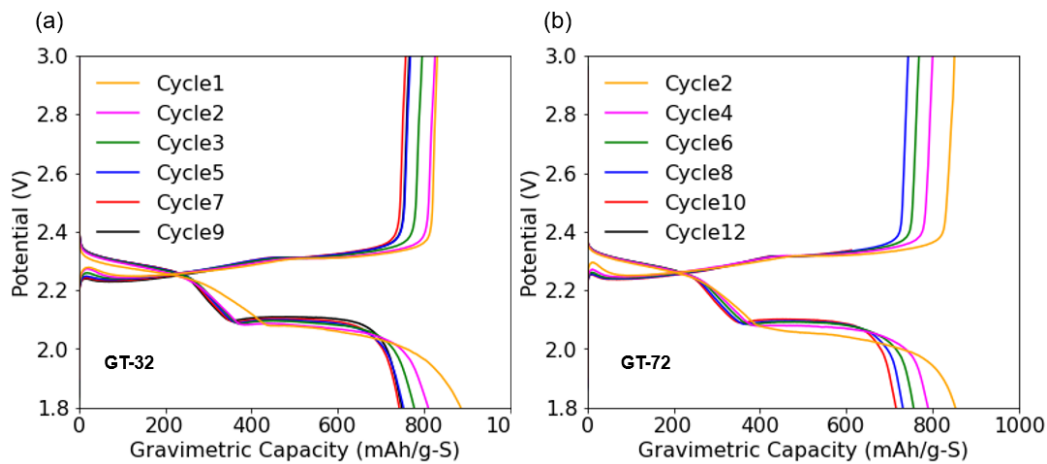


Figure 8.6. | Charge-discharge curves for (a) GT32 and (b) GT72

8.4 OPERANDO TECHNIQUES FOR STUDYING THE CORROSION OF Li^0

ELECTRODEPOSITS IN Li/S BATTERIES

As discussed above in Section 4.1, several challenges hinder the practical deployment of Li-S based batteries.²¹⁸ Below are the main detrimental factors of ‘Li-metal’:

- (1) Poor coulombic efficiency – Lithium metal as an anode is well-known to undergo severe irreversible losses due to the corrosion of high surface area Li^0 electrodeposits during post-charging processes (i.e. storage). Electron loss from the Li-metal facilitates the reduction of the electrolyte to form additional passivation at the Li-metal/electrolyte interface. The increase in SEI film thickness will cause resistance to build-up in the cell. Also, the Li-metal is known to form arborescent tree-like formations and drastic volumetric expansion that can fracture the passivating film, which leads to continual electrolyte consumption at the exposed reactive sites. The loss in active material during charge/discharge results in poor coulombic efficiency.
- (2) Safety issues - Lithium dendrites are a well-known safety hazard as previously discussed in the early chapters of this thesis. The dendrites can result in internal short circuits that lead to rapid discharge and generation of significant heat, resulting in thermal runaway.
- (3) Low lithium utilization – After repetitive charge/discharge, the Li^0 electrodeposits can break off from the bulk electrode and become electronically insulated. The loss in contact results in loss of active material.
- (4) Severe polarization – The anisotropic deposition/dissolution of Li-metal (porosity, different locations/structures) leads to regions with longer diffusion pathways. Also, the SEI continual build-up after each cycle leads to increased resistance. Extreme operating conditions (i.e. fluctuating temperatures, current, and depth-of-discharge) and alterations in the battery chemistry (i.e. additives, fluorination, electrolyte, anodes, cathodes) can result in highly unpredictable degradation

processes (i.e. capacity loss, rapid cell death, and thermal runaway). It is important to understand the effects of temperature on the growth of Li metal and interaction with polysulfides in Li-S batteries. During a previous project, my research group discovered that a graphite/NMC532 ($\text{LiC}_6/\text{LiNi}_{0.5}\text{Mn}_{0.3}\text{Co}_{0.2}\text{O}_2$) cell, which was cycled at low temperatures ($-29\text{ }^\circ\text{C}$) then brought back to room temperature, experienced two disastrous events: one cell vented gases after cycling at room temperature and the other one went into a thermal runaway after room temperature storage (at open circuit voltage).

During post-mortem analysis, a high spatial dependency of degradation processes on both the cathode and anode for a large Li-ion cell was discovered. Extreme conditions was found to exacerbate highly stressed regions (e.g. region of high curvature, edges) and discovered a unique ripple-type current distribution for large format jellyroll-type electrodes. The ripple-type gradients were realized by enhanced optically filtered imaging of post-mortem electrodes that were salvaged from compromised cells. Multiple-location liquid N_2 Raman Spectroscopy confirmed a preferential Li^0 residence at ripple-peaks and absent at ripple-troughs. The root cause derives from severe electrochemical polarization and thermal gradients generated during charge/discharge, which caused drastic electrode warping and non-uniform Li^+ flux from complex current gradients. Toward the edge of the electrode, alternating positive-then-negative striation lines were observed, which correspond to alternating high-then-low Li^0 electrodeposition. Stress-buildup at specific electrode regions can lead to highly vulnerable sites where an internal short circuit can occur.

Li^0 plating is a known hazard that can trigger catastrophic thermal runaway and result in continuous propagation to neighboring cells.²²¹ Li^0 plating occurs on a nucleation site (most notably a Li^0 seed or other mixable materials that can be determined by Pourbaix Diagrams) and crystallizes in various formations depending on the material and operating condition. In rare cases, uniform single layer electrodeposition can occur, but other higher-order growth patterns can form. This phenomenon depends on many factors including the uniformity of the electrodeposition surface (i.e. anisotropy/isotropy of facet orientation, peaks, and valleys, etc.) and whether the system is diffusion-limited. When the distribution of nucleation seeds is not uniform, display high anisotropy in facet orientation, and is diffusion-limited, the Li^0 electrodeposition process favors arborescent tree-like formations known as Li^0 dendrites.¹³⁵ Dendrites have a high surface area and display high reactivity, which increases the number of reaction-zones where electrolyte reduction can occur. Electrolyte reduction (e.g. decomposition of ethylene carbonate, ethyl methyl carbonate, dimethyl carbonate, lithium hexafluorophosphate) can result in severe gas evolution and formation of a partially soluble and partially insoluble film on the surface of the active material. The film, also known as the solid-electrolyte interphase (SEI) acts as a barrier that increases the internal resistance of the cell by slowing down the mass transfer of Li^+ ions that facilitate the redox reaction. SEI formation accelerates performance loss in Li-ion batteries and gassing significantly decreases the safety of the battery. Gasses such as CO , H_2 , O_2 , C_2H_4 , C_2H_6 , POF_3 , and entrained- HF ¹²³ can be released by a minor breach in the casing (either through compromised vents or punctures). The majority of the gasses released are flammable or toxic which pose safety concerns and exacerbate thermal runaway events.

For experimental work, it would be beneficial to the scientific community if further investigation of the degradative processes in Li-S batteries is done. Questions such as, what is the temperature-dependence of Li^0 electrodeposition growth and interaction with polysulfides? What is the surface area and temperature trend for Li^0 electrodeposits? How do polysulfides impact the surface area, resistance build-up, and porosity? What happens to Li^0 under no reductive current and storage? What is the corrosion rate? What gasses are evolved from high surface area Li^0 during storage? Do the gases facilitate other reactions? In answering these questions, the potential adoption of Li-S technology into various applications can be evaluated.

REFERENCES

1. Gür, T. M. Review of electrical energy storage technologies, materials and systems: Challenges and prospects for large-scale grid storage. *Energy Environ. Sci.* **11**, 2696–2767 (2018).
2. Hannan, M. A., Lipu, M. S. H., Ker, P. J., Begum, R. A., Agelidis, V. G. & Blaabjerg, F. Power electronics contribution to renewable energy conversion addressing emission reduction: Applications, issues, and recommendations. *Appl. Energy* **251**, 113404 (2019).
3. Zhang, H., Zhao, H., Khan, M. A., Zou, W., Xu, J., Zhang, L. & Zhang, J. Recent progress in advanced electrode materials, separators and electrolytes for lithium batteries. *J. Mater. Chem. A* **6**, 20564–20620 (2018).
4. Zhu, G. L., Zhao, C. Z., Huang, J. Q., He, C., Zhang, J., Chen, S., Xu, L., Yuan, H. & Zhang, Q. Fast Charging Lithium Batteries: Recent Progress and Future Prospects. *Small* **15**, 1–14 (2019).
5. Lin, X., Salari, M., Arava, L. M. R., Ajayan, P. M. & Grinstaff, M. W. High temperature electrical energy storage: Advances, challenges, and frontiers. *Chem. Soc. Rev.* **45**, 5848–5887 (2016).
6. Nitta, N., Wu, F., Lee, J. T. & Yushin, G. Li-ion battery materials: Present and future. *Mater. Today* **18**, 252–264 (2015).
7. Hu, C., Ye, H., Jain, G. & Schmidt, C. Remaining useful life assessment of lithium-ion batteries in implantable medical devices. *J. Power Sources* **375**, 118–130 (2018).
8. Schmidt, C. L. & Skarstad, P. M. The future of lithium and lithium-ion batteries in implantable medical devices. *J. Power Sources* **97–98**, 742–746 (2001).
9. Rajaeifar, M. A., Tabatabaei, M., Aghbashlo, M., Nizami, A. S. & Heidrich, O. Emissions from urban bus fleets running on biodiesel blends under real-world operating conditions: Implications for designing future case studies. *Renew. Sustain. Energy Rev.* **111**, 276–292 (2019).
10. USABC. *USABC Goals for Advanced High-Performance Batteries for Electric Vehicle (EV) Applications*. (2019).
11. Gao, J., Shi, S. Q. & Li, H. Brief overview of electrochemical potential in lithium ion batteries. *Chinese Phys. B* **25**, 1–27 (2015).

12. Wu, X., Song, K., Zhang, X., Hu, N., Li, L., Li, W., Zhang, L. & Zhang, H. Safety Issues in Lithium Ion Batteries: Materials and Cell Design. *Front. Energy Res.* **7**, 1–17 (2019).
13. Faegh, E., Ng, B., Hayman, D. & Mustain, W. E. Practical assessment of the performance of aluminium battery technologies. *Nat. Energy* (2020). doi:10.1038/s41560-020-00728-y
14. Wu, F. & Yushin, G. Conversion cathodes for rechargeable lithium and lithium-ion batteries. *Energy Environ. Sci.* **10**, 435–459 (2017).
15. Thackeray, M. M., Wolverton, C. & Isaacs, E. D. Electrical energy storage for transportation—approaching the limits of, and going beyond, lithium-ion batteries. *Energy Environ. Sci.* **5**, 7854 (2012).
16. Ping, P., Wang, Q. S., Huang, P. F., Li, K., Sun, J. H., Kong, D. P. & Chen, C. H. Study of the fire behavior of high-energy lithium-ion batteries with full-scale burning test. *J. Power Sources* **285**, 80–89 (2015).
17. Qi, Y., Guo, H., Hector, L. G. & Timmons, A. Threefold Increase in the Young ' s Modulus of Graphite Negative Electrode during Lithium Intercalation Threefold Increase in the Young ' s Modulus of Graphite Negative Electrode during Lithium Intercalation. *J. Electrochem. Soc.* **157**, A558–A566 (2010).
18. Radin, M. D., Hy, S., Sina, M., Fang, C., Liu, H., Vinckeviciute, J., Zhang, M., Whittingham, M. S., Meng, Y. S. & Van der Ven, A. Narrowing the Gap between Theoretical and Practical Capacities in Li-Ion Layered Oxide Cathode Materials. *Adv. Energy Mater.* **7**, 1–33 (2017).
19. Aurbach, D., Markovsky, B., Weissman, I., Levi, E. & Ein-Eli, Y. On the correlation between surface chemistry and performance of graphite negative electrodes for Li ion batteries. *Electrochim. Acta* **45**, 67–86 (1999).
20. Peled, E. & Menkin, S. Review—SEI: Past, Present and Future. *J. Electrochem. Soc.* **164**, A1703–A1719 (2017).
21. Wang, A., Kadam, S., Li, H., Shi, S. & Qi, Y. Review on modeling of the anode solid electrolyte interphase (SEI) for lithium-ion batteries. *npj Comput. Mater.* **4**, (2018).
22. An, S. J., Li, J., Daniel, C., Mohanty, D., Nagpure, S. & Wood, D. L. The state of understanding of the lithium-ion-battery graphite solid electrolyte interphase (SEI) and its relationship to formation cycling. *Carbon N. Y.* **105**, 52–76 (2016).
23. Rodrigues, M.-T. F., Babu, G., Gullapalli, H., Kalaga, K., Sayed, F. N., Kato, K., Joyner, J. & Ajayan, P. M. A materials perspective on Li-ion batteries at extreme temperatures. *Nat. Energy* **2**, 17108 (2017).
24. Chen, S., Dai, F. & Cai, M. Opportunities and Challenges of High-Energy Lithium Metal Batteries for Electric Vehicle Applications. *ACS Energy Lett.* **5**, 3140–3151 (2020).

25. Rodrigues, M.-T. F., Kalaga, K., Trask, S. E., Dees, D. W., Shkrob, I. A. & Abraham, D. P. Fast Charging of Li-Ion Cells: Part I. Using Li/Cu Reference Electrodes to Probe Individual Electrode Potentials. *J. Electrochem. Soc.* **166**, A996–A1003 (2019).
26. Petzl, M. & Danzer, M. A. Nondestructive detection, characterization, and quantification of lithium plating in commercial lithium-ion batteries. *J. Power Sources* **254**, 80–87 (2014).
27. Fan, J. & Tan, S. Studies on Charging Lithium-Ion Cells at Low Temperatures. *J. Electrochem. Soc.* **153**, A1081 (2006).
28. Anseán, D., Dubarry, M., Devie, A., Liaw, B. Y., García, V. M., Viera, J. C. & González, M. Operando lithium plating quantification and early detection of a commercial LiFePO₄ cell cycled under dynamic driving schedule. *J. Power Sources* **356**, 36–46 (2017).
29. Ng, B., Coman, P. T., Faegh, E., Peng, X., Karakalos, S. G., Jin, X., Mustain, W. E. & White, R. E. Low-Temperature Lithium Plating/Corrosion Hazard in Lithium-Ion Batteries: Electrode Rippling, Variable States of Charge, and Thermal and Nonthermal Runaway. *ACS Appl. Energy Mater.* **3**, 3653–3664 (2020).
30. Spinner, N., Zhang, L. & Mustain, W. E. Investigation of metal oxide anode degradation in lithium-ion batteries via identical-location TEM. *J. Mater. Chem. A* **2**, 1627–1630 (2014).
31. Amatucci, G. G. Stabilized iron fluoride cathodes. *Nat. Mater.* **18**, 1275–1276 (2019).
32. Cao, K., Jin, T., Yang, L. & Jiao, L. Recent progress in conversion reaction metal oxide anodes for Li-ion batteries. *Mater. Chem. Front.* **1**, 2213–2242 (2017).
33. Spinner, N. S., Palmieri, A., Beauregard, N., Zhang, L., Campanella, J. & Mustain, W. E. Influence of conductivity on the capacity retention of NiO anodes in Li-ion batteries. *J. Power Sources* **276**, 46–53 (2015).
34. Palmieri, A., Spinner, N., Zhao, S. & Mustain, W. E. Explaining the role and mechanism of carbon matrices in enhancing reaction reversibility of metal oxide anodes for high performance Li ion batteries. *Carbon N. Y.* **130**, 515–524 (2018).
35. Jow, T. R., Delp, S. A., Allen, J. L., Jones, J.-P. & Smart, M. C. Factors Limiting Li + Charge Transfer Kinetics in Li-Ion Batteries. *J. Electrochem. Soc.* **165**, A361–A367 (2018).
36. Soto, F. A., Marzouk, A., El-Mellouhi, F. & Balbuena, P. B. Understanding Ionic Diffusion through SEI Components for Lithium-Ion and Sodium-Ion Batteries: Insights from First-Principles Calculations. *Chem. Mater.* **30**, 3315–3322 (2018).
37. Ng, B., Peng, X., Faegh, E. & Mustain, W. E. Using nanoconfinement to inhibit the degradation pathways of conversion-metal oxide anodes for highly stable fast-charging Li-ion batteries. *J. Mater. Chem. A* **8**, 2712–2727 (2020).

38. Soto, F. A., Marzouk, A., El-Mellouhi, F. & Balbuena, P. B. Understanding Ionic Diffusion through SEI Components for Lithium-Ion and Sodium-Ion Batteries: Insights from First-Principles Calculations. *Chem. Mater.* **30**, 3315–3322 (2018).
39. Chorkendorff, I. & Niemantsverdriet, J. W. *Concepts of Modern Catalysis and Kinetics*. Weinheim: Wiley-VCH (2003).
40. Spinner, N., Zhang, L. & Mustain, W. E. Investigation of metal oxide anode degradation in lithium-ion batteries via identical-location TEM. *J. Mater. Chem. A* **2**, 1627–1630 (2014).
41. Palmieri, A., Yazdani, S., Kashfi-Sadabad, R., Karakalos, S. G., Pettes, M. T. & Mustain, W. E. Cobalt Doping as a Pathway to Stabilize the Solid-State Conversion Chemistry of Manganese Oxide Anodes in Li-Ion Batteries. *J. Phys. Chem. C* **122**, 7120–7127 (2018).
42. Palmieri, A., Yazdani, S., Kashfi-Sadabad, R., Karakalos, S. G., Ng, B., Oliveira, A., Peng, X., Pettes, M. T. & Mustain, W. E. Improved Capacity Retention of Metal Oxide Anodes in Li-Ion Batteries: Increasing Intraparticle Electronic Conductivity through Na Inclusion in Mn₃O₄. *ChemElectroChem* **5**, 2059–2063 (2018).
43. Su, Q., Dong, Z., Zhang, J., Du, G. & Xu, B. Visualizing the electrochemical reaction of ZnO nanoparticles with lithium by in situ TEM: Two reaction modes are revealed. *Nanotechnology* **24**, (2013).
44. Li, L., Jacobs, R., Gao, P., Gan, L., Wang, F., Morgan, D. & Jin, S. Origins of Large Voltage Hysteresis in High-Energy-Density Metal Fluoride Lithium-Ion Battery Conversion Electrodes. *J. Am. Chem. Soc.* **138**, 2838–2848 (2016).
45. Palmieri, A., Yazdani, S., Kashfi-Sadabad, R., Karakalos, S. G., Ng, B., Oliveira, A., Peng, X., Pettes, M. T. & Mustain, W. E. Improved Capacity Retention of Metal Oxide Anodes in Li-Ion Batteries: Increasing Intraparticle Electronic Conductivity through Na Inclusion in Mn₃O₄. *ChemElectroChem* **5**, 2059–2063 (2018).
46. Durmus, Z., Baykal, A., Kavas, H. & Szeri, H. Preparation and characterization of polyaniline (PANI)Mn₃O₄ nanocomposite. *Phys. B Condens. Matter* **406**, 1114–1120 (2011).
47. Bazant, M. Z. Theory of chemical kinetics and charge transfer based on nonequilibrium thermodynamics. *Acc. Chem. Res.* **46**, 1144–1160 (2013).
48. Nalewajski, R. F. & Parr, R. G. Legendre transforms and Maxwell relations in density functional theory. *J. Chem. Phys.* **77**, 399–407 (1982).
49. Ferguson, T. R. & Bazant, M. Z. Nonequilibrium Thermodynamics of Porous Electrodes. *J. Electrochem. Soc.* **159**, A1967–A1985 (2012).
50. Verma, A., Smith, K., Santhanagopalan, S., Abraham, D., Yao, K. P. & Mukherjee, P. P. Galvanostatic Intermittent Titration and Performance Based Analysis of LiNi_{0.5}Co_{0.2}Mn_{0.3}O₂ Cathode. *J. Electrochem. Soc.* **164**, A3380–A3392 (2017).

51. Dalaker, H. Thermodynamic computations of the interaction coefficients between boron and phosphorus and common impurity elements in liquid silicon. *Comput. Methods Mater. Sci.* **13**, 407–411 (2013).
52. Fuller, T. F. & Newman, J. Relaxation Phenomena in Lithium-ion-Insertion Cells. *J. Electrochem. Soc.* **141**, 855 (1994).
53. Doyle, M., Newman, J., Gozdz, A. S., Schmutz, C. N. & Tarascon, J. Comparison of Modeling Predictions with Experimental Data from Plastic Lithium Ion Cells. *J. Electrochem. Soc.* **143**, 1890–1903 (1996).
54. Li, J., Adewuyi, K., Lotfi, N., Landers, R. G. & Park, J. A single particle model with chemical/mechanical degradation physics for lithium ion battery State of Health (SOH) estimation. *Appl. Energy* **212**, 1178–1190 (2018).
55. Tippmann, S., Walper, D., Balboa, L., Spier, B. & Bessler, W. G. Low-temperature charging of lithium-ion cells part I: Electrochemical modeling and experimental investigation of degradation behavior. *J. Power Sources* **252**, 305–316 (2014).
56. Prada, E., Di Domenico, D., Creff, Y., Bernard, J., Sauvant-Moynot, V. & Huet, F. A Simplified Electrochemical and Thermal Aging Model of LiFePO₄-Graphite Li-ion Batteries: Power and Capacity Fade Simulations. *J. Electrochem. Soc.* **160**, A616–A628 (2013).
57. Xu, M., Zhang, Z., Wang, X., Jia, L. & Yang, L. Two-dimensional electrochemical-thermal coupled modeling of cylindrical LiFePO₄ batteries. *J. Power Sources* **256**, 233–243 (2014).
58. Saw, L. H., Ye, Y. & Tay, A. A. O. Electrochemical-thermal analysis of 18650 Lithium Iron Phosphate cell. *Energy Convers. Manag.* **75**, 162–174 (2013).
59. Ye, Y., Shi, Y. & Tay, A. A. O. Electro-thermal cycle life model for lithium iron phosphate battery. *J. Power Sources* **217**, 509–518 (2012).
60. Capron, O., Samba, A., Omar, N., Van Den Bossche, P. & Van Mierlo, J. Thermal behaviour investigation of a large and high power lithium iron phosphate cylindrical cell. *Energies* **8**, 10017–10042 (2015).
61. Tripathi, A. M., Su, W. N. & Hwang, B. J. In situ analytical techniques for battery interface analysis. *Chem. Soc. Rev.* **47**, 736–751 (2018).
62. Zhu, J., Knapp, M., Darma, M. S. D., Fang, Q., Wang, X., Dai, H., Wei, X. & Ehrenberg, H. An improved electro-thermal battery model complemented by current dependent parameters for vehicular low temperature application. *Appl. Energy* **248**, 149–161 (2019).
63. Cui, S., Wei, Y., Liu, T., Deng, W., Hu, Z., Su, Y., Li, H., Li, M., Guo, H., Duan, Y., Wang, W., Rao, M., Zheng, J., Wang, X. & Pan, F. Optimized Temperature Effect of Li-Ion Diffusion with Layer Distance in Li(NixMnyCoz)O₂ Cathode Materials for High Performance Li-Ion Battery. *Adv. Energy Mater.* **6**, 1501309 (2016).

64. Guo, M., Jin, X. & White, R. E. Nonlinear State-Variable Method for Solving Physics-Based Li-Ion Cell Model with High-Frequency Inputs. *J. Electrochem. Soc.* **164**, E3001–E3015 (2017).
65. Wang, C. Y., Gu, W. B. & Liaw, B. Y. Micro-Macroscopic Coupled Modeling of Batteries and Fuel Cells: I. Model Development. *J. Electrochem. Soc.* **145**, 3407–3417 (1998).
66. Subramanian, V. R., Diwakar, V. D. & Tapriyal, D. Efficient Macro-Micro Scale Coupled Modeling of Batteries. *J. Electrochem. Soc.* **152**, A2002 (2005).
67. Guo, M., Jin, X. & White, R. E. An Adaptive Reduced-Order-Modeling Approach for Simulating Real-Time Performances of Li-Ion Battery Systems. *J. Electrochem. Soc.* **164**, A3602–A3613 (2017).
68. Tran, N. T., Vilathgamuwa, M., Farrell, T., Choi, S. S., Li, Y. & Teague, J. A Padé Approximate Model of Lithium Ion Batteries. *J. Electrochem. Soc.* **165**, A1409–A1421 (2018).
69. Cai, L. & White, R. E. Reduction of Model Order Based on Proper Orthogonal Decomposition for Lithium-Ion Battery Simulations. *J. Electrochem. Soc.* **156**, A154 (2009).
70. Forman, J. C., Bashash, S., Stein, J. L. & Fathy, H. K. Reduction of an Electrochemistry-Based Li-Ion Battery Model via Quasi-Linearization and Padé Approximation. *J. Electrochem. Soc.* **158**, A93 (2011).
71. Guo, M., Sikha, G. & White, R. E. Single-Particle Model for a Lithium-Ion Cell: Thermal Behavior. *J. Electrochem. Soc.* **158**, A122 (2011).
72. Schmalstieg, J., Rahe, C., Ecker, M. & Sauer, D. U. Full Cell Parameterization of a High-Power Lithium-Ion Battery for a Physico-Chemical Model: Part I. Physical and Electrochemical Parameters. *J. Electrochem. Soc.* **165**, A3799–A3810 (2018).
73. Schmalstieg, J. & Sauer, D. U. Full Cell Parameterization of a High-Power Lithium-Ion Battery for a Physico-Chemical Model: Part II. Thermal Parameters and Validation. *J. Electrochem. Soc.* **165**, A3811–A3819 (2018).
74. Ekström, H., Fridholm, B. & Lindbergh, G. Comparison of lumped diffusion models for voltage prediction of a lithium-ion battery cell during dynamic loads. *J. Power Sources* **402**, 296–300 (2018).
75. Jiang, J., Shi, W., Zheng, J., Zuo, P., Xiao, J., Chen, X., Xu, W. & Zhang, J.-G. Optimized Operating Range for Large-Format LiFePO₄/Graphite Batteries. *J. Electrochem. Soc.* **161**, A336–A341 (2014).
76. Viswanathan, V. V., Choi, D., Wang, D., Xu, W., Towne, S., Williford, R. E., Zhang, J. G., Liu, J. & Yang, Z. Effect of entropy change of lithium intercalation in cathodes and anodes on Li-ion battery thermal management. *J. Power Sources* **195**, 3720–3729 (2010).

77. Burns, J. C., Kassam, A., Sinha, N. N., Downie, L. E., Solnickova, L., Way, B. M. & Dahn, J. R. Predicting and Extending the Lifetime of Li-Ion Batteries. *J. Electrochem. Soc.* **160**, A1451–A1456 (2013).
78. Ng, B., Coman, P. T., Mustain, W. E. & White, R. E. Non-destructive parameter extraction for a reduced order lumped electrochemical-thermal model for simulating Li-ion full-cells. *J. Power Sources* **445**, 227296 (2020).
79. Campbell, I. D., Marzook, M., Marinescu, M. & Offer, G. J. How Observable Is Lithium Plating? Differential Voltage Analysis to Identify and Quantify Lithium Plating Following Fast Charging of Cold Lithium-Ion Batteries. *J. Electrochem. Soc.* **166**, A725–A739 (2019).
80. Yun, F., Jin, W., Tang, L., Li, W., Pang, J. & Lu, S. Analysis of Capacity Fade from Entropic Heat Coefficient of Li[Ni_xCo_yMn_z]O₂/Graphite Lithium Ion Battery. *J. Electrochem. Soc.* **163**, A639–A643 (2016).
81. Konar, S., Häusserman, U. & Svensson, G. Intercalation compounds from lith and graphite: Relative stability of metastable stages and thermodynamic stability of dilute stage Id. *Chem. Mater.* **27**, 2566–2575 (2015).
82. Dees, D. W., Abraham, D. P., Lu, W., Gallagher, K. G., Bettge, M. & Jansen, A. N. Electrochemical Modeling and Performance of a Lithium- and Manganese-Rich Layered Transition-Metal Oxide Positive Electrode. *J. Electrochem. Soc.* **162**, A559–A572 (2015).
83. Han, B. C., Van Der Ven, A., Morgan, D. & Ceder, G. Electrochemical modeling of intercalation processes with phase field models. *Electrochim. Acta* **49**, 4691–4699 (2004).
84. Schweidler, S., De Biasi, L., Schiele, A., Hartmann, P., Brezesinski, T. & Janek, J. Volume Changes of Graphite Anodes Revisited: A Combined Operando X-ray Diffraction and in Situ Pressure Analysis Study. *J. Phys. Chem. C* **122**, 8829–8835 (2018).
85. Müller, S., Pietsch, P., Brandt, B. E., Baade, P., De Andrade, V., De Carlo, F. & Wood, V. Quantification and modeling of mechanical degradation in lithium-ion batteries based on nanoscale imaging. *Nat. Commun.* **9**, 389–390 (2018).
86. Chung, G.-C., Kim, H.-J., Yu, S.-I., Jun, S.-H., Choi, J. & Kim, M.-H. Origin of Graphite Exfoliation An Investigation of the Important Role of Solvent Cointercalation. *J. Electrochem. Soc.* **147**, 4391 (2000).
87. Lundgren, H., Svens, P., Ekström, H., Tengstedt, C., Lindström, J., Behm, M. & Lindbergh, G. Thermal Management of Large-Format Prismatic Lithium-Ion Battery in PHEV Application. *J. Electrochem. Soc.* **163**, A309–A317 (2016).
88. Cengel, Y. A. *Heat Transfer: A Practical Approach (2nd Edition)*. (McGraw-Hill, 2003).
89. Nguyen, T. Q. & Breitkopf, C. Determination of Diffusion Coefficients Using Impedance Spectroscopy Data. *J. Electrochem. Soc.* **165**, E826–E831 (2018).

90. Sikha, G., Popov, B. N. & White, R. E. Effect of Porosity on the Capacity Fade of a Lithium-Ion Battery. *J. Electrochem. Soc.* **151**, A1104 (2004).
91. Yang, S., Wang, X., Yang, X., Bai, Y., Liu, Z., Shu, H. & Wei, Q. Determination of the chemical diffusion coefficient of lithium ions in spherical Li[Ni_{0.5}Mn_{0.3}Co_{0.2}]O₂. *Electrochim. Acta* **66**, 88–93 (2012).
92. Murbach, M. D. & Schwartz, D. T. Analysis of Li-Ion Battery Electrochemical Impedance Spectroscopy Data: An Easy-to-Implement Approach for Physics-Based Parameter Estimation Using an Open-Source Tool. *J. Electrochem. Soc.* **165**, A297–A304 (2018).
93. Ramadesigan, V., Northrop, P. W. C., De, S., Santhanagopalan, S., Braatz, R. D. & Subramanian, V. R. Modeling and Simulation of Lithium-Ion Batteries from a Systems Engineering Perspective. *J. Electrochem. Soc.* **159**, R31–R45 (2012).
94. Atlung, S., West, K. & Jacobsen, T. Dynamic Aspects of Solid Solution Cathodes for Electrochemical Power Sources. *J. Electrochem. Soc.* **126**, 1311–1320 (1979).
95. Santhanagopalan, S., Guo, Q., Ramadass, P. & White, R. E. Review of models for predicting the cycling performance of lithium ion batteries. *J. Power Sources* **156**, 620–628 (2006).
96. Fuller, T. F., Doyle, M. & Newman, J. Simulation and Optimization of the Dual Lithium Ion Insertion Cell. *J. Electrochem. Soc.* **141**, 1–10 (1994).
97. Yang, S., Wang, X., Yang, X., Bai, Y., Liu, Z., Shu, H. & Wei, Q. Determination of the chemical diffusion coefficient of lithium ions in spherical Li[Ni_{0.5}Mn_{0.3}Co_{0.2}]O₂. *Electrochim. Acta* **66**, 88–93 (2012).
98. Ng, B., Duan, X., Liu, F., Agar, E., White, R. E., Mustain, W. E. & Jin, X. Investigation of Transport and Kinetic Nonideality in Solid Li-Ion Electrodes through Deconvolution of Electrochemical Impedance Spectra. *J. Electrochem. Soc.* **167**, 020523 (2020).
99. Lu, J., Li, L., Park, J. B., Sun, Y. K., Wu, F. & Amine, K. Aprotic and aqueous Li-O₂ batteries. *Chem. Rev.* **114**, 5611–5640 (2014).
100. Yang, X. G., Zhang, G., Ge, S. & Wang, C. Y. Fast charging of lithium-ion batteries at all temperatures. *Proc. Natl. Acad. Sci. U. S. A.* **115**, 7266–7271 (2018).
101. Liu, Y., Zhu, Y. & Cui, Y. Challenges and opportunities towards fast-charging battery materials. *Nat. Energy* **4**, 540–550 (2019).
102. Hosseinzadeh, E., Genieser, R., Worwood, D., Barai, A., Marco, J. & Jennings, P. A systematic approach for electrochemical-thermal modelling of a large format lithium-ion battery for electric vehicle application. *J. Power Sources* **382**, 77–94 (2018).

103. Zhao, J., Liao, L., Shi, F., Lei, T., Chen, G., Pei, A., Sun, J., Yan, K., Zhou, G., Xie, J., Liu, C., Li, Y., Liang, Z., Bao, Z. & Cui, Y. Surface Fluorination of Reactive Battery Anode Materials for Enhanced Stability. *J. Am. Chem. Soc.* **139**, 11550–11558 (2017).
104. Lee, W., Muhammad, S., Sergey, C., Lee, H., Yoon, J., Kang, Y. M. & Yoon, W. S. Advances in the Cathode Materials for Lithium Rechargeable Batteries. *Angew. Chemie - Int. Ed.* **59**, 2578–2605 (2020).
105. Richards, W. D., Dacek, S. T., Kitchaev, D. A. & Ceder, G. Fluorination of Lithium-Excess Transition Metal Oxide Cathode Materials. *Adv. Energy Mater.* **8**, 1701533 (2018).
106. Li, G., Liu, Z., Huang, Q., Gao, Y., Regula, M., Wang, D., Chen, L. Q. & Wang, D. Stable metal battery anodes enabled by polyethylenimine sponge hosts by way of electrokinetic effects. *Nat. Energy* **3**, 1076–1083 (2018).
107. Liu, K., Liu, Y., Lin, D., Pei, A. & Cui, Y. Materials for lithium-ion battery safety. *Sci. Adv.* **4**, eaas9820 (2018).
108. Fan, X., Ji, X., Han, F., Yue, J., Chen, J., Chen, L., Deng, T., Jiang, J. & Wang, C. Fluorinated solid electrolyte interphase enables highly reversible solid-state Li metal battery. *Sci. Adv.* **4**, 9245 (2018).
109. Ng, B., Peng, X., Faegh, E. & Mustain, W. E. Using nanoconfinement to inhibit the degradation pathways of conversion-metal oxide anodes for highly stable fast-charging Li-ion batteries. *J. Mater. Chem. A* **8**, 2712–2727 (2020).
110. Lisbona, D. & Snee, T. A review of hazards associated with primary lithium and lithium-ion batteries. *Process Saf. Environ. Prot.* **89**, 434–442 (2011).
111. Ping, P., Kong, D., Zhang, J., Wen, R. & Wen, J. Characterization of behaviour and hazards of fire and deflagration for high-energy Li-ion cells by over-heating. *J. Power Sources* **398**, 55–66 (2018).
112. Li, W., Wang, H., Zhang, Y. & Ouyang, M. Flammability characteristics of the battery vent gas: A case of NCA and LFP lithium-ion batteries during external heating abuse. *J. Energy Storage* **24**, 100775 (2019).
113. Tarascon, J. M. & Armand, M. Issues and challenges facing rechargeable lithium batteries. *Nature* **414**, 359–367 (2001).
114. Zeng, X., Li, M., Abd El-Hady, D., Alshitari, W., Al-Bogami, A. S., Lu, J. & Amine, K. Commercialization of Lithium Battery Technologies for Electric Vehicles. *Adv. Energy Mater.* **9**, 1900161 (2019).
115. Li, W., Song, B. & Manthiram, A. High-voltage positive electrode materials for lithium-ion batteries. *Chem. Soc. Rev.* **46**, 3006–3059 (2017).
116. Kim, T., Song, W., Son, D. Y., Ono, L. K. & Qi, Y. Lithium-ion batteries: outlook on present, future, and hybridized technologies. *J. Mater. Chem. A* **7**, 2942–2964 (2019).

117. Huang, H., Wang, X., Tervoort, E., Zeng, G., Liu, T., Chen, X., Sologubenko, A. & Niederberger, M. Nano-Sized Structurally Disordered Metal Oxide Composite Aerogels as High-Power Anodes in Hybrid Supercapacitors. *ACS Nano* **12**, 2753–2763 (2018).
118. Poullikkas, A. Sustainable options for electric vehicle technologies. *Renew. Sustain. Energy Rev.* **41**, 1277–1287 (2015).
119. Keil, P. & Jossen, A. Impact of Dynamic Driving Loads and Regenerative Braking on the Aging of Lithium-Ion Batteries in Electric Vehicles. *J. Electrochem. Soc.* **164**, A3081–A3092 (2017).
120. Ren, G., Ma, G. & Cong, N. Review of electrical energy storage system for vehicular applications. *Renew. Sustain. Energy Rev.* **41**, 225–236 (2015).
121. Chin, K. B., Brandon, E. J., Bugga, R. V., Smart, M. C., Jones, S. C., Krause, F. C., West, W. C. & Bolotin, G. G. Energy Storage Technologies for Small Satellite Applications. *Proc. IEEE* **106**, 419–428 (2018).
122. Gao, S., Lu, L., Ouyang, M., Duan, Y., Zhu, X., Xu, C., Ng, B., Kamyab, N., White, R. E. & Coman, P. T. Experimental Study on Module-to-Module Thermal Runaway-Propagation in a Battery Pack. *J. Electrochem. Soc.* **166**, A2065–A2073 (2019).
123. Larsson, F., Bertilsson, S., Furlani, M., Albinsson, I. & Mellander, B. E. Gas explosions and thermal runaways during external heating abuse of commercial lithium-ion graphite-LiCoO₂ cells at different levels of ageing. *J. Power Sources* **373**, 220–231 (2018).
124. Larsson, F., Andersson, P., Blomqvist, P. & Mellander, B. E. Toxic fluoride gas emissions from lithium-ion battery fires. *Sci. Rep.* **7**, 1–13 (2017).
125. Omaye, S. T. Metabolic modulation of carbon monoxide toxicity. *Toxicology* **180**, 139–150 (2002).
126. Lebedeva, N. P. & Boon-Brett, L. Considerations on the Chemical Toxicity of Contemporary Li-Ion Battery Electrolytes and Their Components. *J. Electrochem. Soc.* **163**, A821–A830 (2016).
127. Finegan, D. P., Darcy, E., Keyser, M., Tjaden, B., Heenan, T. M. M., Jarvis, R., Bailey, J. J., Vo, N. T., Magdysyuk, O. V., Drakopoulos, M., Michiel, M. Di, Rack, A., Hinds, G., Brett, D. J. L. & Shearing, P. R. Identifying the Cause of Rupture of Li-Ion Batteries during Thermal Runaway. *Adv. Sci.* **5**, 1700369 (2018).
128. Williard, N., He, W., Hendricks, C. & Pecht, M. Lessons learned from the 787 dreamliner issue on Lithium-Ion Battery reliability. *Energies* **6**, 4682–4695 (2013).
129. Loveridge, M. J., Remy, G., Kourra, N., Genieser, R., Barai, A., Lain, M. J., Guo, Y., Amor-Segan, M., Williams, M. A., Amietszajew, T., Ellis, M., Bhagat, R. & Greenwood, D. Looking deeper into the galaxy (Note 7). *Batteries* **4**, 1–11 (2018).

130. Ng, B., Coman, P. T., Faegh, E., Peng, X., Karakalos, S. G., Jin, X., Mustain, W. E. & White, R. E. Low-Temperature Lithium Plating/Corrosion Hazard in Lithium-Ion Batteries: Electrode Rippling, Variable States of Charge, and Thermal and Nonthermal Runaway. *ACS Appl. Energy Mater.* **3**, 3653–3664 (2020).
131. Steiger, J. & Erlangung, Z. Mechanisms of Dendrite Growth in Lithium Metal Batteries. *Dissertation* (Karlsruher Institut für Technologie (KIT). Karlsruhe, 2015).
132. Lin, D., Liu, Y., Li, Y., Li, Y., Pei, A., Xie, J., Huang, W. & Cui, Y. Fast galvanic lithium corrosion involving a Kirkendall-type mechanism. *Nat. Chem.* **11**, 382–389 (2019).
133. Sun, Y., Liu, N. & Cui, Y. Promises and challenges of nanomaterials for lithium-based rechargeable batteries. *Nat. Energy* **1**, 16071 (2016).
134. Bhattacharyya, R., Key, B., Chen, H., Best, A. S., Hollenkamp, A. F. & Grey, C. P. In situ NMR observation of the formation of metallic lithium microstructures in lithium batteries. *Nat. Mater.* **9**, 504–510 (2010).
135. Liu, Y., Liu, Q., Xin, L., Liu, Y., Yang, F., Stach, E. A. & Xie, J. Making Li-metal electrodes rechargeable by controlling the dendrite growth direction. *Nat. Energy* **2**, 17083 (2017).
136. Guan, T., Sun, S., Yu, F., Gao, Y., Fan, P., Zuo, P., Du, C. & Yin, G. The degradation of LiCoO₂/graphite batteries at different rates. *Electrochim. Acta* **279**, 204–212 (2018).
137. Hellqvist Kjell, M., Malmgren, S., Ciosek, K., Behm, M., Edström, K. & Lindbergh, G. Comparing aging of graphite/LiFePO₄ cells at 22 C and 55 C - Electrochemical and photoelectron spectroscopy studies. *J. Power Sources* **243**, 290–298 (2013).
138. Dedryvère, R., Laruelle, S., Grugeon, S., Gireaud, L., Tarascon, J.-M. & Gonbeau, D. XPS Identification of the Organic and Inorganic Components of the Electrode/Electrolyte Interface Formed on a Metallic Cathode. *J. Electrochem. Soc.* **152**, A689 (2005).
139. Ruschewitz, U. Binary and ternary carbides of alkali and alkaline-earth metals. *Coord. Chem. Rev.* **244**, 115–136 (2003).
140. Thackeray, M. M., Wolverton, C. & Isaacs, E. D. Electrical energy storage for transportation - Approaching the limits of, and going beyond, lithium-ion batteries. *Energy Environ. Sci.* **5**, 7854–7863 (2012).
141. Grey, C. P. & Tarascon, J. M. Sustainability and in situ monitoring in battery development. *Nat. Mater.* **16**, 45–56 (2016).
142. Liu, K., Liu, Y., Lin, D., Pei, A. & Cui, Y. Materials for lithium-ion battery safety. *Sci. Adv.* **4**, 9820 (2018).
143. Kim, N., Chae, S., Ma, J., Ko, M. & Cho, J. Fast-charging high-energy lithium-ion batteries via implantation of amorphous silicon nanolayer in edge-plane activated graphite anodes. *Nat. Commun.* **8**, 812 (2017).

144. Li, Q., Zhu, G., Zhao, Y., Pei, K. & Che, R. Ni_xMn_yCo_zO Nanowire/CNT Composite Microspheres with 3D Interconnected Conductive Network Structure via Spray-Drying Method: A High-Capacity and Long-Cycle-Life Anode Material for Lithium-Ion Batteries. *Small* **15**, 1–12 (2019).
145. Dong, Y., Wang, B., Zhao, K., Yu, Y., Wang, X., Mai, L. & Jin, S. Air-Stable Porous Fe₂N Encapsulated in Carbon Microboxes with High Volumetric Lithium Storage Capacity and a Long Cycle Life. *Nano Lett.* **17**, 5740–5746 (2017).
146. Yuan, H., Wu, M., Zheng, J., Chen, Z. G., Zhang, W., Luo, J., Jin, C., Sheng, O., Liang, C., Gan, Y., Xia, Y., Zhang, J., Huang, H., Liu, Y., Nai, J. & Tao, X. Empowering Metal Phosphides Anode with Catalytic Attribute toward Superior Cyclability for Lithium-Ion Storage. *Adv. Funct. Mater.* **29**, 1–8 (2019).
147. Liu, Z., Yang, S., Sun, B., Chang, X., Zheng, J. & Li, X. A Peapod-like CoP@C Nanostructure from Phosphorization in a Low-Temperature Molten Salt for High-Performance Lithium-Ion Batteries. *Angew. Chemie - Int. Ed.* **57**, 10187–10191 (2018).
148. Chen, C., Xie, X., Anasori, B., Sarycheva, A., Makaryan, T., Zhao, M., Urbankowski, P., Miao, L., Jiang, J. & Gogotsi, Y. MoS₂-on-MXene Heterostructures as Highly Reversible Anode Materials for Lithium-Ion Batteries. *Angew. Chemie - Int. Ed.* **57**, 1846–1850 (2018).
149. Zhan, J., Wu, K., Yu, X., Yang, M., Cao, X., Lei, B., Pan, D., Jiang, H. & Wu, M. α-Fe₂O₃ Nanoparticles Decorated C@MoS₂ Nanosheet Arrays with Expanded Spacing of (002) Plane for Ultrafast and High Li/Na-Ion Storage. *Small* **15**, 1–10 (2019).
150. Li, Z., Zhao, H., Lv, P., Zhang, Z., Zhang, Y., Du, Z., Teng, Y., Zhao, L. & Zhu, Z. Watermelon-Like Structured SiO_x-TiO₂@C Nanocomposite as a High-Performance Lithium-Ion Battery Anode. *Adv. Funct. Mater.* **28**, 1–11 (2018).
151. Luo, J., Ma, B., Peng, J., Wu, Z., Luo, Z. & Wang, X. Modified Chestnut-Like Structure Silicon Carbon Composite as Anode Material for Lithium-Ion Batteries. *ACS Sustain. Chem. Eng.* **7**, 10415–10424 (2019).
152. Li, P., Hwang, J. Y. & Sun, Y. K. Nano/microstructured silicon-graphite composite anode for high-energy-density li-ion battery. *ACS Nano* **13**, 2624–2633 (2019).
153. Cai, X., Liu, W., Yang, S., Zhang, S., Gao, Q., Yu, X., Li, J., Wang, H. & Fang, Y. Dual-Confined SiO Embedded in TiO₂ Shell and 3D Carbon Nanofiber Web as Stable Anode Material for Superior Lithium Storage. *Adv. Mater. Interfaces* **6**, 1–11 (2019).
154. Wang, W., Jiang, B., Xiong, W., Sun, H., Lin, Z., Hu, L., Tu, J., Hou, J., Zhu, H. & Jiao, S. A new cathode material for super-valent battery based on aluminium ion intercalation and deintercalation. *Sci. Rep.* **3**, 3383 (2013).

155. Liu, N., Lu, Z., Zhao, J., Mcdowell, M. T., Lee, H. W., Zhao, W. & Cui, Y. A pomegranate-inspired nanoscale design for large-volume-change lithium battery anodes. *Nat. Nanotechnol.* **9**, 187–192 (2014).
156. Wu, H., Chan, G., Choi, J. W., Ryu, I., Yao, Y., Mcdowell, M. T., Lee, S. W., Jackson, A., Yang, Y., Hu, L. & Cui, Y. Stable cycling of double-walled silicon nanotube battery anodes through solid-electrolyte interphase control. *Nat. Nanotechnol.* **7**, 310–315 (2012).
157. Lanz, M. & Novák, P. DEMS study of gas evolution at thick graphite electrodes for lithium-ion batteries: The effect of γ -butyrolactone. *J. Power Sources* **102**, 277–282 (2001).
158. Steinhauer, M., Risse, S., Wagner, N. & Friedrich, K. A. Investigation of the Solid Electrolyte Interphase Formation at Graphite Anodes in Lithium-Ion Batteries with Electrochemical Impedance Spectroscopy. *Electrochim. Acta* **228**, 652–658 (2017).
159. Steinrück, H. G., Cao, C., Tsao, Y., Takacs, C. J., Konovalov, O., Vatamanu, J., Borodin, O. & Toney, M. F. The nanoscale structure of the electrolyte-metal oxide interface. *Energy Environ. Sci.* **11**, 594–602 (2018).
160. Li, T. & Balbuena, P. B. Theoretical studies of the reduction of ethylene carbonate. *Chem. Phys. Lett.* **317**, 421–429 (2000).
161. Wang, S., Zhang, W., Chen, Y., Dai, Z., Zhao, C., Wang, D. & Shen, C. Operando study of Fe₃O₄ anodes by electrochemical atomic force microscopy. *Appl. Surf. Sci.* **426**, 217–223 (2017).
162. Wang, S., Yang, K., Gao, F., Wang, D. & Shen, C. Direct visualization of solid electrolyte interphase on Li₄Ti₅O₁₂ by: In situ AFM. *RSC Adv.* **6**, 77105–77110 (2016).
163. Shen, C., Wang, S., Jin, Y. & Han, W. Q. In Situ AFM Imaging of Solid Electrolyte Interfaces on HOPG with Ethylene Carbonate and Fluoroethylene Carbonate-Based Electrolytes. *ACS Appl. Mater. Interfaces* **7**, 25441–25447 (2015).
164. Wang, X., Kerr, R., Chen, F., Goujon, N., Pringle, J. M., Mecerreyes, D., Forsyth, M. & Howlett, P. C. Toward High-Energy-Density Lithium Metal Batteries: Opportunities and Challenges for Solid Organic Electrolytes. *Adv. Mater.* **32**, 1905219 (2020).
165. Yan, C., Xu, R., Xiao, Y., Ding, J. F., Xu, L., Li, B. Q. & Huang, J. Q. Toward Critical Electrode/Electrolyte Interfaces in Rechargeable Batteries. *Adv. Funct. Mater.* **30**, 1–21 (2020).
166. Goodenough, J. B. & Kim, Y. Challenges for rechargeable Li batteries. *Chem. Mater.* **22**, 587–603 (2010).
167. Ng, B., Faegh, E., Lateef, S., Karakalos, S. G. & Mustain, W. E. Structure and chemistry of the solid electrolyte interphase (SEI) on a high capacity conversion-based anode: NiO. *J. Mater. Chem. A* **9**, 523–537 (2021).

168. Wang, H., Fu, J., Wang, C., Wang, J., Yang, A., Li, C., Sun, Q., Cui, Y. & Li, H. A binder-free high silicon content flexible anode for Li-ion batteries. *Energy Environ. Sci.* **13**, 848–858 (2020).
169. Elishav, O., Shener, Y., Beilin, V., Shter, G. E., Ng, B., Mustain, W. E., Landau, M. V., Herskowitz, M. & Grader, G. S. Electrospun nanofibers with surface oriented lamellar patterns and their potential applications. *Nanoscale* **12**, 12993–13000 (2020).
170. Liu, H., Li, Q., Yao, Z., Li, L., Li, Y., Wolverton, C., Hersam, M. C., Wu, J. & Dravid, V. P. Origin of Fracture-Resistance to Large Volume Change in Cu-Substituted Co₃O₄ Electrodes. *Adv. Mater.* **30**, 1–8 (2018).
171. Deng, J., Yu, X., Qin, X., Zhou, D., Zhang, L., Duan, H., Kang, F., Li, B. & Wang, G. Co–B Nanoflakes as Multifunctional Bridges in ZnCo₂O₄ Micro-/Nanospheres for Superior Lithium Storage with Boosted Kinetics and Stability. *Adv. Energy Mater.* **9**, 1–11 (2019).
172. Ren, W., Liu, D., Sun, C., Yao, X., Tan, J., Wang, C., Zhao, K., Wang, X., Li, Q. & Mai, L. Nonhierarchical Heterostructured Fe₂O₃/Mn₂O₃ Porous Hollow Spheres for Enhanced Lithium Storage. *Small* **14**, 1–9 (2018).
173. Yan, S., Song, H., Lin, S., Wu, H., Shi, Y. & Yao, J. GeO₂ Encapsulated Ge Nanostructure with Enhanced Lithium-Storage Properties. *Adv. Funct. Mater.* **29**, 1–7 (2019).
174. Hao, J., Zhang, J., Xia, G., Liu, Y., Zheng, Y., Zhang, W., Tang, Y., Pang, W. K. & Guo, Z. Heterostructure Manipulation via in Situ Localized Phase Transformation for High-Rate and Highly Durable Lithium Ion Storage. *ACS Nano* **12**, 10430–10438 (2018).
175. Lu, Y., Nai, J. & Lou, X. W. D. Formation of NiCo₂V₂O₈ Yolk–Double Shell Spheres with Enhanced Lithium Storage Properties. *Angew. Chemie - Int. Ed.* **57**, 2899–2903 (2018).
176. Liu, Z., Yu, X. Y. & Paik, U. Etching-in-a-Box: A Novel Strategy to Synthesize Unique Yolk-Shelled Fe₃O₄@Carbon with an Ultralong Cycling Life for Lithium Storage. *Adv. Energy Mater.* **6**, 3–7 (2016).
177. Shrestha, S. & Mustain, W. E. Properties of Nitrogen-Functionalized Ordered Mesoporous Carbon Prepared Using Polypyrrole Precursor. *J. Electrochem. Soc.* **157**, B1665 (2010).
178. Zhao, D., Feng, J., Huo, Q., Melosh, N., Fredrickson, G. H., Chmelka, B. F. & Stucky, G. D. Triblock copolymer syntheses of mesoporous silica with periodic 50 to 300 angstrom pores. *Science (80-.)*. **279**, 548–552 (1998).
179. Fletcher, S. Tafel slopes from first principles. *J. Solid State Electrochem.* **13**, 537–549 (2009).

180. Bockris, J. O. M. & Nagy, Z. Symmetry factor and transfer coefficient: A source of confusion in electrode kinetics. *J. Chem. Educ.* **50**, 839–843 (1973).
181. Bai, P. & Bazant, M. Z. Charge transfer kinetics at the solid-solid interface in porous electrodes. *Nat. Commun.* **5**, 1–7 (2014).
182. Boyle, D. T., Kong, X., Pei, A., Rudnicki, P. E., Shi, F., Huang, W., Bao, Z., Qin, J. & Cui, Y. Transient Voltammetry with Ultramicroelectrodes Reveals the Electron Transfer Kinetics of Lithium Metal Anodes. *ACS Energy Lett.* **5**, 701–709 (2020).
183. Fletcher, S. Tafel slopes from first principles. *J. Solid State Electrochem.* **13**, 537–549 (2009).
184. Aurbach, D., Moshkovich, M., Cohen, Y. & Schechter, A. Study of surface film formation on noble-metal electrodes in alkyl carbonates/Li salt solutions, using simultaneous in situ AFM, EQCM, FTIR, and EIS. *Langmuir* **15**, 2947–2960 (1999).
185. Aurbach, D., Levi, M. D., Levi, E. & Schechter, A. Failure and stabilization mechanisms of graphite electrodes. *J. Phys. Chem. B* **101**, 2195–2206 (1997).
186. Wang, Y., Nakamura, S., Tasaki, K. & Balbuena, P. B. Theoretical studies to understand surface chemistry on carbon anodes for lithium-ion batteries: How does vinylene carbonate play its role as an electrolyte additive? *J. Am. Chem. Soc.* **124**, 4408–4421 (2002).
187. Ahamad, S. & Gupta, A. A systematic study of kinetics in mesocarbon microbeads anodes in presence of nano-conductive additives. *Electrochim. Acta* **297**, 916–928 (2019).
188. Marcus, R. A. Electron Transfer Reactions in Chemistry: Theory and Experiment (Nobel Lecture). *Angew. Chemie Int. Ed. English* **32**, 1111–1121 (1993).
189. Gilbert, J. A., Bareño, J., Spila, T., Trask, S. E., Miller, D. J., Polzin, B. J., Jansen, A. N. & Abraham, D. P. Cycling Behavior of NCM523/Graphite Lithium-Ion Cells in the 3–4.4 V Range: Diagnostic Studies of Full Cells and Harvested Electrodes. *J. Electrochem. Soc.* **164**, A6054–A6065 (2017).
190. Bock, D. C., Waller, G. H., Mansour, A. N., Marschlok, A. C., Takeuchi, K. J. & Takeuchi, E. S. Investigation of Solid Electrolyte Interphase Layer Formation and Electrochemical Reversibility of Magnetite, Fe₃O₄, Electrodes: A Combined X-ray Absorption Spectroscopy and X-ray Photoelectron Spectroscopy Study. *J. Phys. Chem. C* **122**, 14257–14271 (2018).
191. Chattopadhyay, S., Lipson, A. L., Karmel, H. J., Emery, J. D., Fister, T. T., Fenter, P. A., Hersam, M. C. & Bedzyk, M. J. In situ X-ray study of the solid electrolyte interphase (SEI) formation on graphene as a model Li-ion battery anode. *Chem. Mater.* **24**, 3038–3043 (2012).
192. Wang, Y., Nakamura, S., Ue, M. & Balbuena, P. B. Theoretical studies to understand surface chemistry on carbon anodes for lithium-ion batteries: Reduction mechanisms of ethylene carbonate. *J. Am. Chem. Soc.* **123**, 11708–11718 (2001).

193. Balbuena, P. B. First Principles Modeling of SEI Formation on Bare and Surface / Additive Modified Silicon Anodes. (2015).
194. Vassiliev, S. Y., Sentyurin, V. V., Levin, E. E. & Nikitina, V. A. Diagnostics of lithium-ion intercalation rate-determining step: Distinguishing between slow desolvation and slow charge transfer. *Electrochim. Acta* **302**, 316–326 (2019).
195. Zheng, M., Tang, H., Li, L., Hu, Q., Zhang, L., Xue, H. & Pang, H. Hierarchically Nanostructured Transition Metal Oxides for Lithium-Ion Batteries. *Adv. Sci.* **5**, 1700592 (2018).
196. Zhou, J., Song, H., Chen, X., Zhi, L., Yang, S., Huo, J. & Yang, W. Carbon-encapsulated metal oxide hollow nanoparticles and metal oxide hollow nanoparticles: A general synthesis strategy and its application to lithium-ion batteries. *Chem. Mater.* **21**, 2935–2940 (2009).
197. Ming, J., Park, J. B. & Sun, Y. K. Encapsulation of metal oxide nanocrystals into porous carbon with ultrahigh performances in lithium-ion battery. *ACS Appl. Mater. Interfaces* **5**, 2133–2136 (2013).
198. Luo, L., Wu, J., Xu, J. & Dravid, V. P. Atomic resolution study of reversible conversion reaction in metal oxide electrodes for lithium-ion battery. *ACS Nano* **8**, 11560–11566 (2014).
199. Karki, K., Wu, L., Ma, Y., Armstrong, M. J., Holmes, J. D., Garofalini, S. H., Zhu, Y., Stach, E. A. & Wang, F. Revisiting Conversion Reaction Mechanisms in Lithium Batteries: Lithiation-Driven Topotactic Transformation in FeF₂. *J. Am. Chem. Soc.* **140**, 17915–17922 (2018).
200. Evmenenko, G., Warburton, R. E., Yildirim, H., Greeley, J. P., Chan, M. K. Y., Buchholz, D. B., Fenter, P., Bedzyk, M. J. & Fister, T. T. Understanding the Role of Overpotentials in Lithium Ion Conversion Reactions: Visualizing the Interface. *ACS Nano* **13**, 7825–7832 (2019).
201. Choi, S. H., Lee, J. H. & Kang, Y. C. Perforated Metal Oxide-Carbon Nanotube Composite Microspheres with Enhanced Lithium-Ion Storage Properties. *ACS Nano* **9**, 10173–10185 (2015).
202. Sun, J., Lv, C., Lv, F., Chen, S., Li, D., Guo, Z., Han, W., Yang, D. & Guo, S. Tuning the Shell Number of Multishelled Metal Oxide Hollow Fibers for Optimized Lithium-Ion Storage. *ACS Nano* **11**, 6186–6193 (2017).
203. Du, N., Zhang, H., Chen, J., Sun, J., Chen, B. & Yang, D. Metal oxide and sulfide hollow spheres: Layer-by-layer synthesis and their application in lithium-ion battery. *J. Phys. Chem. B* **112**, 14836–14842 (2008).
204. Tao, S., Yue, W., Zhong, M., Chen, Z. & Ren, Y. Fabrication of graphene-encapsulated porous carbon-metal oxide composites as anode materials for lithium-ion batteries. *ACS Appl. Mater. Interfaces* **6**, 6332–6339 (2014).

205. Lee, D., Wu, M., Kim, D. H., Chae, C., Cho, M. K., Kim, J. Y., Lee, S. S., Choi, S., Choi, Y., Shin, T. J., Chung, K. Y., Jeong, S. & Moon, J. Understanding the Critical Role of the Ag Nanophase in Boosting the Initial Reversibility of Transition Metal Oxide Anodes for Lithium-Ion Batteries. *ACS Appl. Mater. Interfaces* **9**, 21715–21722 (2017).
206. Nordh, T., Younesi, R., Hahlin, M., Duarte, R. F., Tengstedt, C., Brandell, D. & Edström, K. Manganese in the SEI Layer of Li₄Ti₅O₁₂ Studied by Combined NEXAFS and HAXPES Techniques. *J. Phys. Chem. C* **120**, 3206–3213 (2016).
207. Harris, O. C. & Tang, M. H. Molecular Probes Reveal Chemical Selectivity of the Solid-Electrolyte Interphase. *J. Phys. Chem. C* **122**, 20632–20641 (2018).
208. Lin, Z., Du, C., Yan, B., Wang, C. & Yang, G. Two-dimensional amorphous NiO as a plasmonic photocatalyst for solar H₂ evolution. *Nat. Commun.* **9**, 4036 (2018).
209. Chen, Y. M., Yu, X. Y., Li, Z., Paik, U. & Lou, X. W. Hierarchical MoS₂ tubular structures internally wired by carbon nanotubes as a highly stable anode material for lithium-ion batteries. *Sci. Adv.* **2**, e1600021 (2016).
210. Xu, M., Li, W. & Lucht, B. L. Effect of propane sultone on elevated temperature performance of anode and cathode materials in lithium-ion batteries. *J. Power Sources* **193**, 804–809 (2009).
211. Wang, Y., Wang, Z., Chen, Y., Zhang, H., Yousaf, M., Wu, H., Zou, M., Cao, A. & Han, R. P. S. Hyperporous Sponge Interconnected by Hierarchical Carbon Nanotubes as a High-Performance Potassium-Ion Battery Anode. *Adv. Mater.* **30**, 1–10 (2018).
212. Wu, Z., Wang, Y., Liu, X., Lv, C., Li, Y., Wei, D. & Liu, Z. Carbon-Nanomaterial-Based Flexible Batteries for Wearable Electronics. *Adv. Mater.* **31**, 1–25 (2019).
213. Harlow, J. E., Ma, X., Li, J., Logan, E., Liu, Y., Zhang, N., Ma, L., Glazier, S. L., Cormier, M. M. E., Genovese, M., Buteau, S., Cameron, A., Stark, J. E. & Dahn, J. R. A Wide Range of Testing Results on an Excellent Lithium-Ion Cell Chemistry to be used as Benchmarks for New Battery Technologies. *J. Electrochem. Soc.* **166**, A3031–A3044 (2019).
214. Zhang, S. S. The redox mechanism of FeS₂ in non-aqueous electrolytes for lithium and sodium batteries. *J. Mater. Chem. A* **3**, 7689–7694 (2015).
215. Yersak, T. A., Macpherson, H. A., Kim, S. C., Le, V. D., Kang, C. S., Son, S. B., Kim, Y. H., Trevey, J. E., Oh, K. H., Stol dt, C. & Lee, S. H. Solid state enabled reversible four electron storage. *Adv. Energy Mater.* **3**, 120–127 (2013).
216. Ferraro, M. E., Trembacki, B. L., Brunini, V. E., Noble, D. R. & Roberts, S. A. Electrode Mesoscale as a Collection of Particles: Coupled Electrochemical and Mechanical Analysis of NMC Cathodes. *J. Electrochem. Soc.* **167**, 013543 (2020).
217. Ebner, M., Geldmacher, F., Marone, F., Stampanoni, M. & Wood, V. X-Ray Tomography of Porous, Transition Metal Oxide Based Lithium Ion Battery Electrodes. *Adv. Energy Mater.* **3**, 845–850 (2013).

218. Guo, J. & Liu, J. A binder-free electrode architecture design for lithium-sulfur batteries: A review. *Nanoscale Adv.* **1**, 2104–2122 (2019).
219. Pham, C. Van, Liu, L., Britton, B., Walter, M., Holdcroft, S. & Thiele, S. Stabilization of Li-S batteries with a lean electrolyte: Via ion-exchange trapping of lithium polysulfides using a cationic, polybenzimidazolium binder. *Sustain. Energy Fuels* **4**, 1180–1190 (2020).
220. Mandal, M., Huang, G., Hassan, N. U., Mustain, W. E. & Kohl, P. A. Poly(norbornene) anion conductive membranes: homopolymer, block copolymer and random copolymer properties and performance. *J. Mater. Chem. A* **8**, 17568–17578 (2020).
221. Gao, S., Feng, X., Lu, L., Kamyab, N., Du, J., Coman, P., White, R. E. & Ouyang, M. An experimental and analytical study of thermal runaway propagation in a large format lithium ion battery module with NCM pouch-cells in parallel. *Int. J. Heat Mass Transf.* **135**, 93–103 (2019).

APPENDIX A: COPYRIGHT & PERMISSIONS



IOP Publishing, Ltd - License Terms and Conditions

This is a License Agreement between Benjamin Ng / University of South Carolina ("You") and IOP Publishing, Ltd ("Publisher") provided by Copyright Clearance Center ("CCC"). The license consists of your order details, the terms and conditions provided by IOP Publishing, Ltd, and the CCC terms and conditions.
All payments must be made in full to CCC.

Order Date	07-Jan-2021	Type of Use	Republish in a thesis/dissertation
Order license ID	1088928-1	Publisher	IOP Publishing
ISSN	1945-7111	Portion	Image/photo/illustration

LICENSED CONTENT

Publication Title	Journal of the Electrochemical Society	Country	United States of America
Author/Editor	Electrochemical Society.	Rightholder	IOP Publishing, Ltd
Date	01/01/1948	Publication Type	e-Journal
Language	English	URL	http://www.scitation.org/JES

REQUEST DETAILS

Portion Type	Image/photo/illustration	Distribution	Worldwide
Number of images / photos / illustrations	1	Translation	Original language of publication
Format (select all that apply)	Print, Electronic	Copies for the disabled?	No
Who will republish the content?	Academic institution	Minor editing privileges?	No
Duration of Use	Life of current edition	Incidental promotional use?	No
Lifetime Unit Quantity	Up to 499	Currency	USD
Rights Requested	Main product		

NEW WORK DETAILS

Title	DEGRADATIVE PROCESSES OF COMMERCIAL AND NEXT-GENERATION LITHIUM-ION BATTERY MATERIALS	Institution name	University of South Carolina
Instructor name	William E Mustain	Expected presentation date	2021-01-26

ADDITIONAL DETAILS

Order reference number	N/A	The requesting person / organization to appear on the license	Benjamin Ng / University of South Carolina
------------------------	-----	---	--

REUSE CONTENT DETAILS

Title, description or numeric reference of the portion(s)	Figure 1.	Title of the article/chapter the portion is from	Threefold Increase in the Young's Modulus of Graphite Negative Electrode during Lithium Intercalation
Editor of portion(s)	N/A	Author of portion(s)	Electrochemical Society.
Volume of serial or monograph	N/A	Issue, if republishing an article from a serial	N/A
Page or page range of portion	A559	Publication date of portion	2021-01-26

Figure A.1 Copyright permission for **Figure 1.2**. Qi, Y., Guo, H., Hector, L. G. & Timmons, A. Threefold Increase in the Young's Modulus of Graphite Negative Electrode during Lithium Intercalation Threefold Increase in the Young's Modulus of Graphite Negative Electrode during Lithium Intercalation. *J. Electrochem. Soc.* **157**, A558–A566 (2010).

Thank you for your order.

This Agreement between University of South Carolina -- Benjamin Ng ("You") and John Wiley and Sons ("John Wiley and Sons") consists of your license details and the terms and conditions provided by John Wiley and Sons and Copyright Clearance Center.

Your confirmation email will contain your order number for future reference.

License Number	4983940884585	Printable Details	
License date	Jan 07, 2021		
<input checked="" type="checkbox"/> Licensed Content		<input type="checkbox"/> Order Details	
Licensed Content Publisher	John Wiley and Sons	Type of use	Dissertation/Thesis
Licensed Content Publication	Advanced Energy Materials	Requestor type	University/Academic
Licensed Content Title	Narrowing the Gap between Theoretical and Practical Capacities in Li-Ion Layered Oxide Cathode Materials	Format	Print and electronic
Licensed Content Author	Anton Van der Ven, Y. Shirley Meng, M. Stanley Whittingham, et al	Portion	Figure/table
Licensed Content Date	Jul 4, 2017	Number of figures/tables	1
Licensed Content Volume	7	Will you be translating?	No
Licensed Content Issue	20		
Licensed Content Pages	33		

Figure A.2 Copyright permission for **Figure 1.3**. Radin, M. D., Hy, S., Sina, M., Fang, C., Liu, H., Vinckeviciute, J., Zhang, M., Whittingham, M. S., Meng, Y. S. & Van der Ven, A. Narrowing the Gap between Theoretical and Practical Capacities in Li-Ion Layered Oxide Cathode Materials. *Adv. Energy Mater.* **7**, 1–33 (2017).

Thank you for your order.

This Agreement between University of South Carolina -- Benjamin Ng ("You") and Springer Nature ("Springer Nature") consists of your license details and the terms and conditions provided by Springer Nature and Copyright Clearance Center.

Your confirmation email will contain your order number for future reference.

License Number	4984501358569	Printable Details	
License date	Jan 08, 2021		
<input checked="" type="checkbox"/> Licensed Content		<input type="checkbox"/> Order Details	
Licensed Content Publisher	Springer Nature	Type of Use	Thesis/Dissertation
Licensed Content Publication	Nature Energy	Requestor type	academic/university or research institute
Licensed Content Title	A materials perspective on Li-ion batteries at extreme temperatures	Format	print and electronic
Licensed Content Author	Marco-Tulio F. Rodrigues et al	Portion	figures/tables/illustrations
Licensed Content Date	Jul 24, 2017	Number of figures/tables/illustrations	1
		High-res required	no
		Will you be translating?	no
		Circulation/distribution	200 - 499
		Author of this Springer Nature content	no
<input type="checkbox"/> About Your Work		<input type="checkbox"/> Additional Data	
Title	DEGRADATIVE PROCESSES OF COMMERCIAL AND NEXT-GENERATION LITHIUM-ION BATTERY MATERIALS	Portions	Figure 1 (e-h)
Institution name	university of south carolina		
Expected presentation date	Jan 2021		
<input type="checkbox"/> Requestor Location		<input type="checkbox"/> Tax Details	
	University of South Carolina 301 Main St		
Requestor Location	Columbia, SC 29208 United States Attn: University of South Carolina		
\$ Price			
Total	0.00 USD		

Figure A.3 Copyright permission for **Figure 1.4** and **Figure 1.5** Rodrigues, M.-T. F., Babu, G., Gullapalli, H., Kalaga, K., Sayed, F. N., Kato, K., Joyner, J. & Ajayan, P. M. A materials perspective on Li-ion batteries at extreme temperatures. *Nat. Energy* **2**, 17108 (2017).

Thank you for your order.
This Agreement between University of South Carolina -- Benjamin Ng ("You") and Springer Nature ("Springer Nature") consists of your license details and the terms and conditions provided by Springer Nature and Copyright Clearance Center.

Your confirmation email will contain your order number for future reference.

License Number	4984520033811	Printable Details	
License date	Jan 08, 2021		
<input checked="" type="checkbox"/> Licensed Content		<input type="checkbox"/> Order Details	
Licensed Content Publisher	Springer Nature	Type of Use	Thesis/Dissertation
Licensed Content Publication	Nature Materials	Requestor type	academic/university or research institute
Licensed Content Title	Stabilized iron fluoride cathodes	Format	print and electronic
Licensed Content Author	Glenn G. Amatucci	Portion	figures/tables/illustrations
Licensed Content Date	Nov 20, 2019	Number of figures/tables/illustrations	1
		High-res required	no
		Will you be translating?	no
		Circulation/distribution	200 - 499
		Author of this Springer Nature content	no
<input type="checkbox"/> About Your Work		<input type="checkbox"/> Additional Data	
Title	DEGRADATIVE PROCESSES OF COMMERCIAL AND NEXT-GENERATION LITHIUM-ION BATTERY MATERIALS	Portions	Figure 1
Institution name	university of south carolina		
Expected presentation date	Jan 2021		
<input type="checkbox"/> Requestor Location		<input type="checkbox"/> Tax Details	
	University of South Carolina 301 Main St		
Requestor Location	Columbia, SC 29208 United States Attn: University of South Carolina		
\$ Price			
Total	0.00 USD		

Figure A.4 Copyright permission for **Figure 1.7**. Amatucci, G. G. Stabilized iron fluoride cathodes. *Nat. Mater.* **18**, 1275–1276 (2019).

Royal Society of Chemistry - License Terms and Conditions

This is a License Agreement between Benjamin Ng / University of South Carolina ("You") and Royal Society of Chemistry ("Publisher") provided by Copyright Clearance Center ("CCC"). The license consists of your order details, the terms and conditions provided by Royal Society of Chemistry, and the CCC terms and conditions.

All payments must be made in full to CCC.

Order Date	09-Jan-2021	Type of Use	Republish in a thesis/dissertation
Order license ID	1089265-1	Publisher	Royal Society of Chemistry
ISSN	2050-7496	Portion	Chart/graph/table/figure

LICENSED CONTENT

Publication Title	Journal of materials chemistry. A, Materials for energy and sustainability	Country	United Kingdom of Great Britain and Northern Ireland
Author/Editor	Royal Society of Chemistry (Great Britain)	Rightholder	Royal Society of Chemistry
Date	01/01/2013	Publication Type	e-Journal
Language	English	URL	http://pubs.rsc.org/en/journals/journaliss...

REQUEST DETAILS

Portion Type	Chart/graph/table/figure	Distribution	Worldwide
Number of charts / graphs / tables / figures requested	1	Translation	Original language of publication
Format (select all that apply)	Print, Electronic	Copies for the disabled?	No
Who will republish the content?	Academic institution	Minor editing privileges?	No
Duration of Use	Life of current edition	Incidental promotional use?	No
Lifetime Unit Quantity	Up to 499	Currency	USD
Rights Requested	Main product		

NEW WORK DETAILS

Title	DEGRADATIVE PROCESSES OF COMMERCIAL AND NEXT-GENERATION	Institution name	university of south carolina
Instructor name	William Mustain	Expected presentation date	2021-01-26

ADDITIONAL DETAILS

Order reference number	N/A	The requesting person / organization to appear on the license	Benjamin Ng / University of South Carolina
------------------------	-----	---	--

REUSE CONTENT DETAILS

Title, description or numeric reference of the portion(s)	Fig. 1	Title of the article/chapter the portion is from	Investigation of metal oxide anode degradation in lithium-ion batteries via identical-location TEM
Editor of portion(s)	N/A	Author of portion(s)	Royal Society of Chemistry (Great Britain)
Volume of serial or monograph	N/A	Issue, if republishing an article from a serial	N/A
Page or page range of portion	1627	Publication date of portion	2013-01-01

Figure A.5 Copyright permission for **Figure 1.8** and **Figure 3.1-Figure 3.12** Spinner, N., Zhang, L. & Mustain, W. E. Investigation of metal oxide anode degradation in lithium-ion batteries via identical-location TEM. *J. Mater. Chem. A* **2**, 1627–1630 (2014).



IOP Publishing, Ltd - License Terms and Conditions

This is a License Agreement between Benjamin Ng / University of South Carolina ("You") and IOP Publishing, Ltd ("Publisher") provided by Copyright Clearance Center ("CCC"). The license consists of your order details, the terms and conditions provided by IOP Publishing, Ltd, and the CCC terms and conditions.

All payments must be made in full to CCC.

Order Date	07-Jan-2021	Type of Use	Republish in a thesis/dissertation
Order license ID	1088936-1	Publisher	IOP Publishing
ISSN	1945-7111	Portion	Image/photo/illustration

LICENSED CONTENT

Publication Title	Journal of the Electrochemical Society	Country	United States of America
Author/Editor	Electrochemical Society.	Rightsholder	IOP Publishing, Ltd
Date	01/01/1948	Publication Type	e-Journal
Language	English	URL	http://www.scitation.org/JES

REQUEST DETAILS

Portion Type	Image/photo/illustration	Distribution	Worldwide
Number of images / photos / illustrations	9	Translation	Original language of publication
Format (select all that apply)	Print, Electronic	Copies for the disabled?	No
Who will republish the content?	Academic institution	Minor editing privileges?	No
Duration of Use	Life of current edition	Incidental promotional use?	No
Lifetime Unit Quantity	Up to 499	Currency	USD
Rights Requested	Main product		

NEW WORK DETAILS

Title	DEGRADATIVE PROCESSES OF COMMERCIAL AND NEXT-GENERATION LITHIUM-ION BATTERY MATERIALS	Institution name	University of South Carolina
Instructor name	William E Mustain	Expected presentation date	2021-01-26


ADDITIONAL DETAILS

Order reference number	N/A	The requesting person / organization to appear on the license	Benjamin Ng / University of South Carolina
------------------------	-----	---	--

REUSE CONTENT DETAILS

Title, description or numeric reference of the portion(s)	Figure 1, Figure 2, Figure 3, Figure 4, Figure 5, Figure 6, Figure 7, Figure 8, Figure 9	Title of the article/chapter the portion is from	Investigation of Transport and Kinetic Nonideality in Solid Li-Ion Electrodes through Deconvolution of Electrochemical Impedance Spectra
Editor of portion(s)	N/A	Author of portion(s)	Electrochemical Society.
Volume of serial or monograph	N/A	Issue, if republishing an article from a serial	N/A
Page or page range of portion	1-9	Publication date of portion	1948-01-01

Figure A.6 Copyright permission for **Figure 1.8** and **Figure 3.1-Figure 3.12**. Ng, B., Duan, X., Liu, F., Agar, E., White, R. E., Mustain, W. E. & Jin, X. Investigation of Transport and Kinetic Nonideality in Solid Li-Ion Electrodes through Deconvolution of Electrochemical Impedance Spectra. *J. Electrochem. Soc.* **167**, 020523 (2020).




Non-destructive parameter extraction for a reduced order lumped electrochemical-thermal model for simulating Li-ion full-cells
 Author: Benjamin Ng, Paul T. Coman, William E. Mustain, Ralph E. White
 Publication: Journal of Power Sources
 Publisher: Elsevier
 Date: 1 January 2020
 © 2019 Elsevier B.V. All rights reserved.

Please note that, as the author of this Elsevier article, you retain the right to include it in a thesis or dissertation, provided it is not published commercially. Permission is not required, but please ensure that you reference the journal as the original source. For more information on this and on your other retained rights, please visit: <https://www.elsevier.com/about/our-business/policies/copyright#Author-rights>

[BACK](#) [CLOSE WINDOW](#)

Figure A.7 Copyright permission for **Figure 2.2 to Figure 2.5** and . Ng, B., Duan, X., Liu, F., Agar, E., White, R. E., Mustain, W. E. & Jin, X. Investigation of Transport and Kinetic Nonideality in Solid Li-Ion Electrodes through Deconvolution of Electrochemical Impedance Spectra. *J. Electrochem. Soc.* **167**, 020523 (2020).



Low-Temperature Lithium Plating/Corrosion Hazard in Lithium-Ion Batteries: Electrode Rippling, Variable States of Charge, and Thermal and Nonthermal Runaway
 Author: Benjamin Ng, Paul T. Coman, Ehsan Faegh, et al
 Publication: ACS Applied Energy Materials
 Publisher: American Chemical Society
 Date: Apr 1, 2020
 Copyright © 2020, American Chemical Society

PERMISSION/LICENSE IS GRANTED FOR YOUR ORDER AT NO CHARGE

This type of permission/license, instead of the standard Terms & Conditions, is sent to you because no fee is being charged for your order. Please note the following:

- Permission is granted for your request in both print and electronic formats, and translations.
- If figures and/or tables were requested, they may be adapted or used in part.
- Please print this page for your records and send a copy of it to your publisher/graduate school.
- Appropriate credit for the requested material should be given as follows: "Reprinted (adapted) with permission from (COMPLETE REFERENCE CITATION). Copyright (YEAR) American Chemical Society." Insert appropriate information in place of the capitalized words.
- One-time permission is granted only for the use specified in your request. No additional uses are granted (such as derivative works or other editions). For any other uses, please submit a new request.

[BACK](#) [CLOSE WINDOW](#)

Figure A.8 Copyright permission for **Figure 1.8** and **Figure 3.1-Figure 3.12**. Ng, B., Duan, X., Liu, F., Agar, E., White, R. E., Mustain, W. E. & Jin, X. Investigation of Transport and Kinetic Nonideality in Solid Li-Ion Electrodes through Deconvolution of Electrochemical Impedance Spectra. *J. Electrochem. Soc.* **167**, 020523 (2020).

Royal Society of Chemistry - License Terms and Conditions

This is a License Agreement between Benjamin Ng / University of South Carolina ("You") and Royal Society of Chemistry ("Publisher") provided by Copyright Clearance Center ("CCC"). The license consists of your order details, the terms and conditions provided by Royal Society of Chemistry, and the CCC terms and conditions.

All payments must be made in full to CCC.

Order Date	08-Jan-2021	Type of Use	Republish in a thesis/dissertation
Order license ID	1088951-1	Publisher	Royal Society of Chemistry
ISSN	2050-7496	Portion	Chart/graph/table/figure

LICENSED CONTENT

Publication Title	Journal of materials chemistry. A, Materials for energy and sustainability	Country	United Kingdom of Great Britain and Northern Ireland
Author/Editor	Royal Society of Chemistry (Great Britain)	Rightsholder	Royal Society of Chemistry
Date	01/01/2013	Publication Type	e-Journal
Language	English	URL	http://pubs.rsc.org/en/journals/journaliss...

REQUEST DETAILS

Portion Type	Chart/graph/table/figure	Distribution	Worldwide
Number of charts / graphs / tables / figures requested	6	Translation	Original language of publication
Format (select all that apply)	Print, Electronic	Copies for the disabled?	No
Who will republish the content?	Academic institution	Minor editing privileges?	No
Duration of Use	Life of current edition	Incidental promotional use?	No
Lifetime Unit Quantity	Up to 499	Currency	USD
Rights Requested	Main product		

NEW WORK DETAILS

Title	DEGRADATIVE PROCESSES OF COMMERCIAL AND NEXT-GENERATION	Institution name	university of south carolina
Instructor name	William Mustain	Expected presentation date	2021-01-26

ADDITIONAL DETAILS

Order reference number	N/A	The requesting person / organization to appear on the license	Benjamin Ng / University of South Carolina
------------------------	-----	---	--

REUSE CONTENT DETAILS

Title, description or numeric reference of the portion(s)	Figure 1 - Figure 6	Title of the article/chapter the portion is from	Structure and chemistry of the solid electrolyte interphase (SEI) on a high capacity conversionbased anode: NiO
Editor of portion(s)	N/A	Author of portion(s)	Royal Society of Chemistry (Great Britain)
Volume of serial or monograph	N/A	Issue, if republishing an article from a serial	N/A
Page or page range of portion	523-537		

Figure A.9 Copyright permission for **Figure 5.1** to **Figure 5.6**. Ng, B., Faegh, E., Lateef, S., Karakalos, S. G., Mustain, W. E. Structure and Chemistry of the Solid Electrolyte Interphase on High Capacity Conversion-based Anodes: NiO. J. Mater. Chem. A, 2021, 9, 523

Using nanoconfinement to inhibit the degradation pathways of conversion-metal oxide anodes for highly stable fast-charging Li-ion batteries

B. Ng, X. Peng, E. Faegh and W. E. Mustain, *J. Mater. Chem. A*, 2020, **8**, 2712

DOI: 10.1039/C9TA11708C

This article is licensed under a [Creative Commons Attribution 3.0 Unported Licence](#). Material from this article can be used in other publications provided that the correct acknowledgement is given with the reproduced material.

Reproduced material should be attributed as follows:

- For reproduction of material from NJC:
[Original citation] - Published by The Royal Society of Chemistry (RSC) on behalf of the Centre National de la Recherche Scientifique (CNRS) and the RSC.
- For reproduction of material from PCCP:
[Original citation] - Published by the PCCP Owner Societies.
- For reproduction of material from PPS:
[Original citation] - Published by The Royal Society of Chemistry (RSC) on behalf of the European Society for Photobiology, the European Photochemistry Association, and RSC.
- For reproduction of material from all other RSC journals:
[Original citation] - Published by The Royal Society of Chemistry.

Information about reproducing material from RSC articles with different licences is available on our [Permission Requests page](#).

Figure A.10 Copyright permission for

Figure 6.1 to Figure 6.4. Ng, B., Faegh, E., Peng, X., Mustain, W. E. Using nanoconfinement to inhibit the degradation pathways of conversion-metal oxide anodes for highly stable fast-charging Li-ion batteries. *Journal of Materials Chemistry A*. (2020) **8**, 2712-2727

Correction: Poly(norbornene) anion conductive membranes: homopolymer, block copolymer and random copolymer properties and performance

M. Mandal, G. Huang, N. U. Hassan, W. E. Mustain and P. A. Kohl, *J. Mater. Chem. A*, 2020, **8**, 18386

DOI: 10.1039/D0TA90198A

This article is licensed under a [Creative Commons Attribution 3.0 Unported Licence](https://creativecommons.org/licenses/by/3.0/). Material from this article can be used in other publications provided that the correct acknowledgement is given with the reproduced material.

Reproduced material should be attributed as follows:

- For reproduction of material from NJC:
[Original citation] - Published by The Royal Society of Chemistry (RSC) on behalf of the Centre National de la Recherche Scientifique (CNRS) and the RSC.
- For reproduction of material from PCCP:
[Original citation] - Published by the PCCP Owner Societies.
- For reproduction of material from PPS:
[Original citation] - Published by The Royal Society of Chemistry (RSC) on behalf of the European Society for Photobiology, the European Photochemistry Association, and RSC.
- For reproduction of material from all other RSC journals:
[Original citation] - Published by The Royal Society of Chemistry.

Information about reproducing material from RSC articles with different licences is available on our [Permission Requests page](#).

Figure A.11 Copyright permission for **Figure 8.5**. Mandal, M., Huang, G., Hassan, N. U., Mustain, W. E. & Kohl, P. A. Poly(norbornene) anion conductive membranes: homopolymer, block copolymer and random copolymer properties and performance. *J. Mater. Chem. A* **8**, 17568–17578 (2020).